UNIVERSITEIT VAN PRETORIA
UNIVERSITY OF PRETORIA
YUNIBESITHI YA PRETORIA

The characteristics of Rossby wave packets in the South African domain

by

Tsholanang Solomon Rammopo

Submitted in fulfilment of the requirements for the degree

Master of Science in Meteorology

In the Department of Geography, Geoinformatics and Meteorology
Faculty of Natural and Agricultural Sciences
University of Pretoria

Pretoria

12 January 2023

Declaration

I, Tsholanang Solomon Rammopo declare that the dissertation, which I hereby submit for the degree Master of Science in Meteorology at the University of Pretoria, is my own work and has not previously been submitted by me for a degree at this or any other tertiary institution.

T.S Rammopo (13154402)

Signed:

Date: 12 January 2023

Abstract

Aspects of upper tropospheric Rossby wave packets (RWPs) over South Africa (SA) and adjacent oceans were explored. This study used a local finite ampltitude wave activity (LWA, A) diagnostic based on isentropic primitive equations and a feature tracking algorithm to track A pockets resembling RWPs in National Centre for Environmental Predictability (NCEP) re-analysis 2 data. Results of the tracking algorithm are first presented in the context of the Southern Hemisphere, then focus is shifted to the SA domain (0°-45°E; 22°-45°S) by means of a climatology. Morphological structures of tracked A pockets on 330 K and 350 K isentropic surfaces were found to be representative of typical extratropical upper tropospheric RWPs. Seasonal variability of RWP occurrences, intensity, duration, and propagation was examined for SA domain RWPs. Results were found to potentially have relevance in terms of the predictability of severe weather phenomena over the SA domain, in so far as non-linear RWPs may be related to cut-off low pressure systems over the SA domain.

Evolutionary characteristics of A pockets identified on 350 K were also examined based on potential vorticity, ambient zonal flow ($\overline{u_\theta}$), and meridonal wind perturbations ($\overline{v'_\theta}$). Results showed consistency with the well-established baroclinic life cycles. The development of these RWPs was found to conform to the downstream baroclinic development of the eddy kinetic energy (K_e) framework governed by baroclinic conversion and convergence of ageostrophic geopotential fluxes. This RWP representation was compared with the A budget tendency framework, which prompted a discussion of the advantages of combining a set of diagnostics when studying RWP life cycles. Implications of these results on the forecasting of extreme weather in SA are discussed.

Acknowledgements

I would first like to give thanks to God almighty and Badimo ba kwa Rammopo, Machele, le Mathekga for granting me the strength, ability, and courage to complete this Master's dissertation through all the challenges I have endured. This study would not have been possible without the contributions of the following:

1. My dear mother Rosina Flora Rammopo and late Father David Mokgopa Rammopo for being the best parents in the world. The continuous love and support you have showered us with from the day you brought us into this world have not gone unnoticed.

2. My siblings, Karabo Hlatswayo, Lynton Hlatswayo, Tshegofatso Rammopo, and Boipelo Rammopo for being my beacon of hope, source of inspiration, and pillar of strength. I love you guys.

3. My friend, idol, teacher, and supervisor, Professor Thando Ndarana (UP) for the consistent support and faith in me. Thank you very much Bra Prof for everything you have done for me, may you continue to inspire generations to come.

4. Professor Liesl Dyson (UP) for the support, mentorship, and constant encouragement to be the best version of myself. I appreciate it Prof.

5. The Department of Geography, Geoinformatics, and Meteorology (UP), thank you very much Professor Serena Coetzee (UP) for the support, opportunities, and experience throughout my study period in the department.

6. My friends Boipelo, Lesego, Resegofaditswe, Katlego, Steve, Thabo, Modikwe, Gretchen. Thank you for the continuous support and patience with me.

7. The Water Research Commission (WRC) and UP for funding this study.

8. Dr Paolo Ghinassi (Institute for Atmospheric Physics at Johannes Gutenberg University of Mainz) for the LWA scripts and technical support.

List of important acronyms, abbreviations, and some definitions

1. Cut off low pressure system – CoL,
2. Downstream Baroclinic Development – DBD,
3. Eddy Kinetic Energy – EKE (K_e),
4. Eddy Potential Energy – EPE (P_e),
5. Estimated dynamical tropopause PV contour – PV^{TP},
6. Finite amplitude finite amplitude Rossby wave activity – FAWA,
7. Geography, Geoinformatics, and Meteorology – GGM,
8. H_1 – RWP Hotspot 1 located over the Australia-New Zealand sector,
9. H_2 – RWP hotspot 2 located over the Subtropical South Pacific Ocean west of South America,
10. H_3 – RWP hotspot 3 located over the Subtropical South Atlantic Ocean east of South America,
11. Isentropic surface – θ_n, where n denotes the isentropic level in Kelvins (K),
12. KwaZulu-Natal – KZN,
13. Local finite amplitude Rossby wave activity – LWA,

14. Polar front jet stream – PFJ,

15. Polar night jet stream – PNJ,

16. Potential vorticity units – PVU,

17. Potential vorticity – PV,

18. Quasi Geostrophic – QG,

19. Quasi Geostrophic Potential vorticity – QG_{PV},

20. Rossby wave packet – RWP,

21. Rossby wave breaking – RWB,

22. South Africa – SA,

23. South Atlantic Ocean – SAO,

24. South Indian Ocean – SIO,

25. South Pacific Ocean – SPO,

26. South Atlantic Convergence Zone – SACZ,

27. South Pacific Convergence Zone – SPCZ,

28. South Indian Convergence Zone – SPCZ,

29. Subtropical jet stream – STJ,

30. Tropical Temperate Trough – TTT,

31. University of Pretoria – UP,

32. Water Research Commission – WRC.

Table of Contents

Abstract iii

Acknowledgments iv

List of important acronyms, abbreviations, and some definitions vi

Table of Contents x

List of Tables xi

List of Figures xix

1 Introduction 1

1.1 Background 1

1.1.1 The South African climate 1

1.1.2 Rossby waves 2

1.1.3 Rossby Wave Packets 6

1.2 Research Problem and Motivation 8

1.3 Aims and objectives of the study 12

1.4 Dissertation overview 13

2 Literature Review 15

2.1 Potential vorticity 15

2.2 Rossby waves 17

2.2.1 Downstream development of baroclinic Rossby waves 20

2.3 Rossby wave packets . . . 25
2.3.1 Rossby wave packet diagnostics . . . 27
2.3.2 Vertical propagation of RWPs . . . 31
2.3.2.1 The dynamical tropopause . . . 32

3 Data and Methods **35**
3.1 Data . . . 35
3.2 Diagnostics . . . 36
3.2.1 Local finite wave activity (LWA) . . . 36
3.2.1.1 A budget for LWA . . . 42
3.2.2 Eddy Kinetic Energy (K_e) . . . 42
3.2.3 An estimate for the dynamical tropopause . . . 46
3.3 Algorithms . . . 47
3.3.1 FAWA computation . . . 47
3.3.2 RWP tracking . . . 49
3.3.3 Composite analysis . . . 51

4 Climatological aspects of LWA and associated RWPs **54**
4.1 Seasonal variability of LWA . . . 54
4.2 LWA, the Jet stream, and the dynamical tropopause . . . 64
4.3 LWA RWP morphology . . . 67
4.4 Variability of LWA objects tracked . . . 74
4.4.1 Generation, Maturity, and Dissipation regions of SH RWPs . . . 75
4.4.2 Seasonal variability of tracked SH RWPs . . . 80
4.5 RWPs in the SA domain . . . 87
4.5.1 An estimate for the Dynamical Tropopause . . . 87
4.5.2 Seasonal variability of RWPs over South Africa . . . 93
4.5.3 Characteristics of RWPs over SA . . . 98
4.6 Chapter synopsis . . . 111

5 Dynamics of RWPs over SA **114**

5.1 Evolution of RWPs over SA 116

5.1.1 Summer 118

5.1.1.1 Development 118

5.1.1.2 Maturity and Decay 122

5.1.2 Winter Development, Maturity, and Decay 124

5.1.3 The role of the jet stream 129

5.2 Eddy Kinetic Energy and Downstream Development of RWPs 134

5.2.1 Eddy Kinetic Energy 135

5.2.2 Downstream development of RWPs 139

5.2.2.1 Comparison between LWA and EKE 149

5.3 Chapter Synopsis 158

6 Concluding Remarks **161**

6.1 Climatological aspects of RWPs 161

6.2 Evolutionary characteristics 166

References **170**

List of Tables

4.1 A summary of SH RWP seasonal counts and percentages in brackets relative to the total number of RWPs on an isentrope summed between 20°S and 85°S. For each θ surface, the table is arranged as follows: The first row is the sum of all RWPs detected (bold), and the second (third) row is the sum of those RWPs over regions with more than (two or less) detected RWP objects. The highest (lowest) values are highlighted in red (blue). 84

4.2 A summary of the estimated mean PV^{TP} values (PVU). 87

4.3 As in Table 4.1, but for the SA domain 94

List of Figures

1.1 Map showing the southern African domain region of interest. 1

1.2 Depiction of the 350 K autumn (a) and spring (b) jet streams in the Northern and Southern Hemispheres. The split flow regime characterised by the thermally driven subtropical and eddy driven extratropical jets is indicated in the Southern Hemisphere. Adapted from Homeyer and Bowman (2013). 3

1.3 Schematic illustration of an instantaneous meridionally averaged view of a mature RWP in a background flow (dashed curves). Red curves represent the envelope of the RWP amplitude. Blue curves represent the individual disturbances embedded within an RWP. 6

2.1 Schematic illustration of the 3 stages of downstream baroclinic development preceeding SA domain CoL: a,c,e (normal linear Rossby wave: b,d,f) formation described in the text. Black thin contours denote baroclinic Rossby waves, the brown shadings show the intensity of individual K_e centers labelled using Roman numerals I-IV. The locations of weak, strong, and very strong baroclinic conversion are denoted by W-BCC, S-BCC, and VS-BCC, respectively. The barotropic conversion is signified by BTC. The red (black) arrows indicate ageostrophic geopotential (horizontal K_e) fluxes. Dashed closed contours show the size and position of upstream (UJ) and downstream (DJ) jet streaks. Orientation of the ridge and trough axes of interest are represented by the solid and dashed straight lines respectively. Adapted from Ndarana et al. (2023) (under review). 23

2.2 Schematic perspective of a Rossby wave propagating eastward along a latitude circle $x = \lambda$. The Rossby wave is characterised by two RWPs that evolve with time at differing zonal group speeds. See the text for details. Adapted from Vallis (2017). 26

2.3 Schematic perspective of a Rossby wave propagating eastward along a latitude circle as in Figure 2.2, but for one RWP. Key features of RWP propagation, amplification, and decay are highlighted. See the text for further details. Adapted from Wirth et al. (2018). 27

2.4 Mean θ-PV vertical profile where the colorshading denotes the zonally averaged (in the SH) PV in PVU and the -2 PVU contour is highlighted in red. The dashed wavy lines represent zonally averaged (in the SH) θ in K. The over, middle, and underworld regions of the atmosphere are indicated in magenta. (adapted from Hoskins (1991)) 32

3.1 Illustration of Ghinassi et al. (2018) LWA computation in the Southern Hemisphere. A distorted PV contour Q is displaced relative to the reference mass latitude Φ_M. The line integration is done along a longitude λ constrained by the paths of integration l_s and l_n defined in the text. The result of the computation is depicted in the bottom panel. Adapted from Ghinassi et al. (2018). 40

3.2 Illustration of composite analysis relative to the southern African domain highlighted by the red boundary. LWA RWPs (blue ovals with dots) and associated PV contours (black) are used as an example. The RWP centers are denoted by blue dots. The left (right) hand panels represent the geographical (event (E) relative) grid form of composite means. In the last row the composite mean behaviour of LWA and PV are shown in thick magenta and dashed blue contours. Morphological behaviour of PV contours is better elucidated in the event relative grid space centered at (λ_E,ϕ_E). The green arrow denotes the direction of the summation to avoid ambiguity. 53

4.1 Seasonal distribution(a. summer(DJF), b. autumn (MAM), c. winter (JJA), d. spring(SON)) of LWA in ms^{-1} on θ_{330}. The blue contours are the corresponding mean isotachs of the zonal component of the wind ($\overline{u_\theta}$ = 25-30 ms^{-1}: solid, 35-55 ms^{-1}: dashed) and denote the position of the jet stream on θ_{330}. The H1-H3 symbols denote the LWA hotspots referred to in the text. The thick black contour line denotes the corresponding -2 PVU dynamical tropopause. 56

4.2 As in Figure 4.1 but for θ_{350}. 57

4.3 Mean zonally averaged seasonal distribution (summer (DJF) to spring (SON) (a-d)) of LWA ($\overline{A}$) in ms^{-1} with respect to θ. H1-H3 highlight wave activity hotspots. Note that to demonstrate this, the temporal mean was computed for only a 10 year period between 2009 and 2019. 58

4.4 Time lagged composite mean of meridionally averaged v' depicting the zonal extent of an RWP at time t= 0 h of the composite evolution on 330K(a) and 350K(b) isentropic surfaces. The undulations were constructed by computing the meridional average of v' at 850hPa (v'_{850},grey) and 200hPa (v'_{200},black). The red curves filled with blue shading denote the envelopes of the RWP computed using a Hilbert transform, while the dark(light) grey shadings represent areas of enhanced(decreased) baroclinicity. 68

4.5 Time lagged composite mean of RWPs diagnosed based on LWA (top panels) and v' (bottom panels) for the 330K (a) and 350K (b) isentropic surfaces during time t = 0 h when the RWP attains maturity. The shading represents LWA (ms^{-1}), the black closed contours represent isentropic meridional wind perturbations $v'_\theta < 0$ (dashed) and $v'_\theta > 0$ (solid), where only ± 2,10 and 16 ms^{-1} isotachs are shown. The heavy black contours are the PV = -0.7 and -2 PVU isolines in a and b respectively. The bottom panels are as in Figure 4.2, but for the region 90°W - 90°E of the RWP. 70

4.6 Distribution of total number of RWP objects detected on 330K (a) and 350K (b) surfaces (color shading). The panels are arranged as follows: top, middle and bottom panels represent the development (start), maturity, dissipation (end) areas of RWP objects respectively. The climatolgical mean jet stream is represented by the zonal component of the horizontal wind isotachs (thick solid black contours: 25-35 ms^{-1}) The South African (SA) domain is highlighted by the red box where the subdivisions correspond to the subtropical (north) and extratropical (south) subregions of the SA domain. 77

4.7 330K Seasonal distribution(a. summer (DJF), b. autumn (MAM), c. winter (JJA), and d. spring (SON)) of the number of mature RWPs detected. The colored dots represent the maximum LWA intensity ($\overline{A}_{max}$) in ms^{-1} observed during the mature stage of the RWP life cycle. The black solid contour represents the -2 PVU PV contour, and the South African (SA) domain is highlighted by the red box where the subdivisions correspond to the subtropical (north) and extratropical (south) subregions of the SA domain. 82

4.8 As in Figure 4.7, but for 350K. 86

4.9 Illustration of the PV gradient method used to estimate values of the dynamical tropopause (PV^{TP}) associated with extra-tropical RWP events on θ_{350} during summer (a) and winter (b) months. From top to bottom, the panels represent: PV, the meridional gradient of PV, the magnitude of the horizontal wind (u_h), and the product of the meridional PV gradient, and the horizontal wind, all in equivalent latidude (ϕ_e) space. Solid red, dashed, and dotted lines represent the coordinate of the mean, median, and standard deviation (upper and lower bounds) of PV^{TP}, respectively. 88

4.10 Location of the estimated dynamical tropopauses against the ambient zonal flow (u) on θ_{330}. The colorshading in ms^{-1} denotes u_{330} , averaged over each season for the 40 year climatological period (1979-2019). The thick black isoline is the standard dynamical tropopause value, PV = -2 PVU contour, while the peach coloured contours are the estimated dynamical tropopause values (PV^{TP}) based on Kunz et al. (2011a). For these estimates, the solid lines represent the mean of the PV^{TP} estimate based on extratropical and subtropical RWPs in the SA domain. The dashed (dotted) lines are PV^{TP} based on subtropical (extratropical) RWPs. Note that these values are plotted from the $\overline{PV_{330}}$ field calculated in a similar manner as u_{330}. The red rectangular box shows the domain SA domain, with the subtropical (extratropical) residing north (south) of the dotted line within this region. 91

4.11 As in Figure 5.12, but for the θ_{350} isentrope. 92

4.12 θ_{330} (a-d) and θ_{350} (e-h) Seasonal counts of SA RWPs (white-grey shading), and the corresponding zonal wind isotachs (rainbow colorshading in ms^{-1}). Three dynamical tropopause estimates are added here: -2 PVU contour (black solid line), the objectively estimated dynamical tropopause (PV^{TP}) for subtropical and extratropical RWPs (black dotted and dashed lines respectively) taken from Table 4.3. 96

4.13 θ_{330} (a-d) and θ_{350} (e-h) Seasonal counts of SA RWPs (white-grey shading), and the maximum amplitude/intensity (A_{max}) (rainbow colorshading in ms^{-1}). Two dynamical tropopause estimates are added here: -2 PVU contour (black solid line), the mean of the objectively estimated PV^{TP} for subtropical and extratropical RWPs (black dashed lines respectively). . . . 99

4.14 As in Figure 4.13 but for duration (days). 101

4.15 As in Figure 3.12 but for distance travelled by RWP objects in km. 103

4.16 θ_{330} (left panels) and θ_{350} (right panels) seasonal distribution of the number of RWPs (color shading) maturing over the SA region (highlighted by the red box). The blue contour lines denote the spatial distribution of the number of RWPs tied to mature RWPs over the SA at 0.5 intervals beginning from 1. Development regions are denoted by pink circles, maturity points are shown by grey coloured arrows and these are connected by the dark grey lines. Development points were estimated by calculating the composite mean location associated with every maturity point having at least one mature RWP event. The mean direction (solid black arrows) was estimated by computing the mean start and maturity coordinates of all grid points with atleast one RWP specific to each sub domain of SA. 107

4.17 As in Figures 4.12 but for speed (ms^{-1}). 110

5.1 Schematic illustrating the panel configuration used in the discussions pertaining time-lagged composite mean evolution of RWPs identified over the SA domain. The top panels represent the two-dimensional (2D) horizontal domain that captures the instantaneous behaviour of RWPs. In this illustration, LWA (A) is shown in colour shading, with the RWP/LWA pocket isolated by the closed contours in this field, while smaller values are muted using a uniform colour (e.g, white or grey). PV contours are denoted by black curves, and the jet stream is shown by white isotachs. The perturbation isentropic meridional wind (v'_θ) is shown by closed blue isotachs where the dashed (solid) contours denote $v' < 0$ ($v' > 0$). The bottom panel shows the corresponding meridionally averaged (over the extent of the meridional dimension of the SA domain (i.e, 20°S-45°S)) v' field. The red curves are the corresponding RWP envelopes estimated using the Hilbert transform based on the meridionally averaged v' field. Within the region enclosed by these curves, the meridionally averaged diagnostics will be superimposed to show their behaviour relative to the 2D representation of the RWP. 115

5.2 Time lagged composite mean of RWPs diagnosed based on LWA (top panels) and v' (bottom panels) for θ_{330} (left column) and θ_{350} (right column) during their 3 day development phase. The color shading represents LWA (A in ms^{-1}), the blue contours denote $v' < 0$:dashed and $v' > 0$(solid) in ms^{-1} (interval = 4 ms^{-1}) and the thick (thin) black contours are PV isolines estimating PV^{TP} (deforming contours). Bottom panels represent corresponding meridionally averaged v' depicting the zonal extent of an RWP at each time steps. The undulations were constructed by computing the meridional average of v' at 850 hPa (v'_{850}, white) and 200 hPa (v'_{200}, black). The red curves filled with blue shading denote the envelopes of the RWP computed using a Hilbert transform. 120

5.3 As in Figure 5.2, but for the 3 day decay phase of the RWPs. 124

5.4 As in Figure 5.2, but for the winter season. 126

5.5 As in Figure 5.3, but for the winter season. 128

5.6 Composite mean evolution illustrating the interaction of θ_{350} jet streams and RWPs during on summer and winter months respectively (left to right). Colorshading (white contours) represents the full (basic state) isotachs of the zonal components of the horizontal wind $\overline{u}_\theta$ [ms^{-1}]. The red contours denote isotachs of v' (interval = 4 ms^{-1}) as in Figures 5.1-5.4, while the location of LWA pocket centers are shown in green (dashed (solid) for $A_{350} = 25$ ($A_{330} = 30$) ms^{-1}) during winter. For summer: dashed (solid) for $A_{350} = 25$ ($A_{330} = 30$) ms^{-1}. 131

5.7 Summer (a,c,e,g,i,k) and wintertime (b,d,f,h,j,l) time-lagged composite mean evolution of vertically integrated K_e (color shading in $\mathrm{m}^2\mathrm{s}^{-2}$) in relation with v' [red dashed(solid) isotachs: $v' < 0$ ($v' > 0$), contour resolution = $\pm$ 4ms^{-1}]. The solid black lines denote the PV isopleth representative of the estimated dynamical tropopause (PV^{TP}). 138

5.8 Development stage of Summer (left panels) and winter (right panels) time-lagged composite mean evolution of K_e as in Figure 5.7. Included here are $\overline{u}$ (white isotachs), $\cdot(\boldsymbol{V_a}\phi)$ (magenta coloured arrows), and $\cdot(\boldsymbol{V}_{total}K_e)$ (navy blue coloured arrows), the vector scale is represented by the single black arrow in Figure 5.8 (e). Bottom plots are the RWP envelope as in Figures 5.1-5.4 with the isobaric v' and curves removed. Embedded within the RWP structure are meridionally averaged K_e budget terms represented in the legend; ∂tK_e is shown in dashed black curves, while $-\nabla_p \cdot \boldsymbol{V}K_e$, and BRT curves are shown in navy blue, magenta, cream white, and cyan colors in $\mathrm{m^2 s^{-3}}$. 142

5.9 As in Figure 5.8, but for the decay stage of RWPs. 149

5.10 Development stage of Summer (left panels) and winter (right panels) time-lagged composite mean evolution of $K_e = 96$ (summer) and 104 (winter) $\mathrm{m^2 s^{-2}}$ represented by yellow contours. The colorshading denotes $\partial_t K_e$ ($\mathrm{m^2 s^{-3}}$), dashed (solid) magenta contours are $\partial_t A_{avg} \cos\phi < 0$ ($\partial_t A_{avg} \cos\phi > 0$). LWA pockets are represented by green contours, while the solid black contours are the dynamical tropopauses. Bottom panels are as in Figure 5.1 for each time step 153

5.11 Development stage of Summer (left panels) and winter (right panels) time-lagged composite mean evolution of $K_e = 96$ (summer) and 104 (winter) $\mathrm{m^2 s^{-2}}$. The colorshading denotes $T_{c_{avg}}$, while dashed (solid) purple contours are $T_{n_{avg}} < 0$ and $T_{n_{avg}} > 0$. The rest of the features are as in previous plots. 154

5.12 As in Figure 5.10, but for the decay stage. 157

5.13 As in Figure 5.11, but for the decay stage. 158

Chapter 1

Introduction

1.1 Background

1.1.1 The South African climate

The subject of this study is the atmospheric dynamical processes of the Southern African domain, with particular emphasis on the South African (SA) subcontinent. This region/domain is defined here as the boundary box: 0° - 45°E; 22.5° - 45°S highlighted in Figure 1.1 by the white rectangle. The climate of this region is driven by several processes, as well as its varied topography. These processes include ocean currents originating from the cold South Atlantic Ocean (SAO) located west of the land and the warm South Indian Ocean (SIO) located east of the country. These are the cold Benguela and warm Mozambique currents, respectively. The former brings about cold and dry conditions, while the latter is an excellent source of warm moist air for most parts of the country, especially the east coast. Additionally, there exists a warm Agulhas current that is characterised by high velocities and extends from the SIO region (Lutjerhams, 2007). The latitudinal position

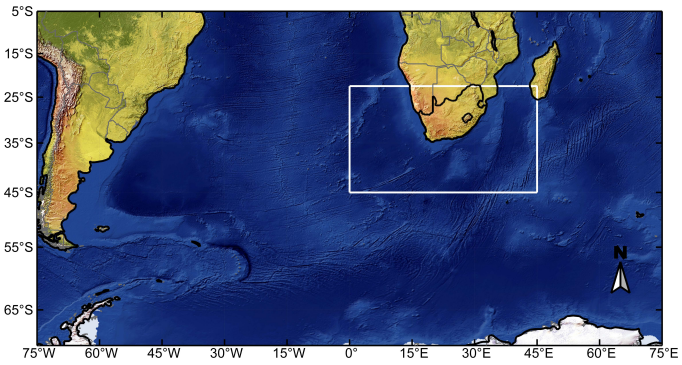

Figure 1.1: Map showing the southern African domain region of interest.

of SA is such that it can be classified as a subcontinent located in the subtropics between 22° and 35°S (Tyson and Preston-Whyte, 2000).

A number of weather systems are of relevance for this region. First, extratropical cyclones associated with cold fronts bring about cold conditions over the interior parts of the country during the predominantly dry winter season. However, along coastal regions, winter rains associated with these extratropical cyclones affect the southern and southern coasts of the country (Weldon and Reason, 2014). The south coast experiences rainfall during all seasons (Engelbrecht et al., 2015). Cold fronts are often followed by the ridging of the South Atlantic Ocean high-pressure system that can bring moisture to the north eastern parts (Ndarana et al., 2021; Ivanciu et al., 2022, Ndarana et al., 2022b). Upper-level processes also affect the region. These include upper-level troughs and, to a more significant extent, cutoff low-pressure systems (CoL) that are significant rain-bearing systems over different parts of the country (Favre et al., 2013). In general, SA experiences the most rainfall during summer due to the pronounced thunderstorm activity during this season as a consequence of the arrival (from lower latitudes) of the Inter Tropical Convergence Zone (ITCZ) which brings in tropical moisture to the country (Taljaard, 1996), also allowing for pronounced convective activity over the northeastern parts of the country (Gill, 2009; Hart et al., 2012; Blamey and Reason, 2012; Hart et al., 2013; Liesker, 2021). Other tropical processes such as the Tropical Temperate Troughs (TTT; Hart et al., 2012; Taljaard, 1996) and Continental Tropical Low Pressure Systems (CTLs; also referred to as Africánes) are also important features of the summertime conditions in SA (Webster, 2019; Viljoen et al., 2022).

1.1.2 Rossby waves

The idealized upper tropospheric flow pattern appears to to be predominantly in an eastward direction along isobars over the midlatitudes as viewed on a map. This picture is likely to be manifest when considering the long-term mean of the flow ($\boldsymbol{V}$), which gives

rise to the notion of a basic/steady-state atmosphere. On a geographical map, the spatial distribution of the basic state flow would appear as a circumglobal pattern of meridionally confined wind vectors/barbs. The flow is commonly described in terms of the zonal component of the horizontal wind. When the temporal mean of this quantity is considered, distinct features appear in the spatial distribution. These manifest themselves as regions of enhanced westerly flow known as jet streams.

In the Southern Hemisphere there are essentially two types of jet streams, namely; the subtropical (STJ) and the extratropical, which is also known as the polar front (PFJ) jet streams. These are shown in Figure 1.2 during autumn and spring months on the 350 K isentropic surface. The STJ is driven by the thermal processes associated with the Hadley cell and is most pronounced during the winter months. In contrast, the PFJ owes its existence to baroclinic eddies and is a constant feature of the Southern Hemisphere over the extratropics (Lee and Kim, 2003; Gallego et al., 2005). When these two jet stream regimes are considered in tandem, the resultant configuration is referred to as the split jet flow (see, e.g., Bals-Elsholz et al., 2001) as indicated in Figure 1.2. The orientation and intensity of these climatological features are very important aspects in the propagation of baroclinic eddies in the upper troposphere (see, e.g., Hoskins and Ambrizzi, 1993; Branstator, 2002).

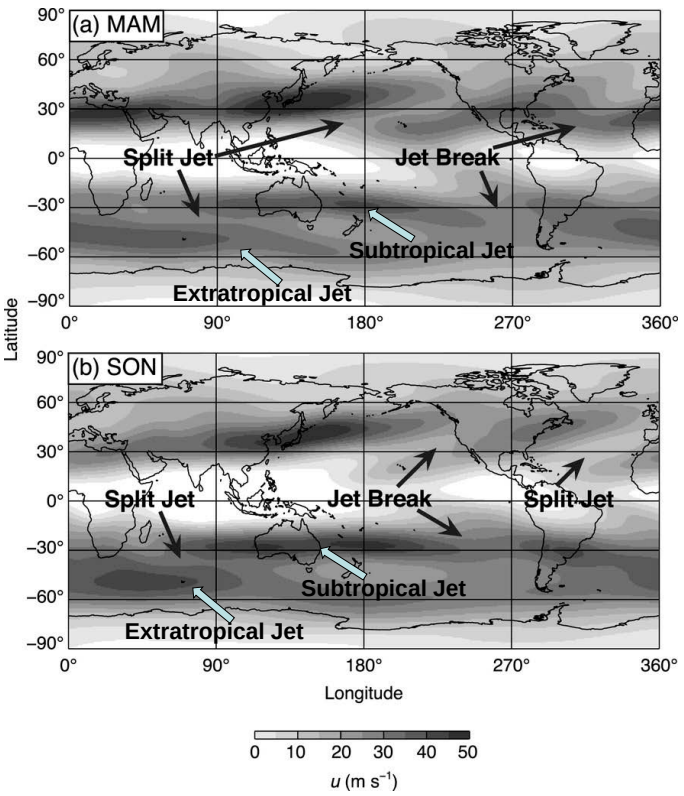

Figure 1.2: Depiction of the 350 K autumn (a) and spring (b) jet streams in the Northern and Southern Hemispheres. The split flow regime characterised by the thermally driven subtropical and eddy driven extratropical jets is indicated in the Southern Hemisphere. Adapted from Homeyer and Bowman (2013).

The upper tropospheric instantaneous flow is however characterized by undulations (disturbances in the meridional direction) as opposed to the purely zonal direction of the westerly flow in question (i.e, zonally oriented jet streams). The signature/pattern of these disturbances are known as Rossby or Planetary waves (Rossby, 1939; Rossby, 1940). Rossby waves conserve absolute vorticity assuming that the atmosphere is a height-invariable (barotropic) and frictionless fluid (Holton and Hakim, 2014). The rotation of the Earth, as well as its sphericity, are important features of the atmospheric model that give rise to the Coriolis effect represented by the Coriolis parameter ($f = 2\Omega \sin \phi$; Ω is the angular velocity of the Earth, ϕ represents latitudes). It is the latitudinal variation of the Coriolis parameter that facilitates the existence of Rossby waves in this barotropic model. More generally, Rossby waves conserve potential vorticity (PV) in a baroclinic atmosphere so that their existence is facilitated by potential vorticity (PV) gradients on isentropic (i.e, surface of constant potential temperature (θ)) coordinates (Holton and Hakim, 2014; Wirth et al., 2018).

For large-scale atmospheric processes, upper-tropospheric Rossby Waves and their properties (e.g propagation mechanisms) are of significant importance. They are capable of transferring kinetic energy, momentum, and moisture over long distances (Charney and Drazin, 1961; Wirth et al., 2018; Ghinassi et al., 2018). Their ability to transmit these quantities from upstream regions to their downstream neighbours suggests that Rossby waves can be seen as a source of the observed association between variables at spatially distant locations, giving rise to the notion of teleconnection patterns (Branstator, 2002; Wirth et al., 2018; Teubler and Riemer, 2020). In a more general sense, it stands to reason that Rossby waves are a crucial part to our understanding of the general circulation model of the atmosphere (Wirth et al., 2018; Ghinassi et al., 2018) through this spatial linkage of variables and processes. A typical demonstration of this linkage involves Rossby wave propagation, as elucidated by the study of Hoskins and Ambrizzi (1993) and Ambrizzi et al. (1995).

These studies (Hoskins and Ambrizzi (1993) and Ambrizzi et al. (1995)) showed that locally forced upper tropospheric Rossby waves tend to propagate northeastward away from an extratropical source region in the absence of a jet stream. In contrast, Rossby waves have a tendency to first propagate northeastward towards the background/basic state flow (jet stream), followed by predominantly eastward propagation along the jet stream. This implies that initial properties (e.g, energy, momentum, wave-activity, moisture) associated with components of Rossby waves can propagate according to the governing Rossby wave propagation regime into remote areas, where they may influence atmospheric conditions. Lin (2019) showed the existence of a summertime Rossby wave train responsible for rainfall and surface temperature variability over parts of Australia. In light of this impact, they view this Rossby wave a teleconnection pattern (termed: SAIO) that extends between the South Atlantic and South Indian Oceans (SAIO) along the extratropical jet stream. 200 hPa meridional wind anomalies revealed that this Rossby wave train likely has its in the tropical eastern Pacific ocean region.

Rossby waves are usually characterized by their zonal extent as represented by the number of troughs and ridges (meridional excursions of air parcels) defining the presumably circumpolar closed chain of disturbances. This gives rise to the zonal wavenumber, where k = 1 (2) refers to a circumpolar Rossby wave characterized by one (two) trough and ridge couplet(s) over the 360° latitudinal circle. Typically, zonal wave numbers 1-3 (>= 5) represent planetary (synoptic) scale Rossby waves (Wirth et al., 2018). For local weather phenomena such as cut-off low pressure systems (Ndarana et al., 2021) and ridging high pressure systems (Ndarana et al., 2022), synoptic scale Rossby waves are often of particular interest. This is because synoptic scale Rossby waves have typical temporal and spatial scale values in the order of those of the weather systems in question (i.e, life spans in the order of $\approx$ 1-2 days, and a zonal extent $\approx$ 1000 km (Holton and Hakim, 2014)). Clearly, when one has the desire to study the dynamics of weather phenomena affecting a specific region, it is imperative to identify the range of wave numbers of interest as a constraint, but this may not be enough. Higher zonal wavenumbers values represent higher frequency

(more number of trough-ridge couplets) synoptic scale Rossby waves. It follows then that it is important to identify specific trough-ridge couplets that are most relevant to the problem at hand. This state of affairs leads to the utility of the concept of a Rossby wave packet (RWP).

1.1.3 Rossby Wave Packets

RWPs are Rossby waves that have a peak in amplitude centred in space, followed by a systematic decrease in amplitude as you move further away from the centre towards the upstream (left) and downstream (right) regions flanking the centre (see Figure 1.3). On a typical upper tropospheric weather map, these would appear as a group of trough-ridge couplets that are confined to a specific sector of the hemisphere. RWPs do not always span the hemispheric extent (Wirth et al., 2018; Ghinassi et al., 2018; Fragkoulidis and Wirth, 2020), and several RWPs of varying amplitudes could coexist, but at different longitudes over the extratropics. Therefore, it is useful to study Rossby waves based on regions of importance, a feat that can be achieved through the utility of RWPs.

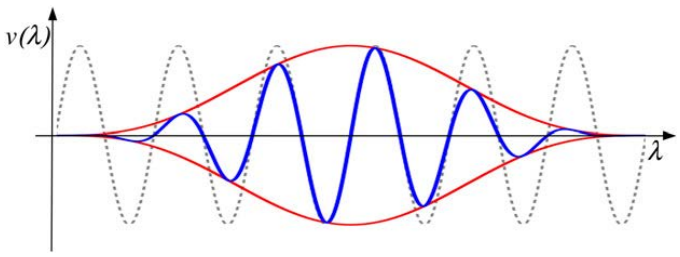

Figure 1.3: Schematic illustration of an instantaneous meridionally averaged view of a mature RWP in a background flow (dashed curves). Red curves represent the envelope of the RWP amplitude. Blue curves represent the individual disturbances embedded within an RWP.

It is beneficial to study Rossby wave propagation from an RWP point of view because it makes it possible to trace and track energy transfer in the upper troposphere. For example, the RWP has a very clear physical structure that is defined by the envelope around the wave group (superimposed zonal depiction of troughs and ridges) propagates at the group velocity. When this group velocity, at which wave energy propagates, is greater than the phase speed, then new disturbances can develop ahead of the RWP though downstream development (Orlanski and Katzfey, 1991), a consequence of the dispersive nature of linear

Rossby waves (Wirth et al., 2018; Ghinassi et al., 2018; Holton and Hakim, 2014). It is through this process that Rossby waves are able to transmit energy from upstream to downstream regions (Charney and Drazin, 1961; Orlanski and Katzfey, 1991; Wirth et al., 2018; Ghinassi et al., 2018; Teubler and Riemer, 2020).

As a consequence of downstream development, RWPs can be seen as precursors to the development of disturbances that may develop into local weather phenomena. Recent studies have demonstrated the existence and influence of this process on the development of CoLs in South Africa (Ndarana et al., 2021) and intense CoLs in the Southern Hemisphere (Pinheiro et al., 2022). Other studies have also made the link between pre existing RWPs and significant weather events such as heavy rainfall (e.g, Martius et al., 2008), temperature extremes (e.g, Fragkoulidis and Wirth, 2020), intense surface cyclones, and heat waves (Parker et al., 2014a; O'Brien and Reeder, 2017) to name a few. It follows then that RWPs can be viewed as sources of predictability, as well as a diagnostic tool for studying dynamics of weather phenomena. Much of the work that has gone into understanding RWPs has been restricted to those Rossby waves (and RWPs) on the midlatitude waveguide. A Rossby wave wave-guide can loosely be understood as a specific channel that allows for RWP propagation so that RWPs propagate along or though it. In both hemispheres, the strong mid-latitude westerly flow known as jet stream serves this role, giving rise to the notion of a jet wave guide (Wirth et al., 2018).

Several RWP diagnostics have been proposed for differing purposes. For example, zonal propagation of RWPs has been studied widely over the years using Hovmöller diagrams (e.g, Hovmöller, 1949; Martius et al., 2006; Glatt et al., 2011), while Zimin et al. (2003) proposed an improved Hilbert transform-based method for constructing an envelope of the meridional wind undulations along a latitude circle. Both of these approaches assume that the propagation and orientation of the RWP are in the zonal direction. This means that their applications have limitations because in the event of non-linear RWPs that may have a meridional component as they propagate, and subsequently assume a tilted orientation so

that a meridional average results in destructive interference of the highly deformed troughs and ridges. In addition, they can be seen as operational tools because they are merely diagnostic tools. To address some of these problems, quantities that have corresponding budget equations have been used. These include the energetics framework, of which the eddie kinetic energy (EKE) is of particular relevance (Orlanski and Katzfey, 1991).

The application of this diagnostic is usually hampered by the fact that EKE is not a globally conserved quantity. Wave activity, a measure of the waviness of a PV contour, emerges as one of the most useful diagnostics for RWPs. Its strength lies in its global conservation property under adiabatic conditions, meaning that the role of conservative and non-conservative processes affecting the evolution of an RWP can be elucidated. The most recent formulation by Ghinassi et al.(2018) is defined in both horizontal directions, under the primitive equation framework on an isentropic vertical coordinate system. Additionally, it makes no assumption about the wave amplitude, so that small and finite amplitude RWPs can be detected using the diagnostic, and studied explicitly using the corresponding tendency equation. This diagnostic is an improvement over earlier versions whose utility was often hampered by the assumptions made in their derivations. For example, the Andrews and McIntyre (1976) formulation is a zonally averaged diagnostc which is only applicable for small amplitude RWPs under quasi-geostrophic conditions. Daily weather maps show that this is far from the reality of things, as RWPs typically depict non-linear behaviour and are often finite/large amplitude segments of Rossby waves (Ghinassi, 2019).

1.2 Research Problem and Motivation

Several studies have examined RWPs in the Southern Hemisphere (SH). These include Souders et al. (2014a, b), O'brien and Reeder (2017), and more recently Peréz et al. (2021). Souders et al. (2014a) introduced a feature tracking algorithm based on the meridional wind envelope. Specifically, a set of rules was applied to a filtered meridional wind

field in a similar manner as in Zimin et al. (2006), and those envelopes meeting the criteria were admitted as RWPs. Subsequently, a global climatology based on tracked objects was produced (Souders et al., 2014b). Souders et al. (2014b) showed consistency with previous studies and ideas about extratropical storm activity, or storm tracks (see, e.g., Hoskins and Hodges, 2005) where RWP activity and RWP objects coincided with the locations of storm track maxima characterised by high baroclinicity (Hoskins and Hodges, 2005; Souders et al., 2014b; Wirth et al., 2018)). A similar approach was adopted by Peréz et al. (2021) to also produce a climatology of RWPs during summertime, and their results corroborate the findings of Souders et al. (2014b). Their main concern in these studies was to investigate the influence of the El-nino Southern Oscillation (ENSO) and Southern Annular Mode (SAM) on the generation of long-lived RWPs in the SH during summertime.

It was found that ENSO played an insignificant role in modulating the occurrence of long-lived RWPs, whereas a negative SAM phase corresponded to an increase in long-lived RWPs, and vice versa. The increase stems from the northward migration of the extratropical jet during this negative phase, particularly over the South Indian Ocean domain, extending into the South Pacific Ocean domain. Although these studies offered valuable insight about SH RWPs' characteristics, RWPs over the SA domain, and much of the subtropics saw little to no signals of RWP activity because of the overwhelming extratropical RWPs' signature. The only subtropical signature of RWPs emerges over Australia during the July months (proxy for winter) in response to the advent of the subtropical jet stream. This appears to make sense when one considers that the extratropical jet stream acts as a wave-guide, throughout the year, while the subtropical jet emerges during winter to offer an additional waveguide branch.

O'Brien and Reeder (2017) studied the time-lagged composite mean evolution of upper-tropospheric summertime RWPs in the SH by leveraging the strong interaction between Rossby waves and the jet stream over different sectors of the SH; Southwest Chile, the entrance of the summertime jet, southwest Africa, the entrance of the summertime jet-

core, Indian Ocean, the exit of the summertime jet-core, southwest Australia, the exit of the summertime jet, and west Pacific, outskirts of the summertime jet-core sectors. The approach taken ensured that the RWPs in question are mobile in nature because the condition of pronounced potential vorticity (PV) gradients had to be satisfied as well. This is especially true because baroclinic Rossby waves owe their existence to and propagate along PV fronts as well (Holton and Hakim, 2014; Wirth et al., 2018). However, this appears to ignore a very important feature of baroclinic RWP life-cycles (Thorncroft et al., 1993), namely, Rossby wave breaking (RWB, McIntyre and Palmer, 1984; Postel and Hitchman, 1999; Hitchman and Huesmann, 2007; Berrisford et al., 2007; Ndarana and Waugh, 2011; Homeyer and Bowman, 2013), which is a dissipative process associated with eddie mixing from an absolute or potential vorticity perspective (Juckes and McIntyre, 1987; Killworth and McIntyre, 1985; Hartmann et al., 1989; Dritschel and McIntyre, 2008; Wirth et al., 2018). The climatology of Souders et al. (2014b) and Peréz et al. (2021) also clearly misrepresented this process. The reason for the coincidence of RWP activity hotspots and the storm tracks stems from the fact that the meridional wind variable is very sensitive to linear RWPs which are still undergoing baroclinic growth (Ghinassi et al., 2018; Ghinassi, 2019). On this basis, maxima in their amplitudes would be achieved sometime before, and upstream the onset region of nonlinear growth (Ghinassi, 2019). Therefore, this study aims to characterise RWPs that undergo RWB in the South African domain.

RWB can be diagnosed when PV contours become irreversibly deformed over over regions where the jet streams and PV gradients are weaker (the so-called surf zones according to: Postel and Hitchman, 1999)) so much that RWP propagation is hampered. It is important to factor RWB into the climatological studies of RWPs because the former is linked to extreme weather. For instance, several studies (e.g, Ndarana and Waugh, 2010; deVries et al., 2021) have shown that RWB is linked to CoLs, which may lead to floods over South Africa, as seen recently (e.g, Pinto et al., 2022). The relevance of this stage in the life-cycle of RWPs over the SA domain is further amplified by the fact that the rainfall associated with CoLs over the SA domain has in more than one occasion resulted in floods over the

south-east coast of SA in the province of Kwa-Zulu Natal (KZN), (e.g, Pinto et al., 2022). These floods resulted in the loss of life and significantly dire economic conditions for residents, and indeed the provincial government of the KZN. In general, CoLs are responsible for other severe weather conditions in SA, such as snowfall and about 25% of days associated with anomalous or extreme rainfall (Favre et al., 2013).

In light of the discussion above, it appears that several aspects of our current understanding of RWPs in the SH are open research questions. First, the climatologies of Souders et al. (2014b) and Peréz et al. (2021) apparently are sensitive to large amplitudes of meridional winds in response to enhanced low-level baroclinicity. As a result, during classification, there is a tendency to capture RWPs well before they mature (Ghinassi, 2019). Note that the maximum wave-amplitude criterion is put into place to ensure that RWPs are identified during their most mature stages. Failure to correctly classify RWP events results in the upstream bias of RWP locations. That is, a RWP could be placed several degrees west of where it actually matures. An interpretation of such a map could result in erroneous forecasting products/techniques that might develop from our knowledge of the RWP climatological spatial distribution. In our bid to study RWPs over the SA region, we must first confront the question: How different are the climatologies of finite-amplitude RWPs from almost-plane waves in the SH? Second, the evolutionary characteristics of finite-amplitude RWPs over the SA domain, and indeed the SH are yet to be studied. This opens up a host of other questions such as; which processes govern the evolution of finite-amplitude RWPs?, and whether or not the long-standing EKE-based paradigm of downstream development (Orlanski and Katzfey, 1991) is able to describe this evolution sufficiently?

It follows then that it is critically important to consolidate the current body of work pertaining to RWPs in the SH as motivated by the current state of affairs. That is, to make some considerable strides in improving the predictability of high-impact weather systems such as CoLs and associated severe weather, we must understand the underlying dynamics

governing their evolution. The utility of a time-asymmetric local finite-amplitude wave activity diagnostic, such as the formulation by Ghinassi et al. (2018), provides us with the opportunity to explicitly identify finite-amplitude nonlinear RWPs. A diagnostic that is based on the primitive set of equations in isentropic coordinates also enables us to select isentropic coordinates based on our latitudinal region of interest. In this way, signals of wave activity would be enhanced at subtropical latitudes by simply selecting the relevant isentropic surface. Conversely, one can also select an isentrope that adequately samples the extratropical latitude bands and combine it with signals over the subtropics to obtain a general view of the various wave guides if they exist.

1.3 Aims and objectives of the study

In light of the issues stated above, the aim of this research is to examine the characteristics of finite-amplitude upper tropospheric RWPs that mature in the SA domain using a diagnostic based on finite-amplitude wave activity. First, we hypothesise that regions of high density of occurrence of finite amplitude RWPs are collocated with with regions of favourable RWB occurrence as these are both associated with non-linearity in the context of Rossby wave morphology. Second, we hypothesise that the evolution of mature RWPs in the SA domain is not entirely on account of extratropical RWPs moving into and maturing in the SA domain (e.g, as in O'brien and Reeder (2017)). Instead, it may be sometimes influenced by subtropical processes; specifically, lower tropospheric level wave-activity over the South Atlantic basin subtropics can interact with extratropical wave-activity that eventually matures in the SA domain. The hypothesis is motivated by the fact that during summermonths, lower (in magnitude) PV isolines over the South Atlantic basin always exhibit significant waviness even in the long-term mean field. Additionally, this region appears to be associated with notable RWB frequencies (e.g, see Figure 7 in Ndarana and Waugh (2011)). Lastly, because eddy kinetic energy-based diagnostics are known to be sensitive to linear phases in the life cycles of RWPs (Ghinassi et al., 2018), they are therefore

unsuitable in the context of describing the full life cycle of finite amplitude RWPs. While this prompted the development of Ghinassi et al. (2018), it is unclear the extent to which the LWA formulation (Ghinassi et al., 2018) is actually able to elucidate the linear aspects of the evolution owing to its sensitivity to non-linear behavior. We therefore hypothesize that perhaps a better explanation of the evolution of RWPs can be obtained by combining the two frameworks/diagnostics. To successfully address the prevailing research goal and test the hypotheses formulated, the study objectives defined below are as follows.

- To create a climatology of local finite-amplitude wave-activity (LWA) and associated RWPs over the Southern Hemisphere.
- to create a climatology of RWPs and characteristics over the southern African domain.
- to establish the evolutionary characteristics of LWA during RWP evolution over the southern African domain,
- to establish whether the life cycle of finite-amplitude RWPs over the southern African domain can be explained by means of the downstream baroclinic development paradigm, and
- to compare finite amplitude wave activity and eddy kinetic energy behaviour during the evolution of RWPs over the southern African domain.

1.4 Dissertation overview

This dissertation is composed of 5 chapters in total. The current chapter is an introductory text. The second chapter consists of a review of the literature of the most important concepts related to RWPs. It serves to assist the reader by providing the necessary tools for the interpretation of the results presented in Chapters 4 and 5. Included in this chapter is a brief review of PV, Rossby waves, the dynamical tropopause, wave-activity and RWPs. A summary of the diagnostics (e.g, LWA, EKE) employed in this study is provided in

Chapter 3, together with a derivation of the local finite-amplitude wave activity (LWA). Additionally, the data and methods (including the tracking algorithm) are also included in chapter 3. Chapter 4 discusses aspects of the climatology of RWPs in both the SH and SA domain. Chapter 5 examines the evolutionary characteristics of FAWA based RWPs. Lastly, chapter 6 contains the discussion of the results, as well as the concluding remarks.

Chapter 2

Literature Review

2.1 Potential vorticity

The study of atmospheric dynamics hinges on our understanding of how the air mass moves. Characteristics of this movement include the direction and location of the flow. Since air masses are invisible to the naked eye, chemical quantities such as water vapour are useful diagnostics for some air mass properties (Sreenath, 1993). Collectively, these are known as chemical tracers (Holton and Hakim, 2014; Sreenath, 1993). The air mass properties can also be characterised using dynamical tracers. This class of tracers include potential temperature (θ), and potential vorticity (PV; P), (Hoskins et al., 1985; Holton and Hakim, 2014).

The mathematical definition of PV exists in different forms, for example, as the quasi-geostrophic PV (QGPV) (Charney and Stern 1962; Hoskins et. al,1985; Berrisford et al, 1993), Rossby (Rossby, 1940), or Ertel's PV (Ertel, 1942a, b) forms (Hoskins et al., 1985; Mofor and Lu, 2008). Of interest in this study is Ertel's formulation with θ as the vertical coordinate, the so called isentropic PV defined as:

$$P \equiv \frac{(\zeta_\theta + f)}{\sigma}, \tag{2.1}$$

Where $\zeta_\theta = \partial_x v - \partial_y u$ is the vertical component of relative vorticity in isentropic coordinates, $f = 2\Omega \sin \phi$ is the Coriolis parameter (planetary vorticity) such that $\zeta_\theta + f$ is the

absolute vorticity in isentropic coordinates and $\sigma = -g^{-1}\partial_\theta p$ is the isentropic layer density, where g is the gravitational acceleration constant (Hoskins et al., 1985; Nakamura and Solomon, 2011; Ghinassi et al., 2018). This term can be written as $\sigma = -g\partial_p\theta$ in isobaric coordinates such that the quantity $\partial_p\theta$ is the static stability parameter that describes the distance between the potential temperature surfaces measured in pressure units (as defined in Holton and Hakim, 2014). PV is measured in potential vorticity units (PVU), where 1 PVU = 10^{-6} K kg^{-1} m^2 s^{-1} (Hoskins et al., 1985; Holton and Hakim, 2014). Note that this formulation is simply an extension of (Rossby, 1940) from a finite number of θ layers to the full vertical extent of the atmospheric column (Hoskins et al., 1985; Mofor and Lu, 2008).

PV and θ are conserved quantities following the motion of an air parcel under dry and frictionless, adiabatic conditions (Hoskins et al., 1985; Holton and Hakim, 2014). This implies that a specific parcel of air will propagate along a specified isotherm of θ under adiabatic conditions when θ is used as a vertical coordinate for meteorological variables. This allows for the air parcel to be uniquely labelled, or "tagged" (Holton and Hakim, 2014), based on the quasihorizontal, or sometimes equator-ward sloping isentrope's magnitude (Holton and Hakim, 2004). Under assumed atmospheric conditions (i.e. frictionless adiabatic flow), an air parcel can be traced following the isocontour lines of PV cast on a θ surface (i.e., the flow is expected to be parallel to the PV isocontours), (Holton and Hakim, 2014). The conservation law for P can be expressed as:

$$D_t P = 0, \tag{2.2}$$

Where $D_t = \partial_t() + \boldsymbol{u} \cdot \nabla()$ is the material derivative following the motion of the hypothetical air parcel. According to Eq. 2.2, provided that the distance between two pressure surfaces remains constant (that is, σ remains constant), a northward (southward) translated air parcel will see a decrease (increase) in relative vorticity: $\zeta_\theta < 0$ ($\zeta_\theta > 0$). Therefore, it is through the change in ζ_θ and f that P would be maintained. Conversely, for a parcel with a non varying relative vorticity (i.e, ζ_θ remains constant), a northward

[southward] translated air parcel will see a decrease [increase] in P through $\sigma < 0$ [$\sigma > 0$] and f. It is through this adjustment of σ, ζ_θ, and f (due to meridional displacements) that Rossby waves are manifested. Because the conserved PV is a material (i.e, airmass) tracing quantity, the only change a PV isocontour can undergo is morphological under advective processes (Hoskins et al., 1985; Mofor and Lu, 2008).

This is a very useful property in tracing isolated airmasses in foreign environments such as when extra-tropical lower stratospheric air is located over the subtropics as a result of RWB or CoL formation (Ndarana and Waugh, 2010, Reyers and Shao, 2019; Barnes et al., 2021). It follows then that PV can be regarded as a key component in the understanding of Rossby waves and their characteristics (e.g. propagation) through its air parcel/mass tracing capability (Starr and Neiburger, 1940; Hoskins et al., 1985; Holton and Hakim, 2014; Mofor and Lu, 2008). An additional key property of PV is its invertibility principle (Hoskins et al., 1985). In simple terms, this principle states that basic meteorological variable fields such as the horizontal wind $\boldsymbol{V} = (u, v)$, geopotential height (z), and temperature (T) can be recovered from only the isentropic PV field constrained by suitable boundary conditions (Hoskins et al., 1985, Davis, 1992; Lackmann, 2011; Mofor and Lu, 2008). The horizontal wind vector $\boldsymbol{V} = (u, v)$ can be written in terms of a streamfunction ψ, so that $u = -\partial_x \psi$ and $v = \partial_y \psi$. Therefore the relative vorticity can also be rewritten in terms of ψ as: $\zeta = \partial_x^2 \psi + \partial_y^2 \psi = \nabla^2 \psi$. It follows then that if one is to solve for ζ, the Laplacian operator ∇^2 has to be 'inverted'.

2.2 Rossby waves

The importance of the Rossby waves described above prompts a review of some of their key characteristics. Although Rossby waves relevant in the context of this study are of a baroclinic nature (during their growth phase), much of their propagation features can be qualitatively described by a dispersion relation based on a barotropic model of the atmosphere with nondivergent horizontal flow (Holton and Hakim, 2014). Below, we summarise

some aspects of the derivation of the dispersion relation of barotropic Rossby waves based on Holton and Hakim (2014) and Vallis (2017).

Under the imposed conditions (i.e., frictionless, adiabatic flow), Eq. 2.1 reduces to $\zeta_a(x,y,t) \equiv \zeta(x,y,t) + f(y)$, absolute vorticity in Cartesian coordinates, and its conservation $D_t\zeta_a = 0$ for a barotropic atmosphere of constant depth. Here, the β-plane approximation (Rossby, 1939; Holton and Hakim, 2014) is applied so that the geometry of the earth's surface is projected on a two-dimensional horizontal plane, so that the coriolis parameter is a linear function of y; $f(y) = f_o + \beta y$, where $\beta = \partial_y f \simeq 2\Omega\cos(\phi/a)$. If linear wave theory is assumed, where any atmospheric variable x may be decomposed into two components; the basic state ($\overline{x}$) and pertubation (x') variables so that $x = \overline{x} + x'$, $|\overline{x}| >> |x'|$. This is known as the perturbation method where $\overline{x}$ is taken to represent the background state, while the perturbation represents a contribution by the eddies. Applied here, this technique yields: $\zeta_a = f + (\overline{\zeta} + \zeta')$. The linearized form of the barotropic vorticity equation (Eq. 2.3) below can then be obtained following the substition of the linearized ζ_a into $D_t\zeta_a = 0$ after ignoring the non-linear terms that materialize in the form of products involving the perturbation terms. Such terms are assumed to be small and thus negligible.

$$(\partial_t + \overline{u}\partial_x)\,\zeta' + \beta v' = 0 \tag{2.3}$$

The perturbation stream function form of the barotropic vorticity equation can also be obtained by replacing ζ' and v' with their perturbation stream function forms, $\zeta' = \nabla^2\psi'$ and $v' = \partial_x\psi'$, respectively to give:

$$(\partial_t + \overline{u}\partial_x)\,\nabla^2\psi' + \beta\partial_x\psi' = 0 \tag{2.4}$$

Under the assumption of linear Rossby waves, the linearized stream function form of the barotropic pertubation vorticity (Eq. 2.4) is assumed to be characterized by plane wave solutions of the form:

$$\psi' = \Re\left[\psi_o e^{i(kx+ly-\nu t)}\right], \tag{2.5}$$

Where $\Re$ denotes that we focus only on the real part of the solution, since we seek real solutions of the equation that have physical meaning. The complex constant, or the constant amplitude is represented by ψ_o, k and l are the zonal and meridional wave numbers respectively, and ν (Eq. 2.6) is the angular frequency of the wave, which defines the dispersion relation of Rossby waves below as:

$$\nu = \overline{u}k - \frac{\beta k}{k^2 + l^2}, \tag{2.6}$$

Here $\nu(k, l)$ is the angular frequency, $\overline{u}$ is the basic state horizontal velocity, and k and l and the zonal and meridional wave numbers. From this dispersion relation of barotropic Rossby waves, key characteristics of their zonal propagation such as earth surface relative zonal phase speed of each trough or ridge (c_{px}), and the group velocity (c_{gx}) of the entire wave structure/envelope can be defined as

$$c_{px} = \frac{v}{k} = \overline{u} - \frac{\beta}{k^2 + l^2}, \tag{2.7}$$

$$c_{gx} = \partial_k \nu = \overline{u} + \beta \frac{k^2 - l^2}{(k^2 + l^2)^2}, \tag{2.8}$$

From Eqs. 2.7 and 2.8, if we consider the propagation of the assumed linear barotropic Rossby waves relative to the background zonal flow so that:

$$c_{px} - \overline{u} = -\frac{\beta}{k^2 + l^2}, \tag{2.9}$$

$$c_{gx} - \overline{u} = \beta \frac{k^2 - l^2}{(k^2 + l^2)^2}, \tag{2.10}$$

We can infer that individual troughs and ridges of these Rossby waves should propagate westward relative to the background flow (that is, the jet stream) since $\beta \simeq 2\Omega \cos(\phi/a) >$

0. Additionally, since $c_{px} - \overline{u} \propto -1/(k^2 + l^2)$, lower-frequency or bigger waves should travel faster westward. On the other hand, $c_{gx} - \overline{u}$ can assume either sign, implying that Rossby waves can propagate either west or eastward, since the overall sign of the right-hand side (rhs) depends on the sign of the numerator of the rhs in Eq. 2.10. However, according to Holton and Hakim (2014), synoptic-scale Rossby waves tend to have $c_{px} > 0$, implying that a group of disturbances characterizing a Rossby wave tend to propagate eastward from a ground based reference, but at a lower speed than c_{gx} in the same eastward direction. Since energy of the Rossby wave is transported at a speed equal to c_{gx}, it follows then that the formation of new disturbances can occur downstream of pre-existing disturbances. This process is known as downstream development (Simmons and Hoskins, 1979; Chang, 1993, Wirth et al., 2018). This is a very important feature of baroclinic Rossby waves' propagation as it has implications on forecasting of weather systems at regions ahead of the location of an active Rossby wave.

2.2.1 Downstream development of baroclinic Rossby waves

The importance of the downstream development of disturbances alluded to above warrants its own brief review discussion. The development of baroclinic Rossby waves and their relationship with synoptic scale disturbances has been largely been understood from the traditional baroclinic-life cycle point of view following some of the earlier works of Charney (1947) and Eady (1949). Essentially, the life-cycle is characterized by a period of baroclinic (barotropic) growth (decay) during the development (termination) stage (Simmons and Hoskins, 1978). The baroclinic growth is classically characterized by a developing lower tropospheric/surface disturbance that arises from steep thermal gradients at that level. These gradients force vertical motion that ultimately interacts with pre-existing PV anomalies at upper tropospheric levels (Hoskins et al., 1985; Orlanski and Katzfey, 1991).

This view of baroclinic life-cycles of Rossby waves was further expanded (Thorncroft et al., 1993) using the Eliassen-Palm flux framework (Edmon et al., 1980) and modelling

experiments. The results for the growth of a baroclinic wave propagating equatorward towards the strongest westerlies were summarized into four stages; *Stage 1*: exponential growth of eddy kinetic energy (EKE) due to baroclinic instability during the fourth day of development. *Stage 2*: At about day 5 non-linear saturation in the lower troposphere takes place, and this stage is associated with surface frontogenesis at lower level isentropes. *Stage 3*: Rossby wave activity (i.e. PV anomalies associated with waviness) propagates upward toward and into the jet stream region. This process dominates the growth of EKE due to baroclinic instability between days 5-7. *Stage 4*: lower stratospheric-upper tropospheric non-linear saturation takes place. This saturation is associated with marked EKE decay following RWB associated with non-linear saturation (Thorncroft et al., 1993).

Much of the details of this process were understood from the point of view of Rossby wave trains or circumglobal Rossby waves, which prompted the eddy energy budget derivations of Orlanski and Katzfey (1991), who recognised that the prevailing notions had not been discussed in the context of local higher wave number synoptic scale Rossby waves manifesting as wave packets. Of particular interest from the set of equations is the budget for the eddy kinetic energy (K_e)

$$\partial_t K_e = -\boldsymbol{V}_3 \cdot \nabla_3 K_e - \nabla_p \cdot (\boldsymbol{v}\phi)_a - \omega^{'}\alpha^{'} - \boldsymbol{v} \cdot (\boldsymbol{v}_3 \cdot \nabla_3)\boldsymbol{V_m} + \boldsymbol{v} \cdot \overline{(\boldsymbol{v}_3 \cdot \nabla_3)\boldsymbol{v}} + \mathit{Residue}, \tag{2.11}$$

where $K_e = \boldsymbol{V} \cdot \boldsymbol{V}/2$, and $\partial_t K_e$ is its local tendency. Equation 2.11 is Orlanski and Katzfey (1991)'s formulation of the local K_e budget equation. For a total variable such as the horizontal wind vector partitioned as $\boldsymbol{V} = \boldsymbol{v} + \boldsymbol{V_m}$, smaller case variables denote the perturbation part of the variable (e.g. $\boldsymbol{v}$), while those tagged with m underscores (e.g., $\boldsymbol{V_m}$) denote the basic state component defined as the 31 day mean (as in Orlanski and Katzfey, 1991) centred about the time of an event of interest since the low frequency basic state has no significant influence on the ensuing analysis of the local K_e energetics budget

(Lackmann et al., 1999; Ndarana et al., 2021). Lastly, the 'underscore 3' appearing in some terms is included to highlight that the variable with this labelling is three dimensional (λ, ϕ, p), and 'underscore p' indicates a constant isobaric surface.

The first term $-\boldsymbol{V}_3 \cdot \nabla_3 K_e$ on the right-hand side (rhs) of Equation 2.11 is the advection of K_e by the three-dimensional flow. The second term $-\nabla_p \cdot (\boldsymbol{v}\phi)_a$ is referred to as the divergence/convergence of the ageostrophic geopotential fluxes. The 'subscript a' represents the ageostrophic wind part of $\boldsymbol{v}$ having removed much of the contribution of the non-divergent part (i.e, the geostrophic wind $\boldsymbol{v_g}$), (Orlanski and Katzfey, 1991). The third term $-\omega^{'}\alpha^{'}$ is known as the baroclinic conversion term describing the conversion of eddy available potential energy P_e to K_e through baroclinic interaction. The term $-\boldsymbol{v} \cdot (\boldsymbol{v_3} \cdot \nabla_3)\boldsymbol{V_m}$ is known as the Reynold's stress term, and sometimes as simply the barotropic conversion term (e.g, Decker and Martin, 2005). The time mean stress is denoted by $\boldsymbol{v} \cdot \overline{(\boldsymbol{v_3} \cdot \nabla_3)\boldsymbol{v}}$, and is associated with the Reynold's stress term (Orlanski and Katzfey, 1991; Decker and Martin, 2005), through their role in the conversion of K_e to mean kinetic energy (K_m). Orlanski and Katzfey (1991) diagnosed the life cycle of a cyclone in the SH using Equation 2.11. The robustness of their initial findings was later tested and confirmed using a primitive model of the atmosphere by Orlanski and Chang (1993). Finally, the findings were summarised in Orlanski and Sheldon (1995), where both idealised and observed cases were examined using this energetics framework which culminated in the now widely known and used paradigm of 'downstream baroclinic development.' Note that this section is concerned with the paradigm of downstream baroclinic development, and not necessarily Equation 2.11. As such, additional details related to this diagnostic are discussed in Chapter 3.

Piva et al. (2010) used this local energetics budget framework to diagnose the energetics of travelling troughs over the South American domain during winter, while Mullër et al. (2015) used it in their study of Rossby waves related to a cold event over the tropical regions of South America. Recently Ndarana et al. (2021) successfully applied it to diagnose the extratropical-subtropical connection of processes leading to CoL formation

over the SA domain, and Pinheiro et al. (2022) studied the energetics of SH intense CoLs. Results of the former summarised in a schematic (Figure 2.1) shows remarkable consistency between the classic schematic of Orlanski and Sheldon (1995), (see their Figure 3). As such, we base the subsequent discussion on Figure 2.1 since they are closely related to the context of the current study through the study region and Rossby wave types at play (i.e., CoLs materialise from the dissipative RWB of non-linear finite-amplitude waves).

Recent studies (see, e.g., Ndarana et al., 2021; Ndarana et al., 2023) found remarkable consistency between the classic schematics of downstream development presented in Orlanski and Sheldon (1995), but for CoLs and upper tropospheric almost planar/-linear Rossby waves. According to this framework, the evolution of a disturbance is characterized by three stages. To summarize these stages, we make reference to a pre-existing disturbance characterized by a ridge-trough-ridge triplet mimicking an RWP in the SH . During time steps preceding the first stage, a pre-existing K_e center is located between the upstream ridge and the central trough as it is undergoing systematic decay. This decay is governed

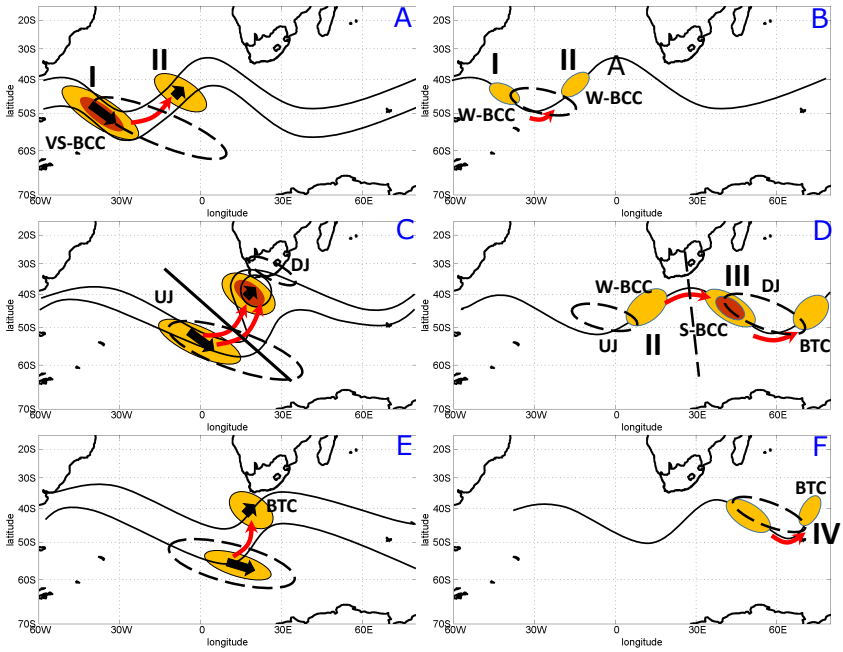

Figure 2.1: Schematic illustration of the 3 stages of downstream baroclinic development preceeding SA domain CoL: a,c,e (normal linear Rossby wave: b,d,f) formation described in the text. Black thin contours denote baroclinic Rossby waves, the brown shadings show the intensity of individual K_e centers labelled using Roman numerals I-IV. The locations of weak, strong, and very strong baroclinic conversion are denoted by W-BCC, S-BCC, and VS-BCC, respectively. The barotropic conversion is signified by BTC. The red (black) arrows indicate ageostrophic geopotential (horizontal K_e) fluxes. Dashed closed contours show the size and position of upstream (UJ) and downstream (DJ) jet streaks. Orientation of the ridge and trough axes of interest are represented by the solid and dashed straight lines respectively. Adapted from Ndarana et al. (2023) (under review).

by ageostrophic geopotential fluxes $(\boldsymbol{v}\phi)_a$ that point to the downstream side of the central trough of the triplet where they converge (that is, $-\nabla_p \cdot (\boldsymbol{v}\phi)_a > 0$) to promote the formation of a K_e centre there in line with a deepening trough and a reduction in the amplitude of the upstream ridge. (Figures 2.2 (a and b)) show the resulting K_e centre (K_{e_I}). K_{e_I} is amplified and maintained by baroclinic conversion (i.e, $-\omega'\alpha' > 0$), where it is very strong for the case of CoLs, and weak for non-CoL related Rossby waves. This signifies that stage 1 is at play, indicative of growth due to baroclinic instability.

The second stage is marked by the development of a downstream $K_{e_{II}}$ center due to $-\nabla_p \cdot (\boldsymbol{v}\phi)_a > 0$ at the apex/center of trough region for CoLs, and the downstream side of the trough for non-CoL related linear Rossby waves. The third and final stage sees this newly formed $K_{e_{II}}$ centre lose energy in a similar fashion to its preexisting counterpart initially located upstream during the first stage, while an additional $K_{e_{III}}$ centre forms between the mature trough and newly developing ridge's axes through ageostrophic flux convergence and strong baroclinic conversion downstream for linear Rossby waves. For CoLs however, the dissipation of $K_{e_{II}}$ is related to barotropic conversion. It is clear from this that only three processes are of particular significance for the generation and dissipation of K_e during this evolution; baroclinic conversion, convergence of ageostrophic geopotential fluxes, and barotropic conversion. Although K_e does not play a dissipative or generation role, it does act to translate or move the K_e centres predominantly eastward (black arrows in Figure 2.1).

We now revert back to the slightly idealised cases, downstream development of baroclinic Rossby waves can also be viewed from a PV perspective as illustrated in Figure 8 of Wirth et al. (2018). This process begins with a pre-existing disturbance in the form of a trough at some time t_1. The meridionally displaced (relative to some reference mid-latitude φ) PV contour envelopes a positive anomaly of PV. This anomaly induces anticyclonic (anticlockwise) flow in the SH, which in turn advects the PV contour poleward (equatorward) to its west (east). As a result, the incipient ridge would be shifted westward, while a new

trough characterized by a negative PV anomaly develops downstream of it at some time t_2. At this point, the Rossby wave consists of a ridge-trough couplet. A ridge-trough-ridge triplet forms at t_3 as a result of the "dipole" anticyclonic-cyclonic circulation induced by of the PV > 0 and PV < 0 anomalies. That is, a ridge develops downstream/east of the PV < 0 anomaly-induced cyclonic flow that acts to advect the PV poleward (equatorward) to its east (west).

2.3 Rossby wave packets

Upper tropospheric Rossby waves seldom exist or occur as a purely sinusoidal and circumpolar quantity (e.g. when viewed from a PV, geopotential height, or meridional wind perspective) in the atmosphere. Instead, they often occur as a zonally confined disturbance characterised by a few troughs and ridges along latitude circles. This disturbance would be associated with a local maximum amplitude, and progressively smaller amplitude troughs and ridges in the zonal direction (see Figure 1.3). We refer to the components of this local maximum, as well as its immediate neighbouring trough-ridge features, as Rossby wave packets (RWPs). As they are essentially zonally confined Rossby waves, some of the properties described above of Rossby waves lend their usefulness to this context as well.

Assuming v as the marker of the troughs and ridges defining an RWP, v' is often used in lieu of v to isolate the contribution of the eddies. v' is computed relative to the basic state ($\overline{v}$) taken as a 31-day time mean centred on the date of an event of interest as in the local energetics framework (Orlanski and Katzfey, 1991). Aspects of RWPs can be described by the linear solution $v'(\lambda, t) = A(\lambda, t)\cos(s\lambda - \nu t)$ where v' is as defined above, A is the time and longitude varying amplitude of the RWP, ν is as defined previously, and $s = ka\cos\phi$ is the zonal wavenumber of the RWP relative to some latitude circle ϕ. This expression reveals that the point of departure from the linear barotropic Rossby wave case is the evolution with time and space (λ) of the amplitude/envelope (A), (Wirth et al.,

2018; Ghinassi, 2019).

Figure 2.2 illustrates an idealized Rossby wave along a latitude circle ϕ where the envelope ($\pm A(\lambda, t)$) is denoted by the black undulating curves, and v' is represented by the blue higher frequency undulations ($v' < 0$ and $v' > 0$ [$v' < 0$ and $v' > 0$]) couplets marking ridge [trough] axis) at time t. A can be constructed by means of a Hilbert transform (Liu, 2012) applied to the v' signal at every time step as in Zimin et al. (2003). This Hilbert transform as an envelope reconstruction technique has its roots in the study and application of digital signals (see Liu (2012) for examples of its applications). This Rossby wave is characterized by two RWPs located at a distance away from each other. RWP1 propagates faster than RWP2 so that at t_2 it appears that RWP1 is catching up with RWP2. As RWP1 approaches RWP2, smaller undulations materialize at its leading edge, signifying the development of new disturbances. This situation illustrates the dispersive nature of Rossby waves, and indeed the motivation for Orlanski and Katzfey (1991). Observations of daily weather maps show that this is a very common situation in the upper troposphere, which serves as motivation to consider RWP diagnostics such as the energetics framework.

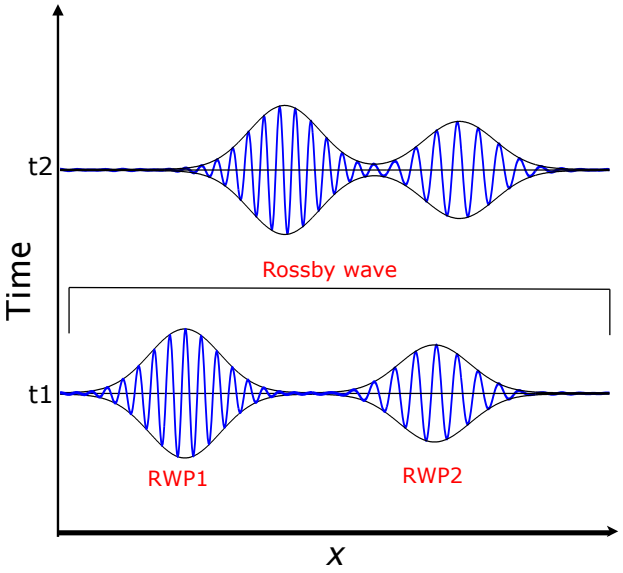

Figure 2.2: Schematic perspective of a Rossby wave propagating eastward along a latitude circle $x = \lambda$. The Rossby wave is characterised by two RWPs that evolve with time at differing zonal group speeds. See the text for details. Adapted from Vallis (2017).

To this end, Wirth et al. (2018) produced a schematic of the typical processes governing the life-cycle of an idealized RWP based on the energetics framework described earlier on. This schematic is presented in Figure 2.3, and serves as the basis for our interpretation of

the results presented in Chapter 5.

At the trailing edge of the RWP shown in Figure 2.3, RWP decay takes place presumably through energy loss that is not maintained by upstream incoming disturbances. Additionally, the decay could be a consequence of the RWB taking place over the central portion of the RWP where the wave amplitude is saturated owing to non-linear growth. The sustained growth over this central part is a consequence of sustained baroclinic conversion in Equation 2.12. Ahead of the RWP over the leading edge area, new disturbances form owing to the convergence of ageostrophic geopotential fluxes.

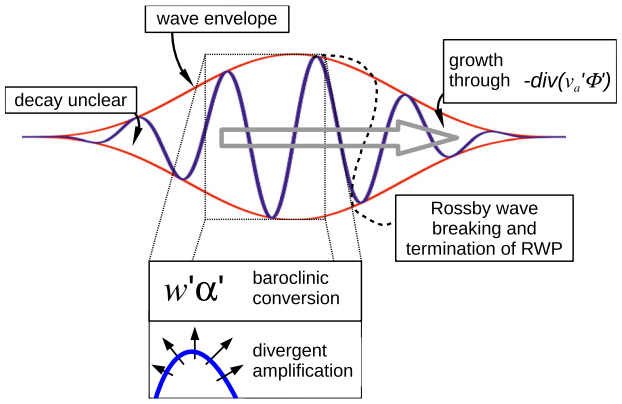

Figure 2.3: Schematic perspective of a Rossby wave propagating eastward along a latitude circle as in Figure 2.2, but for one RWP. Key features of RWP propagation, amplification, and decay are highlighted. See the text for further details. Adapted from Wirth et al. (2018).

2.3.1 Rossby wave packet diagnostics

The preceding discussion illuminated the usefulness of the eddy-kinetic energy based diagnostics (Orlanski and Katzfey, 1991) to diagnose processes involved in the evolution of RWPs. This implies that K_e can be seen as a suitable diagnostic for RWPs (Orlanski and Katzfey, 1991; Chang and Orlanski, 1993). A number of other RWP diagnostics have been developed over the years with varying degrees of known shortcomings. These include (but not limited to); Hovmöller diagrams (Hovmöller, 1949), RWP envelope reconstruction (Zimin et al., 2003; Zimin et al., 2006), and wave-activity-based (Andrews and McIntyre, 1978; Killworth and McIntyre, 1985; Killworth and McIntyre, 1985; Nakamura and Zhu, 2010; Nakamura and Solomon, 2010; Nakamura and Solomon, 2011; Methven, 2013; Huang and Nakamura, 2016; Ghinassi et al., 2018; Wirth et al., 2018) diagnostics. The purpose of RWP detection is crucial to selecting a suitable diagnostic.

For example, when one simply has the desire to operationally identify upper tropospheric troughs and ridges defining an RWP over the extratropics, the Hovmöller diagram (Hovmöller, 1949) approach might be of interest. This approach leverages a field consisting of sinusoidal components like v (Chang, 1993) or v' (Ndarana et al., 2022) to mark the zonal position of disturbances, and how they evolve with time. This technique requires the dimension reduction of a time-varying two-dimensional field by means of selecting a specific latitude/longitude of interest, or calculating the spatial average in one dimension so that only the time and the remaining axis can be shown on a 2D plot (Hovmöller, 1949; Glatt et al., 2011; Wolf and Wirth, 2017; Wirth et al., 2018). Its utility is mostly valid for situations involving planar-like RWPs since the onset of non-linearity is characterised by the reversal of PV and geopotential height contours as in RWB. During this process, a meridional average may result in destructive interference of the wave signals, similar to the situation when there exist multiple RWPs on two wave guides (Wolf and Wirth, 2017; Wirth et al., 2018). An additional advantage of this approach is the relatively simple diagnostic calculations involved in the construction of the diagram.

The envelope reconstruction of the v field-based approach (Zimin et al., 2003; Zimin et al., 2006) is also useful in this case as a diagnostic tool. This method relies on the application of the Hilbert transform on a 2D v field, and finished with a suitable filter to merge individual trough and ridge information. In other words, it identifies the horizontal position and extent of the RWP envelope (RWP object, Wirth et al., 2018). The envelope essentially covers the extent of the trough-ridge couplets characterising an RWP, with large values centering where the signals of the v' are most pronounced. Therefore, it is the extension of the envelope shown in Figures 2.2 and 2.3 to the 2D case. Additionally, the envelope reconstruction approaches, like the Hovmöller diagrams, are only suitable for the detection of planar RWPs. This is a drawback since observed RWPs often exhibit non-linear behaviour (Hoskins, 1975; Wirth et al., 2018).

As Wolf and Wirth (2015) noted, Rossby waves are semigeostrophic in nature. This

means that the size of troughs and ridges are not equal, with the former (latter) often appearing thinner (broader), (Wolf and Wirth, 2015; Wolf and Wirth, 2017; Wirth et al., 2018). This suggests that attempts to remove phase information through standard filtering techniques, such as that applied in Zimin et al. (2003), might encounter difficulties in associating troughs and ridges belonging to the same RWP structure. This is a result of the inconsistent distance between the v maxima and minima defining troughs, and that of minima and maxima defining ridges. A solution to this problem was proposed in the form of a Hilbert transform applied in semigeostrophic coordinates by Wolf and Wirth (2015).

On the other hand, when the interest is the dynamics of an RWP the above diagnostics may not be suitable. In this case, some kind of a budget based diagnostic such as the eddy-kinetic energy based framework is of interest. This K_e tendency equation allows for the quantification of individual processes involved in the generation and decay of K_e centres appearing as $\partial_t K_e > 0$ and $\partial_t K_e < 0$ contours respectively when viewed on a map plot. Like the Hovmöller diagram, this diagnostic retains phase information, which may prove to be less than desirable when trying to objectively and operationally identify RWPs as objects as is possible in the case for the envelope reconstructed RWPs (Zimin et al., 2003; Zimin et al., 2006). Furthermore, K_e is not a globally conserved quantity, therefore, the sources and sinks identified here cannot be taken as a full account of the processes at play (i.e, conservative and non-conservative processes) even under adiabatic and frictionless conditions (conservative flow), (Wirth et al., 2018). Ndarana et al. (2021) and Pinheiro et al. (2022) successfully applied this diagnostic to elucidate the downstream development of CoL cases over regions in the SH, implying that to some extent, this diagnostic can be applied to the cases of RWPs of finite-amplitude.

To satisfy the conservation property required to diagnose conservative and non-conservative sources and sinks of RWPs, wave activity flux-based diagnostics are relevant. This comes as wave-activity is globally conserved. All sources and sinks of wave-activity can be accounted for by a corresponding budget of wave-activity. This suggests that there is a

finite amount of wave-activity at any point on the globe, and that local changes to this wave-activity occur through fluxes and their divergence, which act to move this quantity from region to region (conservative process). Moreover, generation or dissipation can also occur through non-conservative processes which can be seen as external factors (Wirth et al., 2018). Wave-activity simply diagnoses and quantifies the waviness of an instantaneous PV isoline relative to an associated reference/background PV contour (Wirth et al., 2018; Ghinassi et al., 2018). The utility of earlier wave-activity formulations is often hampered by the restrictive nature of the assumption made in their construction; these include the assumption of a quasi-geostrophic flow characterising small-amplitude and planar RWPs (e.g, Andrews and McIntyre, 1976); Plumb, 1986; Takaya and Nakamura, 2001), as well as zonal-averaging which hampers the application for two-dimensional horizontal evolution of RWPs (e.g, Eliasen and Palm, 1961; Andrews and Mcintyre, 1976).

To circumvent the small-amplitude limit of the above wave-activity flux-based diagnostics, finite-amplitude wave activity (FAWA) based diagnostics are of particular interest. Some of the earlier work in this direction includes the computationally complex and expensive formulations of (Killworth and McIntyre, 1985); McIntyre and Shepherd, 1987), as remarked by Ghinassi (2019). Subsequent formulations with varying degrees of utility exist in the form of; e.g, Nakamura and Zhu (2010) who derived FAWA assuming zonally averaged barotropic atmospheric flow in spherical coordinates, Nakamura and Solomon (2010) where quasi-geostrophic (QG) flow was assumed, but still in spherical coordinates and a pressure pseudoheight vertical coordinate. Nakamura and Solomon (2011) extended their earlier QG based formulation to isentropic coordinates. This formulation was still restricted by its non-local nature, since it is a zonally averaged quantity. This inspired the work of Huang and Nakamura (2016), where a formulation for local (in latitude and longitude) FAWA (referred to as LWA) was derived in the QG framework.

While this was indeed an improvement, the QG approximation was always its limiting factor. In light of this, Ghinassi et al. (2018) derived an expression for isentropic LWA in

the primitive equation framework. Their formulation is essentially a combination of results from Nakamura and Solomon (2011) and Huang and Nakamura (2016). This formulation allows for the 2D RWPs (in latitudes and longitudes) in the subtropical and extratropical wave-guides to be elucidated, a feat previous formulations could not achieve. Some consistency between RWPs based on wave-activity of Takaya and Nakamura (2001) and energetics based on Orlanski and Katzfey (1991) has been alluded to (Danielson et al., 2006; Wirth and Wolf, 2017, Wirth et al., 2018) based on case studies. This suggests that the combination of these two diagnostics might reveal a more complete picture of RWP evolution. Specifically, eddy energetics are expected to reveal better signals of the linear, while LWA should be a good representation of the non-linear stages in the development of RWPs. The feasibility of this approach is discussed later for RWPs over the SA domain.

2.3.2 Vertical propagation of RWPs

Much of the preceding discussion of RWPs has been in the context of horizontal propagation. Here we briefly discuss aspects related to RWP, or more generally, wave activity propagation. Nishii and Nakamura (2004) and Nishii and Nakamura (2005) studied the cross tropopause propagation of Rossby wave activity in the SH by means of case studies. Their results suggest that the life-cycle of RWPs occurs in three dimensions (3D) involving upward propagation (across the tropopause into the lower stratosphere) of wave-activity in the vicinity of the storm tracks and the subpolar jet. The polar night jet can serve as a wave guide forcing the wave activity to propagate zonally along it (in a similar fashion as the extratropical jet wave guide), followed by possible downward cross tropopause injection at the polar night jet exit into the extratropical wave guide. Here, the wave activity could either continue propagating downward toward the subpolar jet and the storm tracks, or it could be reflected back into the lower stratosphere; see their Figure 2 for a schematic of this process. As suggested by this process, it is clear that tropopause may be an important feature of the RWP life cycle and therefore warrants a brief discussion.

2.3.2.1 The dynamical tropopause

From a PV-thinking point of view (PV-θ), the vertical extent of the atmosphere can be classified into three layers, namely; the under, middle, and over worlds following Hoskins (1991) on a latitude-θ diagram as in Figure 2.4. These layers are defined by the location and orientation of θ surfaces. The underworld is characterised by θ intercepting the earth's surface, the middle world is located where θ contours intercept the dynamical tropopause, and the overworld resides where θ surfaces are stably stratified above the dynamical tropapause. These layers are illustrated in Figure 2.4.

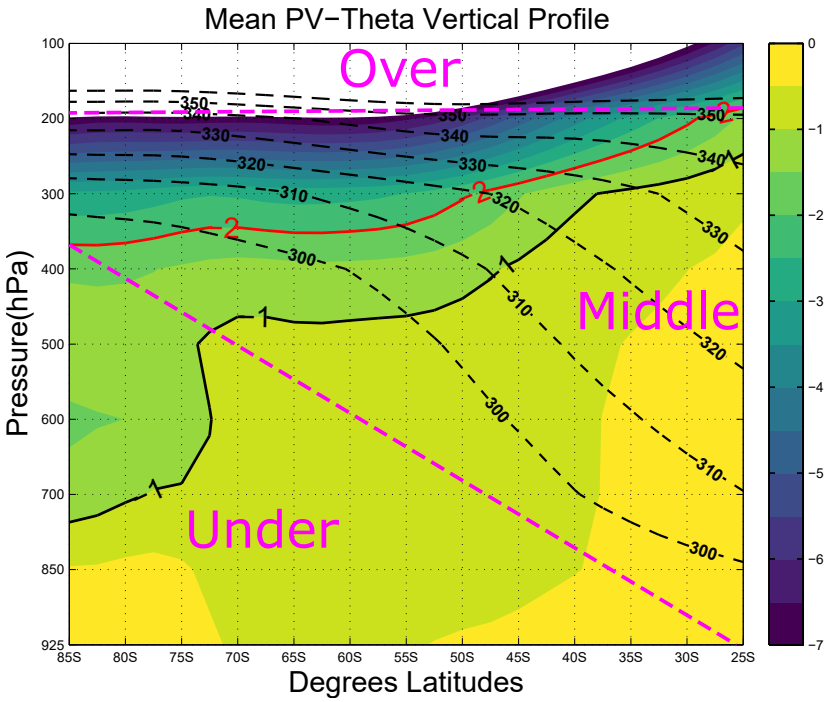

Figure 2.4: Mean θ-PV vertical profile where the colorshading denotes the zonally averaged (in the SH) PV in PVU and the -2 PVU contour is highlighted in red. The dashed wavy lines represent zonally averaged (in the SH) θ in K. The over, middle, and underworld regions of the atmosphere are indicated in magenta. (adapted from Hoskins (1991))

The tropopause is a significant component in the study of upper tropospheric RWP dynamics. Its importance stems from its role in marking the interface between the troposphere and stratosphere whose dynamics enables the study of stratospheric-tropospheric exchange (STE) processes that are known to have an influence on weather phenomena and, indeed, climate at near-surface atmospheric levels (Forster and Shine, 1997; Solomon et al., 2011; Kunz et al., 2011). For example, STE characterised by equatorward (poleward) intrusion of cold (warm) air masses can be diagnosed by the folding of the tropopause, which, when viewed from a horizontal coordinate viewpoint, would represent meridionally elongated tongues of PV that may eventually manifest into cutoff-like struc-

tures (Barnes et al., 2021) if they become deformed enough (Kunz et al.,2015).

Barnes et al. (2021) identified CoLs that from upper tropospheric levels towards the surface. These were further associated with anomalously warm surface potential temperature structure likely associated with cyclogenesis. It should be noted that since much of the variability in the PV distribution is observed in the meridional and vertical directions, we can only focus on these dimensions by zonally averaging to produce a vertical profile of the variables of interest against latitudes (e.g, Figure 2.4).

There exist a variety of other methods to define the tropopause, but their empirical nature can provide some difficulty in adequately determining its location, particularly in reanalysis data (see Ivanova (2013) for a review of some of the definitions) because of the variable nature of the tropopause, as well as the often coarse resolution of reanalysis data in the vertical direction. However, the thermal (T^{TP}) and dynamic (PV^{TP}) tropopause definitions are often the most preferred operationally (Ivanova, 2013). In light of this, we examine the relationship between these two definitions closely in the current work in a bid to obtain an approximate idea of the mean behaviour of the tropopause over the study domain.

T^{TP} is usually defined in terms of the temperature lapse rate in the vertical direction of the atmospheric column($\Gamma \equiv -\partial_z T$). An empirically defined threshold(Γ= 2 K km^{-1}) is widely accepted (Ivanova, 2013; Barroso Pellico, 2017) in the determination of the level of the T^{TP} as prescribed by the World Meteorologcal Organisation(WMO) in conjunction with several other criteria. Specifically, the T^{TP} level is defined as the first level in which Γ = 2 K Km^{-1} or less, provided that the average Γ between this level and its subsequent counterparts within the next 2km does not exceed 2 K km^{-1} (WMO, 1957).

In PV based studies such as those concerning STE, the notion of a dynamical tropopause (PV^{TP}) is more useful. In contrast to T^{TP}, which often regards tropopause as a discon-

tinuous horizontal surface (e.g., pressure level), PV^{TP} is viewed as a continuous quasi-horizontal surface characterised by some PV material surface (Kunz et al., 2015). Such a surface is denoted in Figure 2.4 as PV^{TP} = -2 PVU (solid red curve). In this example, one would have to select a θ surface in the vicinity of θ = 340 K to assess its behaviour on a 2D map in the region between 35° and 30°S. T^{TP} is not strictly defined by a unique pressure level; instead, it is not unusual for T^{TP} to consist of several step-like discontinuities (decreasing with height) in terms of pressure levels toward the poles. This behaviour is often observed in the vicinity of the subtropical jet stream. Correspondingly, the PV surface defining PV^{TP} would slope poleward towards lower altitudes in the vicinity of the jet streams (Ivanova, 2013).

In addition, as with the case of the T^{TP}, PV^{TP} is often conveniently defined by some optimal PV threshold (usually PV = -2 PVU) in the SH, although it is known that no one PV threshold can consistently represent the interface between the stratosphere and the troposphere owing to the temporal and spatial variability of the assortment of PV surfaces in the vicinity of the tropopause (Kunz et al., 2011) as alluded to above. To circumvent this, a range of PV thresholds is usually considered (e.g. -4 to -1) PVU in Kunz et al. (2011) and -2.5 to -1.5) PVU) in Ndarana and Waugh (2010). This approach is consistent with the view that the PV^{TP} can be viewed as a layer, instead of a single PV contour (Ivanova, 2013). While the aforementioned thresholds usually capture processes in the vicinity of the PV^{TP}, the diagnostic employed in the current work requires careful definition of this quasi-material surface. This comes as the dynamical tropopause is a significant marker of vertical propagation of wave-activity as suggested by Nishii and Nakamura (2004a, b). Kunz et al. (2011) proposed a method to objectively estimate the instantaneous PV value associated with the dynamical tropopause based on isentropic potential vorticity gradients in equivalent-latitude space.

Chapter 3

Data and Methods

3.1 Data

To calculate terms appearing in the diagnostics to be presented, we made use of the second National Centres for Environmental Prediction (NCEP) - Department of Energy (DOE) Atmospheric Model Intercomparison Project - II (AMIP - II) reanalysis dataset (NCEP-DOE AMIP reanalysis - 2) (Kanamitsu et al., 2002). From this dataset, only the variables: geopotential height (z), temperature (T), horizontal (u, v) and vertical wind (ω) speeds were sourced corresponding to the horizontal, vertical, and spatial resolutions listed below of this data set.

- Horizontal range and resolution: 0° - 357°E; 90°N - 90°S, at 2.5° x 2.5° longitude-latitude grid spacing,
- Vertical levels: 1000, 925, 850, 700, 600, 500, 400, 300, 250, 200, 150, 100, 70, 50, 30, 20, 10 hPa (17 standard pressure levels),
- Temporal range and resolution: Between 1979 and 2019 sampled 4x daily (6 hourly).

3.2 Diagnostics

3.2.1 Local finite wave activity (LWA)

Proper characterisation of RWPs in the southern African domain requires a suitable diagnostic. The isentropic LWA derived by Ghinassi et al. (2018) is the diagnostic of choice here for RWPs given how it combines the strengths of Nakamura and Solomon (2011), the fact that it is based on primitive equations with θ as a vertical coordinate, and Huang and Nakamura (2016) which is defined locally (i.e, not zonally averaged). This is particularly suitable for the detection of local finite-amplitude, transient Rossby waves. Ghinassi et al. (2018) gives a brief outline of the theory and derivation of the diagnostic, which is an extension of previous formulations. Note that LWA is used to refer to a finite amplitude wave activity diagnostic that is local in nature, while FAWA refers to finite amplitude wave activity that is not local.

In this section, we re-produce the some details of the derivation of LWA. This step is necessitated by the fact that this derivation follows from Nakamura and Solomon (2011) and Huang and Nakamura (2016). This implies that a concise understanding of the results reported by Ghinassi et al. (2018) requires that the results obtained from these three related bodies of work be reconciled in a self-contained review. To achieve this, we begin by deriving the zonally averaged FAWA version of Nakamura and Solomon (2011) in spherical coordinates. This formulation is then extended to include the meridional coordinate using the methods of Huang and Nakamura (2016).

The zonally symmetric isentropic FAWA at a given mass latitude (Φ_M), based on (Nakamura and Solomon, 2011), is defined as

$$A\left(\Phi_M, \theta, t\right) \equiv \int_{DS} qdM - \int_{DN} qdM \tag{3.1}$$

Where D_S and D_N are the north and south domains of integrations, respectively: $\{D_S$:

$[q \geq Q(\Phi_M))] \cap [\phi < \Phi_M]\,; D_N : [q \leq Q(\Phi_M))] \cap [\phi > \Phi_M]\}$.

Equation 3.1 is written in compact notation, so it can be rewritten as

$$A(\Phi_M, \theta, t) = \iint_{D_S} q\sigma dS - \iint_{D_N} q\sigma dS \tag{3.2}$$

by expanding it to its explicit form to elucidate the surface integrals and the area element of integration. $dM = \sigma dS$ relates isentropic layer mass with the isentropic density and volume, where σ is isentropic layer density, and $dS = a^2 \cos\phi d\phi d\lambda$ is the area element of surface integrals on the sphere. a denotes the radius of the earth, and ϕ and λ represent latitudes and longitudes, respectively. To be able to interpret Equation 3.2, an understanding of the meridional coordinate Φ_M is imperative. Φ_M can be viewed as the equivalent latitude (ϕ_e) based on isentropic layer mass. However, its definition is slightly different from the well-known area-equivalent latitude definition (ϕ_e). To understand Φ_M, it is important first to obtain an intuitive understanding of ϕ_e.

$\phi_e = \arcsin(1 - A_r/2\pi R^2)$ is a Lagrangian latitude that encloses the same geographical/horizontal area (A_r) as a specific quantity such as a PV contour would (Allen and Nakamura, 2003; Anẽl et al., 2013). The order of PV contours, especially when temporally averaged, is such that, between the south and north poles, circumglobal PV contours appear to be monotonous. Their order is reminiscent of geographical latitudes decreasing towards zero degrees at the equator from the poles. When PV is studied under frictionless, adiabatic conditions, PV is conserved, which means that instantaneous PV anomalies, such as residual CoL structures left behind during RWB, naturally originate from a remote area. ϕ_e allows for all PV to be brought back to its relevant layer/area so that the underlying dynamics can be studied when all the PV in the atmosphere is accounted for.

In the formulation of Huang and Nakamura (2016), the QG version of LWA, the area buffered/enclosed by a reference quasi-geostrophic (QG) PV contour (Q_{qg}) on pressure surfaces can be seen as a quasi-material equivalent latitude that can be interpreted as a

meridional coordinate. This is enabled by the fact that the QG horizontal winds advecting PV in the QG framework are area-preserving because they are non-divergent under the geostrophic balance. This is particularly relevant for the case where the Coriolis parameter is constant in the Q_{qg} equation (Holton and Hakim, 2014). This allows for the interpretation of Q_{qg} as a meridional (ϕ) coordinate (Nakamura and Solomon, 2011).

In contrast, isentropic horizontal winds are composed of both the divergent and rotational components, implying that they are not area preserving. This means that a slightly different definition of a suitable ϕ_e is needed for primitive equations in θ coordinates. For this reason, Nakamura and Solomon (2011) opted for the use of the concept of an isentropic layer mass.

$$M(Q,\theta,t) = \int\int_{q\leq Q} \sigma dS, \tag{3.3}$$

as the basis for their meridional coordinate (Φ_M) to facilitate the derivation of FAWA in isentropic primitive equations. The approach taken is justified by the fact that $0 \leq M \leq M_{max}$, where the lower (upper) bound corresponds to a situation of no or negligible (maximum mass of the layer) mass at the south (north/equator) poles between which it varies monotonously. Note that these are interpreted relative to each hemisphere, and not the entire meridional extent of the globe. As the set of Q (also taken as a reference contour) contours behave in a similar manner, M can therefore be used as a meridional coordinate of Q. $M(Q,\theta,t)$ is the mass found within an isentropic layer bounded by isentropes θ and $\theta + \delta\theta$, at Q, which is a PV contour of interest such as PV = -2 PVU taken from an array of monotonous PV contours. Note that these values must be valid for the instantaneous PV field ($q(\phi,\lambda,\theta,t)$). Equation 3.3 indicates that the surface integral of the isentropic layer density (σ) taken poleward of the reference Q is equal to $M(Q,\theta,t)$. Having defined M, the second component required in the definition of Φ_M is the quantity

$$\begin{aligned}\overline{M}\,(\Phi,\theta,t) &= \int_{-\frac{1}{2}\pi}^{\Phi}\int_{0}^{2\pi} \sigma a^2 \cos\phi d\lambda d\phi \\ &= 2\pi a^2 \int_{-\frac{1}{2}\pi}^{\Phi} \overline{\sigma}\cos\phi d\phi,\end{aligned} \tag{3.4}$$

which is the zonally averaged form of Equation 3.3, implying that Equation 3.4 is the zonally averaged layer mass southward of some geographical latitude $\phi = \Phi$. Note that Φ is simply a candidate geographical latitude and can be interpreted somewhat in the same way as Q. Φ_M is then defined as the latitude Φ at which condition $M(Q,\theta,t) = \overline{M}(\Phi,\theta,t)$ is satisfied for each candidate reference PV contour Q. This is enabled by the fact that within the defined isentropic layer, $M(Q,\theta,t)$ and $\overline{M}(\Phi,\theta,t)$ are monotonous quantities with values that satisfy the condition $0 \leq M \leq M_{max}$. The definition of Φ_M can therefore be expressed implicitly as

$$\int\int_{q\leq Q} \sigma dS = \int\int_{\phi\leq\Phi} \sigma dS. \tag{3.5}$$

The local (in ϕ and λ) FAWA formulation of Ghinassi et al. (2018) is essentially an extension of zonally symmetric FAWA (Nakamura and Solomon, 2011), Equation 3.2. In the following, we demonstrate the extension of FAWA to LWA (Ghinassi et al., 2018) by applying the methods of Huang and Nakamura (2016) to obtain the QG version of LWA. A schematic of the calculation is provided in Figure 3.1 to aid in the following discussion.

Equation 3.2 can be expanded to give the following.

$$A(\Phi_M,\theta,t) = \frac{1}{2\pi a\cos\Phi_M}\left[\int_0^{2\pi}\int_{\Phi_M+\Delta\phi}^{\Phi_{max}} q(\lambda,\phi,\theta,t)\,\sigma dS - \int_0^{2\pi}\int_{\Phi_M}^{\Phi_{max}} q(\lambda,\phi,\theta,t)\,\sigma dS\right], \tag{3.6}$$

where it is assumed that the flow is instantaneously wavy, meaning that Q is displaced locally by $\Delta\phi$ distance from its reference position Φ_M, (i.e, from $(\lambda,\Phi_M,\theta,t)$ to $(\lambda,\Phi_M+\Delta\phi,t)$). In this expression, the constraint $\{\Delta\phi > 0;\ 0 \leq \Phi_M \leq \Delta\phi\}$ $(\{\Delta\phi < 0;\ 0 \geq \Phi_M \geq \Delta\phi\})$ describes the north (south) areas relative to Φ_M. Φ_{max} denotes the southernmost latitude, which is at the south pole. This means that for each λ, the inner integral of the right hand side (rhs) expression of Equation 3.6 is evaluated as the difference between the instantaneous PV (q) from the coordinate (λ, $\Phi = \Phi_M + \Delta\phi$) coinciding with Q to Φ_{max}, and from Φ_M to Φ_{max}.

Therefore, along this λ, the result is an isolated quantity of $q\sigma$ between Φ_M and $\Phi_M + \Delta\phi$. This quantity can be interpreted as the wave activity associated with Q and Φ_M at λ. Recognising that Equation 3.2 therefore means that $q\sigma$ of interest always resides within a lobe of Q with Φ_M as the origin, Equation 3.6 can be written as

$$A\left(\Phi_M, \theta, t\right) = -\frac{1}{2\pi a \cos\Phi_M} \int_0^{2\pi} \int_{\Phi_M}^{\Phi_M + \Delta\phi} \omega\left(\lambda, \phi, \theta, t\right) dS. \tag{3.7}$$

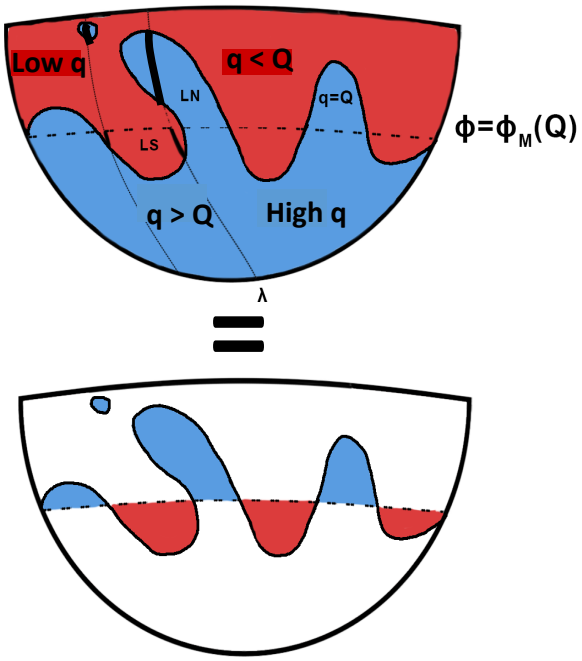

Figure 3.1: Illustration of Ghinassi et al. (2018) LWA computation in the Southern Hemisphere. A distorted PV contour Q is displaced relative to the reference mass latitude Φ_M. The line integration is done along a longitude λ constrained by the paths of integration l_s and l_n defined in the text. The result of the computation is depicted in the bottom panel. Adapted from Ghinassi et al. (2018).

Note that $q = \omega/\sigma$, so that $\omega = q\sigma$, which is the isentropic absolute vorticity. Moreover, the negative sign is introduced because $\Phi_M + \Delta\phi$ is now an upper bound. This is a consequence of the properties of integrals, specifically when the boundaries of a definite integral are interchanged, as in $\int_{-a}^{a} f(x)dx = -\int_{a}^{-a} f(x)dx$. ω or q can be interpolated to $\Phi = \Phi_M + \phi$ coordinates (e.g, $\omega\left(\lambda, \Phi, \theta, t\right)$), so that the horizontal point (λ, Φ_M) corresponds to a fixed point at Φ_M, northern and southern points on Q when $\Delta\phi = 0$, $\Delta\phi > 0$ and $\Delta\phi < 0$ (provided $\Delta\phi = \Phi$ at Q), respectively Equation 3.7 can be written as

$$A\left(\Phi_M, \theta, t\right) = \frac{1}{2\pi} \int_0^{2\pi} \left[-\frac{1}{\cos\Phi_M} \int_0^{\Delta\phi} \left\{\omega_e\left(\lambda, \Phi_M + \phi, \theta, t\right) + \omega_{ref}\left(\Phi_M, \theta, t\right)\right\} a\cos\phi d\phi \right] d\lambda. \tag{3.8}$$

Note that $\omega = \omega_e + \omega_{ref}$ has been decomposed into its eddy(ω_e) and basic state (ω_{ref}) components following the pertubation method in Equation 3.8. The integral in ϕ can be

evaluated to simplify the rhs expression in Equation 3.8 since ω_{ref} is independent on ϕ to give rise to

$$A\left(\Phi_M,\theta,t\right)=\frac{1}{2\pi}\int_0^{2\pi}\left[-\frac{1}{\cos\Phi_M}\int_0^{\Delta\phi}\omega_e a\cos\phi d\phi+\omega_{ref}a\sin\Delta\phi\left(\lambda,\Phi_M+\phi,\theta,t\right)\right]d\lambda. \tag{3.9}$$

The above expression can be simplified further by considering the periodicity of sin(.) in λ (Ghinassi et al., 2020), so that $\int_0^{2\pi}\sin\Delta\approx 0$. This means that $\frac{1}{2\pi}\int_0^{2\pi}\left[\omega_{ref}a\sin\Delta\phi\right]d\lambda=\omega_{ref}a\overline{sin\Delta}\approx 0$. so that zonally symmetric FAWA can be expressed as

$$\begin{aligned}A\left(\Phi_M,\theta,t\right)=&=-\frac{1}{2\pi}\int_0^{2\pi}A(\lambda,\Phi_M,\theta,t)+0\\&=\overline{A(\lambda,\Phi_M,\theta,t)}.\end{aligned} \tag{3.10}$$

Therefore, since $A\left(\Phi_M,\theta,t\right)$ can be recovered upon evaluating the integral of $A(\lambda,\Phi_M,\theta,t)$ in $d\lambda$, then $A(\lambda,\Phi_M,\theta,t)$ defines local isentropic finite amplitude wave activity (LWA). This term can be reexpressed succinctly as in Huang and Nakamura (2016), to produce the compact form of isentropic LWA (Ghinassi et al., 2018)

$$\begin{aligned}A\left(\lambda,\Phi_M,\theta,t\right)&\equiv-\frac{1}{\cos\Phi_M}\int_0^{\Delta\phi}\left[q\left(\lambda,\Phi_M+\phi,\theta,t\right)-Q\left(\Phi_M,\theta,t\right)\right]\sigma a\cos\phi d\phi\\&=-\frac{1}{\cos\Phi_M}\left[\int_{-\Delta\phi}^{0}\left(q-Q\right)\sigma a\cos\phi d\phi+\int_0^{\Delta\phi}\left(q-Q\right)\sigma a\cos\phi d\phi\right]\\&=\frac{1}{\cos\Phi_M}\left[\int_{l_S}\left(q-Q\right)\sigma a\cos\phi d\phi+\int_{l_N}\left(Q-q\right)\sigma a\cos\phi d\phi\right],\end{aligned} \tag{3.11}$$

where l_S and l_N define the arcs at some longitude λ denote the paths of integration and adhere to the boundary conditions: $\{l_S : q\geq Q,\phi<\Phi_M; l_N : q\leq Q,\phi>\Phi_M\}$. The schematic depicted in Figure 3.1 describes the calculation of LWA along a longitude line λ.

3.2.1.1 A budget for LWA

One of the important characteristics of wave activity is its conservation properties, allowing processes governing the evolution and behaviour of wave activity to be diagnosed concisely. A similar budget for LWA can be derived by differentiating LWA A (Equation 3.11) with respect to time to yield:

$$\frac{\partial A}{\partial t}\cos\Phi_M = \underbrace{\int_{\Phi_M}^{\Phi_M+\Delta\phi} \nabla\cdot[(q-Q)\sigma\boldsymbol{v}]a\cos\phi d\phi}_{Tc} + \underbrace{\int_{\Phi_M}^{\Phi_M+\Delta\phi} \frac{\partial Q}{\partial t}\sigma a\cos\phi d\phi}_{T_q} + \underbrace{Residual}_{T_n}. \tag{3.12}$$

Where T_c and T_n denote the contribution of conservative (e.g, momentum exchange of eddies with the flow and advection) and non-conservative processes (e.g., diabatic and moisture related processes) to the LWA tendency, respectively. T_n is calculated here as a residual of all terms, as it has been shown that the sensitivity of the results obtained through explicit and residual calculations of T_n are very similar (Ghinassi et al., 2020). Lastly, T_q describes the modification of Q by remote and non-conservative diabatic processes.

3.2.2 Eddy Kinetic Energy (K_e)

One of the important features defining RWPs is their role in remote energy transmission through. In light of this, it is important to examine this process for the cases of RWPs over the SA domain to determine the extent to which they are consistent with the well-known model of an RWP. This process is typically described using the paradigm of downstream baroclinic development (Orlanski and Katzfey, 1991; Orlanski and Sheldon, 1995). This framework is based on the behaviour of the kinetic energy K_e described through the K_e budget equation according to Orlanski and Katzfey (1991), as discussed in Chapter 2 based on Equation 2.11. Equation 2.11 is actually a variant of an expanded form of the local K_e

budget equation

$$\partial_t K_e = -\boldsymbol{V}_3 \cdot \nabla_3 K_e - \boldsymbol{v} \cdot \nabla_p \phi - \boldsymbol{v} \cdot (\boldsymbol{v}_3 \cdot \nabla_3)\boldsymbol{V_m} + \boldsymbol{v} \cdot \overline{(\boldsymbol{v}_3 \cdot \nabla_3)\boldsymbol{v}} + \textit{Residue}, \tag{3.13}$$

arising from a series of algebraic manipulations of the momentum equations (see page 1979 in Orlanski and Katzfey (1991)), where $-\boldsymbol{v} \cdot \nabla_p \phi$ is the pressure work term, and the rest of the terms are as discussed in Chapter 2. This term can be decomposed by recognising that the pressure work term can be expanded as $-\boldsymbol{v} \cdot \nabla_p \phi = -\omega\alpha - \nabla_p \cdot (\boldsymbol{v}\phi)_a - \partial_p(\omega\phi)$ following Orlanski and Katzfey (1991). Furthermore, for: $(\boldsymbol{v}\phi)_a = \boldsymbol{v}\phi - \boldsymbol{k} \times \nabla\left[\phi^2/2f(y)\right]$ a meridionally varying coriolis parameter (f) is assumed, and the subscript a represents the ageostrophic wind part of $\boldsymbol{v}$ having removed much of the contribution of the non-divergent part (i.e., the geostrophic wind $\boldsymbol{v_g}$), (Orlanski and Katzfey, 1991). This result was the essence of Orlanski and Katzfey (1991), because it allowed the elucidation of the main mechanism responsible for downstream development (i.e. $-\nabla_p \cdot (\boldsymbol{v}\phi)_a > 0$) as also remarked by Chang (2000). Taking this expansion into account, Equation 3.13 can now be rewritten as

$$\partial_t K_e = -\boldsymbol{V}_3 \cdot \nabla_3 K_e - \omega^{'}\alpha^{'} - \nabla_p \cdot (\boldsymbol{v}\phi)_a - \partial p\omega\phi - \boldsymbol{v} \cdot (\boldsymbol{v}_3 \cdot \nabla_3)\boldsymbol{V_m} + \boldsymbol{v} \cdot \overline{(\boldsymbol{v}_3 \cdot \nabla_3)\boldsymbol{v}} + \textit{Residue}. \tag{3.14}$$

Note that Equation 3.14 can also be expressed more succinctly by expressing $-\nabla_p \cdot (\boldsymbol{v}\phi)_a - \partial p\omega\phi$ as one term: $-\nabla_3 \cdot (\boldsymbol{v_3}\phi)_a$ describing the three-dimensional advection of ϕ to give

$$\partial_t K_e = -\boldsymbol{V}_3 \cdot \nabla_3 K_e - \nabla_3 \cdot (\boldsymbol{v_3}\phi)_a - \omega^{'}\alpha^{'} - \boldsymbol{v} \cdot (\boldsymbol{v}_3 \cdot \nabla_3)\boldsymbol{V_m} + \boldsymbol{v} \cdot \overline{(\boldsymbol{v}_3 \cdot \nabla_3)\boldsymbol{v}} + \textit{Residue}. \tag{3.15}$$

Careful examination of Equation 3.15 shows that terms 1 and 2 appearing in the rhs are in different formats, with the former being in advective form and the latter in flux form. Chang (2000) expressed Equation 3.15 as a flux form diagnostic

$$\partial_t K_e = -\nabla_p \cdot \boldsymbol{V} K_e - \partial p \omega K_e - \omega^{'} \alpha^{'} - \nabla_p \cdot (\boldsymbol{v}\phi)_a - \partial p \omega \phi + \boldsymbol{v} \cdot \overline{(\boldsymbol{v_3} \cdot \nabla_3)\boldsymbol{v}} - \boldsymbol{v} \cdot (\boldsymbol{v_3} \cdot \nabla_3)\boldsymbol{V_m} + Residue, \tag{3.16}$$

while Lackmann et al. (1999) and McLay and Martin (2002) also produced similar flux form variants. The flux form of Orlanski and Katzfey (1991) is particularly attractive because it allows one to plot the fluxes of K_e against the divergence field. This arguably allows for an easy and intuitive interpretation of the direction of dispersion and the overall movement of K_e centres based on flux vectors. The use of this diagnostic is also motivated by the fact that a direct comparison between the current LWA formulation and the K_e framework has not yet been made. Specifically, we want to establish the limits of LWA and K_e in the context of explaining the evolution of finite-amplitude RWPs over the SA domain, and whether there is some analytical advantage and benefit to combining the two diagnostics when details of the life cycle of RWPs are important. The labelling convention employed in Equation 3.13 is such that ∇_p indicates that the gradient operator is valid on isobaric surfaces, while the underscore 3 in ∇_3 and $\boldsymbol{v_3}$ symbolises the three-dimensional structure of the vectors (that is, $[\lambda, \phi, p]$). Lastly, the underscore a in the fourth term is to emphasise that the flow is ageostrophic.

Note that in Equation 3.16, the 3D vectors have been separated into horizontal and vertical components so that vertical components can be excluded from the analysis when horizontal motion is of particular relevance, and according to Wirth et al. (2018), it is the horizontal component of K_e that plays a role in the conservation of energy following the motion in 3D. The terms appearing on the right-hand side (rhs) of Equation 3.16 can be classified into radiative and source/sink terms. As the name suggests, the for-

mer are concerned with the three-dimensional (3D) movement/translation of K_e centres. These include $-\nabla_p \cdot \boldsymbol{V} K_e$, $-\nabla_p \cdot (\boldsymbol{v}\phi)_a$, which act to advect and radiate K_e horizontally, respectively. These terms can be combined to form the total horizontal K_e flux ($S_h = -\nabla_p \cdot [\boldsymbol{V} K_e + (\boldsymbol{v}\phi)_a]$, where the symbol S is adopted from Wirth et al. (2018), and the underscore (h) represents horizontal motion), (Chang, 2000). Here, $-\nabla_p \cdot \boldsymbol{V} K_e$ denotes the advective flux of S, which is the horizontal divergence of K_e fluxes due to the total horizontal flow ($\boldsymbol{V}$). $-\nabla_p \cdot (\boldsymbol{v}\phi)_a$ represents the horizontal divergence/advection of the ageostrophic geopotential height fluxes, which is the radiative flux component of S symbolic of the dispersive nature of Rossby waves (Pedlosky, 1987; Chang, 2000). Vertical advection of K_e can be diagnosed by the vertical divergence of K_e fluxes due to the total vertical component of the flow (ω), represented by $-\partial p \omega K_e$, while vertical energy dispersion is denoted by $-\partial p \omega \phi$. Similarly, these can be combined as $S_v = -\partial p \omega [K_e + \phi]$, where the underscore v denotes that this is the total energy flux in the vertical direction, and the first and second terms are the advective and radiative parts, respectively.

The remaining terms are the source/sink terms, namely; baroclinic conversion (BRC) from the eddy available potential energy (P_e) to K_e, $-\omega^{'}\alpha^{'}$, the Reynold's stress term $-\boldsymbol{v} \cdot (\boldsymbol{v_3} \cdot \nabla_3)\boldsymbol{V_m}$, and the time mean stress $\boldsymbol{v} \cdot \overline{(\boldsymbol{v_3} \cdot \nabla_3)\boldsymbol{v}}$ (Decker and Martin, 2005), which when combined as $-[\boldsymbol{v} \cdot \overline{(\boldsymbol{v_3} \cdot \nabla_3)\boldsymbol{v}} + \boldsymbol{v} \cdot (\boldsymbol{v_3} \cdot \nabla_3)\boldsymbol{V_m}]$ can collectively be interpreted as the barotropic conversion term (BRT) according to Chang (2000) and as applied by Pinheiro et al. (2022). These terms can be interpreted as mechanisms responsible for the generation and dissipation of K_e, together with processes such as friction, which are all incorporated into the K_e residue term (*Residue*). When the above modifications are taken into account, Equation 3.16 can be rewritten as

$$\begin{aligned} \partial_t K_e &= S_h + S_v + \mathrm{BRC} + \mathrm{BRT} + \mathit{Residue}, \\ &= \underbrace{S_{3D}}_{flux} + \underbrace{\mathrm{BRC} + \mathrm{BRT} + \mathit{Residue}}_{source/sink}, \end{aligned} \tag{3.17}$$

which is the descriptive/qualitative form of Equation 3.16 according to the combined role of individual terms. In an ideal setting, Equation 3.17 basically illustrates that the local rate of change of K_e should first be influenced first by either of the source terms such as BRC (as found in previous studies such as Orlanski and Sheldon, 1995; Ndarana et al., 2021; Pinheiro et al., 2022) and then it can be radiated to previously undisturbed regions by means of 3D energy fluxes, followed by dissipation due to sink terms such as *Residue*, of which a dissipative mechanism such as friction is a part. This sequence of events is illustrated and implied in Figure 11 of Chang and Orlanski (1993). All terms appearing in Equations 3.16 - 3.17 will be presented as pressure-weighted vertical averages computed as

$$[X] = \frac{1}{p_{850} - p_{100}} \int_{100}^{850} X\,dp, \tag{3.18}$$

(see, e.g., Orlanski and Katzfey, 1991; Ndarana et al., 2021) where $[X]$ is the vertical average of each quantity/term estimated between 850 and 100 hPa isobaric surfaces (tropospheric column) using a simple trapezoidal rule. Unless otherwise stated, all results K_e presented in Chapter 5 should be taken as vertical averages, since the [.] notation will be dropped in Chapter 5 to improve legibility.

3.2.3 An estimate for the dynamical tropopause

As alluded to previously, the dynamical tropopause is somewhat elusive, as it exhibits a high degree of variability, particularly on the seasonal time scale. The selection of one PV value as a representative of the dynamical tropopause is likely to result in an erroneous interpretation of the results, especially in long-term analysis studies (Kunz et al., 2011). In this study, the location of the dynamical tropopause is of relevance because the type of air masses associated with RWPs in the SA domain can have a direct influence on the weather in the region. For example, if RWPs originating from the dynamical tropopause are deep enough, they may transport cold stratospheric to near surface levels (e.g, see Barnes et al.,

2021). The variability associated with PV values that estimate the dynamical tropopause requires one to calculate it on a case-by-case basis. To this end, we employ the method proposed by Kunz et al. (2011) based on isentropic PV gradients in equivalent latitudes space.

An equivalent latitude φ_e is given by the expression: $\varphi_e = \arcsin[1 - A_r(\mathrm{PV})/2\pi r^2]$ where $A_r(\mathrm{PV})$ is the area enclosed by a PV contour, and r is the radius of the Earth. From this expression, it is clear that φ_e is simply the interpolation of isentropic PV contours to the range: $90°\mathrm{N} \leq \varphi_e \leq 90°\mathrm{S}$. Subsequently, the equivalent latitude of the dynamical tropopause value on an isentropic surface is determined through $\varphi_e^{TP}(\theta) = \max[\partial_{\varphi_e} PV(\varphi_e, \theta) \times u_h(\varphi_e, \theta)]$, where $u_h = \sqrt{u^2 + v^2}$ is the magnitude of the horizontal flow. This definition explicitly defines the dynamical tropopause as a region constrained by strong meridional PV gradients ($\partial_{\varphi_e} PV$) and pronounced horizontal flow (i.e, jet streams). The PV value (PV^{TP}) associated with φ_e^{TP} can be easily determined from the established one-to-one relationship between PV and φ_e.

3.3 Algorithms

3.3.1 FAWA computation

To compute A (in Equation 3.11) and the terms appearing in the associated budget equation from gridded data, we adopt the procedure outlined by Ghinassi et al. (2018) and the steps are briefly summarised below:

1. First, one needs to θ select an isentrope that captures upper tropospheric phenomena in line with our study objectives. Usually, processes at the dynamical tropopause level and region are of interest. In such cases, it is common to define an ad hoc PV value (e.g., -2 PVU) that serves as the dynamical tropopause, then the choice of θ would depend on whether an isentrope intersects this PV line over the region of interest or not. Here, we do not impose this constraint, as we are also interested in wave activity that may be unrelated to the dynamical tropopause-related wave guide. As a result, the choice of θ is purely based on the atmospheric level or the layers of interest. The

isentropes $\theta = 330K(\theta_{330})$ and $350K(\theta_{350})$ are chosen here because climatologically, they sample the mid-upper tropospheric layer (see, e.g., Figure 2.4) with the former (latter) sampling the upper (lower) bound of the mid (upper)-troposphere at $\approx$ 400 hPa (200 hPa) at $\approx$ 25°S. Furthermore, and perhaps more importantly, these two surfaces have been found to capture processes over the extratropics (θ_{330}; see, e.g., Ndarana and Waugh, 2010) and the subtropics (θ_{350}) Postel and Hitchman, 1999; Ndarana and Waugh, 2010). This is important because extratropical processes have been found to influence weather phenomena over SA (e.g, Ndarana et al., 2021). Furthermore, a link has been established between South American and South African intraseasonal rainfall, suggesting the existence of a subtropical connection between these two regions (Grimm and Reason, 2015).

2. The second step first involves the linear interpolation of u, v, and T to θ coordinates. Subsequently, the interpolated variables are used to estimate the missing quantities: $\omega = \zeta_\theta + f$, $\sigma = -g\partial_p\theta$, to ultimately get $q = \omega\sigma$ in θ coordinates. The partial derivatives appearing above are estimated using finite-differencing methods such as central differentiation. Specifically, for a 4D variable $\alpha(x, y, \theta, t)$ away from the boundaries: $\partial_t\alpha \approx 0.5[(\alpha(x, y, \theta, t+1) - \alpha(x, y, \theta, t)) + (\alpha(x, y, \theta, t) - \alpha(x, y, \alpha, t-1))]$. At the boundaries, one-sided forms are utilized: $\partial_t\alpha(x, y, \theta, t) \approx 0.5[\alpha(x, y, \theta, t + 1) - \alpha(x, y, \theta, t)]$ for the lower boundary and for the upper boundary $\alpha(x, y, \theta, t) \approx 0.5[\alpha(x, y, \theta, t) - \alpha(x, y, \theta, t - 1)]$. Note that this procedure is used throughout the study to estimate any partial derivative (e.g, $\partial_t K_e$).

3. Calculating A requires establishing a relationship $[Q(\phi, \theta, t)]$ between data/grid latitudes ϕ and the reference PV contour Q. First, we need to determine the values of Q. To this end, we identify the SH instantaneous minimum and maximum q values (i.e, q_{min} and q_{max}). Then we produce an equidistant/linear set of PV values under the constraint $q_{min} \leq q \leq q_{max}$ hereafter referred to as Q, where Q_i represents the i-th Q contour. Using each member Q_i of the Q set, the surface integral appearing on the left-hand-side (LHS) of Eq. 3.11 is estimated by the trapezoidal rule to produce

a set $M(Q_i)$. The surface integral of the right side (RHS) of the same expression is evaluated in a similar way to produce a corresponding set of values $\overline{M_i}$. The reference contours required associated $[Q_i(\phi, \theta, t)]$ with the meridional coordinate ϕ are then obtained by linear interpolation.

4. Finally, LWA (A) is computed from Equation. (3.11) by evaluating the line integrals that appear in the RHS. Subsequently, to remove phase information related to individual troughs and ridges, we applied a zonal filter on the resultant raw A field, yielding coherent LWA structures associated with the extent of highly pertubed PV contours (i.e., wave-activity). The filtering procedure is based on first extracting the instantaneous dominant zonal wave number $[s_d(\phi)]$ associated with the peak zonal Fourier spectrum from the meridional wind (v) through a zonal wavelet transform (see the appendix section in Ghinassi et al. (2018) for a detailed description). Following Ghinassi et al. (2018) and Ghinassi et al. (2020), we also apply a spatial filter based on a moving average with a window $\phi = 10^\circ$ to remove discontinuities in the s_d field. s_d is then used to estimate the local wavelength $[\lambda_d(\phi) = 2\pi a \cos\phi / s_d]$, which is the estimate for the full width at half maximum necessary for the Hanning convolution window (Harris, 1978) used as the zonal filter. Note that the LWA budget terms are evaluated exactly in the same way as for A.

3.3.2 RWP tracking

To detect the actual RWP structures from the calculated LWA field, we make use of a simple hybrid feature tracking algorithm, which entails a combination of point- and object-based techniques as in Souders et al. (2014a). Point-based tracking techniques involve the tracking of a local maxima or minima of a field characterising the tracked atmospheric phenomenon such as tropical (e.g. Hodges, 1994) and extratropical cyclones (e.g. Wang et al., 2006; Souders et al., 2014a). In contrast, object-based algorithms are considerate of the overall morphology of the feature in question (see, e.g., Hodges and Hoskins, 2005; Ndarana and Waugh, 2011; Barnes et al., 2021).

1. Here, we leverage the structure of zonally filtered LWA calculated using the methods described above. We first produce a distribution of LWA contours with a resolution of 1 ms^{-1} on a map. Then we search for closed (i.e. given an arbitrary contour line, the start and end coordinates should be equal) concentric contour lines because a well-defined RWP will be characterised by such a configuration of LWA contours with a local maximum defining its centre.

2. The second step involves determining the centre of a preliminary RWP object. The LWA field is positive definite by design, therefore, the innermost contour line within the array of the closed concentric contour set should be small and must represent the local LWA maximum. To ensure this is the case, a comparison between each of the concentric LWA contours was made in terms of magnitude and size. The closed contour with the largest LWA value, and smallest area enclosed was then classified as the central RWP contour.

3. Using the central RWP contour, the preliminary RWP centre was estimated by computing the median of all coordinates along its perimeter. The median was chosen because RWP objects are known to sometimes assume irregular shapes and are thus not always circular or oval as in the case of ridging anticyclone systems. For RWPs, this is a likely occurrence during the initial stages of development when wave activity extends into a previously undisturbed region. This can result in the centre being placed outside of the area enclosed by the innermost contour, especially when the outlier-sensitive mean (in contrast to the median) is used as the measure of central tendency. We do concede, however, that the median does not entirely address this issue, however, the fact that the resolution of the LWA contour distribution is relatively high is somewhat advantageous because the central (outer) most contour would be the least (most) irregularly shaped. This approach thus minimises the frequency and likelihood of extreme cases of erroneous placement of the central point. The estimated date, centre, and LWA maximum associated with the identified LWA object

are then recorded in a preliminary database.

4. At every time step, the above procedures are performed to track the candidate RWP object because the instantaneous LWA maximum is not unique. To ensure that the recorded features belong to one RWP event, we require the haversine distance between the current (time step), and preceding LWA centres to be $\leq$ 500 km over a 6 hour period. This value is in the range of that used in previous studies such as Souders et al. (2014b), where SH RWPs were found to typically propagate at speeds ranging between 20 and 25 ms^{-1} ($\approx$ 432-540 km $(6h)^{-1}$), and 2200 km day^{-1} ($\approx$ 500 km $(6h)^{-1}$) following Fuenzalida et al. (2005), Reboita et al. (2009), and Ndarana and Waugh (2010) for CoLs. If this condition is satisfied, the instantaneous LWA object is not recorded as a new RWP, and its attributes are only recorded under the first detected structure.

5. Ghinassi et al. (2020) note that the growth of LWA-based RWPs occurs in burst-like events characterised by rapid wave activity growth about 48-24 hours prior to their maturity, followed by similar decay rates after LWA saturation. Therefore, we require the preliminary LWA maximum and centroid to behave in a similar fashion for it to be declared as an RWP.

3.3.3 Composite analysis

To examine the typical properties of RWPs, we turn to composite analysis. This procedure is commonly used when the evolutionary properties of specific phenomena are of interest (e.g, downstream development of cut-off low-pressure systems as in Ndarana et al. (2021) and Pinheiro et al. (2022)). This process can be carried out in two ways, with inherent strengths and weaknesses. The first approach simply involves calculating the spatiotemporal mean of a given field taken as the element-wise sum of that field variable during the time a specific atmospheric phenomenon of interest was observed, divided by the number of times the summation was done (i.e., number of times the phenomenon was observed). This geographical grid-based approach is illustrated in the left panels shown in Figure 3.2

where it is clear that the wide spread nature of the RWP events results in the distortion of the PV morphological signature associated with mature RWPs (i.e., RWB). However, this technique retains geographical information related to the phenomena of interest, such as RWPs. Note that to reconstruct the temporal evolution, we use each date related to an event as the reference/centre point, so that a certain number of time steps before and after the onset of the event can be extracted, and processed in a similar fashion as the event day itself to produce the composite mean field.

In contrast, to address destructive interference related to off-phase events, we employ the event-relative grid approach. This entails the extraction of the central coordinate of an event so that a small window of finite grid points away from this centre can be extracted. The small window of grid points then becomes the subject of the spatio-temporal mean computation described above for geographical composite means. This is illustrated in the right-hand panels in Figure 3.2, where the centres of all events of interest are superimposed onto a grid based on event relative longitude (λ_E) and latitude (ϕ_E). While this approach is useful when the morphology of a phenomenon is important, it comes at the expense of spatial awareness of the phenomenon analysed.

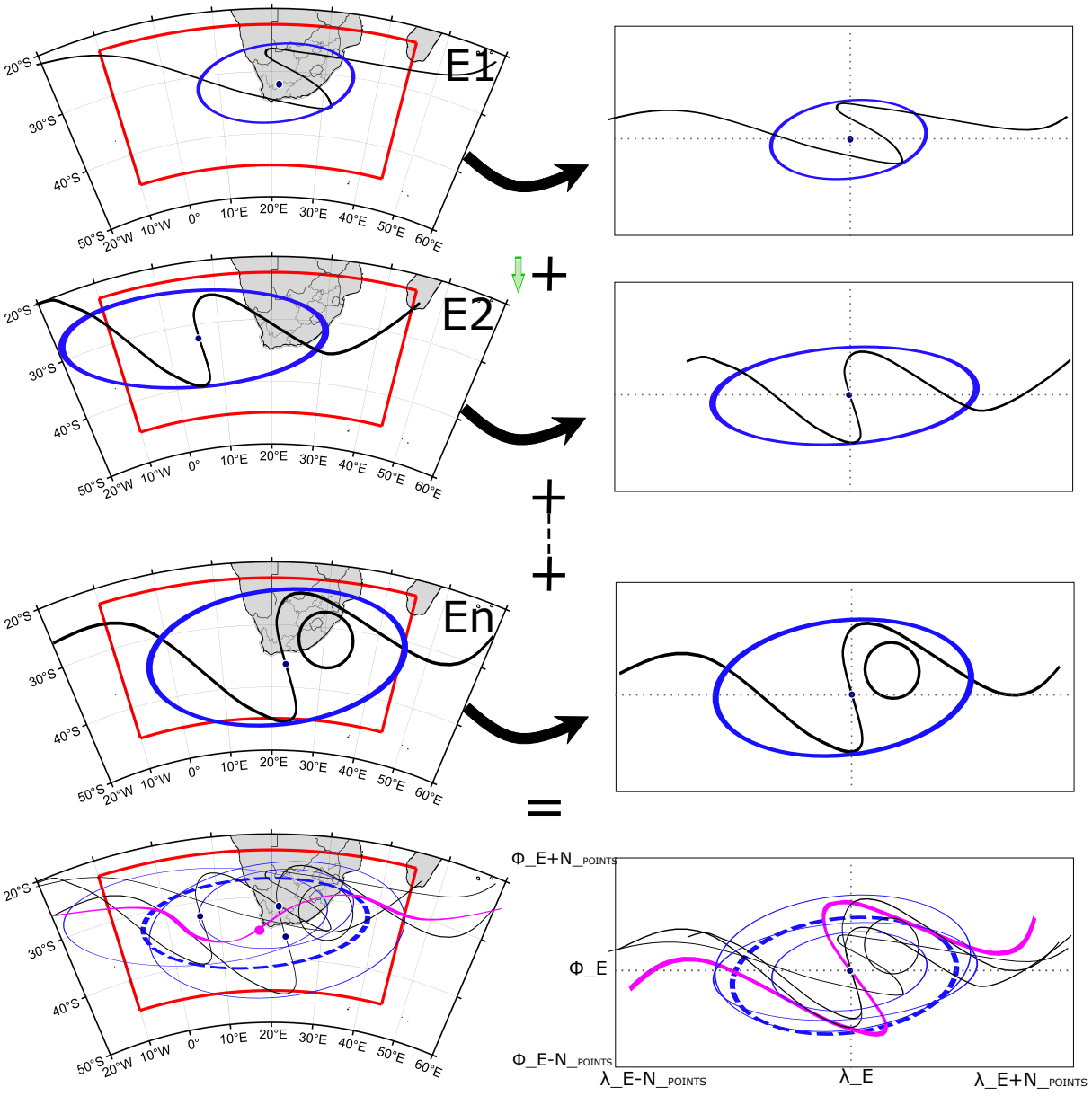

Figure 3.2: Illustration of composite analysis relative to the southern African domain highlighted by the red boundary. LWA RWPs (blue ovals with dots) and associated PV contours (black) are used as an example. The RWP centers are denoted by blue dots. The left (right) hand panels represent the geographical (event (E) relative) grid form of composite means. In the last row the composite mean behaviour of LWA and PV are shown in thick magenta and dashed blue contours. Morphological behaviour of PV contours is better elucidated in the event relative grid space centered at (λ_E,ϕ_E). The green arrow denotes the direction of the summation to avoid ambiguity.

Chapter 4

Climatological aspects of LWA and associated RWPs

In this chapter, we discuss several climatological characteristics of RWPs that occur in the vicinity of South Africa, in view of their potential influence on the weather processes that affect the country. Before we can proceed with the discussion in the context of the SA domain, we have to examine the results of the LWA calculation procedure itself. To this end, we will consider the seasonal variability of the LWA field ($\overline{A}$, the seasonal average of LWA (A)) estimated over a 40-year period (1979-2019) on two isentropic surfaces. This approach is taken to enable us to compare our results with previous studies.

4.1 Seasonal variability of LWA

Figures 4.1 (330 K [θ_{330}]) and 4.2 (350 K [θ_{350}]) show the seasonal evolution of $\overline{A}$ (colour shading) together with the corresponding field $\overline{u_\theta}$ (blue contours: 25 - 30 ms^{-1}-solid, 35 - 55 ms^{-1}-dashed) field representing the SH jet streams. The corresponding -2 PVU contour (solid black line) is included to represent the standard dynamical tropopause as in a number of studies (e.g, Holton et al., 1995; Martius et al., 2007; Ndarana and Waugh, 2010). Note that these climatological mean fields were computed by averaging the 6 hourly time steps over the 40 year period (1979-2019) for each of the seasons. A visual comparison

of Figures 4.1 and 4.2 suggests that the choice of isentropic levels has implications on the intensity/magnitude of the LWA field and, most notably, the presence of LWA hotspots (local LWA maxima). For example, the Southern Hemisphere in the climatology of Ghinassi (2019) consists of one distinct LWA hotspot between 180° and 120°W along 60°S on the 325 K isentropic surface, and has an intensity of about 80-100 ms^{-1} during summer months (DJF), see their Figure 4.14. The same feature is evident in Figures 4.1 and 4.2 (a) but is relatively weaker in intensity on both θ_{330} and θ_{350} relative to their θ_{325} counterpart. Moreover, this hotspot is even weaker on θ_{350}, the upper tropospheric isentrope, as compared to θ_{330} which resides at lower atmospheric levels relative to the former. This reveals that LWA is concentrated/anchored at lower levels of the troposphere during this season, and indeed throughout the year, so that upper-level wave activity can simply be viewed as weak signals of the lower tropospheric core LWA hotspot.

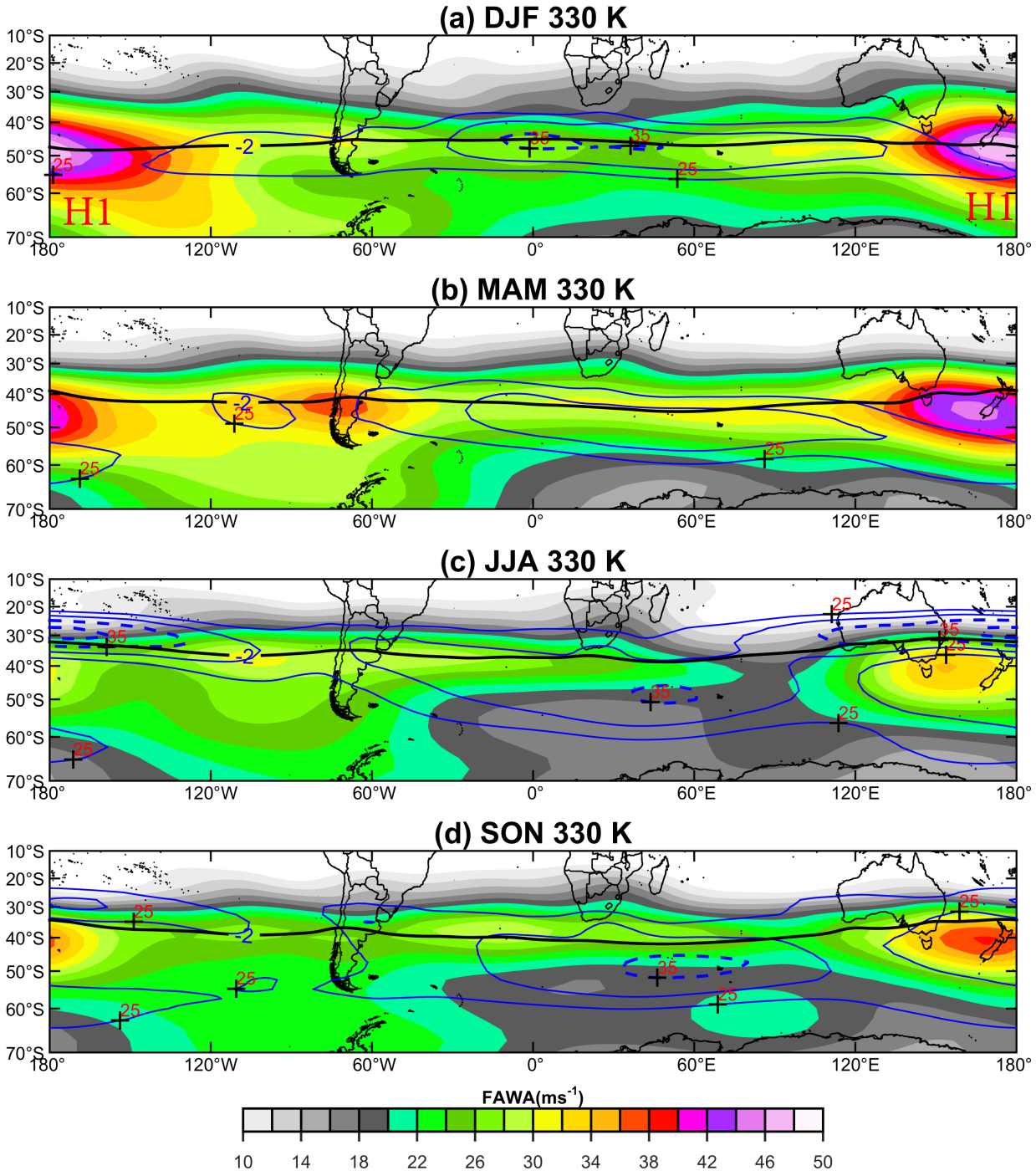

Figure 4.1: Seasonal distribution(a. summer(DJF), b. autumn (MAM), c. winter (JJA), d. spring(SON)) of LWA in ms^{-1} on θ_{330}. The blue contours are the corresponding mean isotachs of the zonal component of the wind ($\overline{u_\theta}$ = 25-30 ms^{-1}: solid, 35-55 ms^{-1}: dashed) and denote the position of the jet stream on θ_{330}. The H1-H3 symbols denote the LWA hotspots referred to in the text. The thick black contour line denotes the corresponding -2 PVU dynamical tropopause.

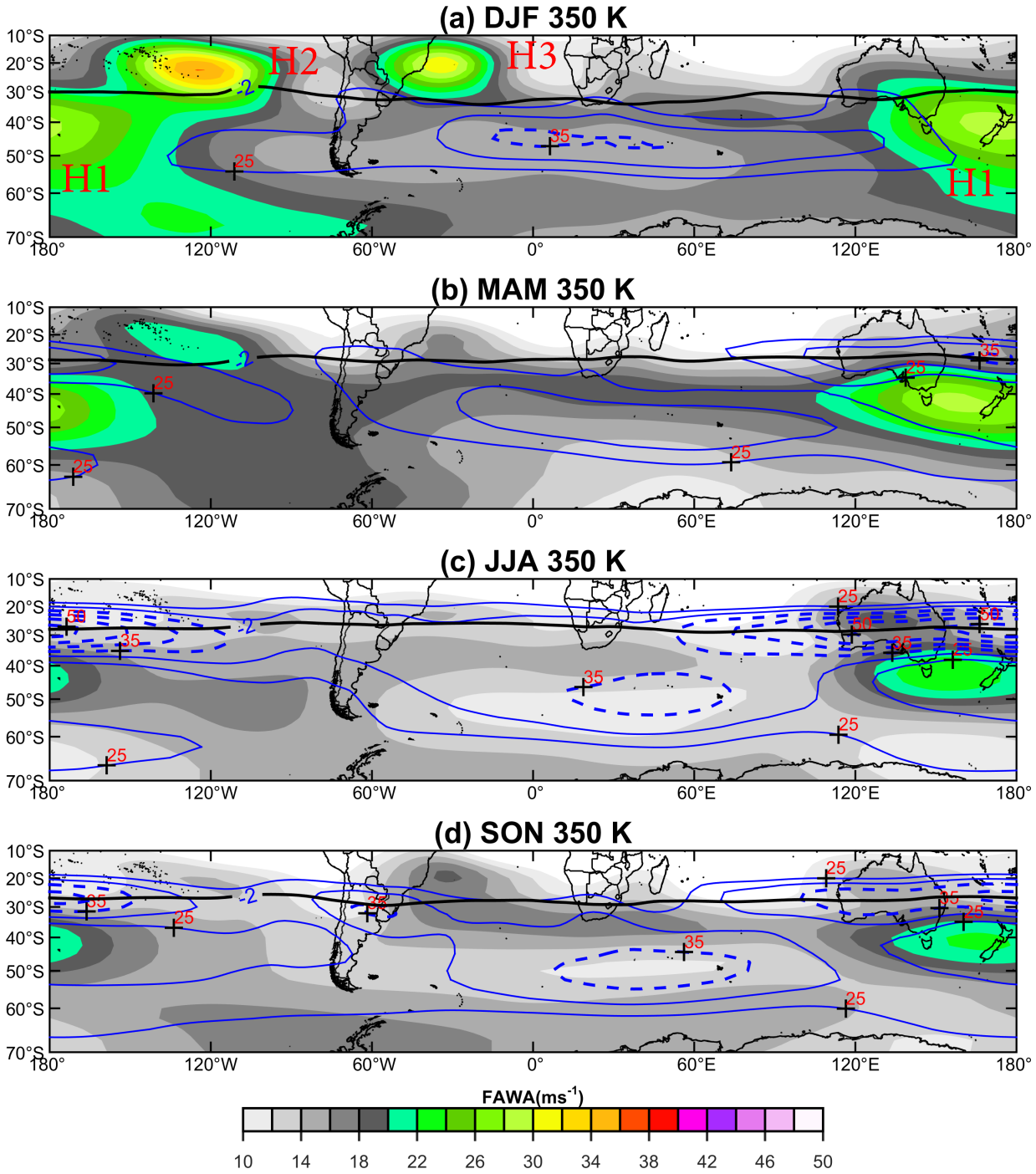

Figure 4.2: As in Figure 4.1 but for θ_{350}.

This view is supported by Figure 4.3 which depicts the latitude (ϕ)-θ seasonal evolution of the zonally averaged $\overline{A}$, where only the 330-360K surfaces are considered as the y axis. In this picture, the largest values of LWA are indeed confined to lower levels of the atmosphere throughout the seasons. This can be seen by monitoring the evolution and behaviour of the LWA hotspot 1 ($H1$) which moves equatorward (to $\approx 30°$S) and downward to levels below θ_{330} between summer (DJF) and spring (SON) months. The entire $\overline{A}$ field appears to shift with this hotspot, and its vertical extent is confined to θ levels below θ_{350} during the winter months (JJA). Additionally, by not considering upper level θ surfaces such as θ_{350}, subtropical/lower-latitude LWA hotspots such as $H2$ and $H3$ in Figure 4.1 (a) would not be captured during summertime.

The quasigeostrophic (QG) framework-based LWA climatology of Nakamura and Solomon (2010) reveals the existence of such upper tropospheric/lower stratospheric features as well. The study revealed that, unlike the mid-latitude wave activity, these features were mostly associated with the behaviour of the mean PV field, instead of the mean flow or the mid-latitude waveguide. These observations give credence to our approach of considering two isentropic surfaces to capture lower- and upper-level details of the LWA field, regardless of their relationship with the mean flow.

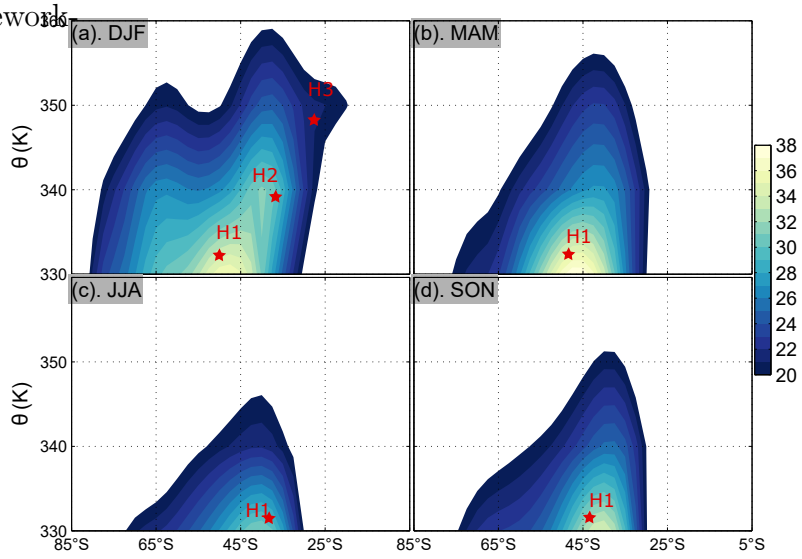

Figure 4.3: Mean zonally averaged seasonal distribution (summer (DJF) to spring (SON) (a-d)) of LWA ($\overline{A}$) in ms^{-1} with respect to θ. H1-H3 highlight wave activity hotspots. Note that to demonstrate this, the temporal mean was computed for only a 10 year period between 2009 and 2019.

As demonstrated in Figure 4.3, 330K (θ_{350}) generally reveals well-defined areas of transient Rossby wave activity over the extratropics (subtropics) defined in this study as the

region below (above) latitude $\phi = 35°S; \phi_{35S}$ as in Ndarana and Waugh (2010). In the extratropics on θ_{330}, there is evidence of zonally confined, lower tropospheric-level circumpolar RWP activity whose spatial distribution can be described as "annular" (seen clearer on a stereographic plot), as did Ghinassi (2019) during all seasons except winter. From the zonally averaged perspective, this distribution is reminiscent of storm track regions (e.g, Hoskins and Hodges, 2005) over the SH because the wave activity is concentrated over the extratropics, consistent with the fact that LWA essentially diagnoses large and finite-amplitude baroclinic eddies. Within this pool of wave activity, there exist LWA hotspots, consistent with Figure 4.3 evident during various seasons. In the extratropics (Figures 4.1 and 4.2 (a-d)) a hotspot ($H1$ in Figure 4.4) is located between 120°W and 120°E, and appears to be a somewhat permanent feature. Note that this is captured on both isentropic surfaces, but appears clearer on θ_{330} due to this surface being located at tropospheric levels relatively closer to the extratropical jet stream core.

This means that PV contours intercepting θ_{330} are subjected to pronounced perturbations, as opposed to those intercepting θ_{350}. Rossby waves have to exist and propagate along the extratropical waveguide (Hoskins and Ambrizzi, 1993; Wirth et al., 2018) first before they undergo RWB. RWB occurs in regions of weak zonal winds, which implies that there must be a direct and positive relationship between the intensity of the storm tracks and the frequency of the RWB events. Studies have suggested the existence of this relationship in the context of eddie mean flow interactions (see, e.g., Strong and Magnusdottir, 2008a,b; Liu et al., 2014). Spatiotemporal distributions of RWB climatologies (e.g, Ndarana and Waugh, 2010) confirm the validity of this argument, as it has been found that more RWB events are identified on θ_{330} as compared to θ_{350}. Since the extratropical jet stream is collocated with Southern Hemispheric extratropical storm tracks (Hoskins and Hodges, 2005; Wirth et al., 2018), this means that θ_{350} only adequately captures the upper bound of the extratropical wave-activity core. This hotspot varies seasonally in terms of its intensity and overall spatial extent, and denotes areas frequented by intense RWPs.

The variability of this hotspot is most evident in the zonal direction, with $H1$ initially rooted between 150°E and 180° during summer months (Figure 4.1 and 4.2 (a)) over New Zealand. The most intense RWPs are likely observed during the summer in this region, with mean intensities $>$ of 45 ms^{-1}. Then it begins to disintegrate between 150°W and 120°W during autumn months (Figure 4.1 (b)) with a slight westward shift of the main centre (initial hotspot) and the development of a secondary hotspot emerging east of this break point, likely marking a new area associated with mature RWPs. The intensity of the incipient hotspot decays (down to approximately 40 ms^{-1}) together with the development of the emergent secondary hotspot over and just south-west of South America associated with moderate intensities in the range of 35 ms^{-1}. During this season (autumn), there is also an increase in Rossby wave activity between the eastern South Atlantic Ocean (SAO) south of SA, and the South Indian Ocean (SIO). Consistent with the observations made in Figure 4.3, the winter months mark a significant reduction in Rossby wave activity over the entire SH so that a discontinuity in the "annular" shape of the distribution of the mature RWP frequency field emerges at about 90°E. This decrease in wave activity is accompanied by the retreat of $H1$ where the centre of this hotspot is then located between New Zealand and Australia. Consistent with this, the secondary hotspot seen during the autumn months also retreats westward away from South America and equatorward towards ϕ_{35S}. $H1$ then begins to intensify again, extending laterally while the annular pattern takes shape again by spring.

In comparison, the most obvious difference between our (and, by extension, Ghinassi (2019)) $\overline{A}$ distributions and the wave packet activity of Souders et al. (2014b) is in the placement of the RWP hotspots. Such a comparison can be made between fields on θ_{330} and those on 300 hPa, since the θ_{330} surface is in close proximity to the former over the extratropics during summer months and over the subtropics during winter months. The mid-latitude $H1$ in our case is located downstream of that observed by Souders et al. (2014b). For example, their global hotspot over the SH, which is also a quasi-stationary feature, is located between Africa and Australia (60°E - 130°E along 45°S) during summer,

while our global hotspot ($H1$) is located over New Zealand and extends up to $\approx$ 120°E between 45°S and 50°S) in Figure 4.1 (a). This is due to the fact that the $\overline{A}$ field tends to reveal more information about regions of RWP maturity, instead of development, because LWA is largest during this stage of the life cycle as reported by Ghinassi (2019), who compared the RWP hotspots in $\overline{A}$ to the winter storm track of Ambaum and Novak (2014) in the Northern Hemisphere and found similar differences to those we find with Souders et al. (2014b). The maturity of LWA occurs after the baroclinic growth of eddies has ceased, and the RWP would have moved some distance downstream during this period (during the onset of decay). In light of this, the relationship between $\overline{A}$ and well-documented storm track regions diagnosed using metrics such as eddy heat fluxes, can be obscure at times since $\overline{A}$ hotspots would be located further downstream of their traditionally used counterparts.

Note that Souders et al. (2014b) utilised the meridional wind (v) based envelope RWP diagnostic of Zimin et al. (2006), which also falls under the category of methods that are usually better suited for the study of approximately linear waves (Ghinassi et al., 2018). A consequence of this is the fact that a one-to-one comparison between the traditional structure and the behaviour of the storm tracks with $\overline{A}$ is not a trivial exercise and possibly requires consideration of other aspects such as RWP types and life span. This thus prompts the need for LWA object tracking since development regions can be traced back in time relative to these regions of maturity, and tracks can be compared with associated intensities/amplitudes. However, other typical characteristics of the storm tracks can be seen in Figure 4.1 (a-d). For example, the downward spiral towards the Antarctic Peninsula at $\approx$ 60 °W throughout the year, and general reduction of SH eddy activity during winter months (Hoskins and Hodges, 2005). The appearance of distinct higher-latitude and subtropical winter tracks is not evident in Figure 4.2 (c) as a result of our choice in θ surface, that is, θ_{330} does not adequately sample wave activity at higher latitudes. This is a reasonable trade-off because the scope of the study is limited to the SA region, which is located in the subtropics.

Recalling that $H1$ on θ_{350} is essentially the upper bound of the lower isentropic level wave activity, we will not discuss it further from the point of view of θ_{350}. However, in the upper tropospheric (θ_{350}) subtropics in Figure 4.2 (e), there exist two notable wave activity hotspots during summer months over the following regions: 1. 150°W-90°W over the South Pacific Ocean (SPO): $H2$, and 2. 60°W-15°W over the South Atlantic Ocean (SAO): $H3$, both between 15°S-30°S. The magnitudes of $\overline{A}$ over these subtropical hotspots are generally lower than the maximum observed during summer over the extratropics. These hotspots appear as distinct bulges emanating from the extratropical pattern such that $H2$ seems to be connected to the extratropical hotspot ($H1$) in the vicinity of New Zealand and Australia, as also suggested by the extension of the $\overline{A}$ field from the weak hotspot region over New Zealand towards 120°W. $H2$ then rejoins the extratropical pattern at about 60°W just below ϕ_{35S}. At this point, it appears that the RWPs tend to mature northeastward of (60°W,35°S) to give rise to $H3$ just east of Brazil, which subsequently rejoins the extratropics at about 0° longitude. It is worth noting that the summer $H2$ and $H3$ coincide with the regions of the South Pacific (see Vincent (1994) for a review) and the South Atlantic (Barros et al., 2000; van der Wiel et al. 2015) Convergence Zones (SPCZ and SACZ) respectively. Note that an additional convergence zone exists (South Indian Convergence Zone (SICZ)) during this season over the South-West Indian Ocean between Madagascar and southern Africa, but it is not captured by the $\overline{A}$ field due to its relatively weak intensity (van der Wiel et al., 2015).

These convergence zones are associated with extensive convective cloud bands that give rise to significant rainfall, particularly during summer months over the SH, and are also a prominent feature in the context of global circulation (Vincent, 1994; van der Wiel et al. 2015). For example, SACZ is a well-known rain-bearing climatological feature of the subtropical summer season over South America and is characterised by the northwest-southeast orientation of convective cloud bands extending over the Amazon basin, over Brazil, and into the west sectors of the SAO (Liebmann et al.,1999; Robertson and Me-

choso, 2000; Carvalho, 2004). The formation of the SACZ has been associated in part with the propensity of wave activity to converge in this region in the vicinity of the coast of Brazil. This feature is especially interesting in the context of this work given the existence of teleconnection patterns between parts of South America and SA in terms of rainfall (Grimm and Reason, 2015). The south-eastward extension of $H3$ gives the impression of an interplay between this region of localised wave activity over the SACZ region and the existence of mature RWPs downstream in the vicinity of SA.

Hoskins and Hodges (2005) attributed such an observation in their SH storm track climatology to the role of the south-west limb of the low-level subtropical anticyclone over the SAO, which also plays a role in the existence of the SACZ. Therefore, the synchronous disintegration of this LWA hotspot and the observed resurgence of wave activity in the vicinity of SA, together with the south-eastward extension of $H3$ into the region, suggest that the latter might be associated with the wave activity finding its way into the SA domain, so it can be seen as a potential source or sink of wave activity for the SA domain. This hypothesis would appear to be reasonable given the findings of Berbery et al. (1992) and Ambrizzi et al. (1995), who found that Rossby wave trains emanating from the south tip of South America can be diverted either equatorward toward the vicinity of the coast of Brazil (large meridional component), towards SA (slightly small meridional component), or more zonally ducted within the extratropical jet stream. Zilli and Hart (2021) also showed that extratropical Rossby wave trains interact with the SACZ during the summer months. Specifically, their findings suggested that amplified convection associated with the SACZ can interact with the background flow to invigorate or suppress downstream extratropical Rossby wave trains. These hotspots decay with the progression of the seasons, so they are weakest in winter (Figure 4.2(c)). Generally, the patterns observed during the transition seasons appear to be a mixture of those observed during the summer and winter months.

4.2 LWA, the Jet stream, and the dynamical tropopause

The LWA maxima are located in regions of weaker zonal wind speeds (e.g, LWA maximum $H1$ is located downstream the PFJ during summer). A similar collocation is observed during winter months where the hotspot is located within an area of weak westerly flow within the 120°E - 120°W sector of the winter split-flow regime characterised by the STJ and weaker PFJ (see, e.g., Bals-Elsholz et al., 2001; Lee and Kim, 2003; Gallego et al., 2004) between Australia and New Zealand on both isentropic surfaces. This then echoes the notion that RWPs are usually associated with RWB during their mature stage, following the shear arguments of Peters and Waugh (2003). That is, the occurrence of, and RWB type can be attributed to the characteristics of the jet stream (Peters and Waugh, 2003) in which it propagates. In addition, Postel and Hitchman (1999) also noted that the "surf zones", which are essentially RWB hotspots, coincide with regions of weak zonal flow, as do the observed RWP hotspots. In contrast, regions of weaker $\overline{A}$ do occasionally coincide with the PFJ, particularly during summer months over the extratropics. This may point to the existence of almost-plane RWPs that do not become non-linear in the vicinity of the jet, as opposed to their finite-amplitude counterparts. During the rest of the seasons, wave activity appears to go around the PFJ, along the equatorward (poleward) flank between 60°W and 120°E (130°E and 60°W). The STJ has a similar effect to $H1$, forcing it to its poleward flank, likely in conjunction with the PFJ during winter.

The fact that the configuration of $\overline{A}$ is clearly influenced by jet streams is a demonstration of their waveguide nature. Following Section 2(b) in Wirth et al. (2018), these waveguides can be regarded as jet waveguides whose waveguidability (e.g. Hoskins and Ambrizzi, 1993; Ambrizzi et al., 1995) is elucidated by the observed LWA hotspots. The role of jet streams as waveguides can be explained by considerations of aspects of Rossby wave propagation. For example, by considering the refractive index (Andrews et al.,1987), Rossby waves propagate along jet streams during the development stages of their life cycles, and can be refracted upon encountering the jet core towards the critical latitude (where $\overline{u} =$

the phase speed (c_p) of the wave) where they may undergo RWB, absorption, or reflection. Such an observation was made by O'Brien and Reeder (2017) in their study of summertime RWPs over the SH on the θ_{350} isentrope. Therefore, jet streams do not only facilitate the eastward propagation of RWPs (see, e.g., Hoskins and Ambrizzi, 1993; Berbery and Vera, 1996; O'Brien and Reeder, 2017), they also influence where they dissipate or undergo RWB (Peters and Waugh, 1996; Peters and Waugh, 2003; Homeyer and Bowman, 2013).

To the extent that the PV = -2 PVU contour shown in Figure 4.1 is a good approximation of the dynamical tropopause, $\overline{A}$ hotspots during summer on the θ_{330} surface can be viewed as those RWPs on the dynamical tropopause since the PV = -2 PVU contour intersects the circumpolar waveactivity. This would then mean that the observed wave activity is likely in response to the waviness of this PV contour for the most part. During autumn months, the dynamical tropopause shifts equatorward to about 40°S, and continues to do so until winter, during which it reaches about 30°S at the western and eastern hemispheres, and remains at $\approx$ 40°S in the vicinity of SA. Although the wave activity belt (more specifically $H1$) appears to shift with the dynamical tropopause, it lags behind and only really shifts equatorward by about 5°S. This then means that $H1$ is probably a lower stratospheric characteristic during all seasons, except in summer in the extratropics. Note that the secondary hotspots observed throughout the year over southern South America are consistently along the dynamical tropopause.

Kunz et al. (2011) demonstrated the variable nature of the dynamical tropopause and the fact that no one value can be a good approximation of the dynamical tropopause. The proposed solution was to objectively estimate the PV value associated with the dynamical tropopause using isentropic potential vorticity gradients. Loosely, a PV contour is a good approximation of the dynamical tropopause if the isentropic gradients and the horizontal/zonal wind speeds are a maximum at the location of that PV contour. Following this approach, it can be useful to view jet streams as a good approximator of the location of the dynamical tropopause, particularly because observations have shown that the strongest PV gradients are usually found in the region of jet streams (Wirth et al., 2018). Using this

line of thinking, we can speculate that the -2 PVU contour is a good approximation of the dynamical tropopause on θ_{330} because it consistently dissects the PFJ along its horizontal axis during summer and autumn when it is most dominant. During winter and spring, this surface attempts to join the STJ and the PFJ, giving rise to the slightly concave contour observed during winter months (recall that it is at lower latitudes in the west and eastern hemispheres).

The PV = -2 PVU surface is located equatorward of the PFJ during summer on the θ_{330} surface, immediately pointing to the need for an objective estimate of the dynamical tropopause, because during this season there is no significant STJ signature that may be associated with the contour of -2 PVU. However, taking into account the position of the PFJ, the subtropical hotspots $H2$ and $H3$ are obviously tropospheric/lower tropospheric features associated with the waviness of lower value PV contours. During the rest of the seasons, the -2 PVU isoline appears to be most influenced by the STJ and less so by the PFJ because at this level the STJ is much stronger (relative to the PFJ) than at the level of θ_{330}. This state of affairs thus emphasises the need for an objective estimation of the dynamical tropopause. The results of Kunz et al. (2011) seem to suggest that the application of the objective method of identifying the dynamical tropopause would be more useful when considering case studies, whereas the standard definition would suffice for more general purposes. In light of this, we will only objectively estimate the dynamical tropopause when discussing RWP events based on our tracking algorithm in the next section. The preceding analysis in this section confirms that the diagnostic used (A) is representative of known climatological entities of the upper troposphere of the SH, such as RWB and storm tracks.

4.3 LWA RWP morphology

Having established that the broad LWA field calculated here is consistent with previous studies and jet streams, we can now assess the results of our LWA pocket tracking algorithm. To this end, we examine the morphological structure of the A field during the most mature stage of all tracked objects in the SA domain. This assessment is done on both the θ_{330} and θ_{350} surfaces, in keeping with the approach taken when the results of the LWA calculation were examined. The main idea of the ensuing discussion is to ensure that the climatological aspects to be discussed in the sections to follow are truly related to the RWP-like features of the upper troposphere, and therefore give credence to our tracking algorithm.

1378 (1192) LWA pockets undergoing maturity were detected on the θ_{330} (θ_{350}) isentropic surfaces over the SA domain. These are a subset of the SH database consisting of 19680 (14979) tracked LWA pockets. Figure 4.4 shows the composite mean fields of the meridionally averaged configuration of meridional wind pertubations ($\overline{v'}$) on θ_{330} (a) and θ_{350} K (b). Note that these are responses to the evolution of LWA RWPs, and a comparison between the two fields is provided in Figure 4.5. In Figure 4.4, the predominant zonal structure of the trough-ridge components defining an RWP associated with a mature LWA object is elucidated. Black (grey) undulations denote the meridionally averaged upper tropospheric 200 hPa: $\overline{v'}_{200}$ (near surface 850 hPa: $\overline{v'}_{850}$) fields showing the Southern Hemispheric extent of the composite RWP during the most mature stage of its life cycle at time t = 0 hours (h) of the time-lagged mean composite evolution.

The intersection of the curves with the $x-$ axis (where $\overline{v'}$ =0) denote the positions of the individual troughs and ridges while the peaks denote their flanks. Here, the location of a trough is characterised by the component of an undulation that starts at $v' = v'_{max}$ and extends to $v' = v'_{min}$. Between these points (where the curve intersects the $x-$ axis) lies the centre of the trough. Similarly, the position of a ridge is defined by the component

of an undulation that starts at $v' = v'_{min}$ and extends to $v' = v'_{max}$. The position of the trough and ridges are labelled by T_n and R_n respectively, where n denotes the perturbation number in the context of a circumglobal RWP. The red curves enveloping the blue shaded region are discrete-time analytic signals of $\overline{v'}_{200}$. These were computed using the Hilbert transform, where the bottom curves are the negative of the resulting analytic signal that encapsulates the positive peaks of the signal to produce a visual impression of instantaneous upper tropospheric RWP envelopes.

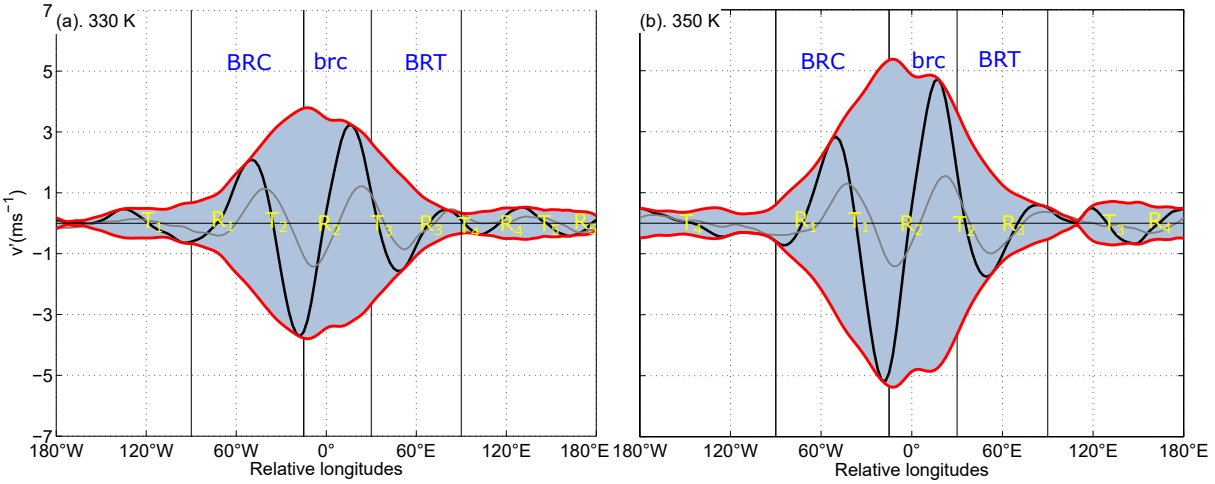

Figure 4.4: Time lagged composite mean of meridionally averaged v' depicting the zonal extent of an RWP at time t= 0 h of the composite evolution on 330K(a) and 350K(b) isentropic surfaces. The undulations were constructed by computing the meridional average of v' at 850hPa (v'_{850},grey) and 200hPa (v'_{200},black). The red curves filled with blue shading denote the envelopes of the RWP computed using a Hilbert transform, while the dark(light) grey shadings represent areas of enhanced(decreased) baroclinicity.

It is evident that on both isentropic surfaces, perturbations are a ubiquitous feature of the Southern Hemisphere (Figure 4.4). On the surface of θ_{330} (θ_{350}), the RWP is characterised by ≈ 5 (4) troughs and ridges so that the zonal wave number can be estimated as $k \approx 5$ ($k \approx 4$). The most prominent/deepest component of the RWP is associated with a ridge (R_2) centred at $\approx 0°$ λ. (R_2) is deepest on θ_{350} (amplitude ≈ 5 ms^{-1}) as compared to its lower tropospheric counterpart on θ_{330} (amplitude ≈ 3.5 ms^{-1}). This suggests that the largest amplitudes of Rossby waves associated with LWA maturity are observed at upper levels of the troposphere in the SA domain. The perturbations on the flanks (west and east of 0°) become progressively weaker with distance towards 180°W and 180°E, which is consistent with the definition of an RWP. Note that T_2 and T_3 collocated with R_2 are

almost comparable in depth/intensity, however T_2 is the most prominent, and this is more evident in Figure 4.2(b). This is consistent with the view that mid-latitude RWPs propagate in a predominantly eastward direction (Hoskins and Ambrizzi, 1993; Wirth et al., 2018), so it stands to reason that perturbations at the upstream end of an RWP would be undergoing progressive weakening, while the downstream end would be in its growth phase as in the paradigm of downstream baroclinic development (Orlanski and Katzfey, 1991; Orlanski and Sheldon, 1995).

The vertical structure of the perturbations is indicated by BRC (baroclinic) and BRT (barotropic) in Figure 4.4. These were estimated on the basis of the zonal distance ($\overline{v_d} = \overline{v'}_{200}$-$\overline{v'}_{850}$) between the peaks of the upper air (thick black) and near the surface (thick grey) v' curves. An area within the RWP is then classified as highly (BRC), weakly (brc), or otherwise equivalent barotropic (BRT) when v'_d is negative and large, negative but smaller than the largest difference, and either negative and smaller than the previous classes or simply positive, respectively. This can be visually diagnosed in Figure 4.4 by comparing the relative distances between 200 and 850 hPa v' peaks. Therefore, it is readily observable that the RWP is highly baroclinic between 90°W - 15°W, while regions 15°W - 30°E and 30°E - 90°E are weakly baroclinic and equivalent barotropic, respectively. In light of this observation, it is thus evident that these RWPs are predominantly baroclinic in nature. As a result, this observation suggests that the evolution of these RWPs can also be discussed in the context of the typical life cycle of a baroclinic Rossby wave as seen in the modelling study of Simmons and Hoskins (1978).

Subsequent time steps (not shown here) reveal that the less baroclinic region eventually becomes equivalent barotropic. This means confirms that time t = 0 h marks the onset of the decay phase of the RWP. This is confirmed by the clear Rossby wave breaking (RWB) signature indicated by the deformation and reversal of the black PV contours in Figure 4.5 as the RWPs seemingly entered a region of significant deformation, which is indicative of the onset of barotropic decay (Wirth et al., 2018). Aspects of the observed RWP in the

context of RWB are briefly discussed below. Since the composite mean fields of v' were calculated based on the LWA-based algorithm employed, the clear signatures of the RWPs seen in Figure 4.4 give credence to the ability of LWA and the tracking algorithm used to produce a realistic database of RWP events.

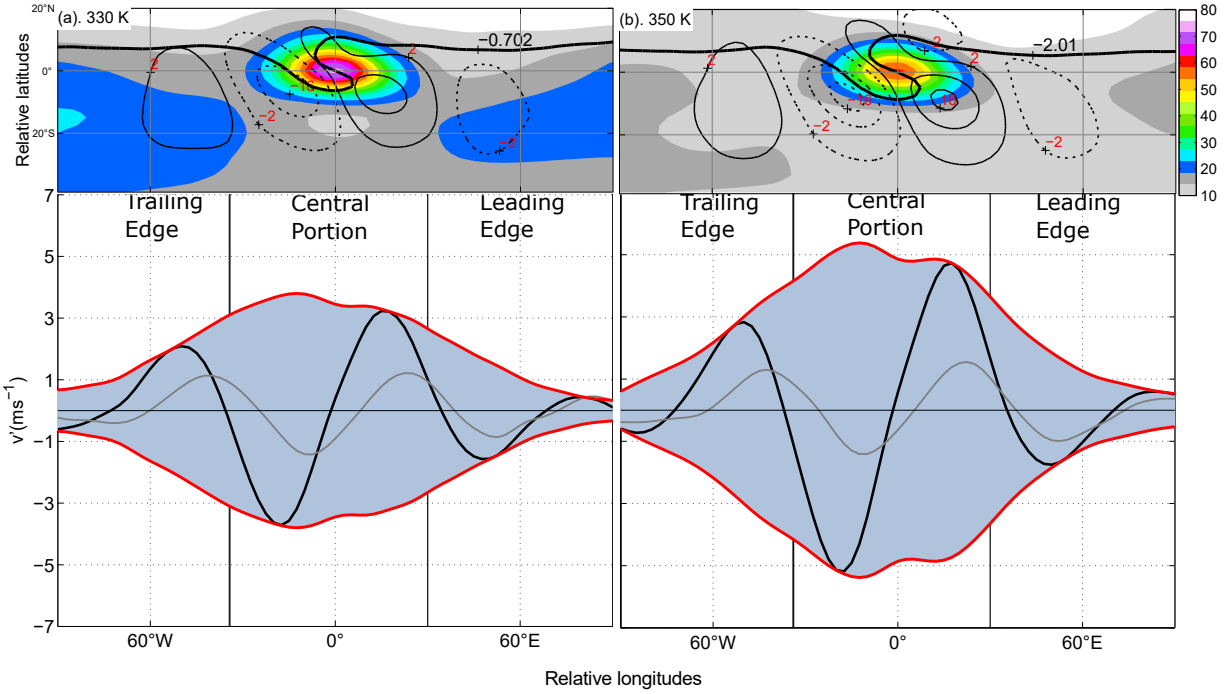

Figure 4.5: Time lagged composite mean of RWPs diagnosed based on LWA (top panels) and v' (bottom panels) for the 330K (a) and 350K (b) isentropic surfaces during time t = 0 h when the RWP attains maturity. The shading represents LWA (ms^{-1}), the black closed contours represent isentropic meridional wind perturbations $v'_\theta < 0$ (dashed) and $v'_\theta > 0$ (solid), where only ± 2,10 and 16 ms^{-1} isotachs are shown. The heavy black contours are the PV = -0.7 and -2 PVU isolines in a and b respectively. The bottom panels are as in Figure 4.2, but for the region 90°W - 90°E of the RWP.

Figure 4.5 provides a comparison between LWA (A) and the v' fields. Above, we established the structure of a composite RWP over the compositing domain using a well-known and intuitive diagnostic and approach. Now we establish the details of the LWA representation of the RWP signature seen in Figure 4.4. Figure 4.5 is a depiction of the time lagged composite mean RWPs undergoing maturity at time t = 0 h on 330K (left panels) and 350K (right panels) isentropic surfaces corresponding to 90°W-90°E of the full RWP depicted in Figure 4.4. In the top panel in Figures 4.5 (a) and (b), the shading represents the LWA representation of the RWP, while the black closed contours represent the cor-

responding isentropic meridional wind perturbations $v'_\theta < 0$ (dashed) and $v'_\theta > 0$ (solid) responses. The v'_θ field serves the role of providing the lost phase information related to individual troughs and ridges of the LWA RWP, as well as details related to the vertical and horizontal source of perturbations associated with the RWP. Here a $v'_\theta < 0 - v'_\theta > 0$ ($v'_\theta > 0 - v'_\theta < 0$) couplet of closed contours denotes a ridge (trough). The black contours in Figure 4.5 (a) [b] are the -0.9 [-2] PVU PV isoline, marking the horizontal position and structure of the PV isolines to illustrate the deformation. The bottom panels show the representation of the composite RWP in terms of isobaric v' as in Figure 4.4.

There exist three LWA maxima, with the central one (at (0°) being the global maximum (hereafter referred to as the LWA RWP object) and characterised by well-defined closed, concentric contours, while the secondary maximum are centred in the vicinity of 90° W and 90° E and extend over a wider region zonally as opposed to the LWA RWP object. Although this holds true for both isentropes, these structures differ in intensity between the two isentropes, with the θ_{330} (Figure 4.5(a) top panel) being associated with larger values of local LWA maxima in general between 90°W and 90°E as compared to the θ_{350} case (Figure 4.3 (b)). In Figure 4.5 (a), the LWA RWP object appears to be in response to the deformation of the PV = -0.7 PVU isoline (signalling RWB), which is characterised by a relatively broad trough tilted in a southeast-northwest direction, and a thin ridge represented by the south-eastward protruding tongue of the PV = -0.7 PVU contour, as in Figure 6 in Ndarana and Waugh (2010).

In the case of the θ_{350} isentrope, the LWA RWP object is also in response to the RWB, but here the -2 PVU is the dynamically important material contour. In contrast to its θ_{330} counterpart, it is characterised by a thin lobed ridge and a broader trough of high PV air (note the north and upstream $v'_\theta < 0$ small scale closed contour). Interestingly, a comparison of the top and bottom panels in Figure 4.5 suggests that the magnitude of LWA does not appear to be related to the amplitude of the perturbation itself. Here, the strength of the LWA appears to be responsive (in addition to the amplitude) to the overall

structure of the lobes that characterise the RWB, so that there is a tendency for the LWA RWP object to be centred within the deeper and broader lobe as seen in Figure 4.5 (a). In Figure 4.5(b), the thin lobe of low PV air associated with a ridge is relatively broader and deeper (see the corresponding v'_{200} curves) than the lobe of high PV air in Figure 4.5 (a) and is almost comparable (morphologically) with the broader downstream lobe of high PV air. This configuration gives rise to a slightly more centrally located LWA RWP object (at the inflection point of the upstream trough lobe) because of this apparent "tug of war" between the PV lobes associated with the RWB.

RWB types can be classified according to the morphology of the deformed PV contour according to the predominant type of shear (cyclonic or anticyclonic), following the idealised modelling study of baroclinic life cycles by Thorncroft et al. (1993). Based on Thorncroft et al. (1993), baroclinic life cycles are classified as life cycles 1 and 2 (LC-1 and 2, respectively), where the former is characterised by cyclonic shear and the latter by anticyclonic shear. In addition, RWB types can be classified based on the predominant meridional direction (equator or poleward) of air transport during RWB (e.g Peters and Waugh, 1996; Peters and Waugh, 2003; Gabriel and Peters, 2008; Ndarana and Waugh, 2011; Homeyer and Bowman, 2013). Figure 4.3 illustrates that, in general, RWPs over the SA domain can feature different RWB types during their maturity stage, particularly in terms of the predominant direction of meridional air transport. This occurs because the anticylonic shear associated with the RWB is readily observable on both isentropic surfaces (LC1 type RWB), while the predominant direction of air transport appears to be in the poleward direction on θ_{330} (P2 following Peters and Waugh (1996)), but is unclear on θ_{350}. The lack of clarity is also indicated by the position of the centre of the LWA RWP object and the amplitude of the PV contour it envelopes. This apparent weak equatorward-poleward symmetry of the PV contours is also documented by Ndarana and Waugh (2010) and Berrisford et al. (2007), indicating the need for a more objective approach such as the calculation of meridional fluxes of wave activity as in Gabriel and Peters (2008), and Ndarana and Waugh (2010). This feature is beyond the scope of this study. The apparent

differences in the morphological characteristics of the RWPs suggest that the evolution of RWPs in the defined SA domain may potentially affect weather in different ways and therefore the variability of the RWPs themselves should be examined.

A comparison of Figures 4.4 and 4.5 reveals that the LWA maxima located on the west and east edges of the picture in Figures 4.1 and 4.2 are likely in response to weak perturbations of higher-latitude PV isolines not included here. These secondary maxima are actually one coherent region of large LWA values centred between 120°E and 180°E and extending from about 30°E to 30°W (not shown). A comparison between Figure 4.2 and this observation leads to this conclusion. Furthermore, this large structure appears to be a climatological feature, as will be discussed in subsequent sections. This has implications on the interpretation of the overall RWP structure. For example, since the LWA RWP object mostly corresponds to a ridge in Figure 4.5 (a), it is evident that the troughs on the west and east flanks of it are associated with these secondary LWA maxima areas. These weaker perturbations appear to be centred at higher latitudes (relative to PV = -0.7 PVU isoline). Therefore, to the extent that the horizontal position of the PV contours can also be seen as markers of the vertical structure of the atmosphere, the west and east flanks of the RWP appear to be rooted at higher altitudes relative to the level in which the RWB takes place. This thus suggests that these RWPs have a "V" shape when viewed from a latitude-height perspective. Note that this feature is more pronounced for the θ_{330} RWP, while the θ_{350} case appears to be slightly more zonally oriented.

Lastly, it is desirable to identify regional aspects of an RWP for brevity, which would simplify the discussion of aspects in the evolution of RWPs discussed in Chapter 5 of this work. The schematic of the RWP (Figure 9) of Wirth et al. (2018) is mainly based on typical processes that affect a mature RWP at different locations in the envelope from the perspective of the framework of eddy-kinetic energy (K_e) . Here we establish three distinct regions of an RWP based on the relative location of the mature LWA object. Here, the region enveloped by concentric contours of the LWA is termed the central portion because

it marks the most active and central area of the RWP. The area west (east) of the central portion is the trailing (leading) edge, since the propagation of an RWP is predominantly eastward. Therefore, the trailing edge would be characterised by the decay (development) region behind (ahead) an RWP.

4.4 Variability of LWA objects tracked

When discussing the climatology of RWPs, $\overline{A}$ is mostly useful when one only seeks to obtain a general picture of RWP activity over the Southern Hemisphere. To discuss properties of regional RWPs in detail, a feature tracking approach can be useful since less prominent regional features that are smoothed out by the temporal averaging can be examined more closely. The key finding in the preceding discussion is the fact that the identified LWA pockets maturing over the SA domain exhibit a structure similar to those of RWPs. This therefore suggests that the tracking algorithm was able to adequately capture mature RWPs. As the climatology of finite-amplitude RWPs tracked in the SA domain has not yet been established (to the knowledge of the authors) for the SA domain, and indeed the SH based on the new LWA diagnostic (Ghinassi et al., 2018), we have to assess the results of our tracking algorithm in the context of the SH. This is to ensure that there is consistency between our findings and typical climatological characteristics of the SH, such as jet streams and storm tracks. To this end, Figure 4.6 shows the annual distributions of the number of detected RWPs detected during their start (top) stages, maturity (middle) and end (bottom) stages of their life cycles (colour shading smoothed using a 3° x 3° window filter) on both θ_{330} (a) and θ_{350} (b).

Even when comparing Figure 4.6 (not seasonal) with Figures 4.1-4.2, the resemblance between the RWP tracks and the distribution of seasonal $\overline{A}$ is evident, with the LWA hotspots identified in the latter (e.g, $H1$) coinciding with the maxima of density RWP hotspots in Figure 4.6 also located in the vicinity of 45°S during maturity. The colloca-

tion of RWP objects with the jet stream is also clear. For example showing its waveguide nature, the climatological PFJ between 60°W and 120°E appears to "guide" most RWPs (e.g, over those regions with $\sim \geq 8$ number of RWPs detected) in its vicinity to its equatorward flank throughout their life-cycle, again pointing to the anticyclonic shear it may be exerting on migrating RWPs potentially leading to anticyclonic RWB (e.g, Peters and Waugh; 1996; Ndarana and Waugh, 2010). Therefore, the distribution of tracked RWPs as seen in Figure 4.6 can be explained using the arguments provided for the distribution of $\overline{A}$ previously and will be examined briefly. In the following discussion, only the spatial distribution of the annual number of RWPs is examined to allow for a direct comparison between the corresponding fields in Souders et al. (2014b).

4.4.1 Generation, Maturity, and Dissipation regions of SH RWPs

A majority of SH RWPs on θ_{330} have a preference to develop (or become detectable in the LWA field as distinct objects) over the region $\approx$ 120°E - 170°E between the southern tip of Australia and Tasmania (Figure 4.6 (a)). These RWPs then have a tendency to propagate south-eastward toward New Zealand where they undergo LWA maturity between Tasmania and New Zealand. The RWP hotspot observed during the maturity phase in the 3 phase life cycle is associated with two local RWP density maxima, where one is anchored over the development region between southern Australia and Tasmania, and the other just west of New Zealand. Although the latter can likely be associated with the initial development of LWA in Tasmania, the former could be associated with RWPs that do not move much after their detection because their detection was very late in their life cycle, just before they reached maturity. There could also be a contribution from those RWPs that saw their first detection very close to the jet stream exit region over the area $\approx$ 120°E - 140°E.

Finally, the sector 150°E - 160°W is most associated with the last position of LWA RWP centroids over the ϕ range 40°S - 50°S. Note that the high-density region : 180° - 160°W seen in the first panel in Figure 4.6 (a) is associated with the termination region : 170°E -

180°E, and is actually an extension of this feature during complete RWP termination. This region appears in the first panel because the algorithm begins at the west most longitude at 180°W (and ends at 180°E), identifying RWP events that have crossed the international dateline, particularly during their termination stage, as "new events". The spuriousness of the "new events" identified over the region: 180° - 160°W in the first panel in Figure 4.6 (a) is revealed by the dramatic decrease in its intensity during the maturity stage, demonstrating that these events failed to satisfy our RWP criterion, which is that an RWP object must undergo clear growth, maturity, then decay. Therefore, the weak RWP hotspot observed at maturity in the 180° - 160°W sector in the second panel of Figure 4.6 (a) can be interpreted as a real RWP hotspot because the identified RWPs would have satisfied the identification criterion of the RWP. This is also confirmed by the existence of a relatively weak development zone between 180° and 150°W in the climatology of the tracked RWPs produced by Souders et al. (2014b); see Figure 3 (a). Although most RWPs fully dissipate between 170°E - 160°W (main dissipation zone), there is a secondary dissipation zone over the Tasman Sea region, which appears to be connected to the main dissipation zone. This could be linked to the upstream region of maturity over Tasmania and thus shows a different class of RWPs propagating differently.

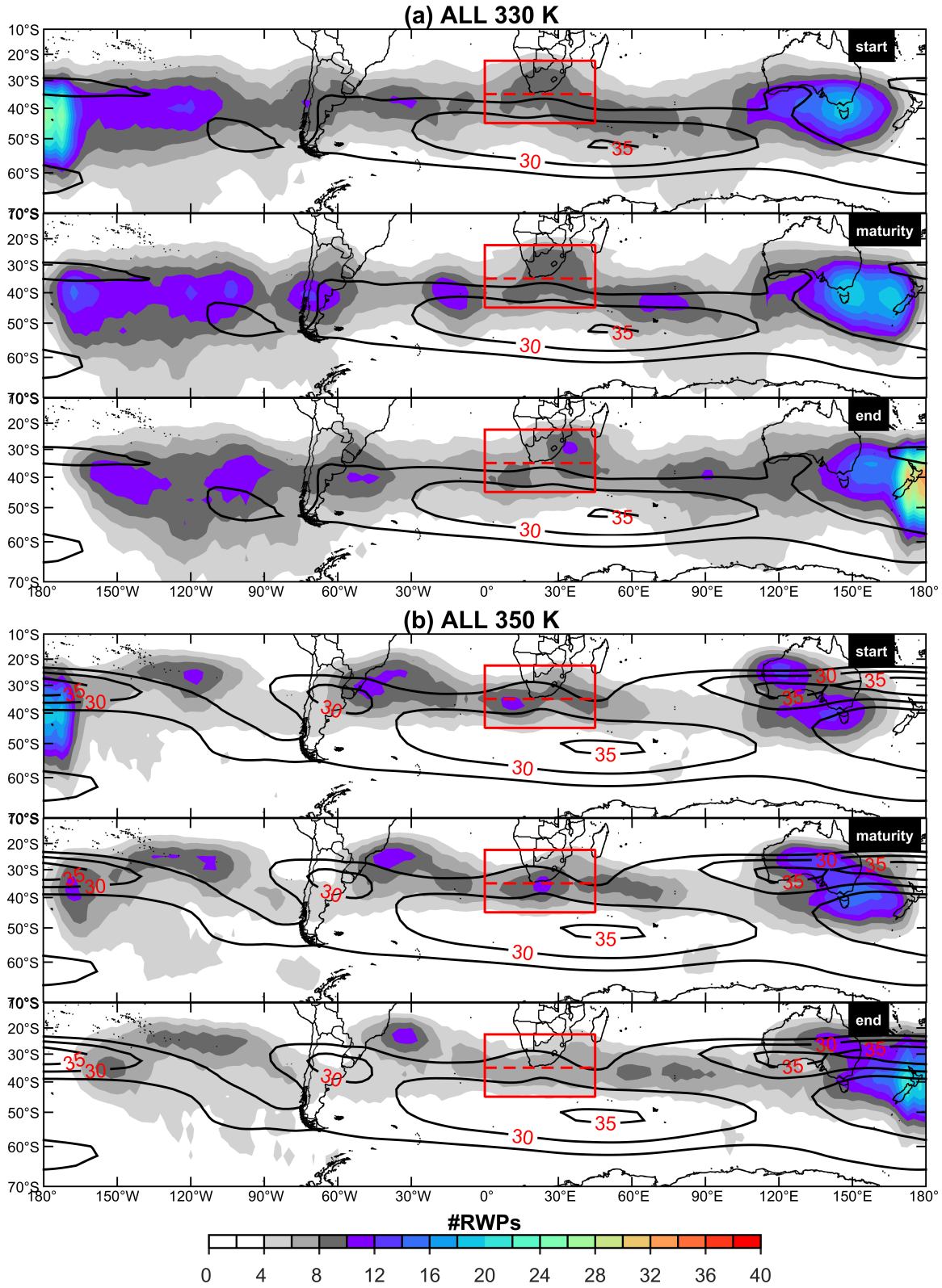

Figure 4.6: Distribution of total number of RWP objects detected on 330K (a) and 350K (b) surfaces (color shading). The panels are arranged as follows: top, middle and bottom panels represent the development (start), maturity, dissipation (end) areas of RWP objects respectively. The climatolgical mean jet stream is represented by the zonal component of the horizontal wind isotachs (thick solid black contours: 25-35 ms^{-1}) The South African (SA) domain is highlighted by the red box where the subdivisions correspond to the subtropical (north) and extratropical (south) subregions of the SA domain.

In general, there are about five more notable regions of preferred RWP development in the SH (when also considering the region 180° - 160°W). These are shown in Figure 4.6 as regions with ≥ 10 detected RWPs appearing as purple-red shading. There is a clear association between these regions and those regions appearing in the subsequent maturity and dissipation panels showing the propagation characteristics of the RWPs. The propagation is predominantly eastward, with a general displacement of $\sim 30°$. There are some indications of latitudinal propagation, but those are not as pronounced as the zonal propagation. In total, there are six preferred locations for maturity and dissipation, one more than regions of development. The additional maturity hotspot emerges along the equatorward flank of the PFJ, and is apparently linked to the trail of RWPs emanating from the SA domain. The extra dissipation hotspot emerges over the Mozambique channel in the SIO east of South Africa. The emergence of RWP maturity and dissipation hotspots not explicitly tied to development hotspots can be seen as an indication of the complexity of regional RWP propagation, particularly between the SAO and SIO region in the vicinity of SA and on the equatorward side of the PFJ core.

Subtropical LWA hotspots ($H2$ and $H3$) previously identified also appear in Figure 4.6 (b) as RWP activity hotspots. As argued previously, the extratropical RWP hotspot on θ_{350} is an indication of the coupling between lower and upper tropospheric levels and will not be discussed here again since it was addressed on θ_{330} above. $H1$ begins developing at $\approx 120°$W between 20°S and 30°S, matures and dissipates a few degrees eastward between 120°W and 105°W. $H1$ has a more pronounced meridional propagation component, preferring to develop, mature, and dissipate at $\approx$ (45°W,30°S), (45°W - 30°W,20°S - 30°S), and (30°W,20°S - 25°S) respectively. These are small eastward displacements relative to the extratropical RWPs observed on θ_{330}, pointing to the quasistationary characteristic of the convergence zones, such as SPCZ we hypothesise that they are associated with. Lastly, there is an RWP development region over the SAO along and south of 35°S. RWPs emanating from this region are likely to mature and dissipate at about 30° E over the southern coast of SA.

A comparison of Figure 4.6 and Figure 3 of Souders et al. (2014b) shows some differences in the placement of the main RWP activity hotspots over the mid-latitudes. For example, their Southern Hemispheric maximum showing the development of RWP events exists between 30°E - 60°E and 45°S - 60°S, while they mostly dissipate over the region 150°E - 120°E along 45°S. However, although this is in stark contrast to our findings, there is a local RWP development hotspot at $\approx 150°$ E, which, although located approximately 10° south of that identified in Figure 4.6 (a), shows that $H1$ exists and is indeed a mid-latitude feature. The reason for the differences in the densities of RWP events over this region can be attributed again to the nature of the diagnostics. That is, LWA is most sensitive to non-linear Rossby waves, whereas the diagnostic employed by Souders et al. (2014b) elucidates better almost planar Rossby waves, as reported by Ghinassi (2019).

This could also explain why the dissipation hotspot over south eastern South America seen in Figure 3(b) in Souders et al. (2014b) appears in the maturity panel in Figure 4.6(a) over the same region. That is, the lifetime of an RWP from their point of origin ends when an RWP matures. Assuming that this argument holds, the development hotspot seen between 120°W and 150°W in Souders et al. (2014b) Figure 3 (a) is actually the true origin of the dissipation hotspot emergent between 60°W and 45°W in Figure 4.6 (a). This also emphasises that RWPs from an LWA perspective usually emerge from the LWA field very late during their life cycle. Furthermore, the trail of RWP events (number of RWPs 8-10) initially developing from SA between 30°E and 90°E is arguably associated with the classic main storm track that appeared as a global maximum in Souders et al. (2014b) and appears only as a weak feature because RWPs in that region are usually in their baroclinic growth stage, which, of course, is a typical attribute of storm tracks (Wirth et al., 2018). In general, it appears that the observed spatial distribution of LWA RWPs θ_{330} is consistent with the findings of Souders et al. (2014b) when their dissipation points are considered as the development/starting point of LWA RWPs in Figure 4.6 (a). Therefore, this confirms that the spatial distribution of LWA RWPs should closely resemble the spatial distribution

of RWB. This notion is examined in the following section where we introduce the seasonality of the spatial distributions of tracked LWA RWP objects.

4.4.2 Seasonal variability of tracked SH RWPs

Recalling that Ghinassi (2019) discussed the climatology of RWPs purely from the point of view of $\overline{A}$, it is now important to closely compare the extent to which this field corresponds to the frequency of individual RWPs identified and tracked in this study. This aspect of the discussion is important because it is possible that a region may be associated with a fair frequency of very weak RWP occurrences (in the context of the SH) during a specific period and on a specific isentropic surface. Such RWP hotspots may likely be smoothed out of the $\overline{A}$ field, leading to the suppression of regional information, at least from a qualitative point of view. The seasonal distributions of maturing RWP tracks (grey shading) overlaid with the corresponding maximum intensity (coloured contour lines: A_{max} in ms^{-1}) are presented in Figures 4.7 and 4.8 on θ_{330} and θ_{350} respectively to address this issue. Furthermore, the total SH RWP counts are summarised in Table 4.1. The counts have been divided according to seasons, θ surface, RWPs over regions with ≤ 2 (low density) and $>$ 2 (high density) RWPs detected at a particular grid point.

A total of 19680 (14979) RWP objects were detected on θ_{330} (θ_{350}) in the SH ϕ domain: 20°S-85°S with an annual frequency of 492 (374) RWPs per year during the 40-year study period 1979-2019. Most RWPs ($\sim$ 29%) were detected during the summer DJF months, while winter corresponds to the suppression of RWPs that contribute only about 22% of the annual events detected on θ_{330}. Overall, there is a general trend of decreasing RWP activity from summer to spring, with high-density regions contributing the most ($\sim$ 67%) to this trend. In low-density regions, the pattern is different, with event maximums (minimums) occurring during summer and spring (autumn and winter).

The overall seasonality is different on θ_{350} since RWPs tend to peak during spring ($\sim$

28%) and are suppressed during summer ($\sim$ 20%). Here, the low-density regions offer a considerable contribution to the overall distribution of RWPs with only a $\sim$ 8.52% difference between this category and the high-density regions, which still contribute the most throughout the year, with the exception of summer when RWPs are scarce (only $\sim$ 9% compared to $\sim$ 33% on θ_{330}). Peaks over high-density regions are observed during the transition seasons, whereas low-density regions see a peak (minimum) during spring (summer). These results suggest that there is considerable variability in the occurrence of RWPs over the SH, and thus it may be useful to categorise these RWPs according to their specific attributes such as spatial preference, intensity/amplitude, duration, size, mobility, etc. However, comparisons can still be drawn between our results, which are very general at this point, and those of previous studies based on some of the typical characteristics of SH RWPs and associated phenomena such as RWB.

A visual comparison between the seasonally corresponding panels in Figures 4.1 and 4.7 confirms that there is good agreement between the spatial distribution of the tracked RWP object and $\overline{A}$ fields on θ_{330}, most notably over the mid-latitude region. For example, the H_1 region established previously is evident during all seasons and is marked by a high density of RWP events, as well as significantly high A_{max} values. It is important to note that the highest values of A_{max} are in the 125-205 ms^{-1} range, about four folds stronger than those values observed on $\overline{A}$ for H_1. This shows that most days over the 40-year period (1979-2019) did not see RWPs over the established hotspot regions. The RWP hotspots (for RWPs those with a lifespan $\geq$ 2 days) identified in Souders et al. (2014b) have a maximum density value of $\sim$ 2 per year. Therefore, while there is a tendency for RWPs to exist over certain regions (i.e., RWP hotspots), RWPs, like Oceanic Rossby waves, can generally be seen as ubiquitous features of the atmosphere (Pinault, 2022) with occasional tendencies to follow certain paths. Although widespread and infrequent RWPs in low-density regions contribute mainly less than their high-density counterparts, their contributions can be somewhat significant during the summer on θ_{350}, as seen in Table 4.1.

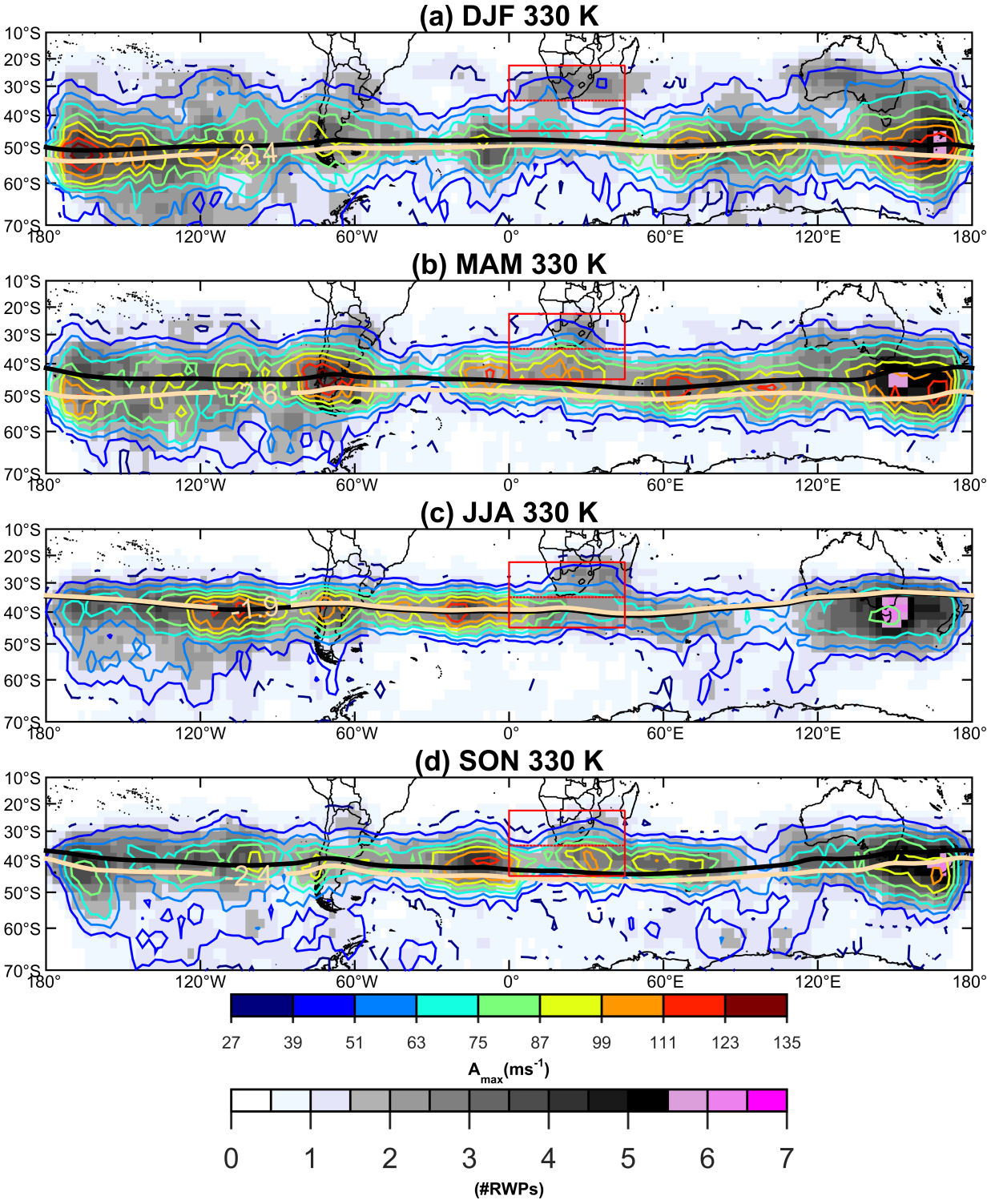

Figure 4.7: 330K Seasonal distribution(a. summer (DJF), b. autumn (MAM), c. winter (JJA), and d. spring (SON)) of the number of mature RWPs detected. The colored dots represent the maximum LWA intensity ($\overline{A}_{max}$) in ms^{-1} observed during the mature stage of the RWP life cycle. The black solid contour represents the -2 PVU PV contour, and the South African (SA) domain is highlighted by the red box where the subdivisions correspond to the subtropical (north) and extratropical (south) subregions of the SA domain.

There is a general pattern that shows that RWP hotspots coincide with large A_{max} values. This points to the large amplitude and, very likely, the non-linear nature of RWPs over those regions. This relationship is also consistent with the overall distribution of $\overline{A}$, however, there are some subtle differences. First, the $\overline{A}$ field suggests that A generally decreases from summer to winter as it becomes concentrated at lower tropospheric levels. This is also evident in Figure 4.7 when considering the A_{max} behaviour over the H_1 region. The RWP counts also follow this pattern in general, except over the H_1 region where there is an increased number of relatively weak RWPs over a small area in south eastern Australia. This shows that the occurrence of RWPs should be studied as a separate entity from their characteristics, of which the amplitude is a part, because the intensity tends to overwhelm the frequency in this apparent "tug of war". Moreover, according to $\overline{A}$ field, H_1 is the most intense region during winter months, while Figure 4.7 (c) shows that its intensity comes only second to that located between 120°W and western South America during winter over the SPO.

RWB detection procedures employed in previous studies (e.g, Postel and Hitchman, 1999; Ndarana and Waugh, 2011; Homeyer and Bowman, 2013) have so far proven to be reliant on the morphology of some material contour, and are thus feature-based. The results are then typically presented as spatial frequency distributions, as we have in Figures 4.7 and 4.8. This gives us the opportunity to compare our results with the results of some of these studies to establish the relationship between RWB and LWA. A simple visual comparison between Figure 4.7 in Ndarana and Waugh (2011), and Figure 4.7 in the current study shows that there is some spatial agreement with some minor differences between the detected RWPs and anticyclonic RWB events found along the subtropical dynamical tropopause on θ_{330}. Much of the correlation is attributable to the region: 180°W-60°W (western sector), while the inconsistencies are seen mostly over the region: 60°E-180°E. The discernible difference is purely based on the placement of the hotspots, rather than the densities.

θ surface	DJF	MAM	JJA	SON	Total	# yr^{-1}
330K	**5641 (28.66%)**	**5027 (25.54%)**	**4398 (22.35%)**	**4614 (23.45%)**	**19680**	492
> 2	3959 (20.12%)	3478 (17.67%)	2849 (14.48%)	2801 (14.23%)	13087 (66.50%)	327
≤ 2	1682 (8.55%)	1549 (7.87%)	1549 (7.87%)	1813 (9.21%)	6593 (33.50%)	165
350K	**3042 (20.31%)**	**3720 (24.83%)**	**4041 (26.98%)**	**4176 (27.88%)**	**14979**	374
> 2	1322 (8.83%)	2306 (15.39%)	2210 (14.75%)	2290 (15.29%)	8128 (54.26%)	203
≤ 2	1720 (11.48%)	1414 (9.44%)	1831 (12.22%)	1886 (12.59%)	6851 (45.74%)	171

Table 4.1: A summary of SH RWP seasonal counts and percentages in brackets relative to the total number of RWPs on an isentrope summed between 20°S and 85°S. For each θ surface, the table is arranged as follows: The first row is the sum of all RWPs detected (bold), and the second (third) row is the sum of those RWPs over regions with more than (two or less) detected RWP objects. The highest (lowest) values are highlighted in red (blue).

The RWB (RWP) maxima exist on the eastern (western) side of Australia throughout the seasons, both maximising during winter. This could be explained by the fact that the distribution of RWB events shown in Ndarana and Waugh (2011) is based on the onset of RWB, instead of the point of maturity, as we have presented the RWP tracks. The consistency in the western sector could be related to the fact that the RWPs in this region propagate only short distances before they fully mature (see Figure 4.8(a)). The θ_{350} distributions are also comparable, where even the subtropical summertime hotspots H_1 and H_3 are evident on the anticyclonically sheared RWBs on these surfaces (see Figure 8(a) in Ndarana and Waugh (2011)). The RWB climatology of Postel and Hitchman (1999) during summer also shows closely resembles the distribution of RWPs in the vicinity of SA during this season on θ_{350}. Recalling the well-established link between cut-off low pressure systems (CoLs) and anticyclonic RWB (Ndarana and Waugh, 2011), the relationship between the $\overline{A}$ and RWP count density fields is further supported by the correspondence between these fields and the spatial distribution of CoL events (CoLs) during the corresponding seasons as presented by Fuenzalida et al. (2005) in Figure 1, Ndarana and Waugh (2010) in their Figure 2, Reboita et al. (2010) in Figure 4, and more recently by Barnes et al. (2021) in their Figure 1.

The spatial distribution of the results of their detection algorithm applied on 250 hPa closely resembles the distribution of RWPs on θ_{350} in particular, although they used the European Centre for Medium-Range Weather (ECMWF) reanalysis (ERA-Interim) dataset

(Dee et al., 2011). Furthermore, the annual frequency of CoLs on 250 hPa ($\sim$ 254 year^{-1}) is in broad agreement with the RWPs in the high-density region ($\sim$ 203 year^{-1}). In general, where there are significant differences, particularly when RWPs exist where RWB is non-existent, it is reasonable to assume that the RWPs observed there were very likely almost planar and did not undergo RWB. Taking into account these factors, it stands to reason that RWP tracks together with $\overline{A}$ simply depict both the distributions of RWB, and tracks of almost planar RWPs typically associated with storm tracks as presented in previous studies (see, e.g., Hoskins and Hodges, 2005).

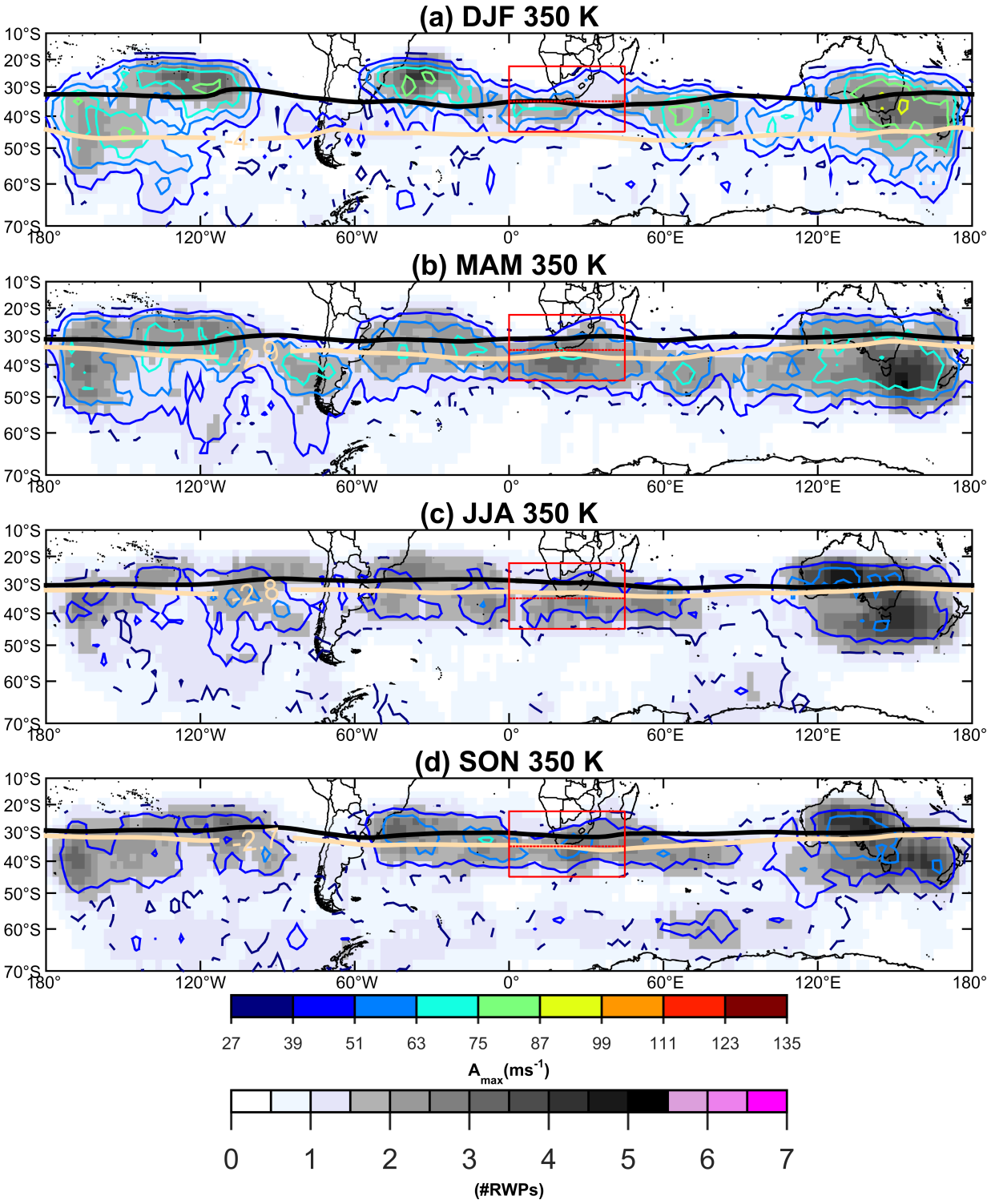

Figure 4.8: As in Figure 4.7, but for 350K.

4.5 RWPs in the SA domain

In line with the study objectives, the variability of RWPs in the SA domain is of particular interest and will be discussed in this section. Above, we set out to assess the merits of the results of our algorithm by drawing qualitative comparisons to well-known SH features, such as linear RWP and storm tracks, as well as RWB. The objective of that discussion was to set the scene for the subsequent discussion pertaining to the characteristics of RWPs in the SA domain (highlighted by the red box in Figures 4.7-4.8). We begin the discussion by examining the seasonality of the RWPs found to mature within the SA domain summarised in Table 4.3 and Figure 4.12. As a preliminary step, it is important to discuss the variability of the objectively defined dynamical tropopause. This step is important because it has been shown that the dynamical tropopause varies in terms of space and time (e.g, Kunz et al., 2011), so much so that it is imperative to define it objectively on a case by case basis.

4.5.1 An estimate for the Dynamical Tropopause

In the discussions to follow, it is important that the position of the dynamical tropopause is adequately represented, as it marks the interface between the upper troposphere and the lower troposphere. The position of the dynamical tropopause (PV^{TP}). Here the composite mean PV^{TP} was estimated using the equivalent latitude PV gradient approach (Kunz et al., 2011) discussed in Chapter 3 based on the RWP events detected over the SA domain (1378 and 1192 on θ_{330} and θ_{350} respectively).

Figure 4.9 illustrates how these values were estimated on θ_{350} only for the extratropical region of the SA domain as an example. During summer months, zonal wind speed (u_h, Figure 4.9 (a, third panel

Season	Subtropical: $\theta_{330}(\theta_{350})$	Extratropical: $\theta_{330}(\theta_{350})$
DJF	-2.29(-3.88)	-2.48(-4.16)
MAM	-2.62(-3.05)	-2.65(-2.81)
JJA	-1.90(-2.74)	-1.90(-2.76)
SON	-2.35(-2.71)	-2.50(-2.59)

Table 4.2: A summary of the estimated mean PV^{TP} values (PVU).

from top)) and the meridional

gradient of PV interpolated to equivalent latitudes ($\partial_{\phi_e} PV$, Figure 4.9 (a, second panel from top))) are both strongest in the midlatitudes Figures 4.9 (a), with the former (latter) being a maximum at ≈ 50°S (45°S). For this situation, the mean location of the maximum of the $u_h \partial PV_{\phi_e}$ distribution is read off slightly equatorward of 45°S (Figure 4.9(a, fourth panel from top))).

This results in an estimated mean PV^{TP} value of -4.16 PVU by reading off the corresponding PV value at this location on the first panel of the PV distribution. During this season, there is a wide range of possible PV^{TP} values, as indicated by the dotted lines that denote the upper and lower bounds of the standard deviation, although the median value is very close to the mean. Using the same approach, the winter mean PV^{TP} value is estimated to be -2.76 PVU. In contrast, the location of the maximum $u_h \partial PV_{\phi_e}$ is found at the lower ϕ_e, clearly under the influence of the STJ that dominates the winter split jet regime. Furthermore, the variability of possible PV^{TP} is significantly lower during this season.

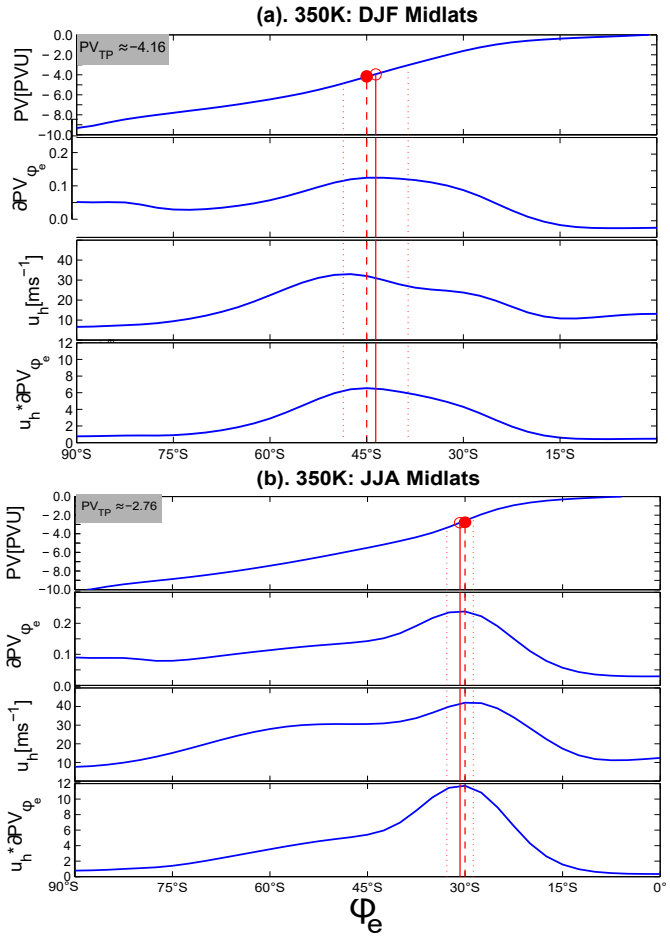

Figure 4.9: Illustration of the PV gradient method used to estimate values of the dynamical tropopause (PV^{TP}) associated with extra-tropical RWP events on θ_{350} during summer (a) and winter (b) months. From top to bottom, the panels represent: PV, the meridional gradient of PV, the magnitude of the horizontal wind (u_h), and the product of the meridional PV gradient, and the horizontal wind, all in equivalent latidude (ϕ_e) space. Solid red, dashed, and dotted lines represent the coordinate of the mean, median, and standard deviation (upper and lower bounds) of PV^{TP}, respectively.

The same method was used to estimate the PV^{TP} values in the subtropical and extratropical regions during the rest of the seasons and on θ_{330} (illustration not shown). The mean values are summarised in Table 4.2.

The RWPs maturing over the subtropical (extratropical) region of SA are associated with dynamical tropopauses characterised by small (large) PV values, as expected. However, transition seasons are an exception to this observation, as the θ_{350} extratropical estimates are smaller than their subtropical counterparts. Furthermore, there are considerable (very small) differences between the estimated PV^{TP} over both regions during summer (winter) on both θ surfaces, as also found by Kunz et al. (2011). Note that with the exception of wintertime on θ_{330}, the estimated PV^{TP} values are constantly greater than -2 PVU (in magnitude). These observations further emphasise the importance of objective estimation of the dynamical tropopause on a case-by-case basis because even when considering the relatively small number of events, the variability is still significant, particularly during summer.

To put the preceding analysis in the context of the SH, the estimated PV^{TP} values are superimposed on seasonal climatological maps of $\overline{u_\theta}$ averaged over the 40-year climatological period considered in this study (1979-2019). These are shown in Figures 4.10 (θ_{330}) and 4.11 (θ_{350}), where the standard PV at the dynamical tropopause (PV = -2 PVU) is shown in black isolines, whereas the PV^{TP} estimates are shown in peach. Dotted (dashed) peach lines show the estimated PV^{TP} based on events maturing over the subtropic (extratropics) region of the SA domain. The average of these two estimates is shown by the solid peach line and essentially illustrates the average PV^{TP} estimate over the SA domain because the employed method (Kunz et al., 2011) was applied only to events that reside over the SA domain, during the maturity of RWPs. There is very little variability between PV^{TP} values based on subtropical and extratropical region maturing RWPs, which is why the broken lines are not easily discernible in Figures 4.10 and 4.11. This implies that the average value can generally be taken as a good approximation of PV^{TP} over the SA domain.

A good PV^{TP} should reside in the vicinity of the jet stream(s). The results of Kunz et al. (2011a) showed this to be true, where the estimated mean PV isolines at the dynamical tropopause (PV^{TP}) either connected two jet streams in a split-flow situation, intercepted a single jet core, or just misses the core of the jet stream. Our results appear to be consistent with this, as can be observed in Figures 4.10 and 4.11 throughout the year on average. Figure 5 in Kunz et al. (2011) is comparable to Figures 4.10 and 4.11, although their analysis was done on the 340 K isentrope. In particular, PV^{TP} estimates during summer are found mainly in the vicinity of the extratropical jet stream in the SH, as in Figures 4.10 and 4.11 (a). During winter, these estimates are collocated with the strong winter SH subtropical jet as in Figures 4.10 and 4.11 (c), while during transitional seasons, the PV contours appear to be located between the extratropical and subtropical jets characterising the split flow. It is important to note that the PV = -2 PVU contour is found close to PV^{TP} contours during all seasons except summer on θ_{350} (Figure 4.11 (a)). The standard dynamical tropopause PV contour lies about 10-15° equatorward of the dominant extratropical jet and PV^{TP} during this season. This suggests that, to the extent that PV^{TP} is a good marker of the dynamical tropopause, the interpretation of PV = -2 PVU in the same way can lead to incorrect interpretation of the results. This is particularly important when stratospheric-tropospheric exchange processes are crucial in a study.

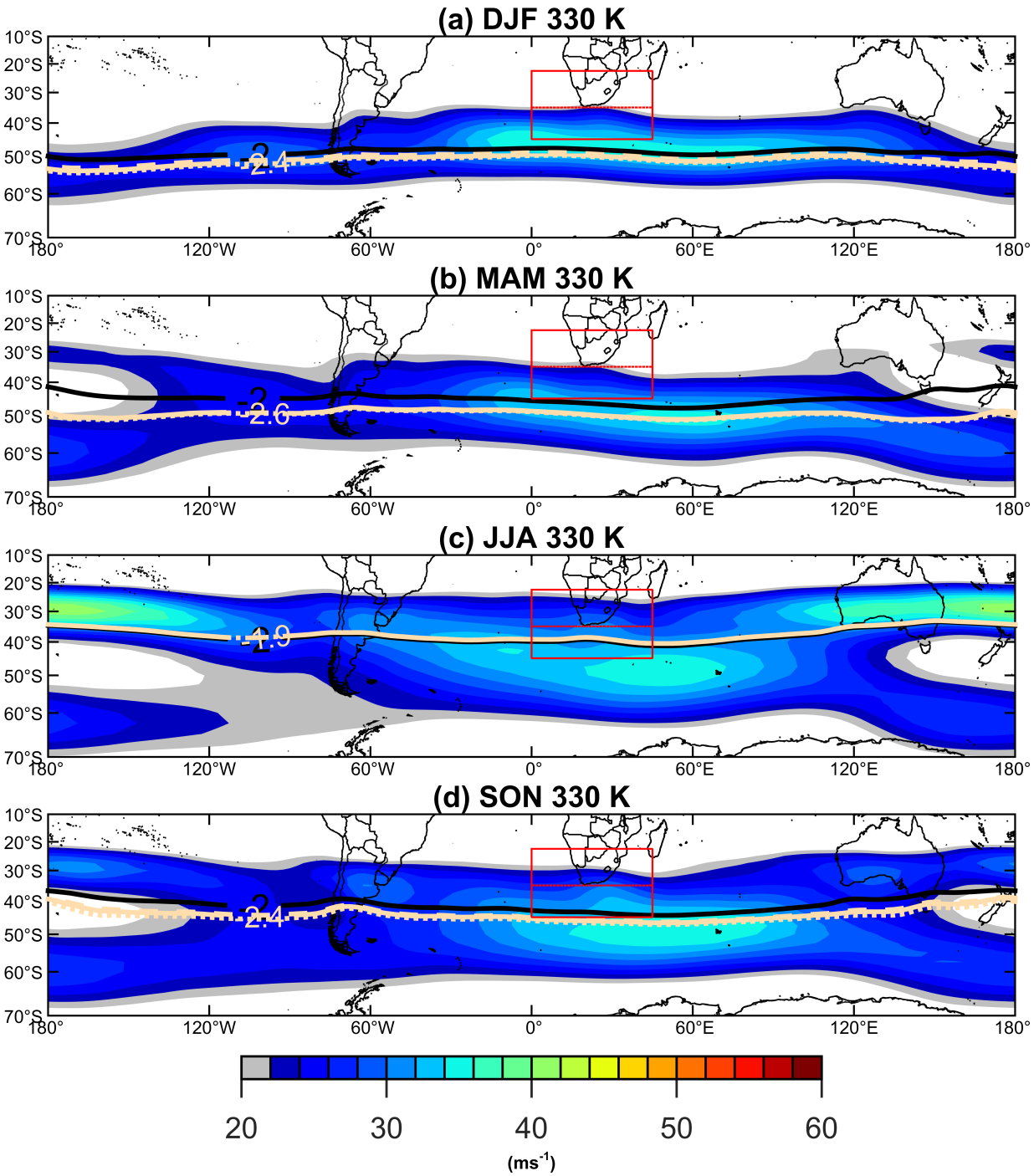

Figure 4.10: Location of the estimated dynamical tropopauses against the ambient zonal flow (u) on θ_{330}. The colorshading in ms^{-1} denotes u_{330} , averaged over each season for the 40 year climatological period (1979-2019). The thick black isoline is the standard dynamical tropopause value, PV = -2 PVU contour, while the peach coloured contours are the estimated dynamical tropopause values (PV^{TP}) based on Kunz et al. (2011a). For these estimates, the solid lines represent the mean of the PV^{TP} estimate based on extratropical and subtropical RWPs in the SA domain. The dashed (dotted) lines are PV^{TP} based on subtropical (extratropical) RWPs. Note that these values are plotted from the $\overline{PV_{330}}$ field calculated in a similar manner as u_{330}. The red rectangular box shows the domain SA domain, with the subtropical (extratropical) residing north (south) of the dotted line within this region.

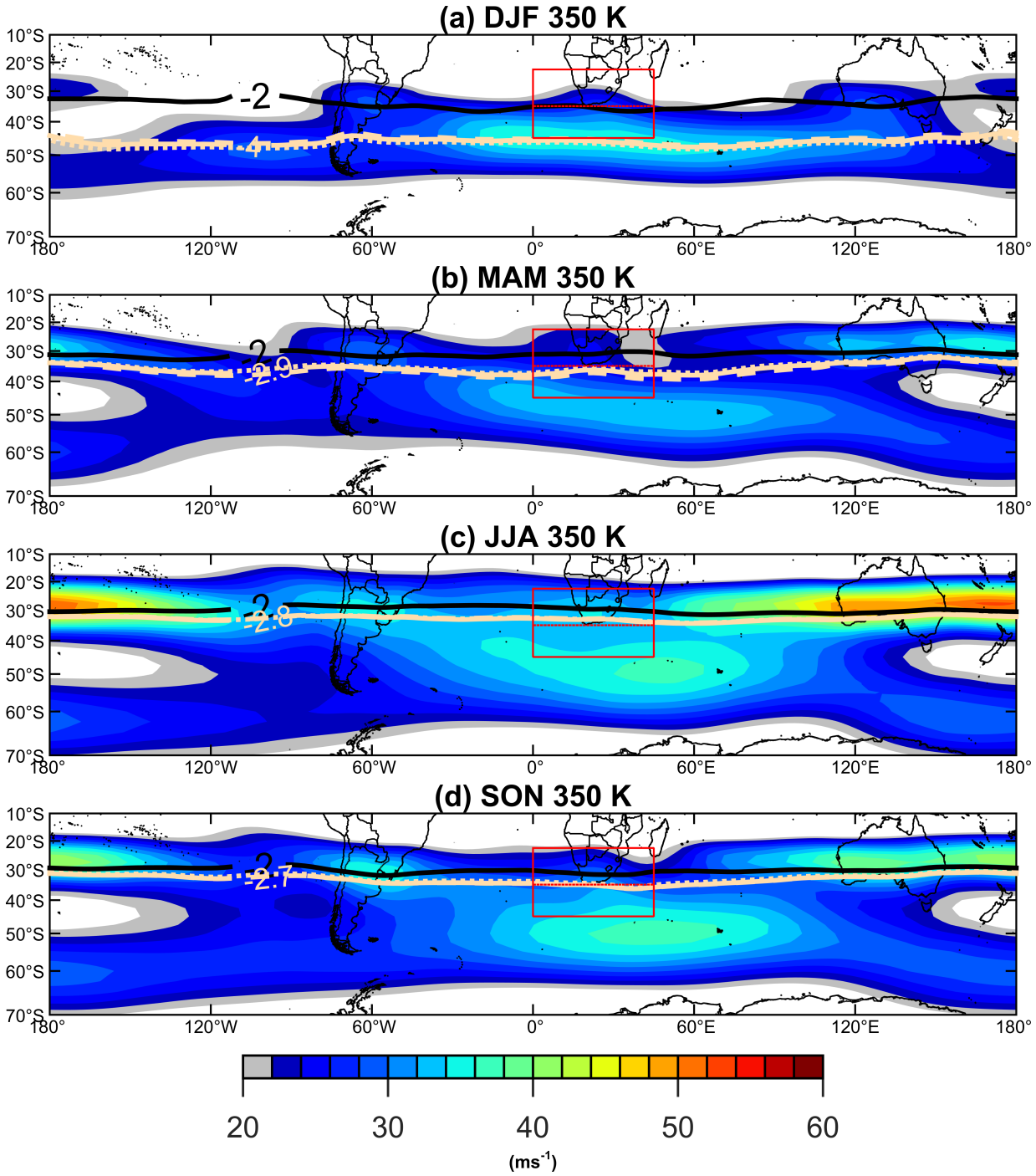

Figure 4.11: As in Figure 5.12, but for the θ_{350} isentrope.

4.5.2 Seasonal variability of RWPs over South Africa

1378 (1192) were detected on θ_{330} (θ_{350}) during the 40-year study period so that RWPs occur over this region at a rate of 35 and 30 RWPs per year on θ_{330} and θ_{350} surfaces, respectively. On θ_{330}, most ($\sim$ 26.56 %) of the RWP objects were identified during winter months as a result of the RWP objects favouring the extratropical subdomain where there is an isolated RWP hotspot south west of southern Africa (Figure 4.12 (c)). Over the subtropical domain, the maturity of RWP tends to be mostly widespread across the land, giving rise to a northeast-southwest type of spatial distribution of RWP events. Smaller-scale isolated RWP hotspots also exist over the subtropical domain, but the significant contribution originates from the hotspot off the coast of Mozambique and extends eastward into the region over the Mozambique Channel between Mozambique and Madagascar. Although the extratropical domain has the largest contribution of RWP events, there is only a $\sim$ 5% difference between the two regions in terms of the percentage of RWPs maturing over each subdomain. During summer, the least number of RWPs was detected, accounting for only $\sim$ 24.09% of annual counts due to the two RWP hotspots observed over the subtropical subregion (Figure 4.12 (a)).

The first RWP hotspot extends between the west coast and into central South Africa, while the second is rooted over the SIO and extends laterally into eastern South Africa. While high density RWP regions over the extratropics are non-existent during this season, this region is associated with $\sim$ 43% of RWPs maturing over the entire SA domain showing that RWP events are widespread, but there is some preference to mature predominantly over the SAO. During this season (summer), the jet stream is centred at about 50°S and does not appear explicitly in Figure 4.12 (a), but SAO RWPs appear to have some association with its anticyclonic flank. During the transition seasons, the RWP counts are comparable with the autumn and spring seasons, accounting for $\sim$ 24.89% and $\sim$ 24.46% of the total RWP counts, respectively. However, the distribution of RWPs differs between these two seasons, with autumn being associated with two isolated RWP hotspots over the subtropical and extratropical areas (Figure 4.12 (b)).

θ surface	DJF	MAM	JJA	SON	Total	# yr^{-1}
330K	**332 (24.09%)**	**343 (24.89%)**	**366 (26.56%)**	**337 (24.46%)**	**1378**	35
> 2	268(19.45%)	285 (20.68%)	326 (23.66%)	265 (19.23%)	1144 (83.02%)	29
≤ 2	64 (4.64%)	58 (4.21%)	40 (2.90%)	72 (5.23%)	234 (16.98%)	6
350K	**207 (17.37%)**	**349 (29.28%)**	**317 (26.59%)**	**319 (26.76%)**	**1192**	30
> 2	80 (6.71%)	308 (25.84%)	244 (20.47%)	247 (20.72%)	879 (73.74%)	22
≤ 2	127 (10.65%)	41 (3.44%)	73 (6.12%)	72 (6.04%)	313 (26.26%)	8

Table 4.3: As in Table 4.1, but for the SA domain

In contrast, the extratropical domain accounts for $\sim 60\%$ of the events, mainly as a result of the broad hotspot between 20°E and 45°E (Figure 4.12 (d)). Table 4.3 also reveals that the variability is largely due to the contribution of the high RWP density regions that account for $\sim 83.02\%$ of the RWP events. In general, there is very little intra-annual variability in RWP occurrences over this region and surface; however, the spatial distribution of RWP events varies considerably. During the first two seasons of the year, RWPs appear to mature at tropospheric levels lower than the dynamical tropopause. During winter, the RWP hotspot south west of SA is associated with PV^{TP}, as well as the undulating anticyclonic side of the jet stream, which has migrated equatorward by this time. This is the only season on θ_{330} that RWPs were detected in very close proximity to, along the dynamical tropopause, and the jet stream, while the spring hotspot is mostly collocated with the anticyclonic flanks of the poleward migrating jet.

As in the case of θ_{330}, the summer months are associated with the least number of RWPs identified ($\sim 17.37\%$) on θ_{350}, however, the peak is observed during the autumn months ($\sim 29.28\%$) with an increase in RWP events by $\sim 67\%$ from the summer to autumn months. Furthermore, the RWP counts during the autumn season on this θ surface are slightly higher (349 RWPs) than the figure observed during the same period on θ_{330} (343). During summer, Table 4.3 shows that the RWPs from low-density regions contribute the most to the overall count and associated distribution. Furthermore, a weak RWP hotspot can be seen extending from the SAO and across SA and at levels lower than PV^{TP} (Figure 4.12 (e)). This hotspot appears to be associated with that seen during the autumn months and covers mainly the extratropical domain, but appears to have intensified while extending

eastward to $\sim$ 30°E along PV^{TP} (Figure 4.12 (f)). This feature accounts for the drastic increase in RWPs during this season, while wider-spread RWPs over the extratropical domain also contribute considerably more than their subtropical counterpart. The autumn hotspot decays almost completely during the winter months, leaving only small isolated remnants over the regions south west and east of South Africa (Figure 4.12 (g)).

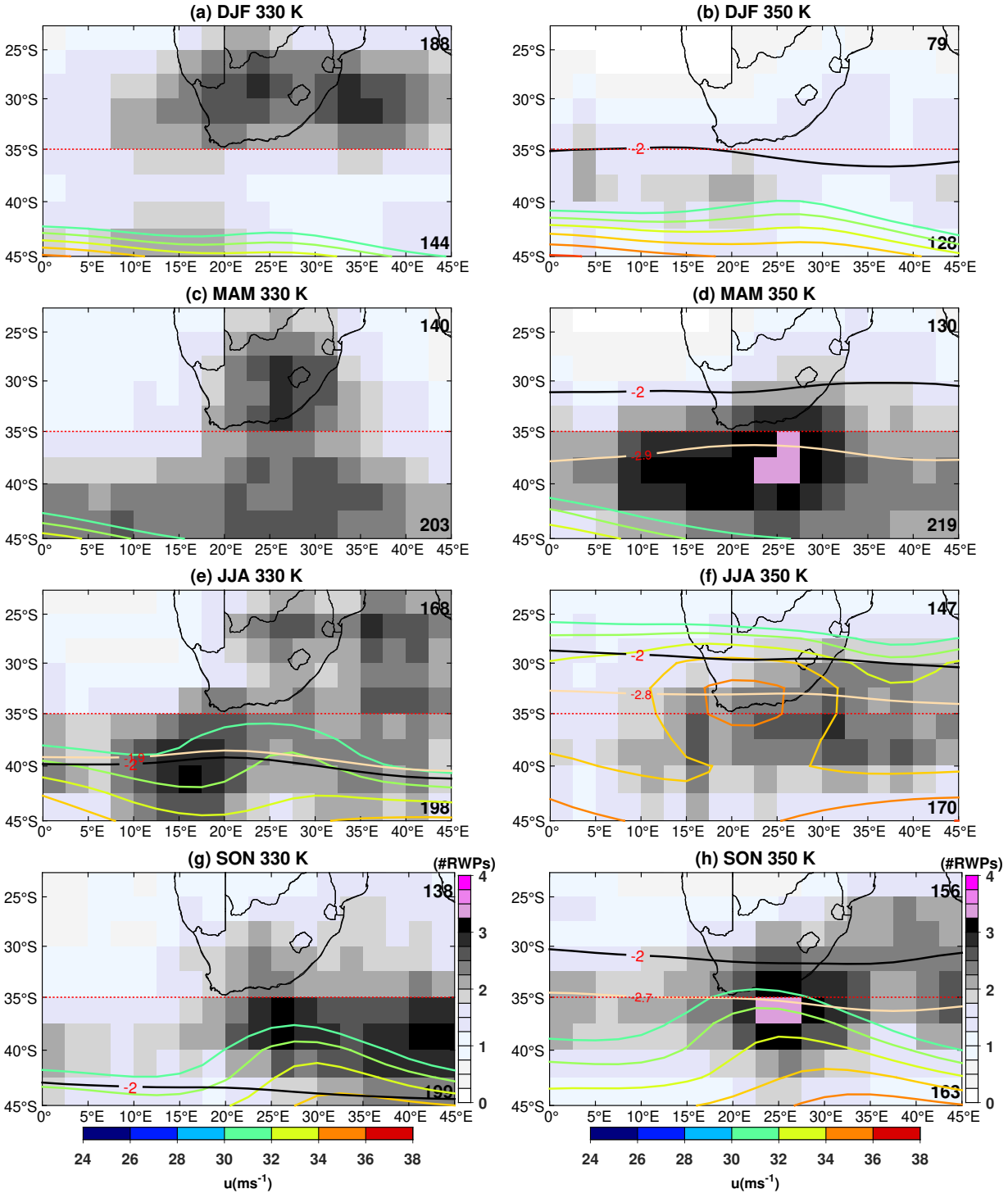

Figure 4.12: θ_{330} (a-d) and θ_{350} (e-h) Seasonal counts of SA RWPs (white-grey shading), and the corresponding zonal wind isotachs (rainbow colorshading in ms^{-1}). Three dynamical tropopause estimates are added here: -2 PVU contour (black solid line), the objectively estimated dynamical tropopause (PV^{TP}) for subtropical and extratropical RWPs (black dotted and dashed lines respectively) taken from Table 4.3.

The sharp decrease in RWP activity appears to coincide with the existence of a small-scale upper-level jet centred over south west South Africa at the PV^{TP}. This decrease is consistent with the view that areas of strong (weak) zonal winds suppress (promote) RWB (Nakamura and Plumb, 1994; Peters and Waugh, 1996; Ndarana and Waugh, 2011; Homeyer and Bowman, 2013) and, by extension, the termination of RWP. Small-scale RWP hotspots on the west and east sides of the small-scale jet are located poleward of PV^{TP} , and therefore suggest that RWPs there tend to mature at lower stratospheric levels, as PV^{TP} is seen as the interface between stratospheric and tropospheric air. In general, there is only a $\sim 9\%$ decrease in RWP events between autumn and winter, as well as spring seasons. An RWP hotspot emerges during spring (Figure 4.12 (h)) and is bisected by $\phi = 35°$S, resulting in an almost uniform distribution of RWP during this season where the subtropical (extratropical) component extends equatorward (poleward) over SA along PV^{TP}.

In contrast to θ_{330}, there are no clear subtropical RWP hotspots that are truly separated from the extratropics on θ_{350}. This implies that θ_{350} seldom intersects low-level wavy PV contours in this region, unlike θ_{330} which is lower poised and tends to slope down and equatorward, thus increasing the likelihood of encountering wave activity at lower tropospheric levels. These would imply that processes such as convection as well as topography are possible role players in the initiation of wave activity detected on θ_{330}, and over the subtropical domain. For example, the RWP hotspot over the north-eastern parts of South Africa and neighbouring countries coincides with the well-known summertime convection-related Tropical Temperate Trough (TTT) activity hotspot (see, e.g., Hart et al., 2010; Ratna et al., 2013; Macron et al., 2014) over Southern Africa. The RWP hotspot on the eastern side of the land seems to coincide with the location of the SIO convergence zone, which is also related to convection (van der Wiel et al., 2015). In general, RWPs on θ_{330} (with the exception of winter RWPs) have a tendency to mature at lower tropospheric levels, while RWPs maturing on the quasi-horizontal θ_{350} amplify in close proximity to the dynamical tropopause (with the exception of summer RWPs).

4.5.3 Characteristics of RWPs over SA

In this section, we examine the characteristics of RWPs detected in the SA region. To this end, Figures 4.13-, 14, 15 and 17 showing the spatio-temporal distributions of RWP maximum amplitude/intensity (A_{max}), duration/life-span (days), distance travelled (km), and mean speed/group speed of propagation (ms^{-1}) are presented below. First, it can be seen in Figure 4.13 that the most intense RWPs tend to mature over the extratropical area throughout the year and are mainly coincident or collocated with RWP hotspots identified previously over this region. The most intense (least intense) RWPs occur during the transitional (summer) seasons on θ_{330} with typical A_{max} values in the 90-108 ms^{-1} (54-72 ms^{-1}) range.

While the wintertime RWP hotspot located south-west of SA appears to be larger and perhaps better defined than the autumn one located south of the country (Figure 4.13 (c)), it is associated with relatively smaller amplitudes. This suggests that, while it is useful to consider the $\overline{A}$ field in studying the climatology of finite-amplitude RWPs, it may be important to consider the two fields separately when focusing on smaller regions, as considering the $\overline{A}$ field may likely be sensitive to the intensity of RWPs, in lieu of their frequency of occurrence. In the subtropical area, the seasonal march of A_{max} is very similar to that observed over its extratropical counterpart. Consistent with the climatology of the LWA, the θ_{350} RWPs are mostly weaker than those on lower level isentropes. The spatiotemporal distribution of A_{max} on θ_{350} shows that the most intense RWPs mature over the SA region during summer and autumn seasons Figure 4.13 (e-f), with a dip during winter and a minor resurgence by spring. However, in general, the variability in A_{max} on θ_{350} is relatively lower, with a difference of ~ 18 ms^{-1} between the seasons of the most intense and weakest RWPs.

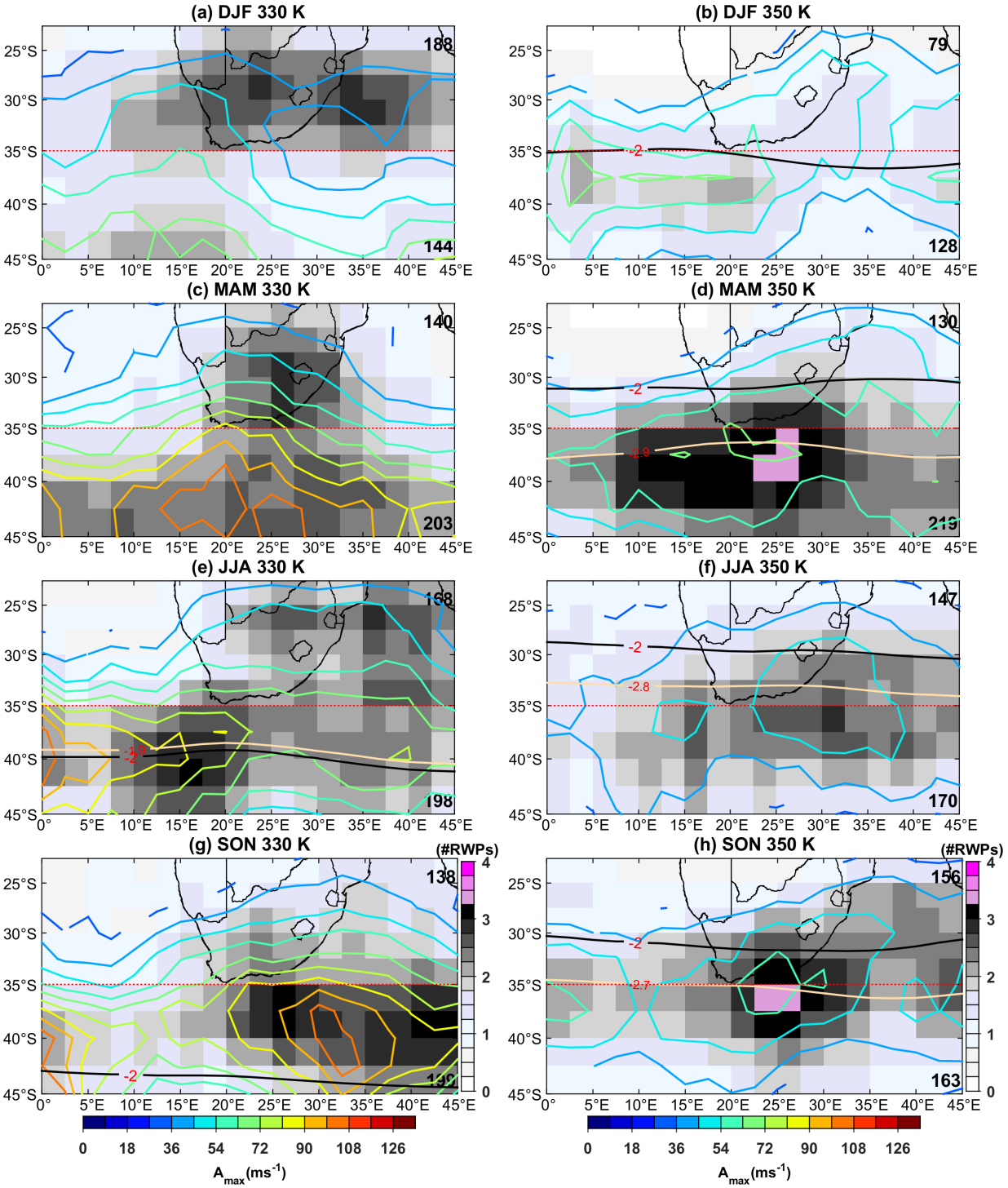

Figure 4.13: θ_{330} (a-d) and θ_{350} (e-h) Seasonal counts of SA RWPs (white-grey shading), and the maximum amplitude/intensity (A_{max}) (rainbow colorshading in ms^{-1}). Two dynamical tropopause estimates are added here: -2 PVU contour (black solid line), the mean of the objectively estimated PV^{TP} for subtropical and extratropical RWPs (black dashed lines respectively).

The second RWP attribute of interest is their life-span, and Figure 4.14 elucidates the considerable spatio-temporal variability in this RWP trait over the SA domain. First, extratropical RWPs generally live longer than those of the subtropics. Summertime, however, is an exception, with longer lived RWPs detected over subtropical RWP hotspots observed across SA, and with a typical life span of about 2-2.5 days on θ_{330} (Figure 4.14 (a)). Over the extratropical area, the longest lived RWPs occur during winter and spring seasons with a lifespan of $\sim$ 3-3.5 days. During winter, there is some indication of RWPs with a similar longevity over the SIO area south of the weak RWP hotspot southeast of SA (Figure 4.14 (c)). Shorter-lived RWPs occur during summer over the extratropics with a typical life span of $\sim$ 1.5 days, followed by autumn RWPs that last approximately 2.5-3 days. The lifespan of subtropical RWPs is typically 2-2.5 days over the subtropics; however, there is a tendency for RWPs over this area to persist for about a day longer during winter, most evidently over SA and the Mozambique Channel RWP hotspot areas. Spatial variability on θ_{350} is arguably less complex; longer-lived RWPs coincide well with RWP hotspots over the extratropical region Figures 4.13 (e-h). The shorter (longer) lived RWPs occur during summer (spring) lasting about 2-2.5 (3.5-4) days, while the autumn and winter seasons are associated with RWPs of comparable longevity in the 3-3.5 days range.

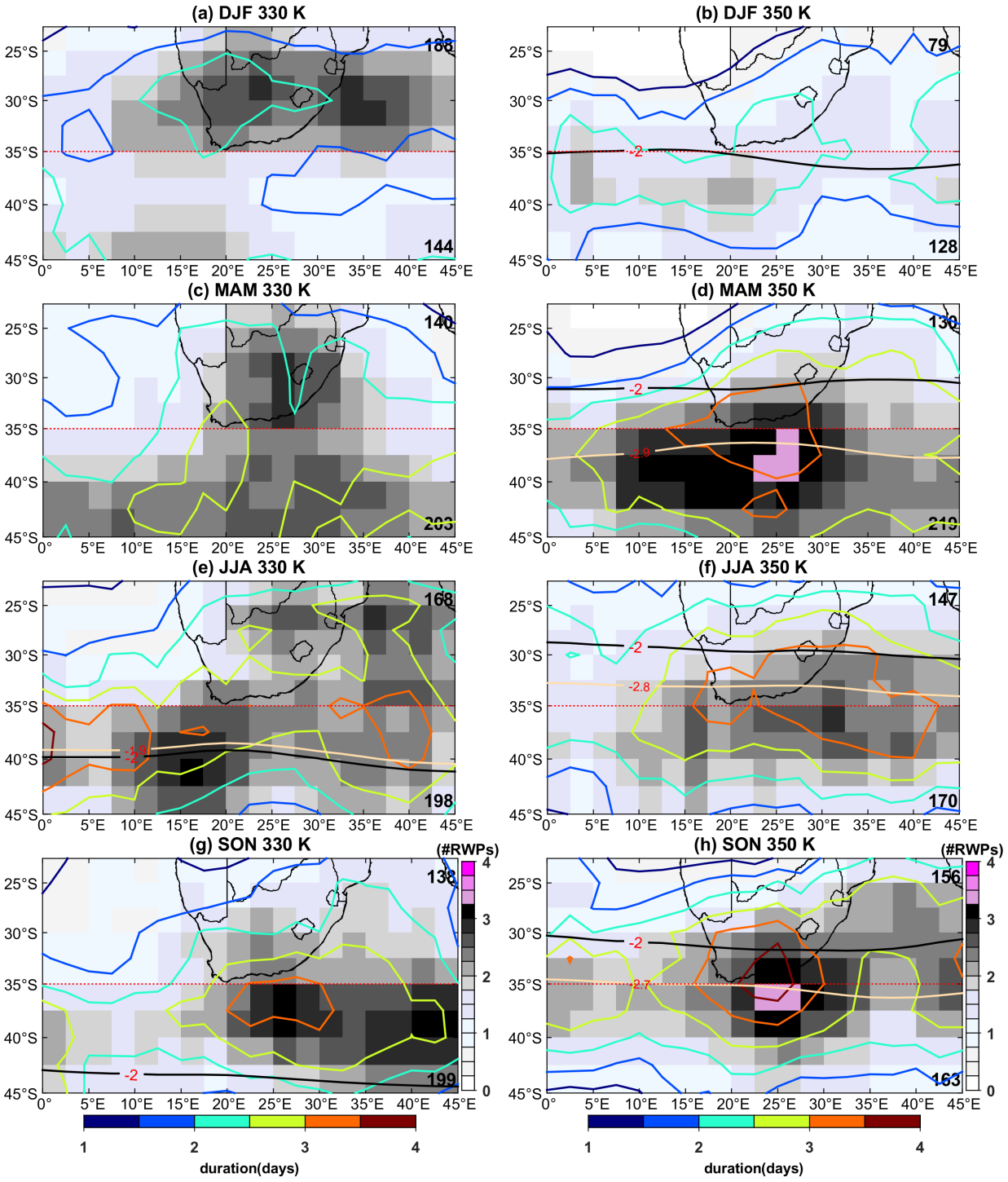

Figure 4.14: As in Figure 4.13 but for duration (days).

The spatial distributions of the RWP distances shown in Figure 4.15 are very similar to those of their duration presented in Figure 4.14. This suggests that longer (shorter) lived RWPs are for the most part the furthest (nearest) travelling over the study region. However, θ_{350} RWPs typically travel the farthest compared to their θ_{330} counterparts. There is little variability, however, during the year, particularly from autumn to spring, with RWPs associated with distances of $\sim$ 4000-4500 km over the extratropical region. In contrast, RWPs in the summer months are only associated with distances of about 3000-3500 km. On θ_{330}, winter RWPs travel the furthest with distances of up to 4000-4500 km, particularly those RWPs maturing south-west of SA during this period. In general, the trend is such that the distances RWPs travel increase between summer and winter, and begin to decrease with the onset of spring. As was the case for the duration, the furthest travelling RWPs coincide with the RWP hotspots over SA during summer months with distances travelled in the 2000-2500 km range (Figure 4.15 (a)).

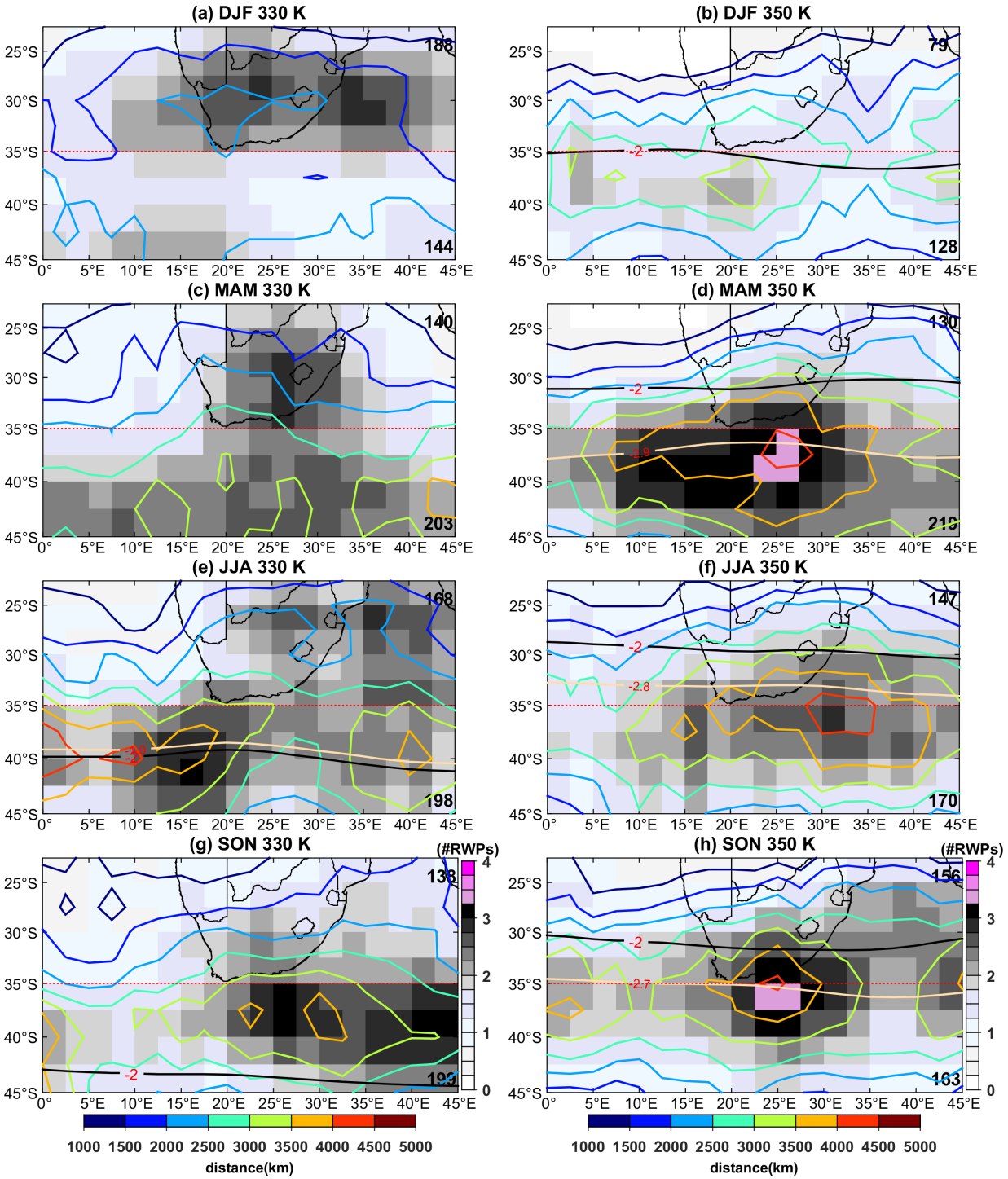

Figure 4.15: As in Figure 3.12 but for distance travelled by RWP objects in km.

To supplement the current discussion, Figure 4.16 is included to show the relationship between development areas associated with RWPs that typically propagate into SA regions of interest on θ_{330} (left panels) and θ_{350} (right panels). The colour shading represents the number of RWPs undergoing maturity over the SA domain, whereas the blue contours denote the corresponding areas of development associated with those mature RWPs. Additionally, start/development (pink-coloured circles) and maturity/intensification (black-coloured arrows) points are included and joined by gray lines to show the general path followed by an RWP between the development and maturity phases of their life cycles. Here, the maturity coordinates were used as reference points. The composite means of all the development locations tied to the selected maturity points were then calculated and thus represent the "source" regions for RWPs maturing over SA. That is, for every maturity point, all associated development (first detection of an RWP) latitude and longitude points were summed up and divided by the number of times the summation was performed to produce one coordinate point that represents the mean development region associated with a given maturity point over the SA region. To reduce the number of points and connections, only the maturity grid points with ≥ 1 RWP event were considered in the composite mean calculations. Lastly, the corresponding estimate (PV^{TP}) for the dynamical tropopause is shown by the thick black contour during all seasons.

During summer on θ_{330} (Figure 4.16 (a)), there are approximately three RWP development zones with at least one RWP associated with each of them. The first two are located $\sim 10^{\circ}$ west (R_1) and east (R_2) of the Greenwich Meridian and stretching between 30°S and 50°S. The former appears to be predominantly associated with the RWPs maturing over the extratropical region of SA, whereas the latter is tied to two propagation regimes of RWPs maturing over SA. The poleward/extratropical lobe of this development zone is associated with RWPs propagating south-eastward and maturing over the extratropical RWP hotspot regions between the Greenwich Meridian and 20∘E. The subtropical lobe is mainly a feeder zone for RWPs maturing over the western regions of SA over the subtropical SA domain. This maturity region coincides with the remaining development region (R_3)

located along 30°S at the western edge of SA and occupies parts of Namibia, the Northern Cape province, and the SAO. This is a typical source region for RWPs maturing over the central and eastern regions of SA, as well as the SIO, and is the most prominent RWP development area during this season. The proximity of R_3 to the mainland suggests that the undulations of the low-level PV contours in that region could be related to smaller-scale convection associated with the topography (central plateau) of the mainland of SA. For example, Barnes et al. (2020) attributed the high density on either side of the SA mainland to the influence of the mountainous feature in question. Given the relationship between RWPs in this study and CoLs, it stands to reason that a similar process gives rise to the development (dissipation) of RWPs on the windward (leeward) side of the SA topography. Additionally, R_3 is located very far from the extratropical jet stream, which effectively reduces the direct influence of the jet stream over processes native to this region. There are a number of development points that fall outside of the development hotspot regions, and this is a consequence of the variability in initial points associated with RWP hotspots.

The onset of autumn (Figure 4.16 (c)) sees the dissipation of R_3, while a new well-defined feeder zone appears in the vicinity of 30°S between the Greenwich Meridian and 10°E, giving the impression of a break-off structure in the northern lobe of R_2. The northwest-southeast band of mature RWPs over the subtropical domain is almost exclusively fed by the "remnant" R_2 zone, with some RWPs developing over different longitudinal sectors between 30°S and 35°S. However, this region is only secondary to R_1 and R_2 during this period, in which the former has a higher density of RWPs with more than two RWPs associated with it on average. Additionally, these two RWP zones exist over the extratropics and mostly act as feeder zones for the RWPs maturing across the extratropical SA domain. These RWPs can either propagate eastward in an almost straight line, south-eastward or north-eastward toward ϕ_{35S}. The overall spatial distribution of the feeder zones is markedly expanded zonally, extending between 30°W and 30°E and features virtually no development areas over SA, with the exception of the area along the west coast. This expansion

leads to the appearance of an additional feeder zone R_4 just south of ϕ_{35S} and northwest of SA, which is an additional source of RWPs that mature over the SIO.

By winter (Figure 4.16 (e)), R_1 and R_2 maintain their intensity, while R_4 becomes well developed as a source region. There is an overall retreat in the extratropical development zones of approximately 5° and is well poised along the dynamical tropopause. The predominant propagation pattern related to R_1 and R_2 then becomes more zonal and south-eastward, giving rise to the two mature RWP hotspots on either side of the extratropical region of SA. Interestingly, those RWPs that mature poleward of the dynamical tropopause have a tendency to propagate north-eastward, while those developing equatorward mostly propagate south-eastward. Some indication of the resurgence of R_3 is visible and is related to RWPs maturing in central SA and the SIO. Finally, during spring (Figure 4.16 (g)), the development zone shifts eastward again, and equatorward of the dynamical tropopause. The two dominant feeder zones R_1 and R_2 appear to disintegrate, as the latter shifts very close to R_4. The predominant direction of propagation is almost south-eastward during this season, with subtropical RWPs propagating across ϕ_{35S} toward the RWP hotspots south east of SA, and over the SIO.

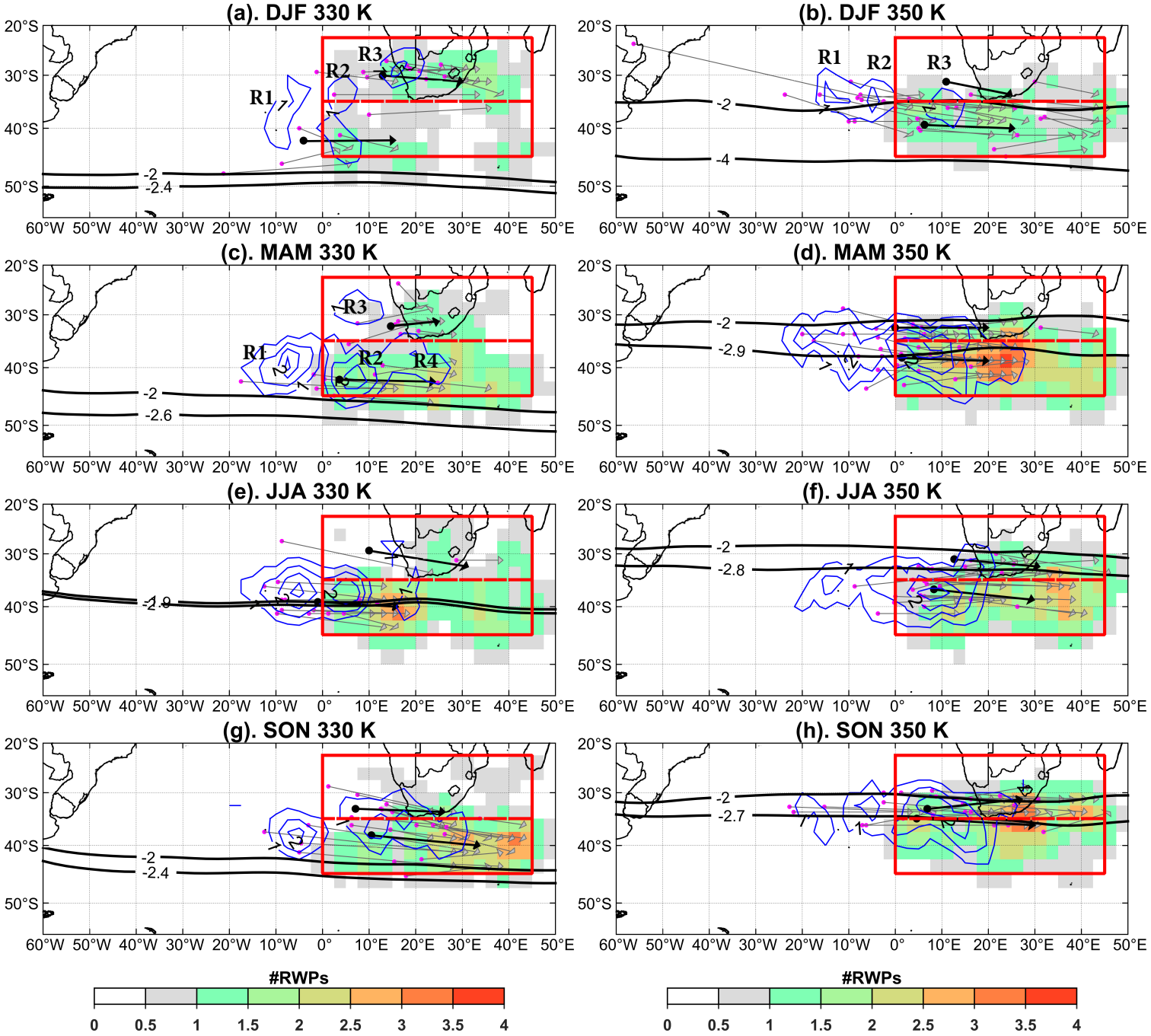

Figure 4.16: θ_{330} (left panels) and θ_{350} (right panels) seasonal distribution of the number of RWPs (color shading) maturing over the SA region (highlighted by the red box). The blue contour lines denote the spatial distribution of the number of RWPs tied to mature RWPs over the SA at 0.5 intervals beginning from 1. Development regions are denoted by pink circles, maturity points are shown by grey coloured arrows and these are connected by the dark grey lines. Development points were estimated by calculating the composite mean location associated with every maturity point having at least one mature RWP event. The mean direction (solid black arrows) was estimated by computing the mean start and maturity coordinates of all grid points with atleast one RWP specific to each sub domain of SA.

The behaviour of the RWPs on θ_{350} is similar to that observed on θ_{330}, but there are also some notable differences. First, summer RWPs are mainly confined within the extratropical domain, with very few RWPs maturing over the subtropical domain (Figure 4.16 (b)). The well defined R_3 feeder zone observed previously on θ_{330} is non-existent on this surface, but there are signs of a development as the 0.5 RWPs contour can be found in the vicinity of the R_3 region. The RWPs that develop in this region tend to propagate eastward toward the eastern regions of SA, where an additional weak development area feeding the SIO exists throughout all seasons. In general, the main feeder zone that encompasses R_1 (most prominent) and R_2 has a northwest-southeast orientation stretching between 30°W and 25°E. The propagation of RWPs developing over this source region assumes a similar orientation. That is, RWPs maturing over the dominant extratropical region appear to emanate from the SIO area, and as far as South American countries such as Brazil during this season. Recalling the summertime distribution of $\overline{A}$ over the SIO, this observed behaviour could be associated with the trail of wave activity emanating from H_3 and toward the south-west regions of SA discussed previously. There are also some RWPs that propagate in a north-eastward direction from the extratropical domain and cross ϕ_{35S} to mature along the south coast of SA.

The orientation of the development regions changes and becomes slightly more zonal and shifts eastward by autumn (Figure 4.16 (d)), and so does the RWP propagation. Recalling that it is only during this season that θ_{350} saw more RWPs than its lower poised counterpart, the RWP activity is very dense and very localised along and in the vicinity of the dynamical tropopause. The predominant propagation of RWPs is eastward from the main feeder zones R_1 and R_2, but RWPs can disperse both north-eastward toward SA mainly from R_2, or south-eastward mainly from R_1. The winter configuration on this surface is very similar to that on θ_{330}, but much of the extratropical RWP development and maturity occurs poleward of the dynamical tropopause, and the general development region has a more zonal orientation. Lastly, the spring picture (Figure 4.16 (h)) is very similar to that of autumn discussed above, but the SIO RWP hotspot culminates as a result of RWPs

propagating north-eastward away from the extratropical domain and across the dynamical tropopause. This is in contrast to the approximate behaviour during autumn when the SIO region is tied to south-eastward propagating RWPs from eastern SA. Reconciling the findings in Figures 4.15 and 4.16, it becomes evident that RWPs on θ_{350} travel the furthest in the eastward direction so that upstream development over regions 40° -60° away from the study region can result in significant weather conditions over or in the vicinity of SA.

Another feature of interest in the mobility of RWPs is their propagation speed (Figure 4.17). As expected, extratropical RWPs appear to propagate faster than those over the subtropics as a result of their close proximity to the extratropical jet stream. The typical speed of RWPs over this region, and on both θ surfaces, lies in the 12-16 ms^{-1} range throughout most months of the year. Lower bound speeds are observed during summer on θ_{330}, and in spring on θ_{350}. It is worth noting that the group velocities of the observed RWPs observed over the extratropics are significantly slower than those of the jet stream, which is likely an indication of the non-linear nature of these RWPs. For example, in their composite study of SH blocking, Dong and Colucci (2015) found that blocking events (which can be viewed as RWB cases) are associated with the slowdown of westerlies during their onset.

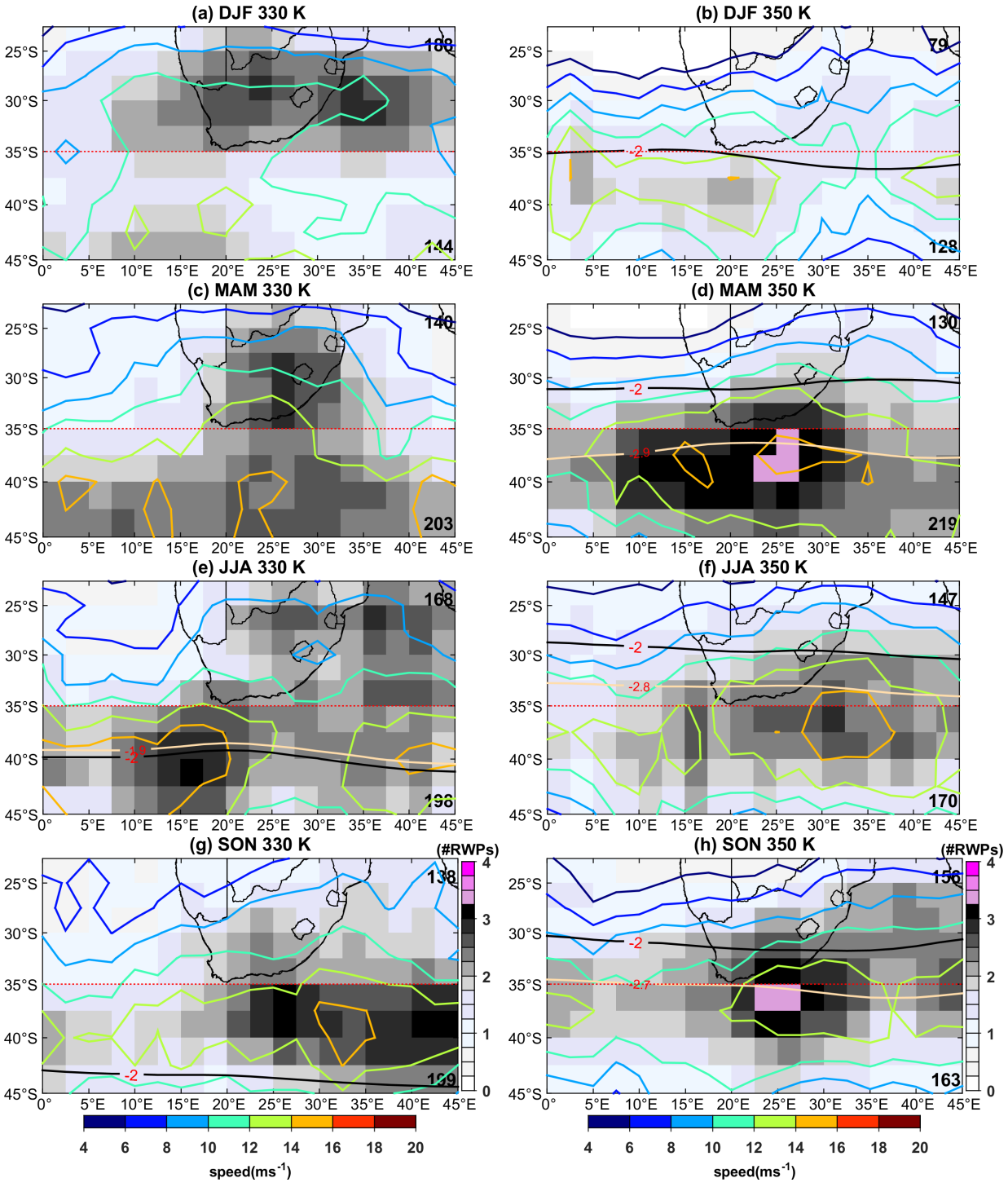

Figure 4.17: As in Figures 4.12 but for speed (ms^{-1}).

4.6 Chapter synopsis

This chapter sought to establish a 40 year (1979-2019) climatology of finite amplitude RWPs that undergo maturity over the SA domain using NCEP Re-analysis 2 data. To this end, an isentropic local finite-amplitude wave activity (LWA, Ghinassi et al., 2018) diagnostic was leveraged to identify possible RWPs features appearing in the instantenous 6 hourly LWA (A) field at the 330 K and 350 K isentropic levels. By design, when a zonal filter (Ghinassi et al., 2018) is applied to the LWA field in the presence of an RWP, the resultant pattern of closed concentric contours tends to represent the center of RWPs (LWA RWP objects). To establish a database for RWPs over the SA domain, a contour tracking algorithm was employed to identify and track in space and time closed contours that may represent RWPs based on a handful of thresholds. Results of the tracking algorithm were verified against the seasonal LWA ($\overline{A}$) spatial distribution, and consistency was established between the fields as well as the seasonal marches of the SH jet streams, storm tracks, RWB, as well as CoLs.

The behavior of the LWA field was found to be linked to the behavior of the jet streams, therefore confirming the long standing idea that the westerly jet streams are an important feature of RWP propagation. Specifically, the lower values of LWA were found to be located within the jet streams, while the higher values were generally found at the entry and exits of the jet streams. This suggests that the most intense LWA objects generally represent RWPs at the maturity stage as soon as they enter regions of weak westerly flows. Furthermore, composite mean fields of LWA, PV and v' were compared at the point in the tracks of RWP objects when LWA was a maximum (t = 0 h). The comparison confirmed that indeed the tracked LWA objects represent finite amplitude RWPs since PV contours indicated that RWB was at play during the maturity of LWA. A total of 19680 (14979) LWA RWP objects were identified by the tracking algorithm on the 330 K (350 K) isentropic surface over the SH (20°S-85°S). On the 330 K (350 K), summer months were associated with the highest (lowest) percentage of RWP detection.

On the 350 K (330 K) surface the peak (minimum) percentage of RWPs detected was observed during spring (summer) months. Over the SA domain, summertime experiences the lowest number of LWA RWPs on both isentropic surfaces, while the peak occurence on 330 K (350 K) was observed during the winter (autumn) period. Characteristics (intensity and duration) of LWA RWPs maturing over the SA domain were also examined. Results revealed that the most intense (least intense) RWPs occur during the transitional (summer) seasons on the 330 K surface with maximum LWA values in the range: 90-108 ms^{-1} (54-72 ms^{-1}). Results from our tracking algorithm have sugested that for regional considerations, such as the SA domain, it is important to consider RWP tracks, instead of the climatological LWA fields as smaller scale features tend to be smoothed out in the $\overline{A}$ field. The typical life-spans of RWPs over the SA domain were found to be in the order if 1.5-3.5 days on both surfaces over the SA domain. In general, RWPs maturing over the extratropical area were found to persist longer than their subtropical counterparts.

These results provide the first glimpse of the climatological characteristics of finite amplitude RWPs that matured over the SA domain, and can be used in the context of understanding extreme weather phenomena over historically vulnerable regions, such as the south east coast of SA. For example, it is quite evident that larger amplitude RWPs that can persist for up to 3.5 days tend to mature over this area, particularly during the transition seasons. This appears to reconcile the idea of RWPs, CoLs, and floods/anomalous rainfall since the presence of CoLs has in recent times been associated with floods over the south east coast of SA in the province of KwaZulu- Natal (e.g, Pinto et al., 2022). Future work will explore the role of RWPs as precursors to anomalous rainfall over the SA domain. It is important to note that only two isentropic surfaces were considered in this study, which inherently limits the generality of our results. The loss of generality is also amplified by the consideration of only one re-analysis dataset. Another limitation of the study is the fact that LWA is not fully conserved on the sphere (Ghinassi et al., 2020). Future work will seek to extend the current approach to multiple isentropic levels, and

re-analysis data.

Chapter 5

Dynamics of RWPs over SA

Chapter 4 described the climatological characteristics of the RWPs that matured over the study domain and its subregions on the θ_{330} and θ_{350} isentropic surfaces. Analysis of the climatological distribution of LWA ($\overline{A}$) and RWP objects revealed that much of the variability of the intensity/amplitude of Rossby waves is likely associated with the behaviour of the time mean zonal flow (jet stream, $\overline{u}$) whose characteristics vary on the seasonal time scale, with height, and horizontally. The greatest contrast between the distributions of the jet is seen when the summer (DJF) and winter (JJA) $\overline{u}$ fields are compared. The transition seasons' (autumn and spring) distributions feature a combination of the characteristics of the adjacent preceding and succeeding months.

Following this observation, this chapter focuses on the evolution and dynamical properties of RWPs that mature over the SA domain during summer and winter months. Additionally, particular emphasis is placed on the upper tropospheric RWPs, hereafter represented by θ_{350}, while those on θ_{330} (loosely considered midtropospheric) are only briefly alluded to. This approach is taken because the $\overline{A}_{330}$ and $\overline{A}_{350}$ fields showed reasonable consistency, particularly over the mid-latitudes, while $\overline{A}_{350}$ elucidated subtropical features that were non-existent on $\overline{A}_{330}$. Therefore, θ_{350} is considered to be a good representative isentropic surface for the capture of wave activity over an extended latitudinal range that includes the Southern African domain defined in Chapter 1 and highlighted, for example,

in Figures 4.7 and 4.8. Figure 5.1, is included to facilitate discussions in this chapter.

Figure 5.1 shows a schematic that illustrates the configuration and framework of the panel used in subsequent discussions pertaining to the time-lagged composite mean evolution of the RWPs identified in the SA domain based on Figure 4.5. The top panels represent the two-dimensional (2D) horizontal domain that captures the instantaneous behaviour of RWPs. In this illustration, the LWA (A) is shown in colour shading, with the RWP/LWA pocket isolated by the closed contours in this field, whereas smaller values are muted using a uniform colour (e.g., white or grey). PV contours are denoted by black curves, and the jet stream is shown by white isotachs. The perturbation isentropic meridional wind flow (v'_θ) is shown by the closed blue isotaches where the dashed (solid) contours denote $v' < 0$ ($v' > 0$). The bottom panel shows the corresponding meridionally averaged (over the extent of the meridional dimension of the SA domain (i.e, 20°S - 45°S)) v' field. The red curves are the corresponding RWP envelopes estimated using the Hilbert transform based on the meridionally averaged v' field. Within the region enclosed by these curves, the meridionally averaged diagnostics will be superimposed to show their behaviour relative to the 2D representation of the RWP (e.g, magenta curve in Figure

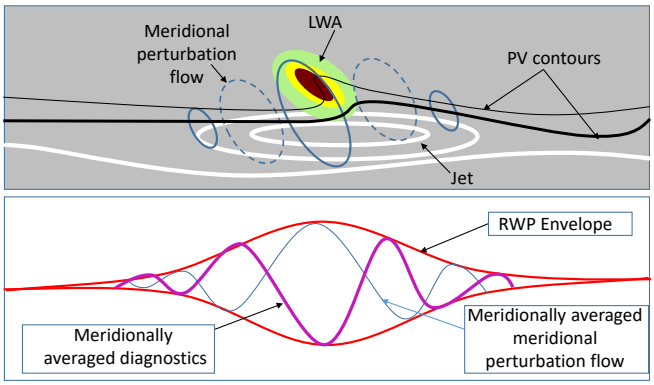

Figure 5.1: Schematic illustrating the panel configuration used in the discussions pertaining time-lagged composite mean evolution of RWPs identified over the SA domain. The top panels represent the two-dimensional (2D) horizontal domain that captures the instantaneous behaviour of RWPs. In this illustration, LWA (A) is shown in colour shading, with the RWP/LWA pocket isolated by the closed contours in this field, while smaller values are muted using a uniform colour (e.g, white or grey). PV contours are denoted by black curves, and the jet stream is shown by white isotachs. The perturbation isentropic meridional wind (v'_θ) is shown by closed blue isotachs where the dashed (solid) contours denote $v' < 0$ ($v' > 0$). The bottom panel shows the corresponding meridionally averaged (over the extent of the meridional dimension of the SA domain (i.e, 20°S-45°S)) v' field. The red curves are the corresponding RWP envelopes estimated using the Hilbert transform based on the meridionally averaged v' field. Within the region enclosed by these curves, the meridionally averaged diagnostics will be superimposed to show their behaviour relative to the 2D representation of the RWP.

5.1). This approach is taken to retain the arguably intuitive meridionally averaged RWP view which enhances aspects of RWP zonal propagation, while retaining some of the anticipated meridional aspects of RWP propagation such as equatorward propagation observed in baroclinic life cycle modelling studies (see, e.g., Thorncroft et al. (1993)). Secondly, this approach will allow us to directly compare aspects of the evolution with existing RWP models such as the one presented in Figure 9 of Wirth et al. (2018). All figures in this chapter will have two panels, as illustrated schematically in Figure 5.1 for each time step, with only Figures 5.6 and 5.7 being the exceptions.

5.1 Evolution of RWPs over SA

The typical evolutionary characteristics of LWA RWP pockets (hereafter referred to as LWA pockets) are discussed below by considering two main stages (i.e., development and decay) in their life cycle over a 6-day period. To this end, Figures 5.2 and 5.3 show the time-lagged composite mean evolution of A (colorshading), PV (black contours, thick: dynamical tropopause [PV^{TP}] determined using the PV gradient method (Kunz et al., 2011) defined in Chapter 3, thin: selected deforming/breaking isoline), v' (blue contours, $v' < 0$: dashed, $v' > 0$: solid), and $\overline{u_\theta}$ (white contours) to represent the basic state/climatological jet stream calculated as a 31-day temporal mean centred about each lagged time step associated with a particular RWP event. In each panel, the bottom plots show the meridionally averaged 200 (black) and 850 hPa (white) v' undulations and their associated envelopes (red curves enveloping the blue area) estimated using the Hilbert transform aligned with their two-dimensionally varying counterparts shown in the top plot. It is important to understand the evolution in the context of the climatology of LWA presented in Chapter 4. Recalling the computation of the composite mean of the fields in this study, we defined the longitudinal range so that the entire longitudinal extent of the SH is captured. This is done so that we may retain some of the geographical information of the resultant composite means cast on the relative ϕ and λ (ϕ_{rel},λ_{rel}) grid. As a result, we can relate the quasi-stationary LWA maxima seen throughout the evolutions depicted in Figures 5.2-5.5

to the climatological features of LWA discussed in the previous chapter.

A comparison between Figures 4.1 and 4.2 (a), Figures 5.2 (a) and (b) reveals that the overall distribution of instantaneous LWA (A) in the initial stages of the evolution of summertime RWPs is comparable to that of the corresponding seasonal distribution $\overline{A}$ field on both θ surfaces. For example, the circumpolar quasi-zonal belt/strip of θ_{330} wave activity previously associated (in Chapter 4) with the Southern Hemisphere storm tracks can be likened to the similarly oriented A distribution observed in Figure 5.2 (a) at t = -72 h. This feature consists of a local A maximum located between λ_{rel} = 120°E and 120°W, and centered at $\phi_{rel} = \approx$ 20°S along the dynamical tropopause (which coincides with the jet stream axis) in Figure 5.2 throughout the evolution of the A field. The position and intensity of this A maximum is clearly indicative of the extratropical LWA hotspot H_1 observed throughout the year, presumed to elucidate some aspects of the SH storm track (like regions of non-linear RWP and RWB), but intensifies during summer months over this region. Additionally, the subtropical LWA maximum over the SACZ (H_3) is also evident between 75° and 30°W above the reference 0° ϕ_{rel} during the early stages of development on θ_{350} because it is closer to the composite relative reference coordinate (0°, 0°). This point is always representative of the centre of an LWA pocket maturing somewhere within the SA domain. The winter LWA configuration in Figure 5.4 (a) also has an overall appearance consistent with the $\overline{A}$ distribution during the same period on θ_{330} as revealed by a visual comparison between Figure 4.1 (c) and Figure 5.4 (a). Having established the correspondence with the climatological setting, we highlight some characteristics of the evolutions at various times of the RWP life cycle.

5.1.1 Summer

5.1.1.1 Development

We begin the analysis by considering the development stages of the time-lagged composite mean evolution during summer months (Figure 5.2). At t = -72 h , a ridge-through-ridge triplet/disturbance exists between 120°W and 30°W along PV^{TP} (Figures 5.2 [a-b]) on the poleward side of the jet stream axis. This feature exists on both θ surfaces, but is most prominent at the upper level surface (θ_{350}). Additionally, there is a weak local A maximum in response to this disturbance to signify the waviness of PV contours over that region. A comparison between the top and bottom panels shows that the incipient disturbance is better elucidated by meridionally averaged v' undulations. The associated envelope of the signals additionally shows that the pre-existing disturbance exhibits an RWP structure of relatively modest amplitude. Furthermore, this RWP structure is characterised by peaks in v'_{200} signals slightly trailing their near surface (850 hPa) counterparts which is characteristic of baroclinic RWPs. This behaviour is, however, accentuated where the RWP peaks exist between 90 and 60°W on both surfaces. Eastward of the RWP envelope peak, the signals appear to be slightly in phase, indicating that the disturbances over these areas at the leading edge of the RWP are likely equivalent barotropic (or weakly baroclinic) in nature.

By t = -48 h the RWPs (on both isentropes) appear to have propagated north-eastward across PV^{TP} towards the equatorward side of the jet stream core. This is signified by the appearance of $v' > 0$ isotachs over this area, while the corresponding v' peaks appear to have shifted eastward by $\approx 5°$ (Figures 5.2 [c-d]). In the case of θ_{350}, the v'_{200} signal at the trailing edge has weakened significantly in conjunction with the eastward translation. Over the central parts of the RWPs, the amplitudes have increased slightly to indicate RWP amplification as they propagate northeastward. At this time, the RWPs are tilted in a southwest-northeast manner across the dynamical tropopause and the jet stream x-axis. The LWA field also portrays the same orientation at this time, so that it appears that wave

activity is protruding from higher latitudes towards lower latitudes between 60° W and 0°.

The leading edge of the RWP can be thought of as being located or extending into, or at upper tropospheric levels lower than the tropopause. This would then suggest that the trailing edge of the RWP is fixed along the dynamical tropopause, while the leading edge extends to lower tropospheric levels across the dynamical tropopause. The distance between the peaks and minima of v'_{200} and v'_{850} in the central parts of the RWPs has increased, with v'_{200} undulations lagging behind the v'_{850} peaks and minima. This situation is reminiscent of the westward tilt of the relative vorticity maxima in Figure 4 of Simmons and Hoskins (1979), therefore, the observed orientation at t = -48 h of the present study marks the characteristic increase in baroclinicity of the RWP during this development stage, while the leading edges are still associated with weak baroclinicity. Although the overall RWP amplitude appears to be in response to the growth and propagation of the incipient RWP on both θ surfaces, the H_3 LWA feature appears to participate in the evolution as it extends south-east toward the jet stream core, and the extratropical wave activity as it intensifies slightly. However, given that the overall meridionally averaged RWP envelope and associated undulations have not been significantly altered and are still similar to those on θ_{330}, it stands to reason that H_3 may not be associated with a distinct and significant RWP structure. This aspect of the discussion will be investigated later in this chapter.

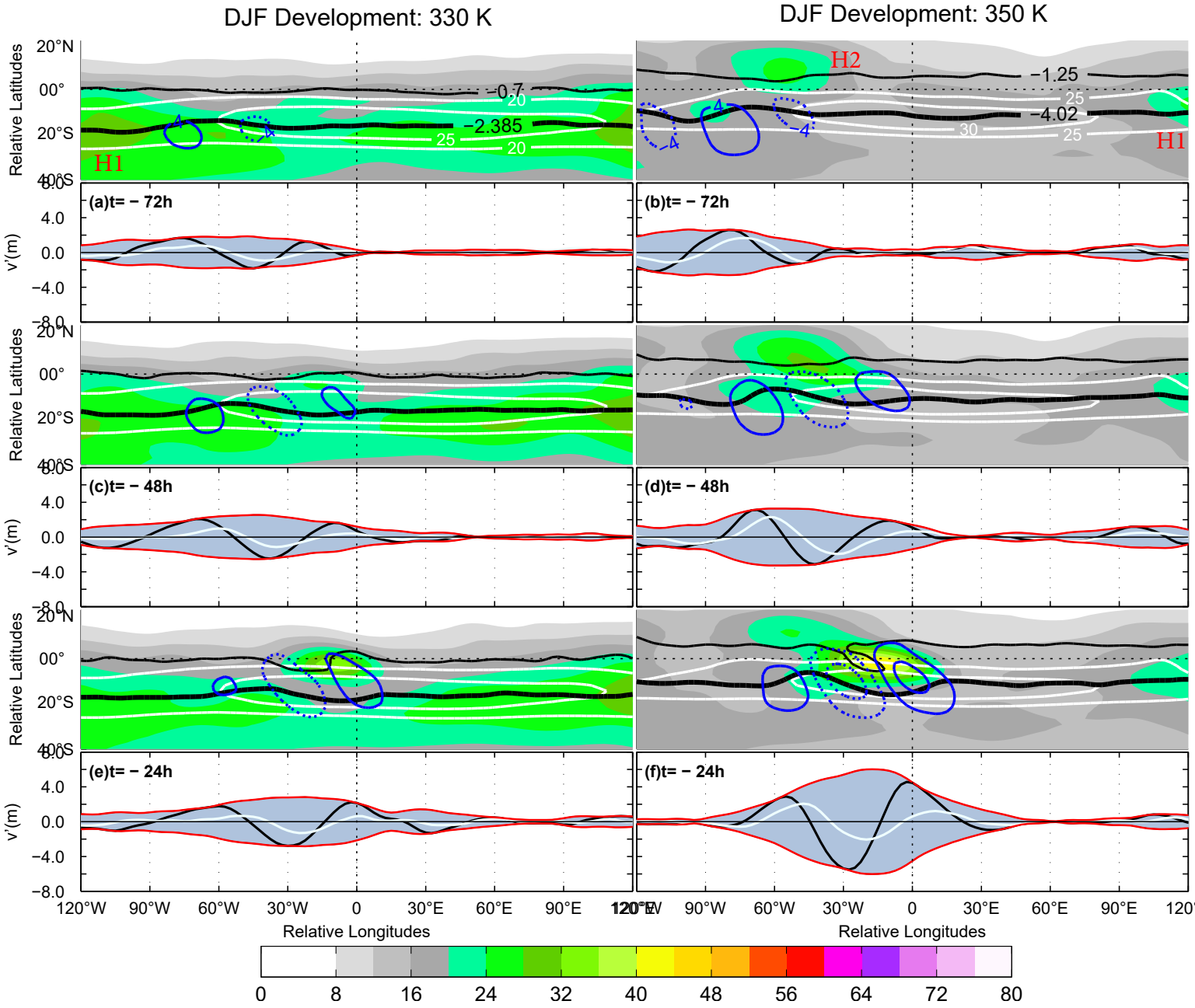

Figure 5.2: Time lagged composite mean of RWPs diagnosed based on LWA (top panels) and v' (bottom panels) for θ_{330} (left column) and θ_{350} (right column) during their 3 day development phase. The color shading represents LWA (A in ms^{-1}), the blue contours denote $v' < 0$:dashed and $v' > 0$(solid) in ms^{-1} (interval = 4 ms^{-1}) and the thick (thin) black contours are PV isolines estimating PV^{TP} (deforming contours). Bottom panels represent corresponding meridionally averaged v' depicting the zonal extent of an RWP at each time steps. The undulations were constructed by computing the meridional average of v' at 850 hPa (v'_{850}, white) and 200 hPa (v'_{200}, black). The red curves filled with blue shading denote the envelopes of the RWP computed using a Hilbert transform.

The meridional extent and amplitude of the leading edge of the RWP continue to increase at t = -24 h to mark the continued development of the RWP while maintaining its implied vertical structure. This marked increase in intensity is also denoted by the formation of the corresponding closed contours in the A field. The v' contours have further propagated across the dynamical tropopause so that the central and leading RWP edges are now centred over the upper troposphere. This is also signified by the waviness of the thinner PV contours north of PV^{TP}. During this time the characteristic RWP signature (i.e., a well-defined peak with progressively decaying amplitudes on either side) has now fully taken shape and marks the initiation of the non-linear stage of the evolution. While the overall LWA field on θ_{330} (θ_{350}) shows more (less) wave activity throughout the domain, the LWA pocket structure on the latter exhibits a larger amplitude. While the RWP structure exhibits a southwest-northeast tilt, the individual disturbances are tilted in a northwest-southeast manner as they edge closer to the jet stream core.

This behaviour is typical of disturbances undergoing life cycle 1 (LC-1) following the convention established by Thorncroft et al. (1993). The observed tilting of the disturbances is attributable to the anticyclonic shearing effect of the jet stream. Note that it is for this reason that the basic state zonal wind component ($\overline{u_\theta}$) was preferred in the context of the current discussion because it excludes the influence of eddies on the jet stream. The elusiveness of the eddie-mean flow interaction is well documented (see, e.g., Wirth, 2020; Wirth and Polster, 2021), therefore we only view and utilise $\overline{u_\theta}$ as a proxy for the Rossby wave guide to facilitate the current discussion. Aspects of the role of the jet stream are discussed later in the chapter. The evolutionary characteristics described from t = -72 h have similarities to some known characteristics of SH Rossby wave propagation. For example, the time-lagged composite Rossby wave trains maturing over the southwest African domain identified by O'Brien and Reeder (2017) also propagate equatorward through the Drake's passage, from the southern tip of South America in the vicinity of the summertime jet stream. Additionally, Zilli and Hart (2021) also elucidated this preferred pathway of both transient and persistent Rossby waves related to the SACZ during summertime.

Ambrizzi et al. (1995) also identified this route as one of the preferred pathways of Rossby waves in their study establishing teleconnection patterns; however, the study focused on wintertime Rossby wave propagation in the SH.

5.1.1.2 Maturity and Decay

Figure 5.3 illustrates some characteristics and behaviour of SA RWPs during their maturity phase from t = 0 h and decay from t = +24 h. Inception of the decay stage of the RWPs is marked by the occurrence of anticyclonic RWB, again, as in LC-1 of Thorncroft et al. (1993), highlighting the dissipative nature of this process. RWB is symbolised by the classic reversal and deformation of the PV contours that turn back onto themselves and may lead to cut-off structures such as in the case of θ_{350} during summer (Figure 5.3(b)). This is illustrated by the previously (at t = -24 h) predominantly poleward (Peters and Waugh, 1996) extending PV tropospheric streamer (PV = -1.25 PVU) forming a cut-off closed contour collocated with the now fully mature LWA pocket over the 30°W-30°E sector. The deforming PV isolines represent elongated PV streamers bringing low (high) PV air toward upper (lower) tropospheric levels. A similar process can be attributed to the observed behaviour on θ_{330}, although a cut-off structure of the deforming PV = -0.7 PVU isoline is not immediately observable in this picture. It is worth noting that the maximum LWA pocket amplitude on θ_{350} is larger and bigger than on θ_{330} because the deformation was more intense on the former, and the associated trough component of the deforming PV = -1.25 PVU streamer seen in Figure 5.2 (f) enclosed a larger area, resulting in more wave activity. Recall that LWA is defined as a measure of the horizontal displacement of a selected PV contour (i.e. Q). The maximum amplitude of the v' envelope during this time is comparable to that observed a day earlier, confirming that the RWP has stopped growing due to RWB, although it is still propagating eastward.

During subsequent time steps following RWB, the RWP amplitudes decrease drastically. The weakening RWP also becomes zonally oriented along the dynamical tropopause

to mark the linearity of the residual RWP propagating eastward along (equatorward) the jet stream axis on θ_{350} (θ_{330}). In line with the dissipation of the RWP, the LWA pocket structures also decrease in intensity while propagating eastward equatorward of PV^{TP} on both surfaces. Furthermore, during time steps beyond t = 0 h, the remnant LWA pocket structures appear to dissociate with the actual RWP structure portrayed by the decaying amplitudes of v' envelopes, with the former (latter) continuing to propagate eastward along (equatorward of) the jet stream. This could be indicative of the possible lasting effects of the RWB process over a specific region while the remnant RWP assumes a different propagation characteristic. By t = +24 h and +48 h, the dissipation of the RWP is also suggested by all v'_{200} and v'_{850} peaks of the RWP coming into phase (i.e, the distance between v'_{200} and v'_{850} peaks approaching zero) to portray an equivalent barotropic RWP vertical structure, marking the complete cessation of baroclinic growth. From an energetics perspective, it is during this period that the energy generating baroclinic conversion of eddy available potential energy to eddy kinetic energy process reaches a minimum, and dissipative processes such as barotropic conversion of eddy kinetic energy to the mean flow, coupled with the divergence of ageostrophic geopotential fluxes (e.,g Pinheiro et al., 2021) take over. These sequence of events reveal that there is little variability in terms of evolutionary characteristics of RWPs maturing over the SA domain during summer months, as viewed from two mid-upper tropospheric isentropes, with the only exception being the RWP amplitudes (i.e, smaller (larger) on θ_{330} (θ_{350})).

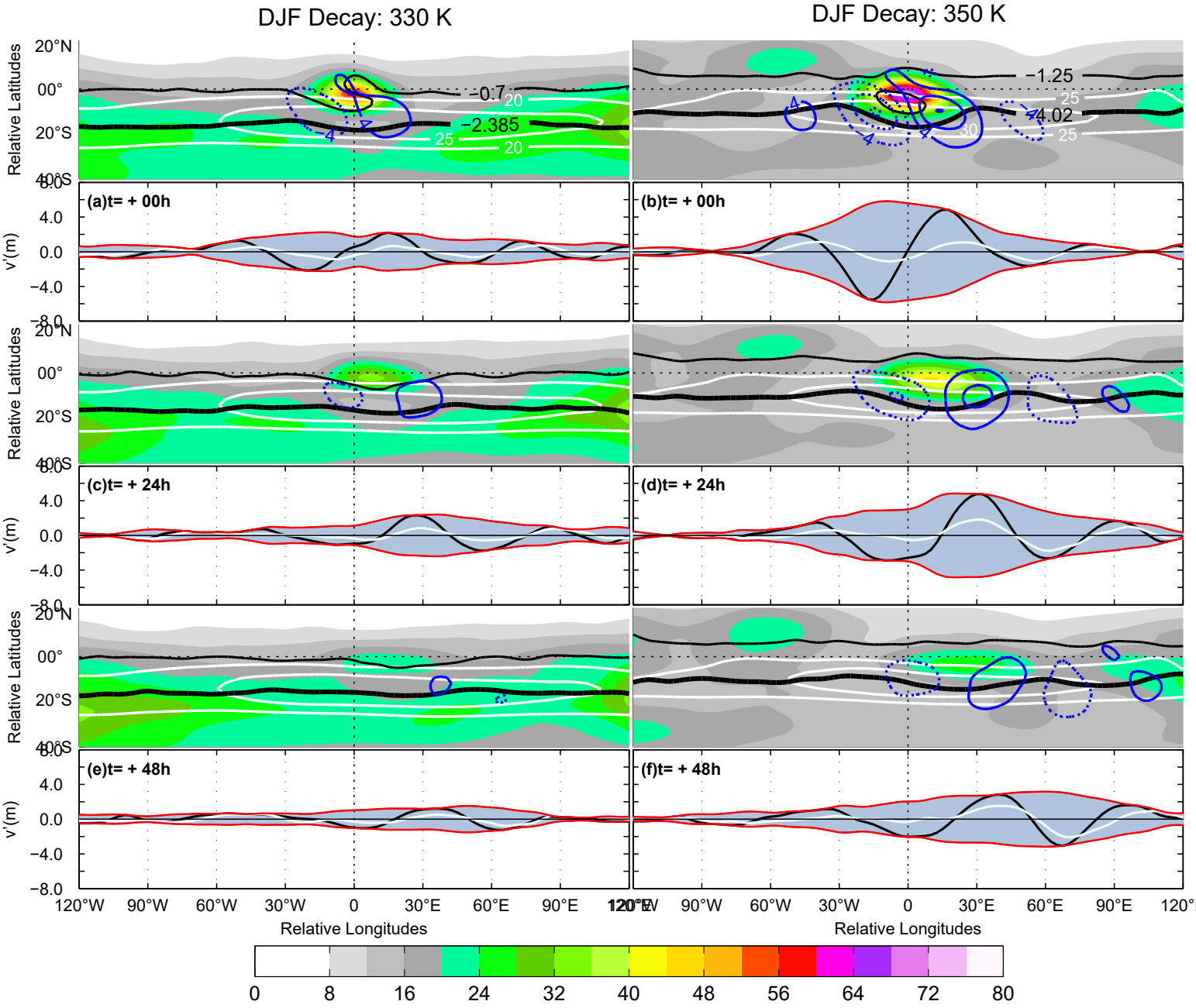

Figure 5.3: As in Figure 5.2, but for the 3 day decay phase of the RWPs.

5.1.2 Winter Development, Maturity, and Decay

The evolution of winter RWPs is very similar to that observed during summer on each corresponding θ surface (e.g, the DJF on θ_{330} is comparable to JJA on θ_{350}). That is, the incipient RWP appears to originate about 120° west of the maturity point (0°,0°). Unlike the summer incipient RWP observed in Figure 5.2 (a-b), this incipient RWP is predominantly characterised by a ridge-trough-ridge-trough equivalent barotropic distur-

bance (Figures 5.3 (a-b)) at t = -72 h. Much of the wave activity is confined to lower levels of the troposphere (i.e., θ_{330}), while only a shadow of these climatological features appears on the upper-level isentrope (i.e., θ_{350}). The propagation is also predominantly in a northeastward direction away from the exit/leading edge of the climatological feature H_1, toward PV^{TP}, and across the jet streak axes prior to 3 days preceding the LWA pocket maturity (Figures 5.3 (a-f)). This is only based on how wave activity is seemingly "spewed" out of H_1 like ink/dye in a fluid dynamics experiment (see, e.g., Illari et al., 2009), during the development phase on both isentropes. This propagation is accompanied by increasing amplitudes to mark the growth of the RWP, and increasing baroclinicity over trailing edge and central parts of the RWP to signal growth due to baroclinic instability. The LWA field during early stages of the development is also reminiscent of the winter LWA field on both surfaces. Here the LWA pocket amplitudes are larger (smaller) on θ_{330} (θ_{350}) due to the morphology of the deforming PV contours near the dynamical tropopause.

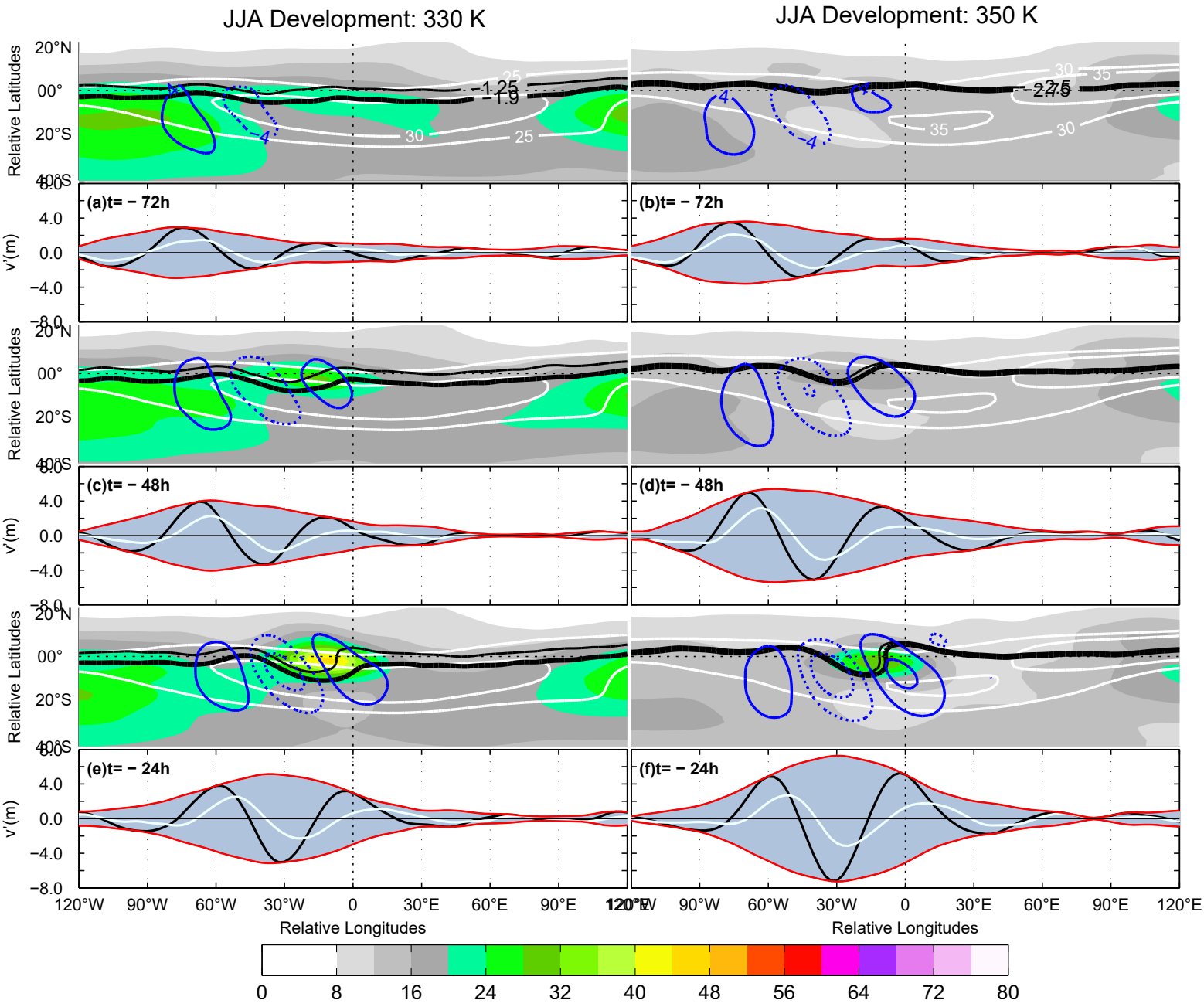

Figure 5.4: As in Figure 5.2, but for the winter season.

Once the RWP is "close enough" to the dynamical tropopause and the jet stream core, RWB takes place at t = 0 h (Figures 5.4 (a-b)) to mark the onset of the RWP termination stage that continues for about 3 days. During this period of marked RWP amplitude decay, v'_{200} and v'_{850} peaks become increasingly equivalent barotropic as in the case of summer RWPs. Here, the LWA pocket amplitudes are larger (smaller) on θ_{330} (θ_{350}) due to the morphology of the deforming PV contours near the dynamical tropopauses. In general, the

evolution between the two seasons and isentropes is qualitatively similar. However, there are some notable differences that become apparent when the two processes are compared closely. First, incipient RWPs exist along (poleward) PV^{TP} during the early stages of the evolution for summertime (wintertime) evolutions. In fact, the winter RWP appears to be anchored poleward of PV^{TP} on θ_{350}, so the deformation related to the RWB takes place at this contour line. This would imply that RWB typically takes place at the dynamical tropopause during this season, while the actual RWP exists at the lower levels of the stratosphere. This is in contrast to the characteristic observed on θ_{330} during this season, and indeed during summer on both θ_{330} and θ_{350}.

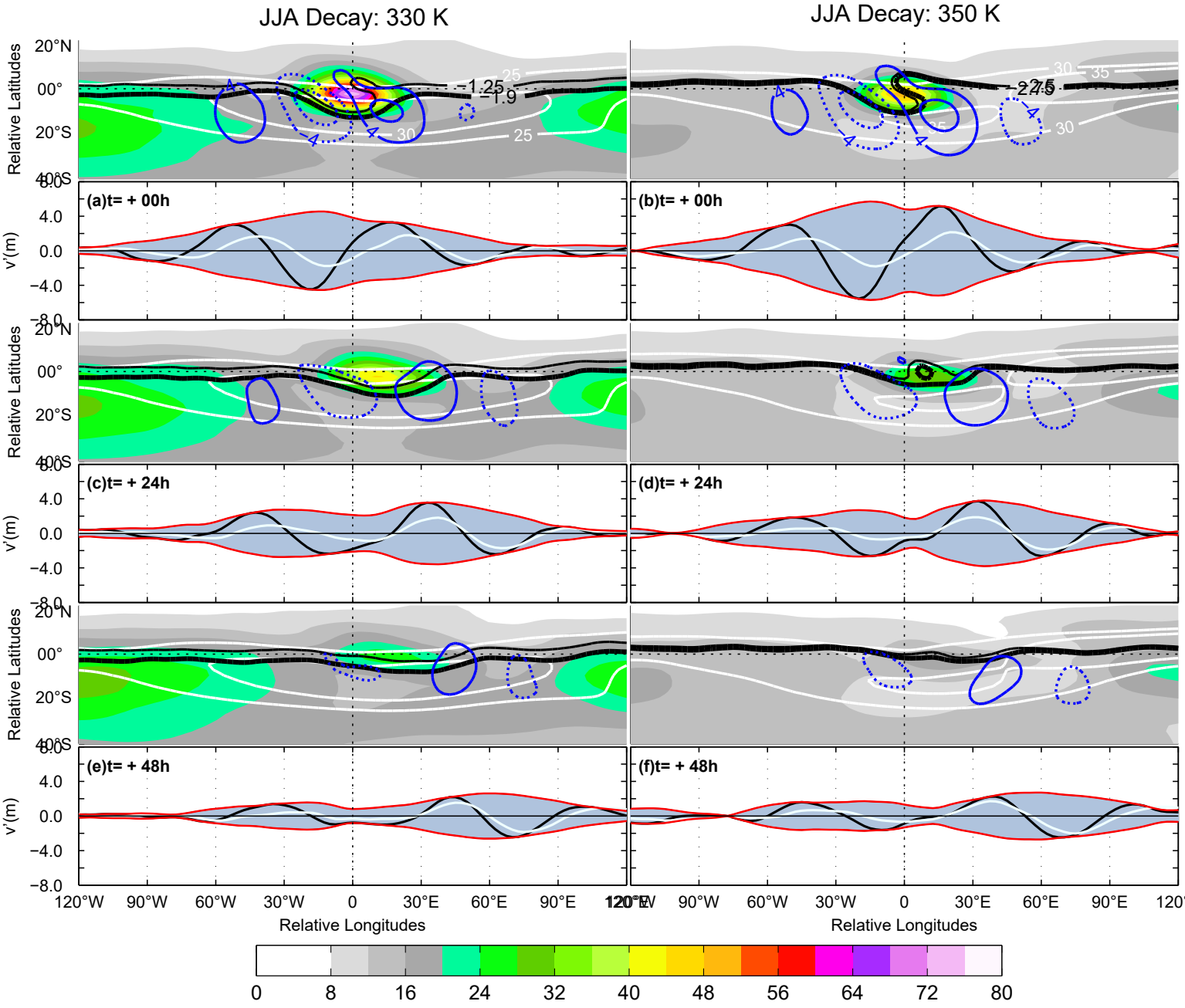

Figure 5.5: As in Figure 5.3, but for the winter season.

Lastly, the mature LWA RWP object observed during summer (winter) is most intense on θ_{350} (θ_{330}). A comparison between the deformed PV contours during the two seasons and on the θ surfaces during RWB suggests that these LWA RWP objects are likely more sensitive to RWB that is not symmetrical. That is, higher LWA values are likely to be observed during RWB that is either predominantly poleward or equatorward. For example, during RWB onset on θ_{350} at t = -24 h (Figure 5.2 (f)), the RWB portrayed by PV

= -1.25 PVU has a very thin ridge filament and a broad trough PV streamer to give the impression of a predominantly equatorward RWB. This characterisation is, of course, qualitative in nature and assumes that we characterise RWB based on the amount of air mass transported in either a poleward or equatorward direction. A concise classification of the RWB type requires the application of a suitable algorithm (e.g, Gabriel and Peters, 2008; Ndarana and Waugh, 2011; Barnes and Hartman, 2012), which is beyond the scope of this study. This observed behaviour and bias is likely accentuated by the zonal filtering procedure applied to the raw LWA field. This is because the filtering window depends on the wavelength of RWPs, which, in turn, is a variable of the areas within the PV lobes. Therefore, when a ridge is significantly deeper and more deformed than a trough, its lobe will contain more wave activity relative to the trough. When the filter is applied to such a situation, the window could cover only the ridge-related wave activity, resulting in fewer points against the quantity when the area average is calculated (resulting in larger values). In contrast, when two lobes are of the same size, the filtering window easily covers the entire area consisting of these features, resulting in more realistic, and symmetrically, as in Figure 5.5 (b), placed RWP centers.

5.1.3 The role of the jet stream

As discussed in Chapter 2, the role of the jet stream is an important consideration in the life cycle of Rossby waves, and indeed RWPs. This then warrants a brief discussion of the behaviour of the jet stream in relation to the RWPs under consideration. Particular emphasis is placed on the orientation, displacement, and intensity of the jet stream during various stages of the LWA RWP evolution, as identified in the preceding section. Recall that the summertime mean zonal flow appears as a mid-latitude confined Southern Hemispheric structure featuring a maximum approximately across the South Atlantic and Indian Oceans, referred to as the eddie driven jet, while in addition, the winter regime consists of a stronger subtropical branch across the pacific ocean known as the thermally driven jet (Gallego et al., 2005; Nakamura and Shimpo, 2004). Figure 5.6 reveals the signals of the

climatological jet streams when $\overline{u}_{350}$ is considered throughout the evolution. In contrast, the full zonal component of the horizontal wind (u_{350}) shows heavily pertubed distributions during various stages of development, to show the pronounced influence of the pertubation component of the zonal wind (u_{350}). For example, in Figures 5.5 (a-b) the signal of the extratropical jet is evident, as indicated by the narrow band of quasi-horizontal isotachs of $u_{350} = 29, 33$ ($u_{350} = 33, 35$) ms^{-1} for summer (winter), although the portion of the jet between 90 and 30°W is highly tilted in a northwest-southeast direction following the downstream limb of the incipient troughs at t = -72 h (Figures 5.5 (a) and (b)).

To the extent that the climatological horizontal jet configurations approximate the basic-state zonal flow, the northwest-southeast tilting of the jet entrance region alluded to has implications on the relationship between the extratropical mean zonal flow and developing disturbances. For example, this orientation of the jet is accentuated during subsequent time steps until t = 0 h during the sustained non-linear growth stage of the RWP life cycle during both seasons. Figures 5.1 and 5.3 showed that RWPs over the SA domain become increasingly baroclinic during the days leading up to maturity at t = 0 h as diagnosed visually by the westward lagging v'_{200} minima and maxima relative to corresponding v'_{850} peaks. Increased baroclinicity is an indicator of baroclinic instability, which is a crucial aspect for the growth of eddies. Ambaum and Novak (2014) likened the equatorward displacement and associated tilting of storm tracks to increased baroclinicity of eddies, which by virtue of the collocation of the SH jet stream waveguides, storm tracks and regions of enhanced baroclinicity (Wirth et al., 2018), would imply that growing disturbances can modulate the behaviour of the jet stream.

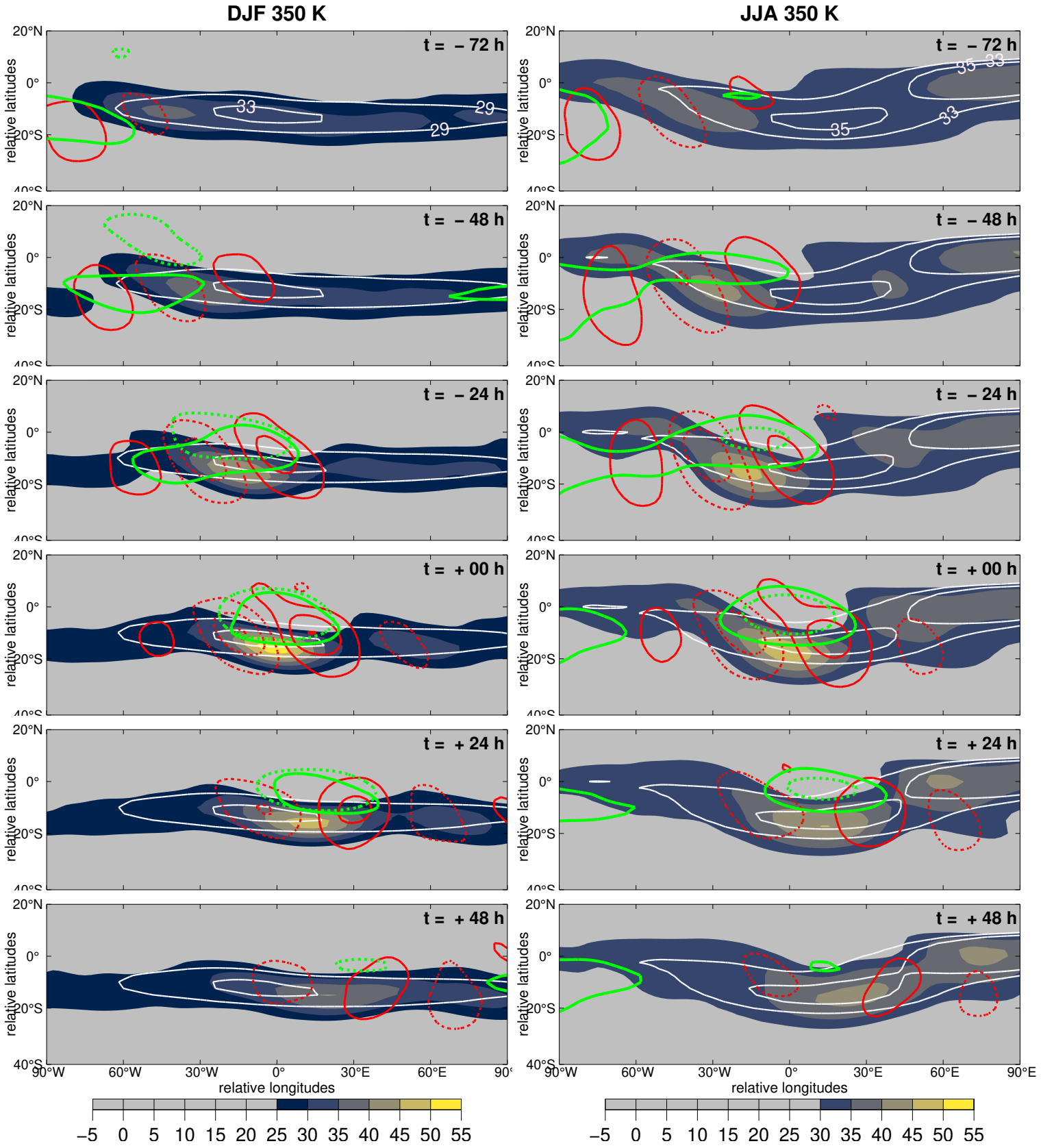

Figure 5.6: Composite mean evolution illustrating the interaction of θ_{350} jet streams and RWPs during on summer and winter months respectively (left to right). Colorshading (white contours) represents the full (basic state) isotachs of the zonal components of the horizontal wind $\overline{u}_\theta$ [ms^{-1}]. The red contours denote isotachs of v' (interval = 4 ms^{-1}) as in Figures 5.1-5.4, while the location of LWA pocket centers are shown in green (dashed (solid) for $A_{350} = 25$ ($A_{330} = 30$) ms^{-1}) during winter. For summer: dashed (solid) for $A_{350} = 25$ ($A_{330} = 30$) ms^{-1}.

Coupled with tilting is the systematic eastward displacement of the jet streaks; this would imply, at least from a qualitative and visual inspection point of view, that the south-west hailing RWP (relative to PV^{TP}) plays an important role in the observed modification of the basic state flow orientation. Additionally, during this period of sustained displacement and deformation of the mean zonal flow structure, the jet stream core increases in intensity and reaches a maximum during LWA RWP saturation. These sequences of events thus point to the eddie-driven nature of this jet stream and would seem to corroborate the view that the waveguidability of the jet stream is dependent on the eddies (Wirth and Polster, 2021). However, as previously noted, the relationship between baroclinic eddies and the jet stream is of a less than trivial nature. When the developing RWP approaches the jet stream core, isotachs of v' defining the ridge component immediately became meridionally elongated and intensified, implying an increase in amplitude of the waves as they tilt in a northwest-southeast direction under the barotropic shearing stress environment in the vicinity of the jet stream. This would imply that the jet stream itself influences the disturbances by amplification, eventually leading to RWB. This could be a possible explanation for the increased baroclinicity of the LWA based RWPs as soon as they encountered the extratropical jet entrance region because since jet stream waveguides usually coincide with the highly baroclinic storm tracks (Wirth et al., 2018). This implies that over such regions, perturbations can grow due to the pre-existing energy embedded within them.

Studies have found that the background flow plays an important role of initiating and determining the RWB type during the life cycle of Rossby waves (e.g, Nakamura, 1994; Nakamura and Plumb, 1994; Peters and Waugh, 1996; Peters and Waugh, 2003; Orlanski, 2003). This is because as the jet streaks intensify during their eastward propagation, they bring about with them barotropic shear, which is a necessary feature for RWB to occur (Nakamura and Plumb, 1994; Peters and Waugh, 1996). Therefore, we may attribute the initiation of the observed anticyclonic RWB to the intensification of the straight jet structure, as supported by barotropic wind shearing arguments presented in Peters and Waugh (2003). A similar process is observed in the case of the RWPs maturing over the

SA domain as RWB takes place at t = 0 h when the intensity of the jet streaks is at a maximum.

Following the observed RWB equatorward of the jet stream axis, the underlying RWP weakens as it propagates eastward along the jet stream downstream and poleward of the RWB breaking region. Interestingly, this highlights the ability of the jet stream to act as a wave guide for almost-planar RWPs. This is particularly evident during the termination stage (t = +24 to +48 h) of the winter RWPs (Figure 5.5) where a "residue" trough of the RWPs continues to propagate eastwards weakens between 30° and 60 °E. On θ_{330}, the orientation of the jet axis at the exit region is southwest-northeast, and the propagation of the RWP residue follows this configuration. On the other hand, the trough appears to propagate in a south-eastward direction. This appears to demonstrate the influence of the subtropical jet, which in this case serves as a barrier to the equatorward propagation of the remnant RWP.

These observations thus re-enforce the notion of the jet stream as an effective wave guide in two ways. First, the overall basic-state jet stream structure can serve as a pathway for RWPs undergoing development. Secondly, the pertubation jet streaks can initiate RWB of RWPs undergoing non-linear growth. The onset of RWB can also play an important role in the behaviour of the jet stream. For example, during early stages of the evolution of winter RWPs on θ_{350}, the region 0-60 °E along the dynamical tropopause is characterised by slower u_{350} that slowly increase with time. The increase appears to be connected initially to the subtropic jet stream up to t = 0 h when the wintertime split-flow configuration is most evident. At times t = +24 and +48 h, the two jet branches appear to connect to form one coherent jet structure oriented in a southwest-northeast direction. Similar observations can be made for the jet stream accompanying the summertime RWPs over the same region. These sequence of events can be seen as an example of the RWB process acting to promote the formation of a new wave guide, as suggested in previous studies (Wirth et al., 2018).

5.2 Eddy Kinetic Energy and Downstream Development of RWPs

In the previous section, we discussed the evolution of θ_{350} LWA-based RWPs during the summer and winter seasons. This section examines the physical mechanisms associated with the various stages in the life-cycle of RWPs. As with previous LWA formulations (e.g, Nakamura and Solomon, 2011; Huang and Nakamura, 2016), the corresponding tendency equation provides the means to achieve this. However, the discussed limitations of the LWA formulation employed in this study unfortunately have implications on the extent to which we can extract the underlying physical mechanisms governing the evolution of RWPs. Specifically, information regarding individual troughs and ridges is immediately lost due to the filtering procedure used to construct the coherent LWA RWP structures. This diagnostic will be examined later in the ensuing analysis.

In light of this, we turn to the well-known energetics framework; paradigm of downstream development, which has been widely used in several previous studies of RWPs (e.g, Orlanski and Katzfey, 1991; Chang, 1993; Orlanski and Sheldon, 1995; Gan and Piva, 2013; Gan and Piva, 2016; Ndarana et al., 2021; Ndarana et al., 2022). The utility of this energetics framework is also motivated by the fact that studies have revealed consistencies between the wave activity and the energetics (i.e., eddy kinetic energy) framework, but the latter is often preferred over the former owing to its self-contained conservation properties (Ghinassi, 2019). That is, while energy in the atmosphere is conserved in its totality, eddy kinetic energy is not (Orlanski and Katzfey, 1991; Ghinassi, 2019) because it is just a component in the conservation of energy, which involves the mean and eddy available potential, and mean available kinetic energies. Moreover and as reviewed in Chapter 2 of this study, one of the key features of RWPs is their ability to initiate the transport of energy to previously undisturbed regions, which can potentially give rise to the development of new systems at these downstream areas at the leading edge of the RWP through the process of downstream development discussed previously. The paradigm of downstream baroclinic

development provides a means to identify and quantify the mechanisms involved during the development process through the utility of the eddy kinetic energy equation and the associated tendency equation. Here its consideration is two fold; first, the extent to which the tracked LWA-based RWPs maturing over the SA domain conform to this framework is unknown. As a result, to admit the tracked LWA objects as true RWP structures, they must conform to the paradigm of downstream baroclinic development. Secondly, if they do indeed exhibit aspects of downstream baroclinic development, what other physical mechanisms may be of importance in the evolution of RWPs over the SA domain? This question is particularly relevant in the context of this study owing to the documented uncertainty related to the mechanism(s) responsible for the upstream decay of mature RWPs as remarked by Wirth et al. (2018).

5.2.1 Eddy Kinetic Energy

Figure 5.7 shows the summer (left panels) and winter time-lagged composite mean evolution (right panels) of eddy kinetic energy (K_e) (colour shading) in relation to v' (blue closed isotachs). The Roman numerals in Figure 5.7 refer to individual K_e centres referred to in the ensuing analysis. During the initial stages of development at t = -72 h (Figure 5.7 (a and g)), there are two K_e centres located in the region 90°-60°W and 60°-30°W which are associated with the broad trough embedded within the incipient RWP poleward of the dynamical tropopauses during both seasons. The first K_e centre (K_{e_1}, labelled as I in Figure 5.7) coincides with the western flank of this trough where $v' > 0$ and appears to be relatively weak compared to its downstream counterpart K_{e_2}. It is also noteworthy that K_{e_2} is positioned at the background flow ($\overline{u}$) jet stream entrance region shown previously in Figure 5.6. Subsequent time steps beyond t = -72 h show that the strength of K_{e_1} decreases in correspondence with the decaying trailing edge of the RWP, while the magnitude of K_{e_2} continues to intensify. By t = +24 h K_{e_1} has virtually disappeared from the picture, while an additional K_e centre (K_{e_3}) emerges ahead of K_{e_2} as K_{e_2} becomes a maximum during this time. Recall that it is during this time that the RWP attained maximum amplitudes

before the onset of LWA maturity. It is also important to recall that the maximum v'_{200} amplitude of wintertime RWPs at t = -24 h in Figure 5.4 (f) is larger than the maximum amplitude of summertime RWPs at the same time step (Figure 5.2 (f)). This explains why the winter K_e centres are more intense than their summer counterparts on θ_{350}. This appears to be consistent with the distribution of the amplitude of RWPs based on the meridional wind, which shows that the amplitude of RWPs over the extratropics in the SA domain is comparatively larger during winter compared to summer months (see Figure 6 in Souders et al. (2014b)). Additionally, the fact that vertically averaged K_e centres coincide with v' maxima also suggests that u' centres (i.e., jet streaks) likely play a secondary role in determining the overall structure of K_e centres.

24 hours later, K_{e_2} has weakened during LWA RWP maturity, while K_{e_3} has continued to grow and achieve magnitudes comparable to its predecessor; K_{e_2}. During this time (t = 0 h), a fourth K_e centre (K_{e_4}) emerges between 30 and 60°E during winter (Figure 5.7 (h)), while it only appears at t = +24 h during summer months (Figure 5.7(i)). Later time steps reveal that the intensity of K_{e_3} decreases beyond the onset of RWP termination in conjunction with the weak generation of K_{e_4}, which propagates zonally at the leading edge of the decaying RWP. Note that while the behaviour during the two seasons is largely similar, the summer K_e maxima are relatively weaker than their winter counterparts on θ_{350} throughout their evolution. The sequence of events examined above serves as a clear indicator of the interplay between the decay and growth of K_e centres at upstream and downstream regions of disturbances within an RWP, respectively. It therefore begs the questions; which mechanism(s) are responsible for this apparent interplay, or K_e centres themselves? Does K_{e_2} grow at the expense of K_{e_1}? The fact that the downstream/leading edge growth comes at a time when the upstream K_e centres lose EKE is a signature of DBD (Orlanski and Katzfey, 1991; Orlanski and Sheldon, 1993; Orlanski and Chang, 1994). Therefore, these observations warrant further analysis to diagnose the extent to which the paradigm of downstream baroclinic development (DBD) governs the evolution of RWPs maturing over the SA domain during summer and winter months. To this end,

we discuss the evolution of the observed K_e centres by means of the K_e tendency, or the budget equation, in the following section.

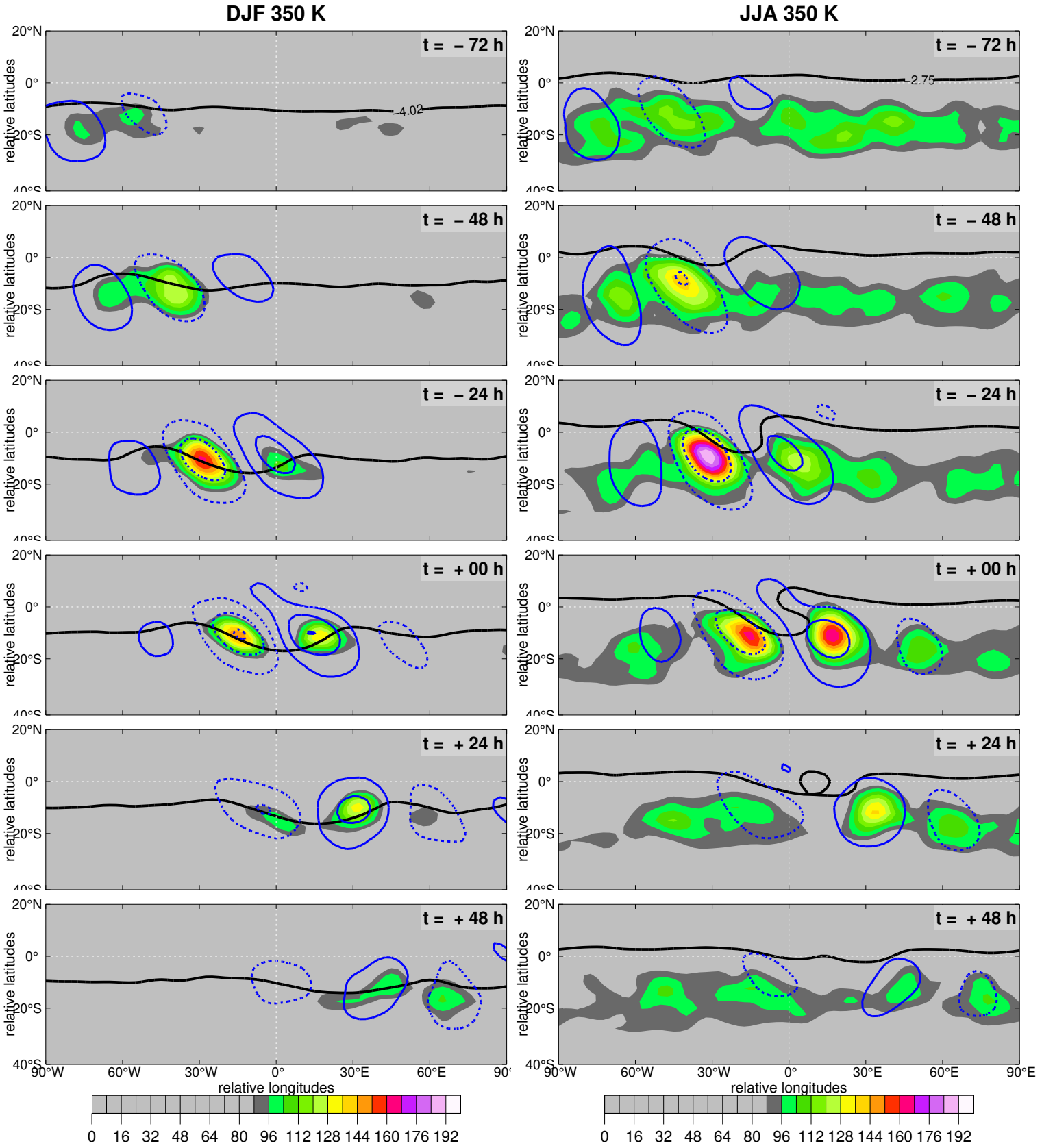

Figure 5.7: Summer (a,c,e,g,i,k) and wintertime (b,d,f,h,j,l) time-lagged composite mean evolution of vertically integrated K_e (color shading in m^2s^{-2}) in relation with v' [red dashed(solid) isotachs: $v' < 0$ ($v' > 0$), contour resolution = $\pm$ 4ms^{-1}]. The solid black lines denote the PV isopleth representative of the estimated dynamical tropopause (PV^{TP}).

5.2.2 Downstream development of RWPs

$$\begin{aligned}\partial_t K_e &= S_{3D} + \mathrm{BRC} + \mathrm{BRT} + \mathit{Residue},\\ &= -[\boldsymbol{V}_3 \cdot \nabla_3 K_e + \nabla_3 \cdot (\boldsymbol{v_3}\phi)_a] - \omega^{'}\alpha^{'} - [\boldsymbol{v} \cdot (\boldsymbol{v}_3 \cdot \nabla_3)\boldsymbol{V_m} + \boldsymbol{v} \cdot \overline{(\boldsymbol{v}_3 \cdot \nabla_3)\boldsymbol{v}}] + \mathit{Residue}.\end{aligned} \tag{5.1}$$

The spatial patterns of vertically averaged $\partial_t K_e < 0$ and $\partial_t K_e > 0$ (left-hand side (lhs) of Equation 5.1) coinciding with K_e centres allow us to identify sinks and sources of K_e based on terms on the right-hand side (rhs) of the EKE budget, respectively. As dictated by the paradigm of DBD, only a handful of terms appearing on the rhs of Equation 5.1 have been found to be of particular importance when diagnosing downstream development of non-linear regimes such as cut-off low pressure systems (e.g, as in Gan and Piva, 2013; Gan and Piva, 2016; Ndarana et al., 2020; Pinheiro et al., 2022). These are the, baroclinic conversion from eddy available potential energy (P_e) to K_e ($-\omega\alpha$), divergence of ageostrophic geopotential fluxes ($-\nabla_3 \cdot (\boldsymbol{v_3}\phi)_a$), and the barotropic conversion of K_e to the mean kinetic energy (MK_e) (BRT). Here, BRT is estimated as $-\left(\boldsymbol{v} \cdot (\boldsymbol{v} \cdot \nabla_3 \boldsymbol{V_m}) + (\boldsymbol{v} \cdot (\overline{\boldsymbol{v} \cdot \nabla_3 \boldsymbol{v}})\right)$ as in Pinheiro et al. (2022) and Chang (2000) because both terms are closely related through their facilitation of energy exchanges between the ambient flow and perturbations (Orlanski and Katzfey, 1991; Decker and Martin, 2005). This implies that the behaviour of the lhs of Equation 5.1 can be approximated based on terms representing prominent sources and sinks of K_e (ignoring the *Residue* term and associated processes) as

$$\partial_t K_e \approx -[\boldsymbol{V}_3 \cdot \nabla_3 K_e + \nabla_3 \cdot (\boldsymbol{v_3}\phi)_a] - \omega^{'}\alpha^{'} - [\boldsymbol{v} \cdot (\boldsymbol{v}_3 \cdot \nabla_3)\boldsymbol{V_m} + \boldsymbol{v} \cdot \overline{(\boldsymbol{v}_3 \cdot \nabla_3)\boldsymbol{v}}], \tag{5.2}$$

where the divergence of K_e fluxes ($-\nabla_3 \cdot (\boldsymbol{V}_3 K_e)$) is retained due to its prominent role in translating K_e. Note that we retain the vertical components in the flux terms (1 and 2 on the rhs of Equation 5.2) because there may be vertical contributions of wave activity in LWA (A) according to Ghinassi et al. (2020), therefore discarding vertical components would effectively hamper our ability to compare LWA and EKE in the subsequent section.

However, the vertical contributions are known to be relatively small as compared to the horizontal contributions (e.g, Orlanski and Katzfey, 1991; Wirth et al., 2018; Pinheiro et al., 2022), therefore we do not expect these contributions to have a significant contribution in the context of this study and are therefore retained for framework consistency. To assess the relative contributions of each of these terms to the evolution of $\partial_t K_e$, time-lagged composite maps of EKE together with the corresponding budget $\partial_t K_e$ are presented in Figure 5.8.

Figure 5.8 shows the evolution of K_e (colorshading) as in Figure 5.7 in the top panels during the development stage of the LWA RWPs detected during the summer (left panels) and winter (right panels) months. Additionally, $\overline{u}$ is shown by white contours to denote the background flow. The joint bottom panels during each time step represent the overall RWP envelope as used in Figures 5.2-5.5, but here the curves embedded within the RWP structure represent the meridionally averaged K_e tendency terms to show the location and magnitude of their contributions relative to the K_e centres and the RWP itself. $\partial t K_e$ is shown in dashed black curves, while $-\nabla_3 \cdot \boldsymbol{V}_3 K_e$, $-\omega\alpha$, $-\nabla_3 \cdot (\boldsymbol{v_3}\phi)_a$, and BRT curves are shown in navy blue, magenta, cream white and cyan colours. Note that this approach was taken instead of computing the spatial averages' time series because multiple K_e centres appear in the evolution, thus computing the spatial average would obscure processes taking place over individual K_e centres observed in Figure 5.7. This would not be a concern in the case of LWA because only one LWA RWP pocket was a feature of interest during most stages of development. Lastly, the vectors representing horizontal components of the EKE (geopotential) fluxes due to the total (ageostrophic) flow, $\boldsymbol{V}_h K_e$ and $\boldsymbol{v_a}\phi$ respectively, are shown in navy blue and magenta arrows, respectively.

During the early stages of RWP development during summer months (t = -72 h, Figure 5.8 (a)), a pre-existing southwest-northeast oriented K_e pattern located between 90° and 45°W is already visible. This pattern extends from the leading edge of the LWA pocket towards the dynamical tropopause ($PV^{TP} = -4.02$ PVU) estimated using Kunz et al. (2011) as in Figures 5.2-5.7. This pattern of K_e is characterised by two local K_e maxima

embedded at its rear and front ends. These K_e centres were previously defined as K_{e_1} and K_{e_2} respectively. To the extent that the LWA pocket envelope signifies the central portion of an RWP, this local K_e maximum can be interpreted as a feature located at the leading edge of the incipient RWP because it is located slightly ahead of the corresponding RWP envelope during this time step. Note that there is good spatial agreement between the peaks of the Hilbert transform-derived RWP envelope and the LWA pocket in Figures 5.2-5.5.

K_{e_1} is associated with very weak K_e tendency signals ($\partial_t K_e \approx 0$) from its centre towards its front end area, while the rear end area is associated with a weak $\partial_t K_e < 0$ feature. K_e decay (growth) takes place where a $\partial_t K_e < 0$ ($\partial_t K_e > 0$) structure coincides with a K_e centre, while $\partial_t K_e \approx 0$ denotes no growth or decay. Therefore, K_{e_1} is undergoing eddy kinetic energy decay at its rear end, while no decay or growth is taking place at its front end. Therefore, this configuration should result in a reduction in the spatial extent of K_{e_1}, particularly over its rear end part. In contrast, K_{e_2} coincides with an area of K_e growth signified by $\partial_t K_e > 0$ as predominantly influenced by the positive contribution of the baroclinic conversion term ($-\omega\alpha > 0$). While this term clearly dominates the generation of K_{e_2}, a combination of $-\nabla_3 \cdot (\boldsymbol{v_3}\phi)_a$ and $-\nabla_3 \cdot (\boldsymbol{V}_3 K_e)$ are also positive contributors to the observed $\partial_t K_e > 0$. However, these are partially balanced by a negative contribution of the barotropic conversion term, elucidating the dissipative role of barotropic processes. This then isolates the baroclinic conversion from P_e (eddy available potential energy) to K_e through baroclinic instability as the main K_e generation process at the leading edge of the incipient RWP. K_{e_2} is exclusively associated with K_e growth, since there are no $\partial_t K_e < 0$ structures associated with it at this time step, which implies that it can only expand laterally (i.e., predominantly eastward) while increasing in magnitude. This implies that in situ growth is at play here. For winter RWPs, a clear spatial pattern of $\partial_t K_e$ related to K_{e_1} is non-existent at t = -72 h (Figure 5.8 (b)) although the observed pattern of K_e structures and v' isotachs is similar to that observed in the case of summertime RWPs.

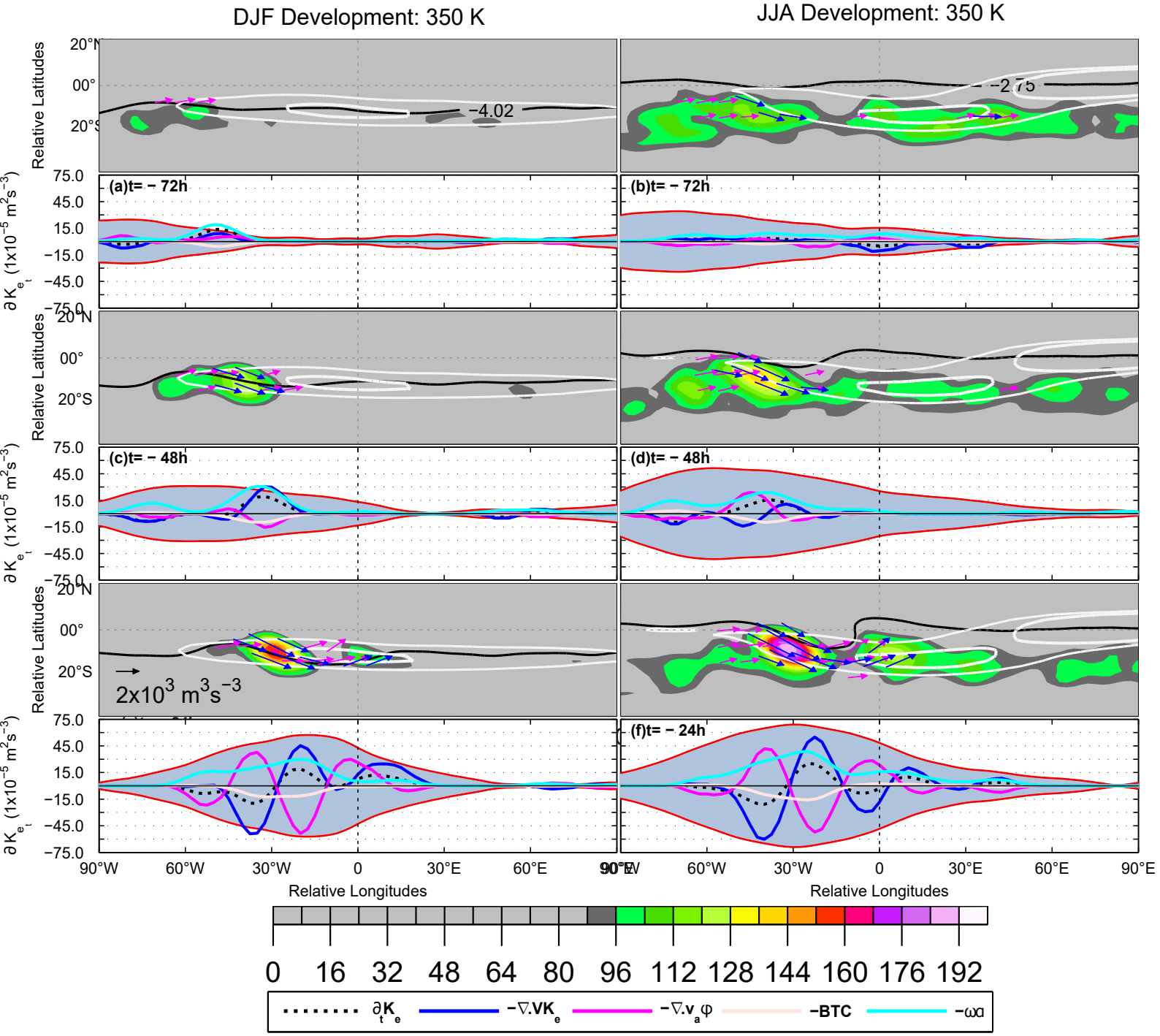

Figure 5.8: Development stage of Summer (left panels) and winter (right panels) time-lagged composite mean evolution of K_e as in Figure 5.7. Included here are $\overline{u}$ (white isotachs), $\cdot(\boldsymbol{V_a}\phi)$ (magenta coloured arrows), and $\cdot(\boldsymbol{V}_{total}K_e)$ (navy blue coloured arrows), the vector scale is represented by the single black arrow in Figure 5.8 (e). Bottom plots are the RWP envelope as in Figures 5.1-5.4 with the isobaric v' and curves removed. Embedded within the RWP structure are meridionally averaged K_e budget terms represented in the legend; ∂tK_e is shown in dashed black curves, while $-\nabla_p \cdot \boldsymbol{V}K_e$, and BRT curves are shown in navy blue, magenta, cream white, and cyan colors in $\mathrm{m^2 s^{-3}}$.

At t = +48 h the overall K_e pattern encompassing both K_e centres appears to have shifted slightly in a northeast direction together with the RWP pocket structure in Figure 5.9 (c). This translation is accompanied by a weak (strong) intensification at its rear (front) end. Over the area of K_{e_1}, the intensification is associated with the eastward propagating baroclinic wave ridge component of the ridge-trough couplet that defines the incipient RWP centred over the 90° - 60°W domain. This is also indicated by the peak in $-\omega\alpha > 0$ observed over the same region so that there now exist two local $-\omega\alpha > 0$ maxima and a minimum located between these two peaks centred at ≈ 50°W. The $-\omega\alpha$ minimum coincides with $\partial_t K_e \approx 0$ to show that a discontinuity point exists over this area within the K_e structure. Over the area covered by K_{e_2}, the growth is also associated with a marked increase in $-\omega\alpha > 0$ that is likely also amplified by the approaching disturbance. The fact that the $v' < 0$ isotach associated with K_{e_2} at t = -24 h coincides with the distinct K_e centre at the front end of the overall K_e structure ascertains that it is indeed K_{e_2} observed previously. Additionally, the fact that $K_e = 0.5(\boldsymbol{V} \cdot \boldsymbol{V}) = 0.5(u^2 + v^2)$ suggests that K_{e_2} is also associated with the observed eastward propagating jet streak observed previously in Figure 5.6 (a-b) between 60° - 30°W because the jet stream core associated with $\overline{u}$ is anchored downstream over the 30°W - 30°E sector as also pointed to by Orlanski and Sheldon (1995) during stage 1 of DBD. This further makes the case for the influence of the eddies on the background flow, and by extension, the storm track (Novak et al., 2015). This state of affairs therefore suggests that stage 1 of DBD may be at play at this time in the evolution.

The rear end of K_{e_1} is however still associated with $\partial_t K_e < 0$, marking the overall decay of K_e over that part of the RWP. Subsequent time steps show that this upstream K_e centre, together with its tendency signals, completely disappears beyond t = -48 h. The dissipation of K_{e_1} at its rear end is predominantly due to the combination of K_e divergence ($-\nabla_3 \cdot (\boldsymbol{V}_3 K_e) < 0$) as well as the divergence of ($\boldsymbol{v_a}\phi$) acting against the coincident $-\omega\alpha > 0$. While the signal of $-\omega\alpha > 0$ is pronounced over the region of K_{e_1}, it is effectively countered by the combination of $-\nabla_3 \cdot (\boldsymbol{v_3}\phi)_a < 0$ and $-\nabla_3 \cdot (\boldsymbol{V}_3 K_e)$ which gives rise to the overall $\partial_t K_e < 0$ centred at ≈ 75°W along the upstream limb of the broad trough

that extends between 75° and 30°W. At the front end of this K_e center, $\partial_t K_e \approx 0$ so that there is no net loss or gain in K_e over that part of the upstream K_e.

The observed $\partial_t K_e \approx 0$ is a culmination of all the tendency terms, first, the local minimum located between the peaks of $-\omega\alpha > 0$ centred just east of 60°W edging closer to $-\omega\alpha \approx 0$ to signify the lack of baroclinic growth along the trough axis. The rest of the terms also tend towards zero at this location, meaning that although the implied role of divergent $\boldsymbol{v_a}\phi$ vectors in the radiation of energy from (towards) front (rear) end of the upstream (downstream) K_e is more pronounced than that of $\boldsymbol{V}_h K_e$, the overall contribution of this process (in the form of $-\nabla_3 \cdot (\boldsymbol{v_3}\phi))_a$ is hampered by other processes represented by the opposing terms. This configuration is detrimental to the existence of upstream K_e, that is, when $\partial_t K_e < 0$ and $\partial_t K_e \approx 0$ patterns are oriented at the rear (front) end of a K_e structure because the net K_e centre cannot grow or propagate eastward any further, resulting in a progressive overall reduction in magnitude (size) at the rear (front) end leading to complete dissipation.

The increased K_e growth rate over K_{e_2} is now coupled with a positive and equally strong contribution by $-\nabla_3 \cdot (\boldsymbol{V}_3 K_e)$. This implies the convergence of K_e fluxes due to the full/total horizontal flow of at ≈ 30°W (Figure 5.12(c)). $\boldsymbol{V}_h K_e$ fluxes are pointed in a northwest-southeastward direction, revealing the energy radiation direction from (toward) the rear end (front end) of K_{e_2} where the divergence (convergence) of K_e takes place. In contrast, $-\nabla_3 \cdot (\boldsymbol{v_3}\phi)_a$ combines with the barotropic conversion term to inhibit K_{e_2} growth, and therefore balances $\partial_t K_e > 0$. The former acts to radiate some of the K_e away from the growth region in an east to northeastward direction as indicated by the $\boldsymbol{v_a}\phi$ vectors. The role of $-\nabla_3 \cdot (\boldsymbol{v_3}\phi)_a$ is also to facilitate some of the growth taking place at the rear end of K_{e_2}. This comes at the expense of the pre-existing K_e at the front end of K_{e_1}, which is already waning in intensity due to a lack of growth at its front end area. This analysis is also applicable for the case of wintertime RWPs at the same time (Figure 5.12(d)), but some differences exist when close comparisons are made.

For example, the growth of the summer K_{e_2} at t = -48 h is governed by $-\omega\alpha > 0$ and $-\nabla_3 \cdot (\boldsymbol{V}_3 K_e) > 0$ at the front end of this K_e centre. The front end K_{e_2} positive growth rate due to $-\nabla_3 \cdot (\boldsymbol{V}_3 K_e) > 0$ surpasses the decay due to the same term at the rear. This implies that the eastward/southeastward advection of K_{e_2} due to the horizontal flow is not yet efficient. This is also reflected by the $\partial_t K_e \approx 0$ curve coincident with K_e decay and growth maxima due to $-\nabla_3 \cdot (\boldsymbol{V}_3 K_e)$ and $\nabla_3 \cdot (\boldsymbol{v_3}\phi)_a$ respectively. A similar dipole configuration leading to a net balance is observed in terms of the baroclinic (positive contribution) and barotropic (negative contribution) conversion terms at the same location. This state of affairs therefore suggests that the K_e advected by $\boldsymbol{V}_h$ is likely mostly generated by $-\omega\alpha$. In contrast, while $-\omega\alpha > 0$ also contributes significantly to much of the $\partial_t K_e > 0$ at the leading edge of winter K_{e_2}, it is $\nabla_3 \cdot (\boldsymbol{v_3}\phi)_a$ that provides the additional growth slightly west (rear) of the $\partial_t K_e > 0$ peak.

This is partially balanced by the observed divergence at the rear of K_{e_2}, as well as the barotropic term. Regarding the former ($-\nabla_3 \cdot (\boldsymbol{V}_3 K_e) < 0$), the decay rate at the rear end of K_e is comparable to the growth rate due to this term at the front end, implying that this term acts to efficiently shift this K_e centre at this time. Therefore, K_e developing due to the converging $(\boldsymbol{v_a}\phi)$ at the rear, and $-\omega\alpha$ closer to the centre of K_e is immediately radiated towards the leading edge by $-\nabla_3 \cdot (\boldsymbol{V}_3 K_e)$ to facilitate its south-eastward propagation. This analysis therefore highlights the importance of $-\omega\alpha$ during the early stages of the K_{e_2} centre as a significant source of EKE as in Pinheiro et al. (2022). In terms of DBD stages of development, the period t = -72 and 48 h closely resembles stage 2 because K_{e_2} growth is predominantly governed by $-\omega\alpha$, with a minor contribution by $-\nabla_3 \cdot (\boldsymbol{v_3}\phi)_a$. This is in contrast to the expected dominance of $-\nabla_3 \cdot (\boldsymbol{v_3}\phi)_a$ during the earlier stages of development. This is particularly true for the summertime evolution because the generation of K_{e_2} at t = -48 h during winter is the culmination of both $-\nabla_3 \cdot (\boldsymbol{v_3}\phi)_a$ and $-\omega\alpha$ acting jointly to generate and maintain K_{e_2}. A similar situation observation was made by Ndarana et al. (2020) in their analysis of DBD during CoL pressure development over SA.

This comes as no surprise given the fact that the finite-amplitude RWPs identified here undergo anticyclonic RWB, which by extension is associated with CoL formation (Ndarana and Waugh, 2010), during their mature phase.

t = -24 h marks the first occurrence of a downstream K_e centre along (poleward of) the dynamical tropopause in the vicinity of $\lambda_{relative} = 0°$ during summer (winter). This essentially marks the beginning of stage 3 of DBD. To support this statement, the advent of this K_e centre is predominantly a consequence of converging $\boldsymbol{v_a}\phi$ vectors emanating from the leading edge of the upstream K_e centre. These vectors are pointed in an eastward-northeastward direction in the direction of the rear of the downstream K_e. To indicate its northeastward propagation, the convergence of K_e at the front end of the downstream K_e centre dominates much of the net K_e growth there. This is also shown by the vectors of $(\boldsymbol{V}_h K_e)$ oriented in a northeastward direction away from $\partial_t K_e < 0$ center coinciding with $-\nabla_3 \cdot (\boldsymbol{v_3}\phi)_a > 0$ and $-\nabla_3 \cdot (\boldsymbol{V}_h K_e) < 0$. This implies that the generated Ke at the rear of the downstream K_e is immediately shifted in a north-eastward direction, representing an overall shift in the K_e centre.

The upstream K_e centre experiences vigorous $\boldsymbol{v_a}\phi$ convergence coming from the decaying upstream K_e at its rear end. This facilitates $\partial_t K_e > 0$ at this part of the K_e centre, which is immediately translated southeastward by means of $(\boldsymbol{V}_h K_e)$ diverging (converging) at the rear (front) end of the K_e centre. The growth due to $-\nabla_3 \cdot (\boldsymbol{v_3}\phi)_a > 0$ at the rear end of K_e is supported by $-\omega\alpha > 0$, which acts across the zonal extent, but only peaks at the front end of this K_e center. There it balances the downstream radiation of some of the energy associated with K_e (due to $-\nabla_3 \cdot (\boldsymbol{v_3}\phi)_a < 0$) responsible for the development of downstream K_e. Barotropic conversion also acts across the zonal extent of upstream K_e to counter any K_e generation and development. As the southeastward propagation of K_{e_2} continues due to the northwest-southeast oriented pattern of $-\nabla_3 \cdot (\boldsymbol{V}_3 K_e) < 0$ and $-\nabla_3 \cdot (\boldsymbol{V}_3 K_e) > 0$, the actual growth of itself has decreased slightly at t = 0 h. Upstream K_{e_2} becomes overwhelmed by $\partial_t K_e < 0$ at the rear, while the intensity of $\partial_t K_e > 0$ at the

front end has waned in comparison (Figure 5.10(a and b)).

This configuration could be attributed to the decrease in the contribution of $-\omega\alpha > 0$, as well as the complete decay of K_{e_1} together with its supply of K_e to K_{e_2}. Moreover, the energy loss due to the divergence of $\boldsymbol{v_a}\phi$ at the front end is also persistent, together with the prevailing deterrent barotropic conversion across K_{e_2}. In contrast, K_{e_3} continues to develop and grow due to the continued convergence $-\nabla_3 \cdot (\boldsymbol{v_3}\phi)_a > 0$ of $\boldsymbol{v_a}\phi$ at the rear stemming from the front end of K_{e_2}. Again, the growth of K_{e_3} is almost exclusively initiated and maintained by this process, while the northeastward translation is catered for by $\boldsymbol{V}_h K_{e_3}$. 24 hours later the contribution of baroclinic and barotropic processes to the evolution of K_{e_3} is virtually non-existent, so that the roles of $-\nabla_3 \cdot (\boldsymbol{v_3}\phi)_a$ (generation [dissipation] of downstream [upstream] K_e) and $-\nabla_3 \cdot (\boldsymbol{V}_3 K_e)$ (horizontal translation of K_e) become neatly isolated. However, the intensity of the remaining processes is significantly reduced, implying that the K_e growth has also decreased. This is reflected by the dominant structures of $\partial_t K_e < 0$ at the rear end of K_{e_3}, which overwhelms the front end growth, ultimately leading to the sustained decay of K_{e_3} during subsequent time steps. The generation and growth mechanism of K_{e_4} is not well defined as the tendency signals over the region eastward of 60°E are non-existent. However, the vectors of $\boldsymbol{V_a}\phi$ emanating from the front end of K_{e_3} suggest that $-\nabla_3 \cdot (\boldsymbol{v_3}\phi)_a$ may be playing a role there, particularly during winter, while $-\omega\alpha$ is more significant for the summer situation. Additionally, K_{e_4} develops at the x axis of the jet stream, away from the jet streak which played a role during the inception of K_{e_2}.

The above sequence of events reveal that the evolution of RWPs over the SA domain exhibits well-known aspects of RWP development from a K_e perspective. Specifically, this confirms that the identified LWA pockets are indeed RWPs that conform to the DBD paradigm consistent with previous studies (see, e.g., Orlanski and Sheldon, 1995; Danielson et al., 2006; Gan and Piva, 2013; Gan and Piva, 2016; Ndarana et al., 2021; Pinheiro et al., 2022; Ndarana et al., 2022). Additionally, this corroborates the existing model of

an RWP as presented in Figure 9 of Wirth et al. (2018), specifying the dominant role of baroclinic conversion and its interplay with the convergence of ageostrophic geopotential fluxes in the development of disturbances ahead of RWPs. In addition, the model suggests that the upstream decay is unclear. Since we have retained the meridional view of the RWP, we have seen that the upstream decay of RWPs over the SA domain is at least in part associated with the divergence of ageostrophic geopotential fluxes and barotropic conversion. It should be noted that processes incorporated in the residual term may also play a role in the upstream dissipation (as discussed by Pinheiro et al. (2022)), however, the extent of this contribution was not examined in this study.

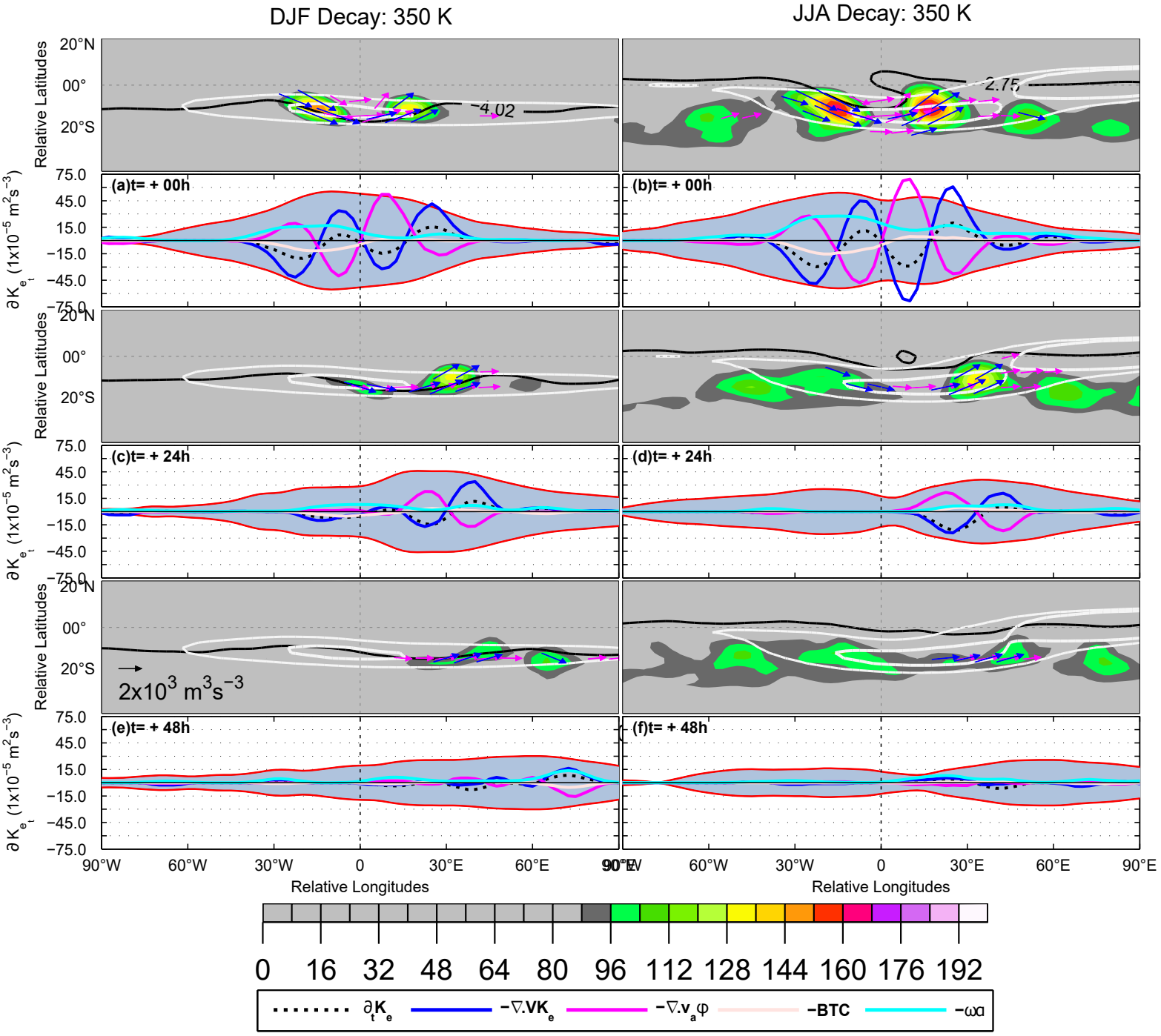

Figure 5.9: As in Figure 5.8, but for the decay stage of RWPs.

5.2.2.1 Comparison between LWA and EKE

A comparison between the LWA pocket and K_e centers' evolution is also a subject of interest because these two diagnostics have commonly been used in the study of RWPs (e.g., Danielson et al., 2006; Wirth et al., 2018). Danielson et al. (2006) found good agreement

between the wave activity of Takaya and Nakamura (2001) and K_e during the evolution of a cyclone over the North Pacific. The wave activity formulation of Takaya and Nakamura (2001) is similar to the one employed here because it is phase independent, while it is different in that it is based on the isobaric quasi-geostrophic (QG) framework. This formulation also assumes linear, small-amplitude Rossby waves, which was interpreted as a limitation in Danielson et al. (2006) because one runs the risk of misinterpreting results when the limits of a small-amplitude diagnostic are stretched (e.g, when applied to Rossby wave breaking) (Magnusdottir and Haynes, 1996; Danielson et al., 2006).

In the present study, we used a finite-amplitude-based wave activity diagnostic to identify mature RWPs over the SA domain over a 40-year period. This provides us with the unique opportunity to compare the characteristics of these two frameworks during the evolution of non-linear RWPs over the SA domain. Magnusdottir and Haynes. (1996) compared the finite-amplitude wave sensitive Cashmir impulse wave activity diagnostic (Andrews and McIntyre, 1978; Haynes, 1988) to area averaged K_e and found that the latter was unable to distinguish between two baroclinic life cycles LC-1 and LC-2 (based on Thorncroft et al., 1993). However, Cashmir impulse wave activity is known to misrepresent wave activity as fragmented filaments (Huang and Nakamura, 2016; Ghinassi et al., 2018), raising questions about the actual representation of wave activity compared to K_e in the first place. Lastly, LWA (Ghinassi et al., 2018), as used here, is to the knowledge of the authors, yet to be compared with K_e. The findings from previous studies alluded to in this subsection (Magnusdottir and Haynes, 1996; Danielson et al., 2006) suggest that it may be useful to use more than one diagnostic when studying Rossby waves. Therefore, we evaluate the validity of this recommendation in the context of LWA and K_e here. Equation 5.3, the budget equation for LWA (A) is provided here from Chapter 3 to aid in the ensuing discussion.

$$\partial_t A \cos\Phi_M = \underbrace{\int_{\Phi_M}^{\Phi_M+\Delta\phi} \nabla\cdot[(q-Q)\sigma\boldsymbol{v}]a\cos\phi d\phi}_{Tc} + \underbrace{\int_{\Phi_M}^{\Phi_M+\Delta\phi} \partial_t\left[Q\sigma\right]a\cos\phi d\phi}_{T_q} + \underbrace{Residual}_{T_n}. \tag{5.3}$$

Figures 5.9-5.10 illustrate the spatial relationship between layer averaged A_{avg} between θ_{330} and θ_{350} (green contour), and K_e centres (yellow contours) in relation to their respective tendency terms, $\partial_t A_{avg}\cos\phi$ (in purple) and $\partial_t K_e$ (colour shading). At t = -72 h (Figures 5.9 (a-b)), there exist pre-existing LWA structures over the 120° - 60°W sector during both seasons with notable differences. First, the summertime LWA structure is local within the 120° - 60°W sector, while its winter counterpart is associated with the LWA feature visible within the 90° - 120°E sector. This means that this LWA object actually spans the λ_{rel} domain: 90°E - 60°W sector. Secondly, the wintertime LWA object is not associated with any evident $\partial_t A_{avg}\cos\phi$ signals throughout the evolution, implying that it is likely a climatological feature as it does not grow, propagate or decay.

In contrast, the summertime object is associated with a $\partial_t A_{avg}\cos\phi < 0$ - $\partial_t A_{avg}\cos\phi > 0$ tendency pattern at its trailing and leading edges, respectively. This is a symptom of an eastward propagating LWA pocket. Ideally, pure propagation as viewed from a tendency field is signalled by the $-$ and $+$ pattern of equal magnitude. This is not the case for the summertime LWA pocket, implying that the dominant $\partial_t A_{avg}\cos\phi > 0$ observed at the leading edge of this RWP could be interacting with other processes. The additional process related to the observed LWA source at the leading edge of the summer LWA pocket is located in the vicinity of the K_e source located over the 60°-30°W sector, which we have identified as a result of baroclinic interaction. During winter, an LWA source is evident over the 60°-30°W as well, and appears to coincide with K_{e_2}.

This has implications on our understanding of the origins of the observed K_{e_1} and K_{e_2} energy centres during both seasons. K_{e_1} is associated with the pre-existing LWA structures, while K_{e_2} is simply an energy centre that grows by means of baroclinic conversion

($-\omega\alpha > 0$) and energy associated with the storm track area coinciding with the jet stream (not shown here). From a LWA perspective, the $\partial_t A_{avg} \cos\phi > 0$ in the vicinity of $-\omega\alpha > 0$ during both seasons can be explained using the conservative term ($T_{c_{avg}}$). Figure 5.9 shows the distribution of LWA tendency terms where $T_{c_{avg}}$ is denoted by the colour shading. At t = -72 h (Figure 5.9 (a)) the spatial pattern of $T_{c_{avg}}$ matches the overall advection pattern shown by $\partial_t A_{avg} \cos\phi < 0$ - $\partial_t A_{avg} \cos\phi > 0$, implying that the conservative process at play has to do with the divergence of the PV anomaly by the full wind implied by $\nabla \cdot [(q - Q)\sigma \boldsymbol{v}]$ under the integral sign. Note that σ is always positive since $-\partial_\theta P > 0$. There is, however, an LWA source located above $\phi_{rel} = 0°$ on the equatorward side of the dynamical tropopause between 60° and 30°W. This is presumably associated with the H_3 hotspot located over the SACZ region.

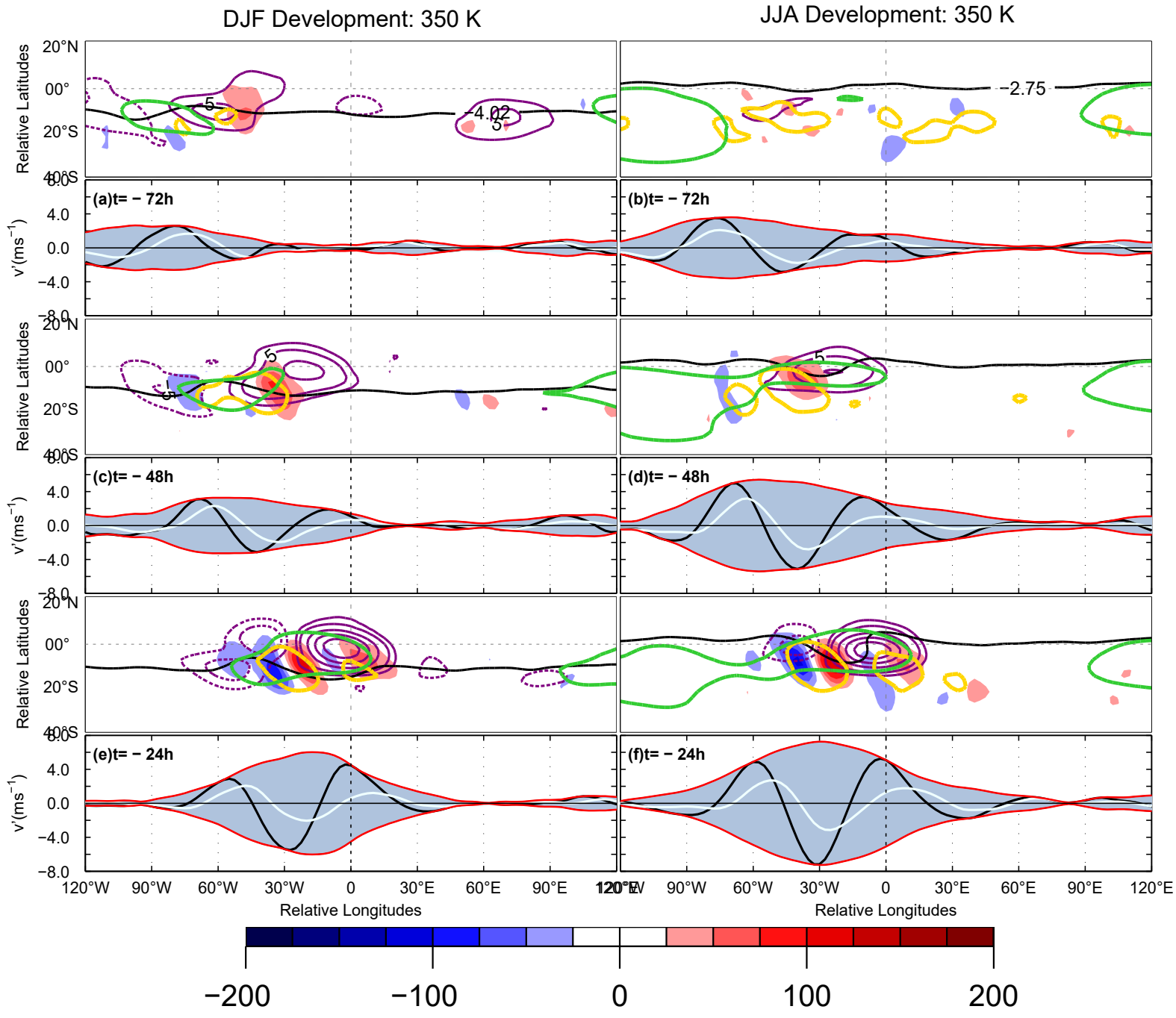

Figure 5.10: Development stage of Summer (left panels) and winter (right panels) time-lagged composite mean evolution of $K_e = 96$ (summer) and 104 (winter) $\mathrm{m^2 s^{-2}}$ represented by yellow contours. The colorshading denotes $\partial_t K_e$ ($\mathrm{m^2 s^{-3}}$), dashed (solid) magenta contours are $\partial_t A_{avg} \cos\phi < 0$ ($\partial_t A_{avg} \cos\phi > 0$). LWA pockets are represented by green contours, while the solid black contours are the dynamical tropopauses. Bottom panels are as in Figure 5.1 for each time step

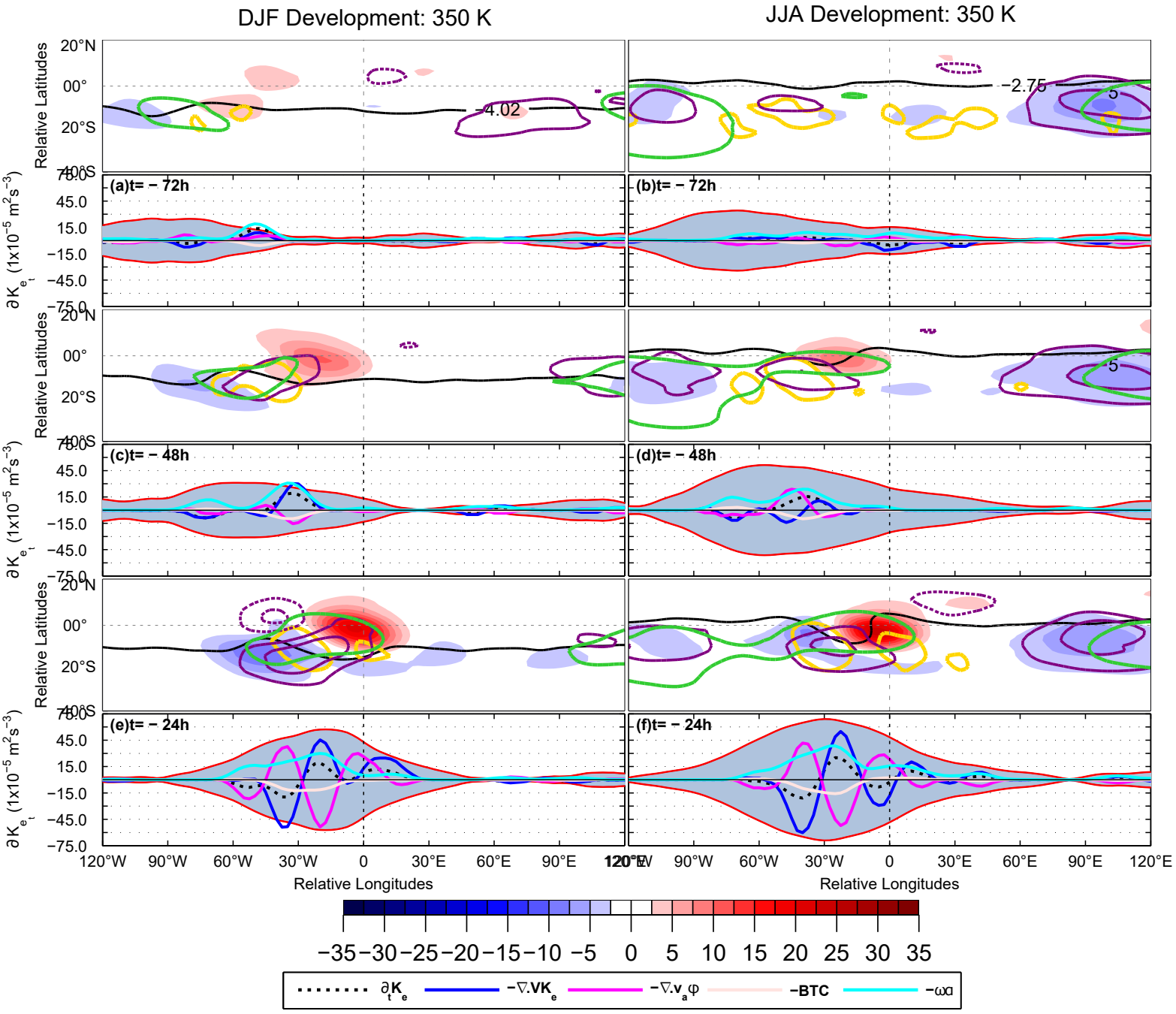

Figure 5.11: Development stage of Summer (left panels) and winter (right panels) time-lagged composite mean evolution of $K_e = 96$ (summer) and 104 (winter) $\mathrm{m^2 s^{-2}}$. The colorshading denotes $T_{c_{avg}}$, while dashed (solid) purple contours are $T_{n_{avg}} < 0$ and $T_{n_{avg}} > 0$. The rest of the features are as in previous plots.

The term T_c is not associated with LWA generation due to its conservation property, meaning that T_n should be the main LWA generator. Therefore, since the subtropical $T_{c_{avg}} > 0$ feature has no accompanying $T_{c_{avg}} < 0$ structure, it can only mean that this particular LWA source is associated with vertical propagation/advection. This is consistent with the fact that LWA in primitive isentropic coordinates accounts for vertical wave activity propagation embedded within the conservative term (Ghinassi et al., 2020). The orientation of the advection pattern shown by $\partial_t A_{avg} \cos\phi < 0$ - $\partial_t A_{avg} \cos\phi > 0$ is tilted in a southwest-northeast manner so that the propagation of the pre-existing LWA pocket is in a northeastward direction, this is better elucidated in Figure 5.9(b). Therefore, this pattern suggests that there might be a lower tropospheric subtropical LWA contribution that combines with the extratropical pre-existing disturbance during early development of the summertime RWP. Regarding the winter situation, the extratropical contribution is non-existent, so it also benefits from vertical LWA injection at the dynamical tropopause as seen at t = -48 h. Nevertheless, the vertical LWA injection appears to be consistent with the observed $-\omega\alpha > 0$ since both processes are associated with vertical advection.

Although $T_{n_{avg}}$ is generally smaller than $T_{c_{avg}}$ during the early stages of the development, it largely acts unopposed as a sink over the upstream subtropical part of the RWP, while $T_{c_{avg}}$ does so over the extratropical domain poleward of the dynamical tropopause during summer at t = -24 h. Interestingly, $T_{n_{avg}}$ appears to be closely related to the amplifying ridge during this time for both seasons. To the extent that moist and thermodynamic processes are well represented by this term, there appears to be consistency with the results reported by Teubler and Riemer (2020), who found that latent heat release is associated with ridge amplification. The spatial structures presented here are, however, filtered in the same manner as the LWA field to give an overall impression of the LWA pocket, therefore it is difficult to associate processes represented by the filtered LWA budget terms to individual disturbances. The only caveat could be during the case where a tendency signal is localised within one disturbance, in which case it would come out as the dominant term over that particular disturbance. The role of $T_{c_{avg}}$ at this time is to propel the LWA pocket

across the dynamical tropopause and into the subtropical domain in a northeastward direction. At this time however, this propagation is slightly balanced by $T_{n_{avg}} > 0$ at the trailing edge of the southwest-northeast tilted LWA pocket.

The spatial relationship between the K_e centres and LWA appears to be diminishing from t = -24 h as the PV contours become increasingly non-linear during their deformation on the equatorward side (along) of the dynamical tropopause during summer (winter). K_e centres are a maximum (minimum) when waves are linear (non-linear) due to maximisation of v' along the flanks of disturbances. It is therefore evident that for non-linear RWPs, processes taking place during the non-linear stages are not well represented by the K_e framework, as shown in previous studies (e.g. Magnusdottir and Haynes, 1996; Danielson et al., 2006), and as argued by Ghinassi et al. (2018). For example, if the LWA contours were not superimposed and only K_e was superimposed on the PV field, it would be difficult to interpret the evolution, since the K_e centres are shown to be approximately zonally oriented. Recalling that linear wave theory assumes that $\overline{u} >> u'$, it could be argued that K_e implicitly assumes linear wave theory, in that its definition $K_e = (u'.u' + v'.v')/2$ does not have a contribution from $\overline{u}$ and $\overline{v}$, when K_e is examined in isolation, away from other energy forms involved in the Lorenz energy cycle (Holton and Hakim, 2014).

On the other hand, LWA can be fixated on the non-linear processes as seen at t = 0 h (Figure 5.13 (a) and (b)) during summer, while K_e centres continue to propagate eastward. The onset of the decay phase is marked by an increased $T_{n_{avg}}$ and $T_{c_{avg}}$ sink at the subtropical trailing edge of the RWP, while the extratropical $T_{n_{avg}}$ source decays. As RWB takes place during this time, it makes sense that $T_{n_{avg}} < 0$ would be amplified as RWB is a dissipative, non-conservative process. This implies that PV mixing by the eddies is at play. This analysis therefore confirms that the point of departure between the two diagnostics is during the onset of non-linearity. It therefore follows that at the very least, the combination of the K_e and LWA approaches to studying RWP is likely more superior to considering only one of the two, as recommended by Magnusdottir and Haynes (1996).

Specifically, K_e (LWA) would serve the role of elucidating linear (non-linear) propagation and growth aspects of RWP evolutions, both of which are important steps in baroclinic life cycles (see, e.g., Thorncroft et al., 1993; Magnusdottir and Haynes, 1996).

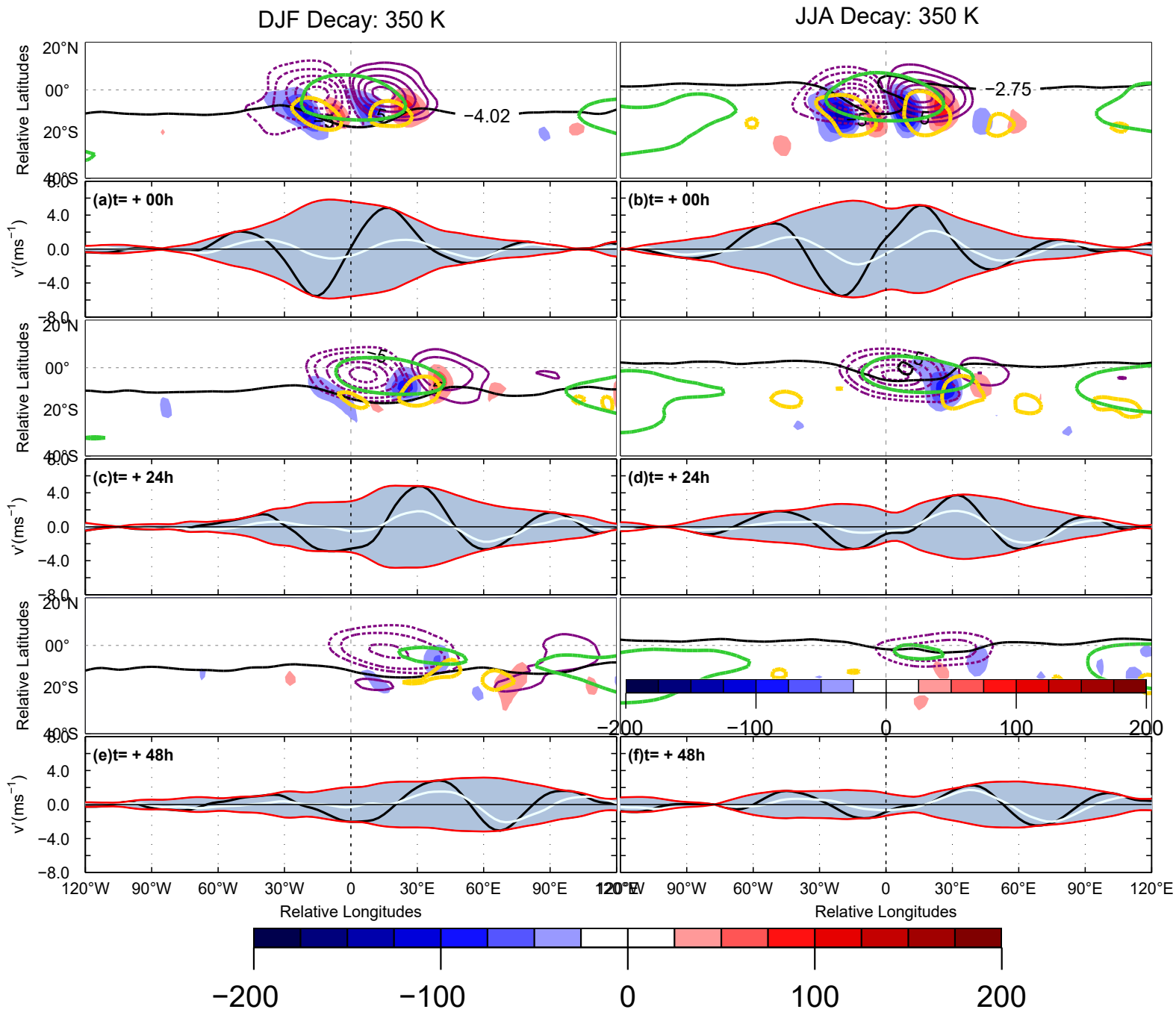

Figure 5.12: As in Figure 5.10, but for the decay stage.

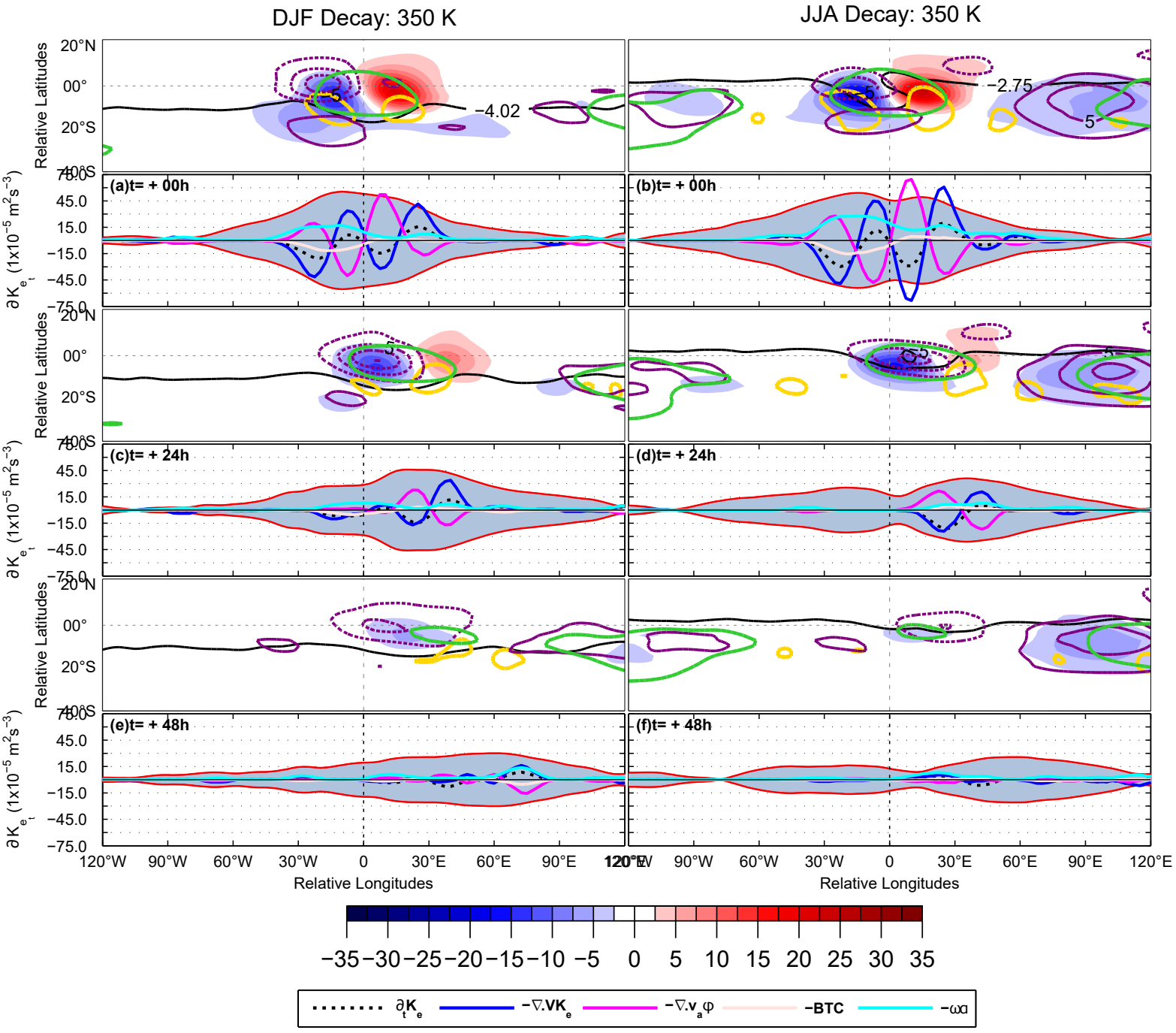

Figure 5.13: As in Figure 5.11, but for the decay stage.

5.3 Chapter Synopsis

This chapter investigated the evolutionary characteristics of tracked LWA RWP objects that matured over the Sa domain by means of composite analysis. First, the spatial distributions of LWA, PV, v'_θ and $\overline{u}$ were compared during the evolution to establish the

connection between these fields. Visual comparisons during the 6 day evolution of the summer and winter time LWA RWP objects showed that the identified LWA objects do indeed represent RWP-like features on the 330 K and 350 K surfaces. During the first three days of the 6 day evolutionary period, an initial disturbance propagates in a north east direction toward the extratropical jet stream as it increases in amplitude the closer it gets to the jet stream. The increase in amplitude is accompanied by a marked increase in the LWA field, upon which distinct closed contours develop to mark the center of the incipient disturbance exhibiting an RWP structure. By t = 0 h the LWA object reaches saturation as signalled by a decrease in A_{max} during subsequent steps, while PV contours are irreversibly deformed to elucidate the onset of RWB during t = 0 h. Since the occurrence of RWB denotes the onset of the decaying stage of RWPs in their life cycles, it is clear that the tracked LWA objects are representative of RWPs at finite amplitudes. The evolution of LWA during summertime on 350 K is slightly made complicated, and perhaps interesting by the presence of the climatological LWA H_3 hotspot. The north east propagation of the incipient LWA appears to be influenced by a contribution of LWA emanating from H_3 in a south east direction. Upon converging, these two structures of LWA appear to act in unison to form a coherent LWA RWP object.

This discussion is purely based on the morphology of PV and v'_θ contours, and so it is important to investigate whether the LWA objects not only look like RWPs, but the behave like them. This then leads to the examination of the dynamical characteristics of the tracked LWA objects by means of the LWA budget equation. Results revealed that conservative processes (T_c) tend to dominate over non-conservative (T_n) during the development stages of the RWP life cycle, while the contribution of T_n tends to become comparable to that of T_c during the decay/termination phases. The K_e of the RWPs was also explored, and results indicate that the evolution of the RWPs can be explained by the paradigm of DBD. The development stage is initially dominated by the baroclinic conversion term ($-\omega\alpha$) to give rise to an incipient K_e center. The EKE associated with this center is then radiated to the downstream/leading edge of the LWA RWP object by means

of the convergence of ageostrophic geopotential fluxes to facilitate the development of a secondary/downstream K_e center. When taken together, the above analysis confirms that the tracked LWA objects look and indeed behave like typical RWPs in the upper troposphere. The last aspect of this chapter involved the comparison of the K_e framework with the LWA framework to establish the extent to which these two approaches are comparable. It was found that the K_e and associated budget equation better elucidated the dynamical aspects of the development stage, particularly over the linear portion of the higher latitude portion of the RWP. This diagnostic failed to capture the RWB and key aspects associated with the maturity of LWA RWPs. In contrast, LWA and the associated budget better represented the mature stage of the LWA RWP object, while the earlier stages were not well represented. This state of affairs suggests that a combination of the two approaches is likely a better approach.

Chapter 6

Concluding Remarks

RWPs are known entities in the atmosphere that can drive regional weather phenomena, particularly over mid-latitudes (e.g., Wirth et al., 2018). In light of this, the present study sought to assess the extent of applicability and relevance of this statement over, and for the South African (SA) domain defined in this study as the region: (0° - 45°E; 22°S - 45°S). To this end, the NCEP reanalysis II dataset in conjunction with a filtered local finite-amplitude wave activity (LWA, Ghinassi et al., 2018) diagnostic was used to establish a 40-year (1979-2019) climatology of RWPs over the SA domain. This diagnostic was found suitable here as opposed to more commonly used diagnostics such as eddy kinetic energy (K_e) because central to the investigation were those RWPs exhibiting non-linear behaviour because the complete life cycle of baroclinic Rossby waves entails Rossby wave breaking (RWB) at its most mature stage (Thorncroft et al., 1993). A contour tracking algorithm was applied to the resultant filtered LWA (A) field to identify individual LWA pockets represented as closed countors, and presumed to represent RWPs as seen in Ghinassi (2019).

6.1 Climatological aspects of RWPs

Before evaluating the results of the tracking algorithm, the seasonal spatial distributions of LWA ($\overline{A}$) on the 330 K and 350 K surfaces were examined, $\overline{A}$ on 330 K was compared

with recent wave activity climatologies (i.e, Souders et al., 2014b; Ghinassi, 2020) to address the first objective of the study (to create a climatology of LWA and RWPs over the Southern Hemisphere (SH)) in Chapter 4. The results showed consistency between results presented in Ghinassi (2019), however this was not the case for Souders et al. (2014b), but consistency with the jet stream was shown. The apparent mismatches in the spatial distributions of wave activity was attributed to the almost linear nature of the meridional wind-based envelopes (Zimin et al., 2003), while LWA is sensitive to non-linearity. This means that where wave activity at 300 hPa in Souders et al. (2014b) is a maximum, it is likely that LWA is not so because non-linearity sets in much later than the linear maturity in the life cycle of baroclinic eddies (Thorncroft et al., 1993) and downstream of the location of linear maturity. This then suggested that the spatial distribution of wave activity is closely related to the Southern Hemisphere storm tracks, while $\overline{A}$ hotspots (regions of pronounced LWA) should be comparable to RWB hotspots. In general, $\overline{A}$ was found to be collocated with the jet streams throughout the year, suggesting that jet streams may have an influence on the behaviour of LWA.

In the $\overline{A}$ field on 350 K, subtropical LWA hotspots collocated with the SH convergence zones (South Pacific (SPCZ) and South Atlantic Convergence Zones (SACZ)) were identified during summer. Of interest in the present study is the SACZ, due to its close proximity to the SA domain, and an apparent LWA trail extending from the $\overline{A}$ hotspot (H_3) coincident with the SACZ and into the SA domain. It was hypothesised that this trail of wave activity may be indicative of a path of wave activity that spills over into the SA domain and possibly affecting weather processes there. Having established that our LWA calculations sufficiently reflected the known features of the Southern Hemisphere, the results of the LWA feature tracking were also presented in Chapter 4 before the examination of LWA pocket attributes and climatological characteristics. It was found that the classic "intuitive" meridionally averaged view of a baroclinic RWP (as in Figure 9 in Wirth et al. (2018)) was well reproduced by the meridional wind anomaly (v') at upper and lower levels (v'_{200} and v'_{850}, respectively) of the atmosphere during the most mature

stage in the evolution of composite mean LWA pockets on the 330 K and 350 K isentropic surfaces. Moreover, it was confirmed that LWA was able to identify RWPs that have non-linear characteristics because during LWA maturity, PV contours on both isentropic surfaces demonstrated that RWB was at play.

A total of 19680 (14979) RWP objects were identified over the SH on 330 K (350 K) using our LWA object tracking algorithm, where 1378 (1192) of the events belonged to the SA domain. Interpreted as RWPs, LWA pockets were found to occur at a rate of 492 (374) per year on 330 K (350 K) over the SH, while over the SA domain they only appeared at a rate of 35 (30) RWPs per year. On the seasonal time scale, the counts of LWA pockets were found to exhibit no distinct trends, as there is high variability between seasons, and when the counts on isentropes are compared. This was attributed to the fact that the overall tracks may consist of a combination of RWB and some storm track-related large-amplitude eddies. The spatiotemporal distribution of tracked LWA pockets/objects counts and maximum amplitude/intensity (A_{max}) closely resembles that of $\overline{A}$, confirming that $\overline{A}$ can in general be seen as an actual representation of LWA RWPs as previously insinuated by Ghinassi (2020) on both isentropic surfaces over the Southern Hemisphere. The connection between tracked LWA pockets and RWB climatologies (e.g. Ndarana and Waugh, 2011) was confirmed and also extended to cut-off low pressure systems by visual comparison (e.g. Ndarana and Waugh, 2010; Pinheiro et al., 2017; Barnes et al., 2021). Having established that LWA pockets are representative of well-known entities in the Southern Hemisphere, more details of the climatological attributes of RWPs over the smaller SA domain were presented in Chapter 4.5 to address the second objective of the study, which was to produce a climatology of RWPs maturing over the SA domain.

As a prerequisite to this presentation, the seasonal variability of potential vorticity values estimating the dynamical tropopause based on the PV gradient method outlined by Kunz et al. (2011) was presented to facilitate follow-up discussions. This calculation was done for all the cases of identified LWA pockets over the SA domain by means of simple

composite analysis. This step was taken because the dynamical tropopause is an important interface between the lower stratosphere and upper troposphere, implying that undulations in such a material contour would represent the exchange of distinctly different air masses that may eventually affect surface conditions. As important as the dynamical tropopause is, it is usually assumed to be estimated by the PV = -2 PVU isoline, but studies have shown that the PV value of the dynamical tropopause exhibits high variability (e.g, Kunz et al., 2011; Martius et al., 2007). Since the dynamical tropopause or any PV contour was not explicitly defined in the tracking algorithm, we deemed it important to attempt to accurately represent the location of the dynamical tropopause so that we may be able to interpret the vertical structure and orientation of LWA based RWPs during their evolution. A comparison between PV = -2 PVU and an estimated dynamical tropopause PV isoline (PV = PV^{TP}) suggested that during summer, PV = -2 PVU may not be a good representation of the dynamical tropopause, whereas PV^{TP} was found to be close to the jet stream, suggesting that it is a relatively better estimate.

The climatological characteristics of LWA RWPs over the SA domain was shown by maps of seasonal counts of identified LWA pocket objects. While RWP occurrences were found to be widespread throughout the year and region, some preferred regions of maturity (hotspots) were identified. Several of such hotspots were identified over the subtropical area (22°S - 35°S) of the SA domain on 330 K particularly between summer and autumn months, while no such features were evident on the 350 K isentrope. These were presumed to be related to surface processes such as convection and the influence of topography. However, the majority of events were found over the extratropical area (35°S - 45°S) of the SA domain on both isentropic surfaces as expected due to the proximity of this region to the area of the domain to the extratropical jet stream. Over this region, an increase in RWP occurrences was observed during the transition seasons on both surfaces, while summer months were associated with a decrease in RWP events. In contrast, a notable RWP event hotspot was identified southwest of SA on 330 K during winter, while it only appeared faintly on 350 K.

Some attributes of SA domain LWA pockets were also examined, and also revealed the high variability when the characteristics are compared between the 330 K and 350 K isentropes. These included the maximum intensity of mature LWA pockets (A_{max}), the duration (days) of LWA pocket events, the distance travelled (km) by the LWA pockets, and the propagation speed of the LWA pocket centres interpreted as the RWP group speed of (ms^{-1}) here. The comparison between the spatial distribution of RWP counts over the SA domain and each of the RWP attributes considered revealed a general collocation of maxima in RWP occurrences and the corresponding maxima in attributes on 330 K and 350 K isentropic surfaces. A_{max} was found to be in the 90-108 ms^{-1} range on 330 K during the transition seasons, while very low values were observed on 350 K throughout the year. The longest lasting RWPs were identified on 350 K during spring with life spans of up to 4 days, a day longer than the corresponding maximum on 330 K. It is only during summer on both surfaces do RWPs have a maximum life span of less than 3 days.

Lastly, group speeds (4-16 ms^{-1}) were found to be generally slower than the jet stream on both surfaces because the detected LWA pockets were already in their non-linear stage. The South Atlantic Ocean (SAO) region adjacent to the continent of SA was found to be associated with zones of frequent RWP development that eventually mature over the SA domain on both surfaces. RWPs maturing over the SA domain were tracked in space and time and were found to have origins in the subtropical and extratropical regions of the SAO throughout the year on both surfaces. However, there appeared to be an average northwest to southeast preferred direction from the subtropics into the SA domain on 330 K (except for summer), while a more eastward and northeastward propagation tendency was observed on 350 K between autumn and spring. On 330 K, however, there exists a local LWA pocket development spot over the border of Namibia and South Africa that acts as a source for RWPs that propagate across SA and mature over the Mozambique channel east of the land during summer. When the climatological attributes of RWPs are combined together, it makes the case for the careful consideration of RWP hotspots in the context of extreme weather over the SA domain.

For example, the collocation of long-lived and intense LWA RWPS could signal a severe weather situation because LWA RWPs are associated with RWB. RWB has previously been associated with CoLs (Ndarana and Waugh, 2010), meaning that if the observed LWA RWPs conform to the life cycle-1 (LC-1) regime of Thorncroft et al. (1993), they can be interpreted as CoLs over the SA domain. This association is particularly important in the context of SA, because CoLs have in recent times been responsible for flooding events over the south eastern coast of South Africa. A more recent example of such an occurrence is the devastating floods over the province of Kwa Zulu-Natal, which was associated with a CoL event that persisted for about 3 days on 11-13 April 2022. Our results therefore emphasise that the ability to predict autumn and spring RWPs over the SA domain, on the medium-range forecasting time scale of RWPs, is an issue of the utmost importance due to their climatological characteristics.

6.2 Evolutionary characteristics

The preceding discussion is based on the climatology of RWPs over the SA domain is based only on the morphological structure of the LWA field and the corresponding PV and v' fields. Beyond the fact that the tracked LWA pockets exhibited the expected structure of a mature RWP in Chapter 4, the dynamics of these tracked objects were deemed important to ensure that all aspects of upper tropospheric extratropical RWPs were satisfied. To this end, Chapter 5 elucidated the time-lagged composite mean evolutionary characteristics of the LWA (A) and corresponding PV, $\overline{u_\theta}$, v'_θ, as well as meridionally averaged v'_{850} and v'_{200} fields for RWPs maturing over the SA domain on 330 K and 350 K isentropic surfaces in line with the third objective of the study. In the early stages of the development, the summer and winter spatial distribution of A resembles the summer and winter climatology of LWA (A) on both isentropic surfaces. An incipient extratropical RWP characterised by a ridge-trough couplet was found to propagate in a northeastward direction toward the dy-

namical tropopause and the jet stream during summer and winter seasons. This baroclinic RWP becomes tilted in a northwest-southeast manner as it enters and propagates along the barotropic shear environment of the jet stream.

At the point of LWA pocket maturity (t = 0 hours (h)), RWB signatures became prevalent, as signified by the reversal deformation of PV contours, to mark the maturity of the RWP. Subsequently, the RWP structure disintegrates to mark the decay phase in the evolution. The observed sequence of events are consistent with aspects of the stages in the life-cycle of baroclinic Rossby waves based on Thorncroft et al. (1993). Specifically, stages 1-3 are reflected during the period t = -48h to 0h of the evolution of the LWA pocket. Subsequently, stage 4 is associated with a marked weakening of the RWP amplitudes. A possible subtropical contribution emanating from the climatological H_3 hotspot presumably associated with the SACZ is also evident on 350 K, therefore corroborating our hypothesis that this climatological feature may play a role in the development of RWPs over the SA domain. However, the extent of this contribution was not examined in the present study.

The essence of upper tropospheric RWPs is their ability to transfer eddy kinetic energy (K_e) to downstream areas as they propagate eastward, through downstream baroclinic development (Orlanski and Sheldon, 1995). To establish whether the downstream development paradigm can explain the evolution of finite-amplitude RWPs maturing over the SA domain, in line with the fourth study objective, the eddy kinetic energy equation was used. Using the vertically averaged eddy kinetic energy framework, we found that this process is the main mechanism governing the evolution of RWPs over the SA domain. Specifically, baroclinic conversion was found to be responsible for the early growth of an upstream K_e centre. At later time steps, this K_e centre begins to lose energy towards its downstream region, leading to the development of a new K_e. This new development is facilitated by the divergence (convergence) of ageostrophic geopotential fluxes from (toward) the upstream (downstream) K_e centre. The contribution of the barotropic conversion term

to the tendency of K_e centres was found to be consistently negative throughout evolution, implying that this term acts as a sink of K_e. In general, these findings are consistent with previous studies (e.g. Orlanski and Sheldon, 1995; Gan and Piva, 2013; Gan and Piva, 2015; Ndarana et al., 2021; Pinheiro et al., 2022). Wintertime K_e centres were also found to be much stronger than those during summer months, and this was attributed to the pronounced amplitude of linear RWPs during this season over the storm tracks as observed in Souders et al. (2014b).

The last objective of the study involved a comparison between the LWA and K_e framework, as it has been suggested before that a combination of diagnostics should better explain the dynamical aspects of Rossby wave life cycles (e.g, Magnusdottir and Haynes, 1996; Danielson et al., 2006). This was found to be the case in this study, where it was seen that layer averaged A_{avg} (K_e) diagnostics tend to be sensitive to non-linear (linear) behaviour and aspects of the RWP evolution. Therefore, this suggests that it may be beneficial to utilise these two diagnostics in tandem when the full extent of the dynamics of RWPs is of interest. Therefore, the results in Chapter 5 confirm that the identified LWA pockets are indeed RWPs that conform to the classical model of an RWP as outlined in Wirth et al. (2018). These findings have potential implications for the predictability of severe weather phenomena over the SA domain and may facilitate the development of early warning systems. For example, a forecasting framework that incorporates the paradigm of downstream baroclinic development would essentially look for baroclinic conversion and the convergence of ageostrophic geopotential fluxes in forecasting data.

This implies that when this process is better represented by numerical weather prediction models (NWP) in medium-range forecasting data, there is potential to improve early signals of potentially severe weather associated with a downstream developing K_e. This is particularly relevant in the context of our study because Ndarana et al. (2021) showed that the development of CoLs is associated with a slightly different signature of downstream baroclinic development compared to our findings. The only difference is the

fact that the downstream K_e centre develops northeast of the upstream K_e centre, while for the general RWPs presented here the relative orientation of the K_e centres is more zonal.

RWPs were only identified on 330 K and 350 K isentropic surfaces, and only the dynamics of the latter were examined. This has limited our study to a more horizontal interpretation of the evolution of RWPs over the SA domain. This has effectively hampered our ability to closely and quantitatively compare our findings with the known stages of baroclinic life cycles (Thorncroft et al., 1993). Furthermore, the budget of the employed LWA formulation (Ghinassi et al., 2020) is not exactly conserved on the sphere (Ghinassi et al., 2020). This has hindered the representation of the tendency of LWA in terms of the divergence of a flux such as the Eliassen Palm (EP) flux, which is a very important tool in the description of Rossby wave activity propagation.

Results of the tracking algorithm suggest that LWA pockets become visible in reanalysis datasets during the non-linear stage of development. This has resulted in very close starting and ending positions of tracked LWA pockets, which made it difficult to compare our results with existing climatologies that were relatively more sensitive to linear stages of development. In light of this, future work will explore how previous finite-amplitude wave activity and K_e diagnostics can be combined to form a more coherent picture of RWP dynamics over the SA domain by leveraging strengths of each, and testing the limits of their applicability over the SA domain and adjacent oceans. This is to be done with the intention of developing predictability tools and early warning systems for severe weather over the SA domain.

References

Allen, D. R., & Nakamura, N. (2003). Tracer equivalent latitude: A diagnostic tool for isentropic transport studies. *Journal of the atmospheric sciences*, *60*(2), 287–304.

Ambaum, M. H., & Novak, L. (2014). A nonlinear oscillator describing storm track variability. *Quarterly Journal of the Royal Meteorological Society*, *140*(685), 2680–2684.

Ambrizzi, T., Hoskins, B. J., & Hsu, H.-H. (1995). Rossby wave propagation and teleconnection patterns in the austral winter. *Journal of Atmospheric Sciences*, *52*(21), 3661–3672.

Andrews, D., & McIntyre, M. (1978). Generalized eliassen-palm and charney-drazin theorems for waves on axismmetric mean flows in compressible atmospheres. *Journal of Atmospheric Sciences*, *35*(2), 175–185.

Andrews, D., & Mcintyre, M. E. (1976). Planetary waves in horizontal and vertical shear: The generalized eliassen-palm relation and the mean zonal acceleration. *Journal of Atmospheric Sciences*, *33*(11), 2031–2048.

Añel, J. A., Allen, D. R., Sáenz, G., Gimeno, L., & de la Torre, L. (2013). Equivalent latitude computation using regions of interest (roi). *Plos one*, *8*(9), e72970.

Bals-Elsholz, T. M., Atallah, E. H., Bosart, L. F., Wasula, T. A., Cempa, M. J., & Lupo, A. R. (2001). The wintertime southern hemisphere split jet: Structure, variability, and evolution. *Journal of climate*, *14*(21), 4191–4215.

Barnes, E. A., & Hartmann, D. L. (2012). Detection of rossby wave breaking and its response to shifts of the midlatitude jet with climate change. *Journal of Geophysical Research: Atmospheres*, *117*(D9).

Barnes, M. A., Ndarana, T., & Landman, W. A. (2021). Cut-off lows in the southern hemisphere and their extension to the surface. *Climate Dynamics*, *56*(11), 3709–3732.

Barros, V., Gonzalez, M., Liebmann, B., & Camilloni, I. (2000). Influence of the south atlantic convergence zone and southatlantic sea surface temperature on interannual summerrainfall variability in southeastern south america. *Theoretical and Applied Climatology*, *67*(3), 123–133.

Barroso Pellico, J. Á. (2017). Analysis of tropopause variability in observations and in an idealized model.

Berbery, E. H., Nogués-Paegle, J., & Horel, J. D. (1992). Wavelike southern hemisphere extratropical teleconnections. *Journal of the atmospheric sciences*, *49*(2), 155–177.

Berbery, E. H., & Vera, C. S. (1996). Characteristics of the southern hemisphere winter storm track with filtered and unfiltered data. *Journal of the Atmospheric Sciences*, *53*(3), 468–481.

Berrisford, P., Hoskins, B., & Tyrlis, E. (2007). Blocking and rossby wave breaking on the dynamical tropopause in the southern hemisphere. *Journal of the Atmospheric Sciences*, *64*(8), 2881–2898.

Berrisford, P., Marshall, J., & White, A. (1993). Quasigeostrophic potential vorticity in isentropic coordinates. *Journal of Atmospheric Sciences*, *50*(5), 778–782.

Branstator, G. (2002). Circumglobal teleconnections, the jet stream waveguide, and the north atlantic oscillation. *Journal of Climate*, *15*(14), 1893–1910.

Carvalho, L. M., Jones, C., & Liebmann, B. (2004). The south atlantic convergence zone: Intensity, form, persistence, and relationships with intraseasonal to interannual activity and extreme rainfall. *Journal of Climate*, *17*(1), 88–108.

Chang, E. K. (1993). Downstream development of baroclinic waves as inferred from regression analysis. *Journal of Atmospheric Sciences*, *50*(13), 2038–2053.

Chang, E. K. (2000). Wave packets and life cycles of troughs in the upper troposphere: Examples from the southern hemisphere summer season of 1984/85. *Monthly Weather Review*, *128*(1), 25–50.

Chang, E. K., & Orlanski, I. (1994). On energy flux and group velocity of waves in baroclinic flows. *Journal of the atmospheric sciences*, *51*(24), 3823–3828.

Charney, J. (1947). The dynamics of long waves in a baroclinic. *Westerly Current, J. Meteorol*, *4*.

Charney, J. G., & Drazin, P. G. (1961). Propagation of planetary-scale disturbances from the lower into the upper atmosphere. *Journal of Geophysical Research*, *66*, 83-109.

Charney, J. G., & Stern, M. E. (1962). On the stability of internal baroclinic jets in a rotating atmosphere. *Journal of the Atmospheric Sciences*, *19*(2), 159–172.

Danielson, R. E., Gyakum, J. R., & Straub, D. N. (2006). A case study of downstream baroclinic development over the north pacific ocean. part ii: Diagnoses of eddy energy and wave activity. *Monthly weather review*, *134*(5), 1549–1567.

Davis, C. A. (1992). Piecewise potential vorticity inversion. *Journal of the atmospheric sciences*, *49*(16), 1397–1411.

Decker, S. G., & Martin, J. E. (2005). A local energetics analysis of the life cycle differences between consecutive, explosively deepening, continental cyclones. *Monthly weather review*, *133*(1), 295–316.

Dee, D. P., Uppala, S. M., Simmons, A. J., Berrisford, P., Poli, P., Kobayashi, S., ... others (2011). The era-interim reanalysis: Configuration and performance of the data assimilation system. *Quarterly Journal of the royal meteorological society*, *137*(656), 553–597.

de F. Forster, P. M., & Shine, K. P. (1997). Radiative forcing and temperature trends from stratospheric ozone changes. *Journal of Geophysical Research: Atmospheres*, *102*(D9), 10841–10855.

De Vries, A. J. (2021). A global climatological perspective on the importance of rossby wave breaking and intense moisture transport for extreme precipitation events. *Weather and Climate Dynamics*, *2*(1), 129–161.

Dritschel, D., & McIntyre, M. (2008). Multiple jets as pv staircases: The phillips effect and the resilience of eddy-transport barriers. *Journal of the Atmospheric Sciences*, *65*(3), 855–874.

Eady, E. T. (1949). Long waves and cyclone waves. *Tellus*, *1*(3), 33–52.

Edmon Jr, H., Hoskins, B., & McIntyre, M. (1980). Eliassen-palm cross sections for the troposphere. *Journal of Atmospheric Sciences*, *37*(12), 2600–2616.

Eliassen, A. (1960). On the transfer of energy in stationary mountain waves. *Geophy. Publ.*, *22*, 1–23.

Engelbrecht, C. J., Landman, W. A., Engelbrecht, F. A., & Malherbe, J. (2015). A synoptic decomposition of rainfall over the cape south coast of south africa. *Climate Dynamics*, *44*(9), 2589–2607.

Ertel, H. (1942a). Ein neuer hydrodynamischer erhaltungssatz. *Naturwissenschaften*, *30*(36), 543–544.

Ertel, H. (1942b). Ein neuer hydrodynamischer wirbelsatz. *Met. Z.*, *59*, 277–281.

Favre, A., Hewitson, B., Lennard, C., Cerezo-Mota, R., & Tadross, M. (2013). Cut-off lows in the south africa region and their contribution to precipitation. *Climate dynamics*, *41*(9), 2331–2351.

Fragkoulidis, G., & Wirth, V. (2020). Local rossby wave packet amplitude, phase speed, and group velocity: Seasonal variability and their role in temperature extremes. *Journal of Climate*, *33*(20), 8767–8787.

Fuenzalida, H. A., Sánchez, R., & Garreaud, R. D. (2005). A climatology of cutoff lows in the southern hemisphere. *Journal of Geophysical Research: Atmospheres*, *110*(D18).

Gabriel, A., & Peters, D. (2008). A diagnostic study of different types of rossby wave breaking events in the northern extratropics. *Journal of the Meteorological Society of Japan. Ser. II*, *86*(5), 613–631.

Gallego, D., Ribera, P., Garcia-Herrera, R., Hernandez, E., & Gimeno, L. (2005). A new look for the southern hemisphere jet stream. *Climate Dynamics*, *24*(6), 607–621.

Gan, M. A., & Dal Piva, E. (2013). Energetics of a southeastern pacific cut-off low. *Atmospheric Science Letters*, *14*(4), 272–280.

Gan, M. A., & Piva, E. D. (2016). Energetics of southeastern pacific cut-off lows. *Climate Dynamics*, *46*(11), 3453–3462.

Ghinassi, P. (2019). *Investigating the dynamics of rossby wave packets using local finite*

amplitude wave activity (Unpublished doctoral dissertation). Johannes Gutenberg-Universität Mainz.

Ghinassi, P., Fragkoulidis, G., & Wirth, V. (2018). Local finite-amplitude wave activity as a diagnostic for rossby wave packets. *Monthly Weather Review*, *146*(12), 4099–4114.

Gill, T. (2009). *Initial steps in the development of a comprehensive lightning climatology of south africa* (Unpublished doctoral dissertation). University of the Witwatersrand.

Glatt, I., Dornbrack, A., Jones, S., Keller, J., Martius, O., Muller, A., ... Wirth, V. (2011). Utility of hovmöller diagrams to diagnose rossby wave trains. *Tellus A: Dynamic Meteorology and Oceanography*, *63*(5), 991–1006.

Grimm, A. M., & Reason, C. (2015). Intraseasonal teleconnections between south america and south africa. *Journal of Climate*, *28*(23), 9489–9497.

Harris, F. J. (1978). On the use of windows for harmonic analysis with the discrete fourier transform. *Proceedings of the IEEE*, *66*(1), 51–83.

Hart, N., Reason, C., & Fauchereau, N. (2010). Tropical–extratropical interactions over southern africa: Three cases of heavy summer season rainfall. *Monthly weather review*, *138*(7), 2608–2623.

Hart, N. C., Reason, C. J., & Fauchereau, N. (2012). Building a tropical–extratropical cloud band metbot. *Monthly weather review*, *140*(12), 4005–4016.

Hart, N. C., Reason, C. J., & Fauchereau, N. (2013). Cloud bands over southern africa: Seasonality, contribution to rainfall variability and modulation by the mjo. *Climate dynamics*, *41*(5), 1199–1212.

Hartmann, D., Chan, K., Gary, B., Schoeberl, M., Newman, P. A., Martin, R. L., ... Strahan, S. (1989). Potential vorticity and mixing in the south polar vortex during spring. *Journal of Geophysical Research: Atmospheres*, *94*(D9), 11625–11640.

Haynes, P. H. (1988). Forced, dissipative generalizations of finite-amplitude wave-activity conservation relations for zonal and nonzonal basic flows. *Journal of Atmospheric Sciences*, *45*(16), 2352–2362.

Hitchman, M. H., & Huesmann, A. S. (2007). A seasonal climatology of rossby wave breaking in the 320–2000-k layer. *Journal of the Atmospheric sciences*, *64*(6), 1922–

1940.

Hodges, K. I. (1994). A general method for tracking analysis and its application to meteorological data. *Monthly Weather Review*, *122*(11), 2573–2586.

Holton, J., & Hakim, G. (2014). *An introduction to dynamic meteorology. 5th 566 ed.* Elsevier Academic Press.

Holton, J. R., Haynes, P. H., McIntyre, M. E., Douglass, A. R., Rood, R. B., & Pfister, L. (1995). Stratosphere-troposphere exchange. *Reviews of geophysics*, *33*(4), 403–439.

Homeyer, C. R., & Bowman, K. P. (2013). Rossby wave breaking and transport between the tropics and extratropics above the subtropical jet. *Journal of the Atmospheric Sciences*, *70*(2), 607–626.

Hoskins, B. J. (1975). The geostrophic momentum approximation and the semi-geostrophic equations. *Journal of Atmospheric Sciences*, *32*(2), 233–242.

Hoskins, B. J. (1991). Towards a pv-θ view of the general circulation. *Tellus A: Dynamic Meteorology and Oceanography*, *43*(4), 27–36.

Hoskins, B. J., & Ambrizzi, T. (1993). Rossby wave propagation on a realistic longitudinally varying flow. *Journal of Atmospheric Sciences*, *50*(12), 1661–1671.

Hoskins, B. J., & Hodges, K. I. (2005). A new perspective on southern hemisphere storm tracks. *Journal of Climate*, *18*(20), 4108–4129.

Hoskins, B. J., McIntyre, M. E., & Robertson, A. W. (1985). On the use and significance of isentropic potential vorticity maps. *Quarterly Journal of the Royal Meteorological Society*, *111*(470), 877–946.

Hovmöller, E. (1949). The trough-and-ridge diagram. *Tellus*, *1*(2), 62–66.

Huang, C. S., & Nakamura, N. (2016). Local finite-amplitude wave activity as a diagnostic of anomalous weather events. *Journal of the Atmospheric Sciences*, *73*(1), 211–229.

Illari, L., Marshall, J., Bannon, P., Botella, J., Clark, R., Haine, T., ... others (2009). "weather in a tank"—exploiting laboratory experiments in the teaching of meteorology, oceanography, and climate. *Bulletin of the American Meteorological Society*, *90*(11), 1619–1632.

Ivanciu, I., Ndarana, T., Matthes, K., & Wahl, S. (2022). On the ridging of the south

atlantic anticyclone over south africa: The impact of rossby wave breaking and of climate change. *Geophysical Research Letters*, *49*(20), e2022GL099607.

Ivanova, A. (2013). The tropopause: Variety of definitions and modern approaches to identification. *Russian Meteorology and Hydrology*, *38*(12), 808–817.

Juckes, M., & McIntyre, M. (1987). A high-resolution one-layer model of breaking planetary waves in the stratosphere. *Nature*, *328*(6131), 590–596.

Kanamitsu, M., Ebisuzaki, W., Woollen, J., Yang, S.-K., Hnilo, J., Fiorino, M., & Potter, G. (2002). Ncep–doe amip-ii reanalysis (r-2). *Bulletin of the American Meteorological Society*, *83*(11), 1631–1644.

Killworth, P. D., & McINTYRE, M. E. (1985). Do rossby-wave critical layers absorb, reflect, or over-reflect? *Journal of Fluid Mechanics*, *161*, 449–492.

Kunz, A., Konopka, P., Müller, R., & Pan, L. (2011). Dynamical tropopause based on isentropic potential vorticity gradients. *Journal of Geophysical Research: Atmospheres*, *116*(D1).

Kunz, A., Sprenger, M., & Wernli, H. (2015). Climatology of potential vorticity streamers and associated isentropic transport pathways across pv gradient barriers. *Journal of Geophysical Research: Atmospheres*, *120*(9), 3802–3821.

Lackmann, G. (2011). Isentropic analysis. In *Midlatitude synoptic meteorology* (pp. 67–78). Springer.

Lee, S., & Kim, H.-k. (2003). The dynamical relationship between subtropical and eddy-driven jets. *Journal of the atmospheric sciences*, *60*(12), 1490–1503.

Liebmann, B., Kiladis, G. N., Marengo, J., Ambrizzi, T., & Glick, J. D. (1999). Submonthly convective variability over south america and the south atlantic convergence zone. *Journal of Climate*, *12*(7), 1877–1891.

Lin, Z. (2019). The south atlantic–south indian ocean pattern: A zonally oriented teleconnection along the southern hemisphere westerly jet in austral summer. *Atmosphere*, *10*(5), 259.

Liu, C., Ren, X., & Yang, X. (2014). Mean flow-storm track relationship and rossby wave breaking in two types of el-niño. *Advances in Atmospheric Sciences*, *31*(1), 197–210.

Liu, Y.-W. (2012). Hilbert transform and applications. *Fourier Transform Applications*, 291–300.

Lutjeharms, J. (2007). Three decades of research on the greater agulhas current. *Ocean Science*, *3*(1), 129–147.

Macron, C., Pohl, B., Richard, Y., & Bessafi, M. (2014). How do tropical temperate troughs form and develop over southern africa? *Journal of Climate*, *27*(4), 1633–1647.

Magnusdottir, G., & Haynes, P. H. (1996). Wave activity diagnostics applied to baroclinic wave life cycles. *Journal of the atmospheric sciences*, *53*(16), 2317–2353.

Martius, O., Schwierz, C., & Davies, H. (2007). Breaking waves at the tropopause in the wintertime northern hemisphere: Climatological analyses of the orientation and the theoretical lc1/2 classification. *Journal of the atmospheric sciences*, *64*(7), 2576–2592.

Martius, O., Schwierz, C., & Davies, H. (2008). Far-upstream precursors of heavy precipitation events on the alpine south-side. *Quarterly Journal of the Royal Meteorological Society: A journal of the atmospheric sciences, applied meteorology and physical oceanography*, *134*(631), 417–428.

Martius, O., Schwierz, C., & Davies, H. C. (2006). A refined hovmöller diagram. *Tellus A: Dynamic Meteorology and Oceanography*, *58*(2), 221–226.

McIntyre, M., & Palmer, T. (1984). The 'surf zone'in the stratosphere. *Journal of atmospheric and terrestrial physics*, *46*(9), 825–849.

McIntyre, M. E., & Shepherd, T. G. (1987). An exact local conservation theorem for finite-amplitude disturbances to non-parallel shear flows, with remarks on hamiltonian structure and on arnol'd's stability theorems. *Journal of Fluid Mechanics*, *181*, 527–565.

McLay, J. G., & Martin, J. E. (2002). Surface cyclolysis in the north pacific ocean. part iii: Composite local energetics of tropospheric-deep cyclone decay associated with rapid surface cyclolysis. *Monthly weather review*, *130*(10), 2507–2529.

Methven, J. (2013). Wave activity for large-amplitude disturbances described by the primitive equations on the sphere. *Journal of the atmospheric sciences*, *70*(6), 1616–

1630.

Mofor, L. A., & Lu, C. (2009). Generalized moist potential vorticity and its application in the analysis of atmospheric flows. *Progress in Natural Science*, *19*(3), 285–289.

Müller, G. V., Gan, M. A., Piva, E. D., & Silveira, V. P. (2015). Energetics of wave propagation leading to cold event in tropical latitudes of south america. *Climate Dynamics*, *45*(1), 1–20.

Nakamura, H., & Shimpo, A. (2004). Seasonal variations in the southern hemisphere storm tracks and jet streams as revealed in a reanalysis dataset. *Journal of Climate*, *17*(9), 1828–1844.

Nakamura, M. (1994). *Characteristics of potential vorticity mixing by breaking rossby waves in the vicinity of a jet* (Unpublished doctoral dissertation). Massachusetts Institute of Technology.

Nakamura, M., & Plumb, R. A. (1994). The effects of flow asymmetry on the direction of rossby wave breaking. *Journal of Atmospheric Sciences*, *51*(14), 2031–2045.

Nakamura, N., & Solomon, A. (2010). Finite-amplitude wave activity and mean flow adjustments in the atmospheric general circulation. part i: Quasigeostrophic theory and analysis. *Journal of the atmospheric sciences*, *67*(12), 3967–3983.

Nakamura, N., & Solomon, A. (2011). Finite-amplitude wave activity and mean flow adjustments in the atmospheric general circulation. part ii: Analysis in the isentropic coordinate. *Journal of the atmospheric sciences*, *68*(11), 2783–2799.

Nakamura, N., & Zhu, D. (2010). Finite-amplitude wave activity and diffusive flux of potential vorticity in eddy–mean flow interaction. *Journal of the Atmospheric Sciences*, *67*(9), 2701–2716.

Ndarana, T., Mpati, S., Bopape, M.-J., Engelbrecht, F., & Chikoore, H. (2021). The flow and moisture fluxes associated with ridging south atlantic ocean anticyclones during the subtropical southern african summer. *International Journal of Climatology*, *41*, E1000–E1017.

Ndarana, T., Rammopo, T. S., Reason, C. J., Bopape, M.-J., Engelbrecht, F., & Chikoore, H. (2022). Two types of ridging south atlantic ocean anticyclones over south africa

and the associated dynamical processes. *Atmospheric Research*, *265*, 105897.

Ndarana, T., & Waugh, D. W. (2010). The link between cut-off lows and rossby wave breaking in the southern hemisphere. *Quarterly Journal of the Royal Meteorological Society*, *136*(649), 869–885.

Ndarana, T., & Waugh, D. W. (2011). A climatology of rossby wave breaking on the southern hemisphere tropopause. *Journal of the Atmospheric Sciences*, *68*(4), 798–811.

Nishii, K., & Nakamura, H. (2004). Lower-stratospheric rossby wave trains in the southern hemisphere: A case-study for late winter of 1997. *Quarterly Journal of the Royal Meteorological Society*, *130*(596), 325–345.

Nishii, K., & Nakamura, H. (2005). Upward and downward injection of rossby wave activity across the tropopause: A new aspect of the troposphere–stratosphere dynamical linkage. *Quarterly Journal of the Royal Meteorological Society: A journal of the atmospheric sciences, applied meteorology and physical oceanography*, *131*(606), 545–564.

Novak, L., Ambaum, M. H., & Tailleux, R. (2015). The life cycle of the north atlantic storm track. *Journal of the Atmospheric Sciences*, *72*(2), 821–833.

O'Brien, L., & Reeder, M. J. (2017). Southern hemisphere summertime rossby waves and weather in the australian region. *Quarterly Journal of the Royal Meteorological Society*, *143*(707), 2374–2388.

Orlanski, I. (2003). Bifurcation in eddy life cycles: Implications for storm track variability. *Journal of the atmospheric sciences*, *60*(8), 993–1023.

Orlanski, I., & Chang, E. K. (1993). Ageostrophic geopotential fluxes in downstream and upstream development of baroclinic waves. *Journal of Atmospheric Sciences*, *50*(2), 212–225.

Orlanski, I., & Katzfey, J. (1991). The life cycle of a cyclone wave in the southern hemisphere. part i: Eddy energy budget. *Journal of Atmospheric Sciences*, *48*(17), 1972–1998.

Orlanski, I., & Sheldon, J. (1993). A case of downstream baroclinic development over

western north america. *Monthly Weather Review*, *121*(11), 2929–2950.

Orlanski, I., & Sheldon, J. P. (1995). Stages in the energetics of baroclinic systems. *Tellus A*, *47*(5), 605–628.

Parker, T. J., Berry, G. J., Reeder, M. J., & Nicholls, N. (2014). Modes of climate variability and heat waves in victoria, southeastern australia. *Geophysical Research Letters*, *41*(19), 6926–6934.

Pedlosky, J., et al. (1987). *Geophysical fluid dynamics* (Vol. 710). Springer.

Pérez, I., Barreiro, M., & Masoller, C. (2021). Enso and sam influence on the generation of long episodes of rossby wave packets during southern hemisphere summer. *Journal of Geophysical Research: Atmospheres*, *126*(24), e2021JD035467.

Peters, D., & Waugh, D. W. (1996). Influence of barotropic shear on the poleward advection of upper-tropospheric air. *Journal of Atmospheric Sciences*, *53*(21), 3013–3031.

Peters, D., & Waugh, D. W. (2003). Rossby wave breaking in the southern hemisphere wintertime upper troposphere. *Monthly weather review*, *131*(11), 2623–2634.

Pinault, J.-L. (2022). A review of the role of the oceanic rossby waves in climate variability. *Journal of Marine Science and Engineering*, *10*(4), 493.

Pinheiro, H. R., Hodges, K. I., Gan, M. A., Ferreira, S. H., & Andrade, K. M. (2022). Contributions of downstream baroclinic development to strong southern hemisphere cut-off lows. *Quarterly Journal of the Royal Meteorological Society*, *148*(742), 214–232.

Pinto, J. A., Singh, Thalheimer, L., van Aalst, M., Li, S., Sun, J., Vecchi, G., ... Dipura, R. (2022). *Climate change exacerbated rainfall causing devastating flooding in eastern south africa.*

Piva, E. D., Gan, M. A., & Rao, V. B. (2010). Energetics of winter troughs entering south america. *Monthly Weather Review*, *138*(4), 1084–1103.

Plumb, R. A. (1986). Three-dimensional propagation of transient quasi-geostrophic eddies and its relationship with the eddy forcing of the time—mean flow. *Journal of Atmospheric Sciences*, *43*(16), 1657–1678.

Postel, G. A., & Hitchman, M. H. (1999). A climatology of rossby wave breaking along

the subtropical tropopause. *Journal of the Atmospheric Sciences*, *56*(3), 359–373.

Ratna, S. B., Behera, S., Ratnam, J. V., Takahashi, K., & Yamagata, T. (2013). An index for tropical temperate troughs over southern africa. *Climate dynamics*, *41*(2), 421–441.

Reboita, M. S., Ambrizzi, T., & Rocha, R. P. d. (2009). Relationship between the southern annular mode and southern hemisphere atmospheric systems. *Revista Brasileira de Meteorologia*, *24*, 48–55.

Reboita, M. S., Nieto, R., Gimeno, L., Da Rocha, R. P., Ambrizzi, T., Garreaud, R., & Krüger, L. F. (2010). Climatological features of cutoff low systems in the southern hemisphere. *Journal of Geophysical Research: Atmospheres*, *115*(D17).

Reyers, M., & Shao, Y. (2019). Cutoff lows off the coast of the atacama desert under present day conditions and in the last glacial maximum. *Global and Planetary Change*, *181*, 102983.

Robertson, A. W., & Mechoso, C. R. (2000). Interannual and interdecadal variability of the south atlantic convergence zone. *Monthly weather review*, *128*(8), 2947–2957.

Rossby, C.-G. (1939). Relation between variations in the intensity of the zonal circulation of the atmosphere and the displacements of the semi-permanent centers of action. *Journal of Marine Research*, *2*, 38–55.

Rossby, C.-G. (1940). Planetary flow pattern in the atmosphere. *Quarterly Journal of the Royal Meteorological Society*, *66*, 68–87.

Simmons, A. J., & Hoskins, B. J. (1978). The life cycles of some nonlinear baroclinic waves. *Journal of the Atmospheric Sciences*, *35*(3), 414–432.

Simmons, A. J., & Hoskins, B. J. (1979). The downstream and upstream development of unstable baroclinic waves. *Journal of the Atmospheric Sciences*, *36*(7), 1239–1254.

Solomon, S., Daniel, J. S., Neely III, R. R., Vernier, J.-P., Dutton, E. G., & Thomason, L. W. (2011). The persistently variable "background" stratospheric aerosol layer and global climate change. *Science*, *333*(6044), 866–870.

Souders, M. B., Colle, B. A., & Chang, E. K. (2014a). The climatology and characteristics of rossby wave packets using a feature-based tracking technique. *Monthly Weather*

Review, *142*(10), 3528–3548.

Souders, M. B., Colle, B. A., & Chang, E. K. (2014b). A description and evaluation of an automated approach for feature-based tracking of rossby wave packets. *Monthly Weather Review*, *142*(10), 3505–3527.

Sreenath, N. (1993). Atmosphere tracer dynamics. *Systems Representation of Global Climate Change Models: Foundation for a Systems Science Approach*, 157–165.

Starr, V. P., & Neiburger, M. (1940). Potential vorticity as a conservative property. *J. Marine Res*, *3*, 202–210.

Strong, C., & Magnusdottir, G. (2008a). How rossby wave breaking over the pacific forces the north atlantic oscillation. *Geophysical research letters*, *35*(10).

Strong, C., & Magnusdottir, G. (2008b). Tropospheric rossby wave breaking and the nao/nam. *Journal of the atmospheric sciences*, *65*(9), 2861–2876.

Takaya, K., & Nakamura, H. (2001). A formulation of a phase-independent wave-activity flux for stationary and migratory quasigeostrophic eddies on a zonally varying basic flow. *Journal of the Atmospheric Sciences*, *58*(6), 608–627.

Taljaard, J., & Bureau, S. A. W. (1996). *Atmospheric circulation systems, synoptic climatology and weather phenomena of south africa: Rainfall in south africa* (No. pt. 6). Government Printer. Retrieved from `https://books.google.co.za/books?id=d3p8QgAACAAJ`

Teubler, F., & Riemer, M. (2021). Potential-vorticity dynamics of troughs and ridges within rossby wave packets during a 40-year reanalysis period. *Weather and Climate Dynamics*, *2*(3), 535–559. Retrieved from `https://wcd.copernicus.org/articles/2/535/2021/` doi: 10.5194/wcd-2-535-2021

Thorncroft, C., Hoskins, B., & McIntyre, M. (1993). Two paradigms of baroclinic-wave life-cycle behaviour. *Quarterly Journal of the Royal Meteorological Society*, *119*(509), 17–55.

Tyson, P. D., & Preston-Whyte, R. A. (2000). *Weather and climate of southern africa*. Oxford University Press.

Vallis, G. K. (2017). *Atmospheric and oceanic fluid dynamics*. Cambridge University

Press.

Van Der Wiel, K., Matthews, A. J., Stevens, D. P., & Joshi, M. M. (2015). A dynamical framework for the origin of the diagonal south pacific and south atlantic convergence zones. *Quarterly Journal of the Royal Meteorological Society*, *141*(691), 1997–2010.

Viljoen, E., Dyson, L., & Moyo, I. (2022). Africánes in southern africa: attributes and contribution to rainfall of a continental tropical low. *Climate Dynamics*, 1–19.

Vincent, D. G. (1994). The south pacific convergence zone (spcz): A review. *Monthly weather review*, *122*(9), 1949–1970.

Wang, X. L., Swail, V. R., & Zwiers, F. W. (2006). Climatology and changes of extratropical cyclone activity: Comparison of era-40 with ncep–ncar reanalysis for 1958–2001. *Journal of Climate*, *19*(13), 3145–3166.

Webster, E. M., et al. (2019). *A synoptic climatology of continental tropical low pressure systems over southern africa and their contribution to rainfall over south africa* (Unpublished master's thesis). University of Pretoria.

Weldon, D., & Reason, C. (2014). Variability of rainfall characteristics over the south coast region of south africa. *Theoretical and applied climatology*, *115*(1), 177–185.

Wirth, V. (2020). Waveguidability of idealized midlatitude jets and the limitations of ray tracing theory. *Weather and Climate Dynamics*, *1*(1), 111–125.

Wirth, V., & Polster, C. (2021). The problem of diagnosing jet waveguidability in the presence of large-amplitude eddies. *Journal of the Atmospheric Sciences*, *78*(10), 3137–3151.

Wirth, V., Riemer, M., Chang, E. K., & Martius, O. (2018). Rossby wave packets on the midlatitude waveguide—a review. *Monthly Weather Review*, *146*(7), 1965–2001.

WMO, M. (1957). A three-dimensional science. *WMO bull*, *6*, 134–138.

Wolf, G., & Wirth, V. (2015). Implications of the semigeostrophic nature of rossby waves for rossby wave packet detection. *Monthly Weather Review*, *143*(1), 26–38.

Wolf, G., & Wirth, V. (2017). Diagnosing the horizontal propagation of rossby wave packets along the midlatitude waveguide. *Monthly Weather Review*, *145*(8), 3247–3264.

Zilli, M. T., & Hart, N. C. (2021). Rossby wave dynamics over south america explored

with automatic tropical–extratropical cloud band identification framework. *Journal of Climate*, *34*(20), 8125–8144.

Zimin, A. V., Szunyogh, I., Hunt, B. R., & Ott, E. (2006). Extracting envelopes of nonzonally propagating rossby wave packets. *Monthly weather review*, *134*(4), 1329–1333.

Zimin, A. V., Szunyogh, I., Patil, D., Hunt, B. R., & Ott, E. (2003). Extracting envelopes of rossby wave packets. *Monthly weather review*, *131*(5), 1011–1017.